Computational Design of Transparent Polymeric Laminates subjected to Low-velocity Impact

Guillaume Olivier Antoine

Dissertation submitted to the faculty of the Virginia Polytechnic Institute and State University in partial fulfillment of the requirements for the degree of

Doctor of Philosophy
In
Engineering Mechanics

Romesh C. Batra, Chair
David A. Dillard
Saad A. Ragab
Robert C. Rogers
Shane D. Ross

9.16.2014
Blacksburg, Virginia

Keywords: Laminates, Low-velocity impact, Finite element analysis, Thermoelastoviscoplasticity, Constitutive equations, Design optimization

Computational Design of Transparent Polymeric Laminates subjected to Low-velocity Impact

Guillaume Olivier Antoine

Abstract

Transparent laminates are widely used for body armor, goggles, windows and windshields. Improved understanding of their deformations under impact loading and of energy dissipation mechanisms is needed for minimizing their weight. This requires verified and robust computational algorithms and validated mathematical models of the problem.

Here we have developed a mathematical model for analyzing the impact response of transparent laminates made of polymeric materials and implemented it in the finite element software LS-DYNA. Materials considered are polymethylmethacrylate (PMMA), polycarbonate (PC) and adhesives. The PMMA and the PC are modeled as elasto-thermo-visco-plastic and adhesives as viscoelastic. Their failure criteria are stated and simulated by the element deletion technique. Values of material parameters of the PMMA and the PC are taken from the literature, and those of adhesives determined from their test data. Constitutive equations are implemented as user-defined subroutines in LS-DYNA which are verified by comparing numerical and analytical solutions of several initial-boundary-value problems. Delamination at interfaces is simulated by using a bilinear traction separation law and the cohesive zone model.

We present mathematical and computational models in chapter one and validate them by comparing their predictions with test findings for impacts of monolithic and laminated plates. The principal source of energy dissipation of impacted PMMA/adhesive/PC laminates is plastic deformations of the PC. In chapter two we analyze impact resistance of doubly curved monolithic PC panels and delineate the effect of curvature on the energy dissipated. It is found that the improved performance of curved panels is due to the decrease in the magnitude of stresses near the center of impact.

In chapter three we propose constitutive relations for finite deformations of adhesives and find values of material parameters by considering test data for five portions of cyclic loading. Even though these values give different amounts of energy dissipated in the adhesive, their effect on the computed impact response of PMMA/adhesive/PC laminates is found to be minimal. In chapter four we conduct sensitivity analysis to identify critical parameters that significantly affect the energy dissipated. The genetic algorithm is used to optimally design a transparent laminate in chapter five.

Acknowledgements

First, I wish to express my gratitude to my advisor, Dr. Romesh C. Batra, who gave me guidance and support throughout the years of my doctoral studies. His encouragements and high level of expectations gave me the motivation to share his passion for science and dedicate myself to research.

I would like to thank my other committee members, Dr. David Dillard, Dr. Saad A. Ragab, Dr. Robert C. Rogers and Dr. Shane D. Ross for their insightful comments and for the time they shared with me. I also thank the faculty and staff of the Engineering Science and Mechanics department for their valuable help.

I acknowledge my colleagues and friends for the help and suggestions they provided me. In particular I would like to thank Dr. Alireza Chadegani and Grant Vogl with whom I have had countless exciting conversations. The time we spent together, in the office as well as outside, was a unique experience and I wish them the best of luck for their future.

I would like to thank all my friends from Blacksburg and especially my soccer teammates for the good times they shared with me during the three and half years I spent there.

Finally, I cannot close this section without expressing my deepest feelings for my wife Elizabeth. Her love and support greatly helped me during these sometimes difficult years.

Table of Contents

List of Figures

List of Tables

1 Low Speed Impact of Laminated Polymethylmethacrylate/Adhesive/ Polycarbonate Plates

G. O. Antoine and R. C. Batra*
Department of Engineering Science and Mechanics, M/C 0219
Virginia Polytechnic Institute and State University
Blacksburg, VA 24061, USA
Email: antoineguil@gmail.com; rbatra@vt.edu
*Corresponding author; Tel: 540-231-6051; Fax: 540-231-4574

The contents of this chapter have appeared in Composite Structures, **116**, 193-210, 2014.

1.1 Abstract

We study three-dimensional finite transient deformations of transparent poly-methyl-methacrylate (PMMA)/adhesive/polycarbonate (PC) laminates impacted at low speed by a hemispherical nosed rigid cylinder using the commercial finite element (FE) software LS-DYNA. The two glassy polymers PMMA and PC are modeled as thermo-elasto-visco-plastic materials by using the constitutive relation proposed by Mulliken and Boyce and modified by Varghese and Batra. For the nearly incompressible viscoelastic bonding layer, the elastic response is modeled by the Ogden relation and the viscous response by the Prony series. Delamination at interfaces between the adhesive and the polymeric sheets is simulated by using the cohesive zone model incorporated in LS-DYNA. The effective plastic strain, the maximum principal stress, and the maximum stress based failure criteria are used for delineating failure in PC, PMMA and the adhesive, respectively. Failed elements are deleted from the analysis domain. The three layers are discretized by using 8-node brick elements and integrals over elements are numerically evaluated by using a reduced Gauss integration rule. The coupled nonlinear ordinary differential equations obtained by the Galerkin approximation are integrated by using the conditionally stable explicit algorithm. Results have been computed for at least two different FE meshes. The computed number and configurations of cracks in the PMMA are found to qualitatively agree with the test observations. It is also found that the energy dissipated due to plastic deformations in the PC is considerably more than that due to cracks formed in the PMMA.

Key Words: Laminates, impact, cracks, damage, finite elasto-plastic deformations

1.2 Introduction

Polymers are composed of long chains of monomers while a metal is generally a polycrystalline material. This difference in the microstructure explains why their thermo-mechanical response is quite different. Polymers usually exhibit strong strain-rate dependence in their mechanical response and are widely used as transparent armors because of their high specific impact performance, e.g., see Radin and Goldsmith [1]. Sands et al. [2] have reported that polymethylmetha-acrylate (PMMA) and polycarbonate (PC) polymers have better impact resistance than most glasses. Rabinowitz et al. [3] used a high pressure torsion test to experimentally investigate the effect of pressure on the quasi-static shear stress-shear strain response and on the fracture strain of PMMA and poly(ethylene terephthalate). They found that an increase in the hydrostatic pressure increases the yield strain, the yield stress and the fracture stress of the materials but decreases the fracture strain.

The mechanical behavior of glassy polymers has been experimentally and computationally studied by several investigators. Duckett et al. [4] experimentally studied the strain rate and pressure dependence of the yield stress of PMMA and poly (ethylene terephthalate) deformed in uniaxial compression at strain rates from 10^{-6}/s to 10^{-1}/s. They found that the yield stresses in compression and torsion increase monotonically with increasing strain-rate and decreasing temperature. This was confirmed by Arruda et al. [5] in the same range of strain rates and by Mullliken and Boyce [6] for low to high strain rates (up to 10^{3}/s). Similar conclusions about the dependence of the yield strain and the yield stress upon the strain rate and the temperature hold for the PC material [6-11]. Moy et al. [8] performed uniaxial compression tests on Lexan 9034A PC from 10^{-4}/s to 4600/s strain rates. They used an Instron test machine for the quasi-static tests and a split-Hopkinson (Kolsky) bar for the high strain rate experiments. Rittel et al. [12] studied heating of PMMA samples subjected to uniaxial compressive cyclic loading at stress levels above the yield stress of the PMMA and at strain rates up to 0.1/s. They related the temperature rise to the chain mobility of the polymers. Rittel [13] and Rittel and Rabinowitz [14] performed uniaxial tensile and cyclic tests on PMMA and PC at low strain rates and measured the temperature rise.

Schmachtenberg et al. [15] proposed a method to find values of material parameters for modeling the mechanical behavior of thermoplastics. Arruda et al. [5] performed uniaxial compression tests on PMMA samples at various strain rates and temperatures, and developed a material model for the PMMA based on the multiplicative decomposition of the deformation gradient into elastic, thermal and inelastic parts. Moreover, they assumed that a part of the energy dissipated due to inelastic deformations is converted into heating while the remainder contributes to the back stress. Richeton et al. [9-11] used shift factors for the strain rate and the stresses to model the temperature and strain rate dependence of the yield stress of amorphous polymers. Richeton et al. [16] and Tervoort et al. [17] employed a spring in series with a dashpot and a Langevin spring to derive constitutive equations for polymers. Buckley and Jones [18] modeled the behavior of amorphous polymers near the glass transition temperature by decomposing the stress into two components, a bond stretching stress (partially irreversible) and a reversible conformational stress, and introduced a shift factor for the temperature and the strain rate dependence of the elastic moduli. Alavarado-Contreras et al. [19] used a simple chemical description of the amorphous and the crystalline phases to derive equations describing the mechanical behavior of amorphous semicrystalline materials. An eight-chain model is used for the amorphous phase and the stress tensor for this phase is the sum of a conformational stress tensor and a back-stress tensor. The deformation of the crystalline phase is assumed to be driven by effective shear stresses along its eight slip systems. Furthermore, they introduced two scalar variables that represent damage in each phase, proposed their evolution relations, and considered the loss of stiffness of the material due to progressive damage prior to failure. Boyce et al. [20] and Mulliken and Boyce [6] introduced a rate dependent model for the behavior of glassy polymers that assumes the coexistence of three different phases with the same values of the deformation gradient at a material point. Two of these phases have similar constitutive equations with different values of material parameters, and the third phase contributes to the general stress via a back-stress component. This material model has been generalized by Varghese and Batra [21, 22] to account for the dependence of the elastic moduli upon the temperature and temperature dependent strain softening. Predictions from this work for uniaxial tensile and compressive deformations compare well with the test results at low and high strain rates.

The damage initiation and evolution, and the failure of polymers have been studied experimentally and numerically. Lajtai [23] studied the failure of pre-cracked specimens subjected to compressive loading

and used a modified Coulomb model to study the final stages of their failure. Saghafi et al. [24] proposed a criterion to predict mode II and mixed-mode fracture toughness of brittle materials. Using data obtained from three-point bend tests on marble specimens they found that their criterion predicted better the failure of specimens than that given by the maximum tangential stress (MTS) criterion. Seweryn [25] proposed a criterion for brittle fracture of structures with sharp notches based on modes I, II and III stress intensity factors. Seweryn and Lukaszewicz [26] analyzed crack initiation in brittle specimens with V-shaped notches under mixed mode loading and found good agreement between the experimental measurements and the J-integral computed with the boundary element method. Vandenberghe et al. [27] proposed a model of crack formation in PMMA plates impacted at normal incidence. They considered energy dissipated due to crack formation and for flexural deformations of petals formed in the cracked plate. They could accurately predict the number of cracks formed in the plate as a function of the impact speed and the plate thickness.

Schultz [28] has related the failure of semicrystalline polymers to the spherulitic structure of the material and the inter- and intra-spherulitic fracture. Zaïri et al. [29] proposed constitutive equations to describe the progressive void growth in elasto-viscoplastic polymers, and showed that their model could predict well the stress-strain response of rubber-modified PMMA deformed in uniaxial tension. Ayatollahi et al. [30] performed fracture tests on semi-circular PMMA specimens containing an edge crack and modeled crack propagation using the finite element method (FEM) and the MTS failure criterion. They accurately predicted the crack trajectory in semi-circular bend (SCB) specimens. For small pre-existing cracks in an infinite PMMA medium, Beaumont et al. [31] investigated the relation between the crack propagation speed and the stress intensity factor at the crack tip for mode I failure of sharply-notched specimens. Wada et al. [32] experimentally studied the impact fracture toughness of edge-cracked PMMA specimens and computationally analyzed their 3D deformations using the FEM. Marshall et al. [33] introduced a factor to account for the notch size in the calculation of the energy release-rate for the PMMA material, which enabled them to derive a material specific energy/area that is independent of the specimen geometry. In their work the ratio of the initial crack length to the width of the sample ranged between 0.03 and 0.5. Moy et al. [34] found that the failure of PMMA is ductile at strain rates $\ll 1/s$ and brittle at strain rates $\gg 1/s$. Weerasooriya et al.'s [35] test data have revealed that the fracture toughness of PMMA for strain rates >100/s is almost twice that for quasi-static loading.

The failure modes of PC are quite different from those of PMMA. Chang and Chu [36] study the effect of temperature and notch-tip radius on the fracture mode of PC and of a modified PC. They found the existence of a semi-ductile fracture mode at low temperatures (–40 °C) for some notch-tip radii and proposed a diagram describing the 2D-fracture mode of PC as a function of the temperature and of the notch-tip radius. Mills [37] performed Charpy impact tests on notched PC bars and studied the effect of annealing on the ductile to brittle failure transitions. Fraser and Ward [38] investigated the effect of the notch-tip radius on the impact fracture behavior of PC samples. Allen et al. [39] measured the Charpy impact strength of notched polydiancarbonate and found that the polymer exists in two different varieties with different yield and failure properties, but did not relate this difference to the morphology of the polymers. Rittel et al. [40] tested cracked specimens and delineated two failure mechanisms, opening and shear banding, in PC as a function of the mode-mixity. Rittel and Levin [41] used two different experimental set-ups to study crack propagation in PC with either mode-I dominant or mode-II dominant deformations. They found that the same mechanisms govern the failure of PC regardless of the mode-mixity. Curran et al. [42] analyzed the fracture of PC disks subjected to dynamic flat-plate impact and

predicted the level of damage induced in the PC sample with a damage model based on the nucleation, growth and coalescence of cracks. Plati and Williams [43, 44] compared the energy release rate of different polymers including PMMA and PC obtained with Charpy and Izod tests at different temperatures, and found that they gave essentially the same value of the energy release rate. Adams et al. [45] used three-point bend specimens made of five different polymers (PC, polyacetal, two nylons and PMMA) to measure the plane strain fracture toughness of these materials under impact loading. Ogihara et al. [46] examined fracture mechanisms of polymeric materials by high velocity impact and quasistatic perforation tests and compared the static and the dynamic perforation energies of PMMA plates with various edge lengths and thicknesses. Fleck et al. [47] pointed out that craze nucleation was the principal failure mechanism for both PMMA and PC at high strain rates despite PMMA exhibiting brittle failure and PC ductile failure. Livingstone et al. [48] and Richards et al. [49] used a bulk strain based failure criterion to model damage in PC and a principal tensile stress criterion to model the failure of polyurethane interlayer during their simulations of the impact of a glass/interlayer/PC laminate. They accurately simulated the fracture pattern of the impacted plate, and predicted the ballistic limit (v_{50}) within 10% accuracy. Kelly [50] used the Johnson-Holmquist failure criterion to simulate damage in PC and PMMA.

Kihara et al. [51] measured the impact shear strength of adhesive interlayers, and developed an experimental apparatus that can be used to deform an adhesive in shear at high strain rates. They used it in conjunction with the FE simulations to determine the maximum shear stress in the sample at fracture and showed that it equals the impact shear strength.

The study of failure of plates subjected to low speed impact is important for analyzing the survivability of goggles, aircraft canopy and windshields. Tsai and Chen [52] have investigated the fracture of a glass plate impacted by a spherical (deformable or rigid) body. They related the critical stress developed in the plate to the impact velocity, the plate thickness and the support span. They found that the Hertzian fracture (formation of a fracture cone under the impact site) is predominant for short support span and the sample fails due to flexural fracture for large support spans. Fountzoulas et al. [53] used the FEM to investigate the effect of defects on the impact response of aluminate spinel ($MgAl_2O_4$), polyurethane and PC plates. Gilde et al. [54] performed ballistic impact tests on monolithic PMMA plates and on glass/PMMA/PC laminates, and exploited the synergy between glass and polymers to create a lightweight transparent armor with improved ballistic resistance. They showed that the laminated structure rather than a monolithic glass increased the ballistic limit by nearly 50% for the same areal density. In numerical work, the v_{50} of a structure equals the minimum impact speed required to perforate it.

Zee et al. [55] used a gas gun to conduct impact tests on composites made of epoxy matrix reinforced with polyethylene and polyester fibers. They found that the energy loss mechanisms are the fracture of the target and the generation of frictional heat due to the passage of the projectile through the composite. Tarim et al. [56] experimentally studied the ballistic impact performance of polymer-based composites. They performed high velocity (between 180 and 425 m/s, bullets with mass ranging from 3.2 to 15.55 grams) impact experiments on composites and showed that adding layers to the structure increases its bending and tensile stiffness and reduces the residual velocity of the bullet for perforated targets.

The low-velocity impact of composite panels is often modeled as quasi-static indentation. Wu and Chang [57] used the finite element method to study the quasi-static impact of a graphite/epoxy sandwich beam

with an elasto-plastic foam core. They found that matrix cracking could be predicted by comparing the principal stresses in the matrix with the transverse strength of the lamina and used the strain-energy release rate (SERR) to predict the delamination. Tita et al. [58] studied the low-velocity impact (indentation) response of carbon fiber reinforced epoxy disks by using a user defined subroutine implemented in the FE code ABAQUS. They accounted for progressive damage of the material by degrading the material properties, i.e., the elastic moduli, and found that the damage induced by indentation is more localized than that for impact. Palazotto et al. [59] developed an analytical model for the quasi-static impact of composite sandwich plates. They used stress-based criteria to predict initiation of damage and degraded the stiffness of the materials to study its progression. The model accurately predicted the indentation response of the laminate panel and the core failure load. Cheon et al. [60] proposed that the progressive damage of glass fiber-reinforced composites during a Charpy impact test be simulated by deleting the fractured part of the specimen at each stage of the loading which degrades the stiffness of the composite and causes the energy to dissipate. Batra et al. [61] used constitutive relations based on a micromechanical approach to model the impact response of a carbon fiber-reinforced polymer composite plate. They implemented the material model in a user-defined subroutine in the finite element code ABAQUS and considered inertia effects in the impact simulations. They could predict accurately the contact force and the damage and failure of the plate.

Stenzler and Goulbourne [62] and Stenzler [63] performed impact tests on PMMA/Adhesive/PC laminated plates with DFA4700, IM800A and VHB4905 as adhesives. The examination of the post failure of plates revealed that the front PMMA plate had radial cracks whereas the adhesive and the PC layers remained undamaged (no failure of the adhesive interlayer or of the PC rear plate was visually noticed). Zhang et al. [64] and Tekalur et al. [65] studied the low speed impact of a PMMA plate, and reported crack patterns typical of brittle failure. Gunnarsson et al. [66] performed impact tests on monolithic PC plates of various thicknesses. They reported time histories of the maximum deflection of 3.0, 4.45 and 5.85 mm thick plates for impact velocities between 10 and 50 m/s, and found that the penetration velocity for the 5.85 and 3.0 mm thick plates equaled 80 m/s and 65 m/s, respectively. Gunnarsson et al. [67] conducted impact tests at velocities between 10 and 50 m/s on monolithic and laminated structures involving PMMA, PC and an adhesive. They found that PMMA (PC) has brittle (ductile) failure. Stickle and Shultz [68] simulated oblique ballistic (~750 m/s) impact on a PMMA plate, used the Johnson-Cook damage model (accounting for limited plastic deformations of PMMA), and combined it with a principal stress fracture criterion (accounting for the brittle failure (spalling) of PMMA under tensile loading) to model damage and failure of PMMA.

The mechanical behavior and failure of the PMMA, PC and TPUs (thermoplastic polyurethanes) materials taken separately can be accurately modeled for a wide range of strains, strain rates and temperatures. However, the impact response of composite PMMA/adhesive/PC laminates has mostly been studied experimentally. Here we propose a mathematical and a computational model that accounts for the complex response of the polymeric materials including effects such as strain-rate and temperature dependence, plasticity, viscosity, brittle and ductile failure and predicts the impact response and survivability of monolithic and laminated plates. The model includes brittle and ductile failure of the various constituents of the plate (failure within the materials) as well as interfacial failure on faces of the bonding interlayers (delamination). It can predict well the response of laminates to low velocity impact. It can be used to improve our understanding of their impact response, and delineate the role of the different

constituents and interactions amongst them. We note that in our simulations the steel impactor is regarded as rigid and all contact surfaces as smooth.

The rest of the paper is organized as follows. Section 1.2 gives the mathematical model of the problem (i.e., problem description, constitutive relations for different constituents of the laminate, failure criteria for the PMMA, the PC, the TPUs, and values of material parameters). The computational model is described in Section 1.3, and results of several problems are presented in Section 1.4, and discussed in Section 1.5. Conclusions from this work are summarized in Section 1.6.

1.3 Mathematical Model

1.3.1 Problem Description

A schematic sketch of the problem studied is exhibited in Fig.1–1. The laminated rectangular plate of sides L_1 and L_2, and made of PMMA/adhesive/PC layers is impacted at normal incidence by a slow moving steel cylinder of height h and a hemispherical nose of diameter d_0. We use rectangular Cartesian coordinate axes with origin at the centroid of the top face of the rectangular laminated plate clamped on all four edges, the positive x-axis pointing to the right and the positive z-axis pointing upwards. The thicknesses of the top PMMA, the middle adhesive and the bottom PC layers are denoted by h_1, h_2 and h_3, respectively. The mathematical model developed and the analysis technique is applicable to an arbitrary number of layers in the laminate, and their materials.

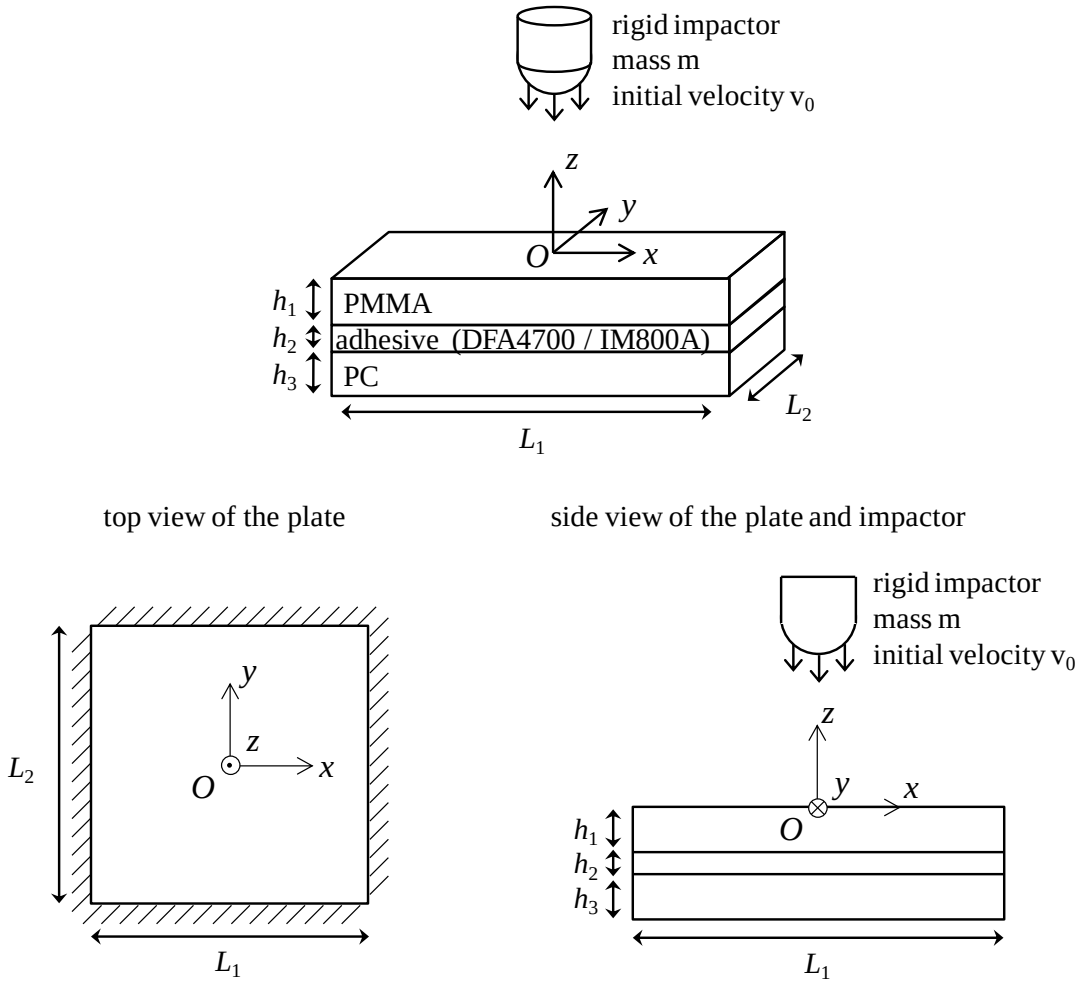

Fig.1–1: Sketch of the impact problem studied.

1.3.2 Equations of Motion

We use the Lagrangian description of motion to study deformations of the laminate. Thus balance laws governing deformations of the body are:

$$\begin{aligned} &\text{mass:} && \rho J = \rho_0 \\ &\text{linear momentum:} && \rho_0 \dot{\mathbf{v}} = \hat{\nabla} \cdot \mathbf{T} \\ &\text{moment of momentum:} && \mathbf{T} \cdot \mathbf{F}^{\mathrm{T}} = \mathbf{F} \cdot \mathbf{T}^{\mathrm{T}} \end{aligned} \qquad (1\text{–}1)$$

Here ρ and ρ_0 are mass densities in the current and the reference configurations, respectively, $J = \det(\mathbf{F})$ is the Jacobian of the deformation, $\mathbf{F} = \partial \mathbf{x} / \partial \mathbf{X}$ is the deformation gradient that maps a material point from the reference position $\mathbf{X}$ to its current location $\mathbf{x}$, a superimposed dot indicates the material time derivative, $\mathbf{v}$ is the velocity of a material point, $\mathbf{T}$ is the first Piola-Kirchhoff stress tensor related to the Cauchy stress tensor $\boldsymbol{\sigma}$ by $\mathbf{T} = J\boldsymbol{\sigma} \cdot \mathbf{F}^{-\mathrm{T}}$, and $(\hat{\nabla} \cdot)$ is the divergence operator with respect to $\mathbf{X}$.

For low impact speeds, deformations of the steel impactor are assumed to be negligible as compared to those of the composite laminate. Thus we regard the impactor as rigid. Equations governing the translational and rotational motion of the rigid impactor are:

$$\begin{aligned} &\text{translation} && \dot{\mathbf{p}} = \mathbf{f} \\ &\text{rotation} && \dot{\mathbf{H}}_{\mathrm{C}} = \mathbf{M}_{\mathrm{C}} \end{aligned} \tag{1–2}$$

Here $\mathbf{p}$ and $\mathbf{H}_{\mathrm{C}}$ are the linear momentum and the moment of linear momentum (or the angular momentum) of the rigid impactor, respectively, $\mathbf{f}$ is the resultant force acting on the impactor, $\mathbf{M}_{\mathrm{C}}$ is the moment of forces acting on it, and the subscript C on a quantity implies that it is calculated with respect to the center of mass C of the rigid body.

1.3.3 Initial, Boundary and Continuity Conditions

We study problems with bounding surfaces of the laminate, except for the surface contacting the impactor, either clamped or free. At a clamped edge, the three displacement components are set equal to zero. At a free surface, the surface tractions vanish. The contact surface between the impactor and the laminated plate is assumed to be smooth. Thus on it the following continuity conditions are imposed.

$$\begin{aligned} &\text{normal velocity:} && [\![\dot{\mathbf{u}}]\!]\cdot\mathbf{n} = 0 \\ &\text{normal traction:} && [\![\mathbf{t}]\!]\cdot\mathbf{n} = 0 \\ &\text{tangential traction on the contact surface:} && \big([\![\mathbf{t}]\!]\cdot\mathbf{n}\big)\times\mathbf{n} = \mathbf{0} \end{aligned} \tag{1–3}$$

Here double brackets enclosing a variable indicate the jump in it across the contact surface, $\mathbf{n}$ is a unit normal to the contact surface, $\mathbf{u}$ is the displacement field, $\mathbf{t}$ is the traction vector, and the symbol $\times$ denotes the cross product between two vectors.

The PMMA, the PC and the adhesive are initially at rest, stress free and at the uniform temperature of 300 K. At $t = 0$, the impactor just contacts the top surface of the laminated structure.

1.3.4 Constitutive Equations for PMMA and PC

The thermo-elasto-visco-plastic response of the PMMA and the PC polymers are modeled following the work of Mulliken and Boyce [6] with the modifications suggested by Varghese and Batra [21]. It assumes that the total Cauchy stress tensor $\boldsymbol{\sigma}$ at a material point equals the sum of contributions from three phases, namely B, α and β, i.e., $\boldsymbol{\sigma} = \boldsymbol{\sigma}_{\mathrm{B}} + \boldsymbol{\sigma}_{\alpha} + \boldsymbol{\sigma}_{\beta}$. The three phases coexist at a material point and have the same value of the deformation gradient $\mathbf{F}$. The phase B behaves like a non-linear elastic Langevin spring for which

$$\boldsymbol{\sigma}_{\mathrm{B}} = \frac{C_{\mathrm{R}}}{3}\frac{\sqrt{N_l}}{\lambda^{\mathrm{p}}} L^{-1}\left(\frac{\lambda^{\mathrm{p}}}{\sqrt{N_l}}\right)\overline{\mathbf{B}}'_{\mathrm{B}} \tag{1–4}$$

Here $\boldsymbol{\sigma}_{\mathrm{B}}$ is the Cauchy stress tensor, $\overline{\mathbf{B}}'_{\mathrm{B}}$ the deviatoric part of $\overline{\mathbf{B}}_{\mathrm{B}} = J^{-2/3}\mathbf{F}\mathbf{F}^{\mathrm{T}}$, $\lambda^{\mathrm{p}} = \sqrt{\mathrm{tr}(\overline{\mathbf{B}}_{\mathrm{B}})/3}$ a measure of stretch, $\mathrm{tr}()$ the trace operator, L^{-1} the inverse of the Langevin function defined by $L(\beta) \equiv \coth\beta - 1/\beta$, N_l the limiting stretch, $C_{\mathrm{R}} \equiv n_{\mathrm{R}} k\theta$ the rubbery modulus, θ the temperature in Kelvin, k Boltzmann's constant, and n_{R} a material parameter.

The other two phases, α and β, are modeled with the same constitutive equations but with different values of material parameters. For each phase the deformation gradient **F** is decomposed into elastic and plastic parts, e.g., see Kroner [69] and Lee [70]:

$$\mathbf{F} = \mathbf{F}^{\mathrm{e}}_{\alpha}\mathbf{F}^{\mathrm{p}}_{\alpha} = \mathbf{F}^{\mathrm{e}}_{\beta}\mathbf{F}^{\mathrm{p}}_{\beta} \tag{1–5}$$

Neither $\mathbf{F}^{\mathrm{e}}_{\alpha}$, $\mathbf{F}^{\mathrm{e}}_{\beta}$ nor $\mathbf{F}^{\mathrm{p}}_{\alpha}$, $\mathbf{F}^{\mathrm{p}}_{\beta}$ is gradient of a vector field. The plastic deformation gradients $\mathbf{F}^{\mathrm{p}}_{\alpha}$ and $\mathbf{F}^{\mathrm{p}}_{\beta}$ map a material point in the reference configuration to a material point in the intermediate configuration obtained after elastically unloading the current configuration to a stress-free state.

The rate of the plastic deformation gradient in phases α and β is given by

$$\dot{\mathbf{F}}^{\mathrm{p}}_{\alpha} = \mathbf{F}^{\mathrm{e}^{-1}}_{\alpha}\tilde{\mathbf{D}}^{\mathrm{p}}_{\alpha}\mathbf{F} \quad , \quad \dot{\mathbf{F}}^{\mathrm{p}}_{\beta} = \mathbf{F}^{\mathrm{e}^{-1}}_{\beta}\tilde{\mathbf{D}}^{\mathrm{p}}_{\beta}\mathbf{F} \tag{1–6}$$

where $\tilde{\mathbf{D}}^{\mathrm{p}}_{i}$ is the plastic strain rate tensor in phase i ($i = \alpha, \beta$), and it has been assumed that the plastic spin tensors in phases α and β identically vanish. We note that $\tilde{\mathbf{D}}^{\mathrm{p}}_{i}$ does *not* equal the symmetric part of the velocity gradient (with respect of **x**) of phase i.

The Hencky elastic strain tensors of phases α and β are defined as

$$\boldsymbol{\varepsilon}^{\mathrm{e}}_{\alpha} = \ln\left(\sqrt{\mathbf{F}^{\mathrm{e}}_{\alpha}\mathbf{F}^{\mathrm{e}^{\mathrm{T}}}_{\alpha}}\right) \quad , \quad \boldsymbol{\varepsilon}^{\mathrm{e}}_{\beta} = \ln\left(\sqrt{\mathbf{F}^{\mathrm{e}}_{\beta}\mathbf{F}^{\mathrm{e}^{\mathrm{T}}}_{\beta}}\right) \tag{1–7}$$

and the corresponding Cauchy stress tensors are given by

$$\boldsymbol{\sigma}_{\alpha} = \frac{1}{J}\left[2\mu_{\alpha}\boldsymbol{\varepsilon}^{\mathrm{e}}_{\alpha} + \lambda_{\alpha}\mathrm{tr}(\boldsymbol{\varepsilon}^{\mathrm{e}}_{\alpha})\boldsymbol{\delta}\right] \quad , \quad \boldsymbol{\sigma}_{\beta} = \frac{1}{J}\left[2\mu_{\beta}\boldsymbol{\varepsilon}^{\mathrm{e}}_{\beta} + \lambda_{\beta}\mathrm{tr}(\boldsymbol{\varepsilon}^{\mathrm{e}}_{\beta})\boldsymbol{\delta}\right] \tag{1–8}$$

where Young's moduli of phases α and β of PMMA and PC and consequently Lame's constants, λ and μ, are temperature and strain-rate dependent. They partly capture the temperature and the strain-rate dependence of the material response while Poisson's ratio is taken to be constant. Using test data given in the Appendix of Mulliken's thesis [71], we compute the temperature and the strain-rate dependence of Young's moduli of PMMA and PC. These results depicted in Fig.1–2 and Fig.1–3 imply that the total Young's modulus of each material increases with an increase in the strain-rate and decreases with a rise in the temperature. We note that Eq.(1–8) is valid for finite deformations and accounts for all geometric nonlinearities.

The plastic strain rates are assumed to be coaxial with the deviatoric Cauchy stress tensors in their respective phases, that is,

$$\tilde{\mathbf{D}}_{\alpha}^{\mathrm{p}} = \dot{\gamma}_{\alpha}^{\mathrm{p}} \frac{\boldsymbol{\sigma}_{\alpha}^{'}}{\left|\boldsymbol{\sigma}_{\alpha}^{'}\right|} \quad , \quad \tilde{\mathbf{D}}_{\beta}^{\mathrm{p}} = \dot{\gamma}_{\beta}^{\mathrm{p}} \frac{\boldsymbol{\sigma}_{\beta}^{'}}{\left|\boldsymbol{\sigma}_{\beta}^{'}\right|} \tag{1–9}$$

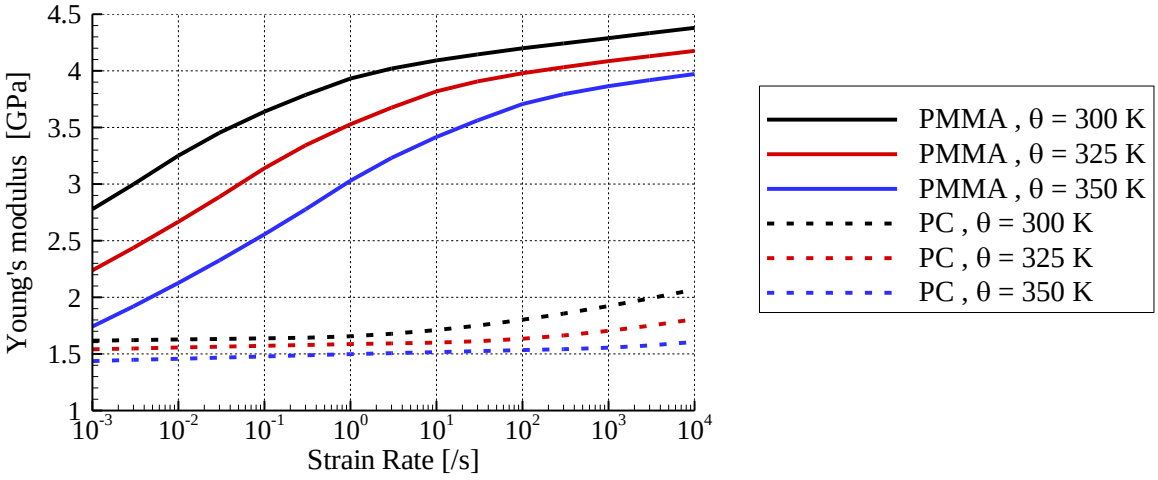

Fig.1–2: Variation with the strain rate of the total Young's modulus (E_{α}+E_{β}) of the PMMA and the PC.

where $\boldsymbol{\sigma}_{i}^{'}$ (i = α, β) is the deviatoric part of the Cauchy stress in phase i, $\left|\boldsymbol{\sigma}_{i}^{'}\right| = \sqrt{\mathrm{tr}\left(\boldsymbol{\sigma}_{i}^{\prime}\boldsymbol{\sigma}_{i}^{\prime}\right)}$ is the magnitude of $\boldsymbol{\sigma}_{i}^{'}$, and $\dot{\gamma}_{i}^{\mathrm{p}}$ is the effective plastic strain rate in phase i. This equation implies that $\mathrm{tr}(\tilde{\mathbf{D}}_{i}^{\mathrm{p}}) = 0$.

The effective plastic strain rates in α and β phases are given by

$$\dot{\gamma}_{i}^{\mathrm{p}} = \dot{\gamma}_{0i}^{\mathrm{p}} \exp\left[-\frac{\Delta G_{i}}{k\theta}\left(1 - \frac{\tau_{i}}{t_{i}\hat{s}_{i} + \alpha_{i}^{\mathrm{p}} p}\right)\right] \quad , \quad i = \alpha, \beta \tag{1–10}$$

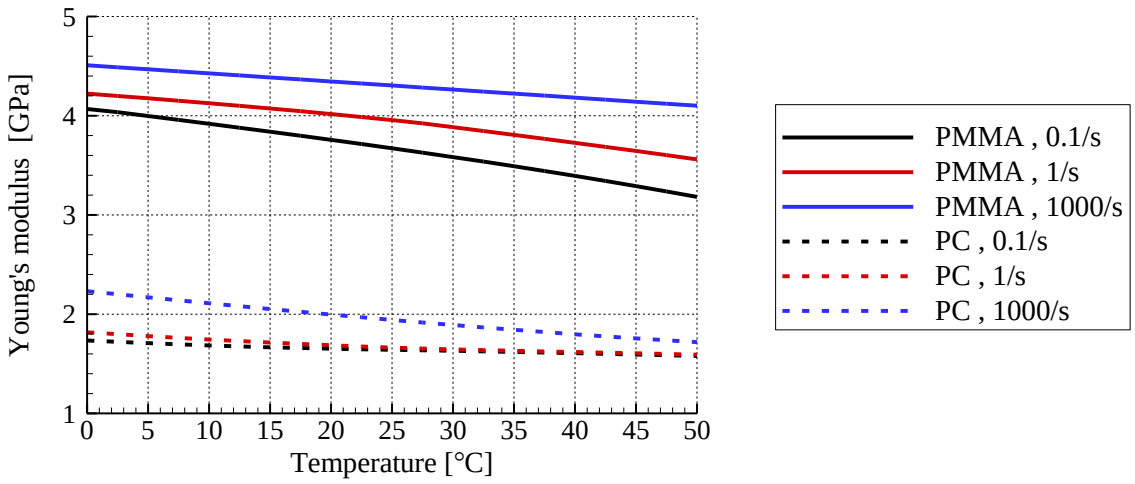

Fig.1–3: Variation with the temperature of the total Young's modulus (E_α+E_β) of the PMMA and the PC.

where $\dot{\gamma}_{0i}^{\mathrm{p}}$ ($i = \alpha, \beta$) is the pre-exponential factor, ΔG_i the activation energy, $p = -\operatorname{tr}(\boldsymbol{\sigma})/3$ the pressure, $\tau_i = \sqrt{0.5\operatorname{tr}\left(\boldsymbol{\sigma}_i^{'}\boldsymbol{\sigma}_i^{'}\right)}$ the equivalent shear stress, α_i^{p} the pressure coefficient, $\hat{s}_i = 0.077\mu_i/(1-\nu_i)$ the athermal shear strength, ν_i Poisson's ratio, k Boltzmann's constant, and t_i an internal variable that evolves with plastic deformations. The variable $\hat{s}_i$ is function of μ_i and is, therefore, temperature and strain-rate dependent. Since no yield surface is postulated plastic deformations always occur. The evolution of internal variable t_i in phases α and β is given by

$$\dot{t}_i = \frac{h_i}{\hat{s}_i^0}\left(1-\frac{t_i}{t_i^{\mathrm{ss}}}\right)\dot{\gamma}_i^{\mathrm{p}} \quad , \quad i = \alpha, \beta \tag{1–11}$$

where t_i^{ss} and h_i are softening parameters, and $\hat{s}_i^0$ is the reference value of $\hat{s}_i$ given by the reference values of μ_i and ν_i. Eq.(1–11) implies that the internal variable t_i remains constant for elastic deformations.

We postulate that the energy dissipated during plastic deformations in the α and β phases is converted into heat, that is

$$\dot{Q} = J \cdot \left(\boldsymbol{\sigma}_\alpha : \tilde{\mathbf{D}}_\alpha^{\mathrm{p}} + \boldsymbol{\sigma}_\beta : \tilde{\mathbf{D}}_\beta^{\mathrm{p}}\right) \tag{1–12}$$

where $\dot{Q}$ is the heat generated per unit volume in the reference configuration. It is assumed that heating is mostly adiabatic for the impact problems studied here because there is not enough time for the heat to be conducted away, and neglecting heat conduction facilitates numerical integration of the governing differential equations. Thus the temperature rise is given by

$$\rho_0 c\dot{\theta} = \dot{Q} \tag{1–13}$$

where *c* is the specific heat of either the PMMA or the PC.

We refer the reader to Mulliken and Boyce [6] and Varghese and Batra [21] for the determination of values of material parameters from the test data for the PMMA and the PC, and for the comparison of the computed and experimental axial stress vs. axial strain curves.

1.3.5 Constitutive Equations for the Adhesives

We assume that the adhesive can be modeled as a nearly incompressible rubberlike material [63] with the elastic response given by the Ogden strain energy density function *W* and the viscoelastic response by the Prony series [72, 73]. That is,

$$W = \sum_{n=1}^{N} \frac{\mu_n}{\alpha_n}\left(\tilde{\lambda}_1^{\alpha_n} + \tilde{\lambda}_2^{\alpha_n} + \tilde{\lambda}_3^{\alpha_n} - 3\right) + K\left(J - 1 - \ln(J)\right) \tag{1–14}$$

where *N* is an integer, $\tilde{\lambda}_i = (J)^{-1/3}\lambda_i$ is the volumetric independent principal stretch, α_n and μ_n are material parameters, and *K* and *G*, respectively, the initial bulk and the shear moduli given by $K = \frac{2(1+\nu)}{3(1-2\nu)}G$, $G = \mu = \frac{1}{2}\sum_{n=1}^{N}\alpha_n\mu_n$

The viscoelastic response of the adhesive is assumed to obey the following constitutive relation proposed by Christensen [73].

$$\overset{\bullet}{\hat{\boldsymbol{\sigma}}}^{\text{ve}} = \sum_{m=1}^{M} 2G_m\hat{\mathbf{D}}^{\text{dev}} - \sum_{m=1}^{M} 2\beta_m G_m \int_{\tau=0}^{t} e^{-\beta_m(t-\tau)}\hat{\mathbf{D}}^{\text{dev}}(\tau)d\tau \tag{1–15}$$

Here M is the number of terms in the summation, $\overset{\bullet}{\hat{\boldsymbol{\sigma}}}^{\text{ve}}$ is the co-rotated rate of stress tensor (see [74] for the definition of co-rotated tensors), $\hat{\mathbf{D}}^{\text{dev}}$ is the co-rotated deviatoric rate-of-deformation tensor, and G_m and β_m are material parameters representing, respectively, the shear moduli and the inverse of relaxation times. Note that there are 2 terms that determine the instantaneous elastic response of the material: Eq.(1–14) and the 1st term on the right-hand side of Eq.(1–15)

Heating of the adhesive caused by the energy dissipated due to viscous deformations is neglected since it is usually very small.

We use the test data of Stenzler [63] to find values of material parameters for the DFA4700 and the IM800A. Stenzler tested these materials in uniaxial tension at engineering strain rates of 0.01, 0.1, 1.0 and 5.0/s and in uniaxial compression at 0.001/s. The tests at 0.01/s and 0.001/s are assumed to correspond to the static nonlinear elastic response of the material and are used to find values of material parameters in the strain energy density potential (see Eq.(1–14)). As described below, for the DFA4700 (IM800A), two (one) terms in Eq.(1–14) are necessary to achieve satisfactory agreement (within 5% deviation) between the computed and the experimental axial stress – axial strain curves. Assuming that the adhesive material is incompressible, the axial stress – axial strain relation for a uniaxial tensile test conducted at constant engineering strain rate is:

$$\sigma^{\text{True}} = \sum_{n=1}^{N} \mu_n \left(\exp\left(\alpha_n \varepsilon^{\text{True}}\right) - \exp\left(-\frac{1}{2} \alpha_n \varepsilon^{\text{True}} \right) \right) + \sum_{m=1}^{M} 3G_m \exp\left(-\frac{\exp(\varepsilon^{\text{True}})}{\dot{\varepsilon}^{\text{Eng}}} \beta_m \right) \left[\text{Ei}\left(\frac{\exp(\varepsilon^{\text{True}})}{\dot{\varepsilon}^{\text{Eng}}} \beta_m \right) - \text{Ei}\left(\frac{\beta_m}{\dot{\varepsilon}^{\text{Eng}}} \right) \right] \quad (1\text{–}16)$$

where σ^{True} is the axial Cauchy stress, $\varepsilon^{\text{True}}$ the axial logarithmic strain, $\dot{\varepsilon}^{\text{Eng}}$ the constant engineering strain rate at which the test is conducted, and $\text{Ei}(x) = -\int_{t=-x}^{\infty} \frac{e^{-t}}{t} dt$. The software MATHEMATICA was used to find values of parameters in Eq.(1–16) so that the computed axial stress – strain curve is close to the experimental one. A single term in the series for the IM800A and two terms for the DFA4700 adhesive were found to be sufficient. The values of material parameters are given in Table 1–1, and the computed and the experimental stress – strain curves are depicted in Fig.1–4 for the DFA4700 and in Fig.1–5 for the IM800A. The deviations between the two sets of curves are listed in Table 1–2. We note that the two adhesives are assumed to be slightly compressible because we could not model incompressible materials in LS-DYNA. The three different values, 0.490, 0.495 and 0.498, of Poisson's ratio showed no noticeable differences among the computed results. The numerical results presented and discussed herein are obtained with Poisson's ratio = 0.498 which gives the initial bulk modulus of about 250 times the initial shear modulus. Values of Poisson's ratio greater than 0.498 significantly increase the computational cost, and were not considered. We note that only the monotonic part of the experimental axial stress-strain curve has been employed to find values of material parameters.

	DFA4700		IM800A	
	Mass density [mg/mm^3]	Initial Poisson's ratio	Mass density [mg/mm^3]	Initial Poisson's ratio
	1.08	0.498	1.04	0.498
	Elastic properties (strain rate independent response) for the Ogden strain energy density *W*)			
n	μ_n [MPa]	α_n	μ_n [MPa]	α_n
1	0.0421	5.70	2.55	1.28
2	-4.49	-1.03		
	Viscoelastic properties (strain rate dependent response, parameters in Prony series) Shear modulus, 1/relaxation time			
m	G_m [MPa]	β_m [s^{-1}]	G_m [MPa]	β_m [s^{-1}]
1	2.63	3.76	0.358	0.391
2	0.563	0.139		

Table 1–1: Values of material parameters of the DFA4700 and the IM800A adhesives.

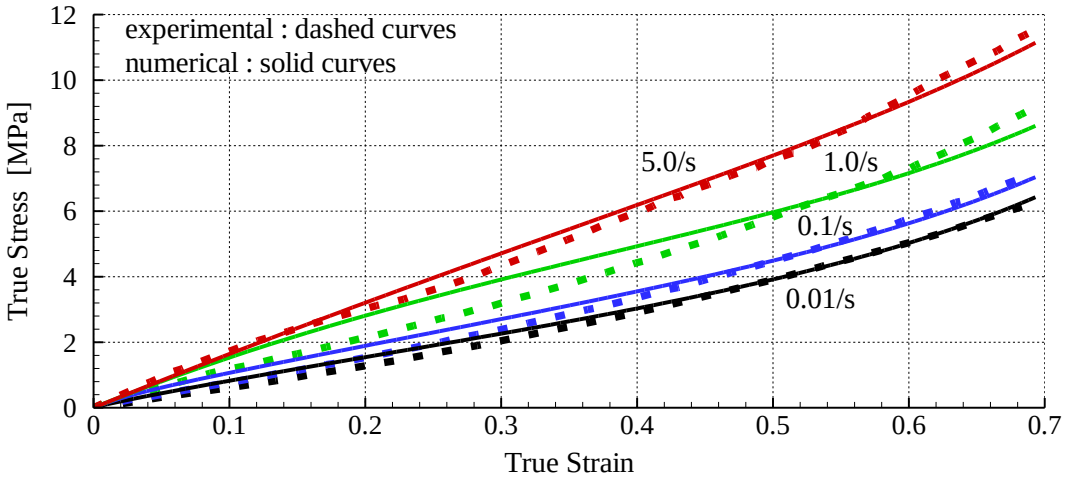

Fig.1–4: Experimental and numerical results for the uniaxial tensile deformations of DFA4700 at different engineering strain rates.

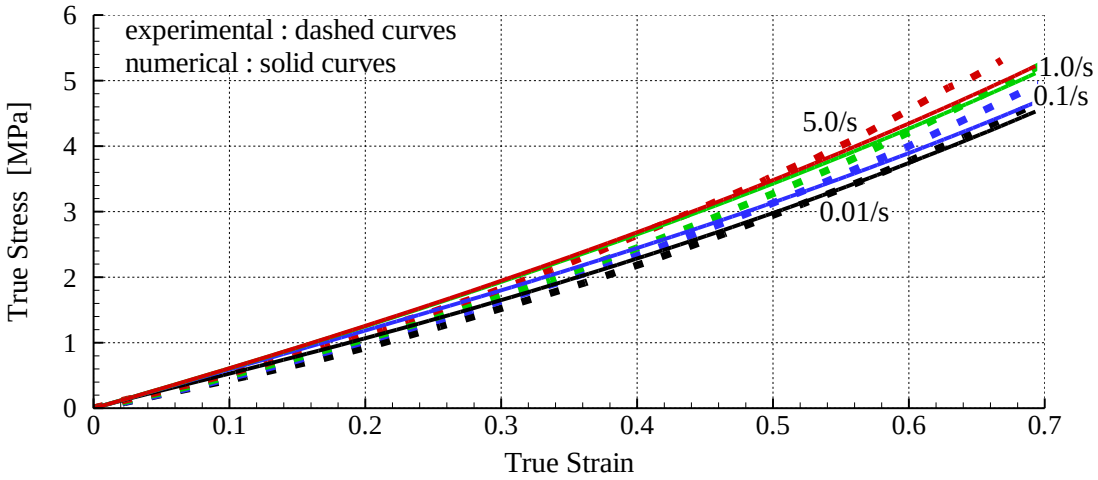

Fig.1–5: Experimental and numerical results for the uniaxial tensile deformations of IM800A at different engineering strain rates.

Engineering strain rate	0.01/s	0.1/s	1.0/s	5.0/s
DFA4700	5.01%	6.50%	9.87%	3.74%
IM800A	3.97%	5.10%	5.81%	4.50%

Table 1–2: Deviations in L^2-norm between the predicted and the experimental responses of the DFA4700 and the IM800A subjected to axial loading.

1.3.6 Failure Models

We model the brittle failure of PMMA in tension by using the following maximum tensile stress based criterion proposed by Fleck et al. [47]:

$$\sigma_f = \frac{1}{v_f}\left(kT\ln\left(\frac{\dot{\varepsilon}}{\dot{\varepsilon}_0}\right) + Q_f \right) \tag{1–17}$$

Here $\dot{\varepsilon}$ is the effective strain rate, $\dot{\varepsilon}_0$ =1.0/s the reference effective strain rate, k the Boltzmann constant, σ_f the tensile stress at failure, T the local temperature in Kelvin, Q_f = 2.95×10^{-19} J and v_f = 2.30×10^{-18} mm^3 . These values of Q_f and v_f correspond to 178 kJ/mol activation energy and 2.3 nm^3 activation volume and are comparable to the values given in [47] (54 kJ/mol activation energy and 4 nm^3 activation volume for tensile tests). According to Eq.(1–17) the tensile stress at failure increases with the increase in the strain rate.

A strain based failure criterion is used to model the ductile failure of the PMMA and the PC. That is, the material point is assumed to fail when the accumulated logarithmic equivalent plastic strain in either phase α or phase β reaches a critical value of 5% for the PMMA [68] and 200% for the PC [49]. We note that there are two failure criteria for the PMMA – one given by Eq.(1–17) for the brittle failure and the 5% plastic strain for the ductile failure.

Following the work of Richards et al. [49] the failure of the DFA4700 and the IM800A adhesives is assumed to be controlled by the maximum principal tensile stress. Folgar [75] and MacAloney et al. [76] performed quasi-static uniaxial tensile tests on the IM800A polyurethane until specimens failed. The manufacturer documentation [75] lists an ultimate elongation of 510% at failure (1.8 true strain) with 28 MPa ultimate engineering stress (170 MPa true stress) while ultimate elongations between 1400% and 1500% (2.7–2.8 true strain) were measured by MacAloney et al. [76]. The manufacturer documentation of the DFA4700 adhesive [77] lists 500% ultimate elongation with 37.9 MPa ultimate strength for a uniaxial tensile test. This corresponds to the true axial strain of 1.8 and the true axial stress of 225 MPa.

In the results presented below, it has been assumed that the DFA4700 (IM800A) fails when the maximum principal tensile stress equals 225 MPa (170 MPa).

1.3.7 Delamination Criterion

We use the bilinear traction-separation relation, exhibited in Fig.1–6, in the cohesive zone model (CZM) to simulate delamination at an interface between two distinct materials, e.g., see Gerlach et al. [78]. The ultimate displacements in modes I and II have the same value δ^{f}, the damage initiation displacements in modes I and II also have the same value δ^0, and we take $\delta^0 = \delta^{\mathrm{f}}/2$. For mixed-mode deformations, we define $\delta_{\mathrm{m}} = \sqrt{\delta_{\mathrm{I}}^2 + \delta_{\mathrm{II}}^2}$ where δ_{I} is the separation in the normal direction (mode I) while δ_{II} is the relative tangential displacement (mode II). The mixed-mode damage initiation displacement is $\delta_{\mathrm{m}}^0 = \delta^0$. Likewise the mixed-mode ultimate displacement is $\delta_{\mathrm{m}}^{\mathrm{f}} = \delta^{\mathrm{f}}$.

Different values of the ultimate displacement δ^f between 0.01 and 0.05 mm gave essentially the same values of the resisting force experienced by the impactor and the energy dissipated. Here we have assumed that δ^f = 0.05 mm. The value of the maximum traction in the CZM is determined from the value of the critical strain energy release rate for the interface.

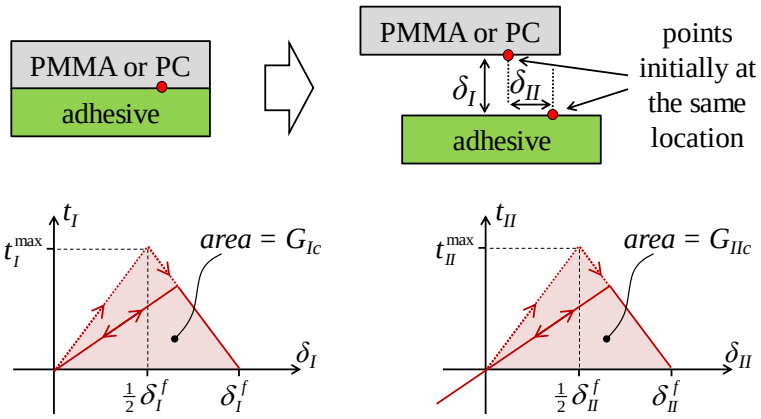

Fig.1–6: Traction-separation law for delamination in mode I (bottom, left) and mode II (bottom, right).

Pickett et al. [79] have conducted 90° peel tests on aluminum/DFA4700/PC assemblies, and reported the peel strength of 26.18 kN/m for one adhesive/PC configuration. Thus 26.2 N/mm (or equivalently 0.02618 J/mm^2) corresponds to the mode I toughness of the DFA4700/PC interface. Due to lack of data about the mode II toughness of this interface, we assume that $G_{\mathrm{II,C}} = 2\ G_{\mathrm{I,C}}$, which is typical for an interface between a soft polyurethane adhesive and a material with surface properties similar to those of PC. Furthermore, it is assumed that the PMMA/DFA4700 and DFA4700/PC interfaces have the same toughness values.

The manufacturer documentation for the IM800A (Folgar [75]) gives results of 90° peel tests of the IM800A from a glass substrate. For 80, 90, 100 and 120 °C temperature, the IM800A/glass peel force equals, respectively, 144, 155, 160 and 138 pli (pounds per linear inch). A linear fit of the peel force vs. the temperature through the first three data points gave the peel strength of 17 N/mm at 20 °C.

It was then assumed that the PMMA/IM800A and the IM800A/PC interfaces have the same properties as the IM800A/glass interface, and that $G_{\mathrm{II,C}} = 2\ G_{\mathrm{I,C}}$.

1.4 Computational Model

1.4.1 General description

We use the commercial FE software LS-DYNA with explicit solver in which constitutive relations for the PMMA and the PC have been implemented in a user-defined subroutine written in FORTRAN. The software has in-built material model to simulate deformations of the adhesives.

For an impact problem, Khalili et al. [80] computed numerical results for different choices of the shell element, the integration scheme and the FE mesh. They found that the “unstructured” mesh gave better results in terms of convergence vs. computational cost. We also observed a similar trend (see description

of the FE mesh later in this section). They also showed that assuming the impactor to be rigid reduces the computation time with minor effects on the numerical results.

As stated above, the impactor has been modeled as a rigid body translating with a uniform velocity normal to the impact surface. All contact surfaces are assumed to be frictionless. Non-interpenetration of one material into the other is satisfied by using a penalty-based contact algorithm that considers the newly formed surfaces due to the deletion of failed elements.

In LS-DYNA, the governing partial differential equations are first reduced to nonlinear and coupled ordinary differential equations (ODEs) in time by using the Galerkin approximation. The ODEs are integrated with respect to time by using the explicit conditionally stable central-difference method using the lumped mass matrix. The critical time step size equals the time taken for an elastic wave to propagate through the smallest element in the FE mesh. We set the time step size equal to a fraction of the critical time step to ensure stability of the computed solution. The effect of the time step size on the numerical solution was investigated and the time step is fixed to a value for which the numerical solution converged. Of course, each FE mesh requires a different time step size.

The FE mesh consisted of 8-node brick elements with one point integration (reduced integration) used to evaluate element matrices. Since zero energy deformation modes (or hourglass modes) can arise due to using reduced integration rule, an hourglass control algorithm was used. The suitability of this algorithm was checked with a 3D-patch test. A cube is discretized into seven irregularly shaped hexahedrons (one for each face and one for the center, see Fig.1–7). The master cube is then quasi-statically deformed in uniaxial tension. Results computed with the default and the Belytschko–Bindeman formulations are shown in Fig.1–8 for an isotropic elastic material with Young's modulus = 1 GPa and Poisson's ratio = 0.25. The later formulation was selected for all numerical simulations presented herein. The energy of hourglass mode deformations was found to be less than 5% of the peak strain energy of the elastic cube implying that the hourglass modes did not introduce significant errors in the numerical solution.

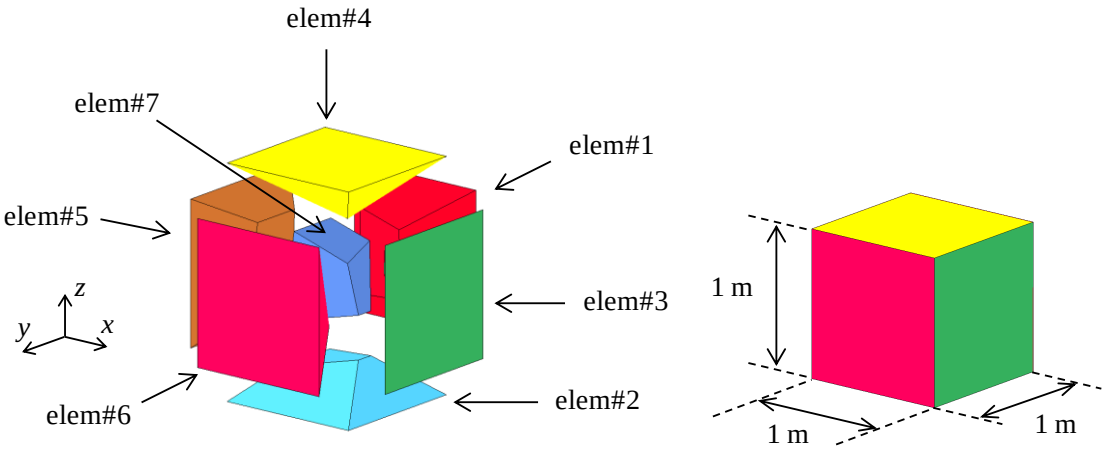

Fig.1–7: Master cube formed with 7 irregularly shaped hexahedrons used to check the hourglass control formulation.

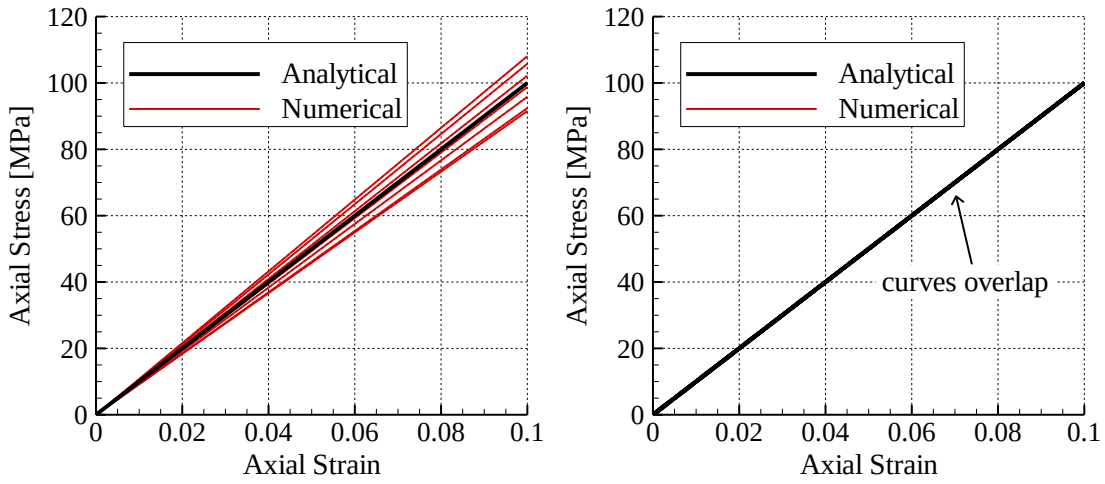

Fig.1–8: Analytical stress and the computed stress in the seven hexahedron elements for the uniaxial tensile test of the master cube. Left (Right): with the default (the Belytschko-Bindeman) hourglass control.

For the Hertz contact problem analyzed with LS-DYNA, the maximum difference between the computed and the analytical reaction force was found to be 9.1%.

For each impact problem studied in this paper, results were computed with at least two FE meshes. The FE mesh A was uniformly refined to obtain a finer mesh B having at least 30% more nodes than those in mesh A. The solution with two FE meshes was taken to have converged if the difference in two values of the reaction force, the energy dissipated and the length of the radial cracks was less than 10%. For brevity we describe here the mesh used for the impact simulations of the laminate discussed in subsection 1.5.3 (and that gave the converged solution). For each one of the three layers the mesh in the *xy*-plane is the same. The PMMA, the interlayer and the PC are discretized, respectively, with 9, 6 and 9 uniform elements through the thickness. The CZM elements are initially flat and placed at the adhesive interfaces. The pattern of the FE mesh in the *xy*-plane is obtained by partitioning the plate along its diagonals. Then each of the four quarters of the plate is partitioned by a 10-mm radius circle centered at the point of impact. Each quarter of circumference of the circle, the part of each one of the four diagonals that are within the circle, and each edge of the plate are discretized with 55 uniform elements. The outer part of the plate diagonals, i.e., the part located more than 10-mm from the plate center, was divided into 64 segments of different lengths so that the ratio of the smallest segment – located near the circle – to the largest segment – located at the corner – equaled 15. The mesh in the impactor near the contact region was refined until the element size there was comparable to that of the elements at the plate center. The rest of the impactor was discretized with coarse elements. The FE mesh had 19,680 elements in the impactor, 209,376 elements in the PMMA and the PC layers, 139,584 elements in the adhesive interlayer, and 23,264 flat CZM elements in each interface.

The computed values of the time histories of the reaction force and the energy dissipated with perfect bonding at the PMMA/adhesive and the adhesive/PC interfaces differed from those computed considering delamination at these interfaces by less than 5%. Thus we present and discuss here only the results obtained using CZM elements at the adhesive interfaces.

1.4.2 Calculation of the Energy Dissipation

There are two main sources of energy dissipation, namely, energy dissipated due to failure of the materials (modeled with element deletion) and the energy dissipated due to inelastic deformations of the material (plasticity, viscosity, softening). When a failed element is deleted from the computational domain, its internal energy and kinetic energy are also removed. This decreases the energy of the remaining system. This change in energy is referred to as the eroded energy in LS-DYNA. The eroded energies calculated by LS-DYNA were verified using a set of simple problems for which internal and kinetic energies could be analytically determined and compared with the computed ones.

The energy dissipated due to viscous deformations of the adhesives is computed during the post-processing phase. The energy dissipated due to inelastic deformations of the PMMA and the PC is calculated for each element at each time step inside the subroutine developed for these materials. There are two sources of dissipation for these materials: energy dissipated by plastic deformations, and energy dissipated by the softening of the material attributed to decrease in Young's modulus caused by the temperature rise. This latter contribution to the energy dissipated will be referred to as "softening energy". An analogy for 1D linear elasticity and discrete stiffnesses (i.e., springs) is shown in Fig.1–9. Due to stretching of the springs elastic energy is stored in the system. Subsequent heating reduces the stiffness of the material that can be simulated by removing a spring which dissipates a part of the elastic energy stored in the spring that is taken out of the system.

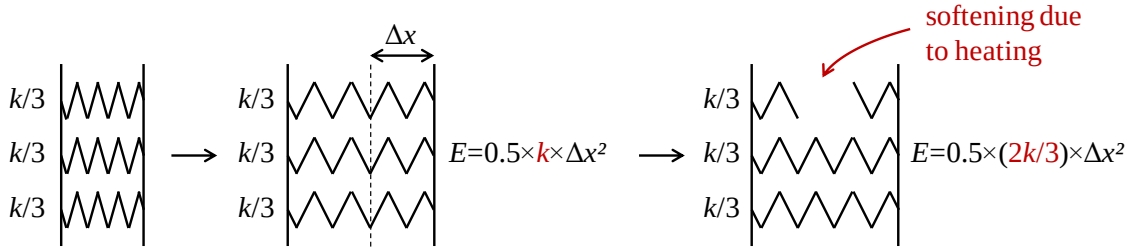

Fig.1–9: Visualization of the energy dissipated due to material softening for 1D linear elastic system with a discrete spring model.

1.5 Results and Discussion

1.5.1 Impact of Monolithic PMMA Plates

We first simulate the impact experiments of Zhang et al. [64] in which initially stationary and stress free clamped circular 6.35 mm thick PMMA plates of 76.2 mm diameter are impacted at normal incidence by 6.95 kg cylindrical impactor with hemispherical nose of 12.7 mm diameter translating at 0.7, 1.0, 2.0, 3.0 or 5.0 m/s. It is clear from the experimental and the computed fracture patterns in the plates impacted at 2.0 m/s and 3.0 m/s shown in Fig.1–10 that the two sets of results agree well qualitatively. Both in tests and in simulations radial cracks but no hole developed in the plate impacted at 2.0 m/s, while the panel impacted at 3.0 m/s had radial cracks and had been perforated by the drop weight. The computed number of cracks and the crack patterns differ from those found experimentally.

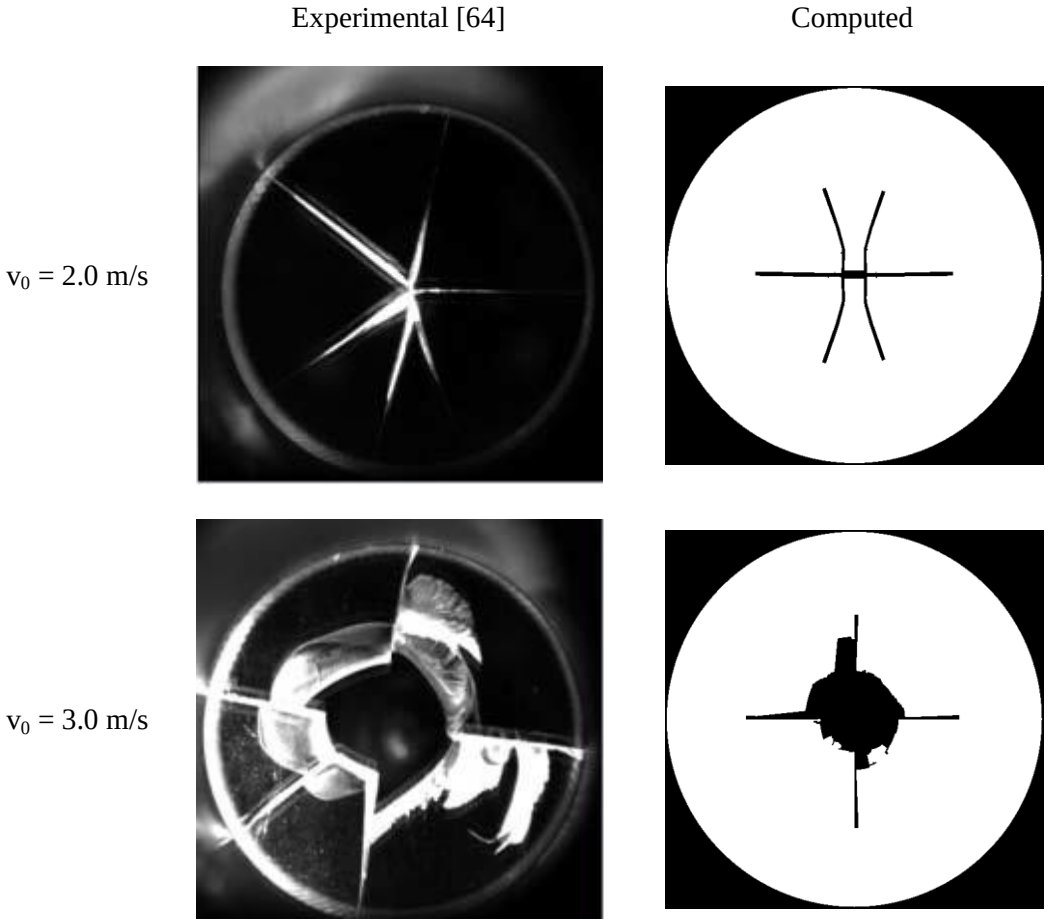

Fig.1–10: Experimental and computed fracture patterns in the PMMA panels impacted at normal incidence by the rigid cylindrical impactor translating at 2.0 and 3.0 m/s.

1.5.2 Impact of Monolithic PC Plates

We now simulate impact experiments of Gunnarsson et al. [66] in which initially stationary and stress free clamped square PC plates of side 25.4 cm and different thicknesses are impacted at normal incidence by a 104 g cylindrical steel impactor with hemispherical nose of 12.7 cm diameter. For various values of the plate thickness and the impact speed, we have compared in Table 1–3 the experimentally measured and the computed maximum deflections of the center of the back surface of the plates. The maximum difference in the two sets of values of 10.3% validates the mathematical model for the impact of the PC plate, at least for finding the maximum deflections. In Fig.1–11 we have plotted time histories of the experimental and the computed deflections of the center of the back surface of the 5.85 and 12.32 mm thick panels impacted at various velocities. While the time of return to 0 deflection is well captured by the model for the 12.32 mm thick panel, it is not so for the 5.85 mm thick panel especially at the higher impact speed of 50.6 m/s.

Panel thickness [mm]	Impact velocity [m/s]				
	10	20	30	40	50
	Experimental (computed) maximum deflection [mm]				
3.00	13.2 (13.0) error: -1.5%	16.1 (17.1) error: +6.2%			
4.45	9.4 (9.0) error: -4.3%	12.9 (13.1) error: +1.6%			
5.85	6.5 (7.1) error: +9.2%	10.9 (10.2) error: -6.4%	15.2 (14.8) error: -2.6%	19.2 (19.0) error: -1.0%	22.0 (22.7) error: +3.2%
9.27			10.2 (10.4) error: +2.0%	11.3 (12.1) error: +7.1%	14.0 (14.8) error: +5.7%
12.32			6.9 (7.3) error: +5.8%	8.7 (9.6) error: +10.3%	10.7 (11.3) error: +5.6%

Table 1–3: Comparison of the experimental and the computed maximum deflections (measured at the center of the back face of the plate) of the clamped circular PC panels.

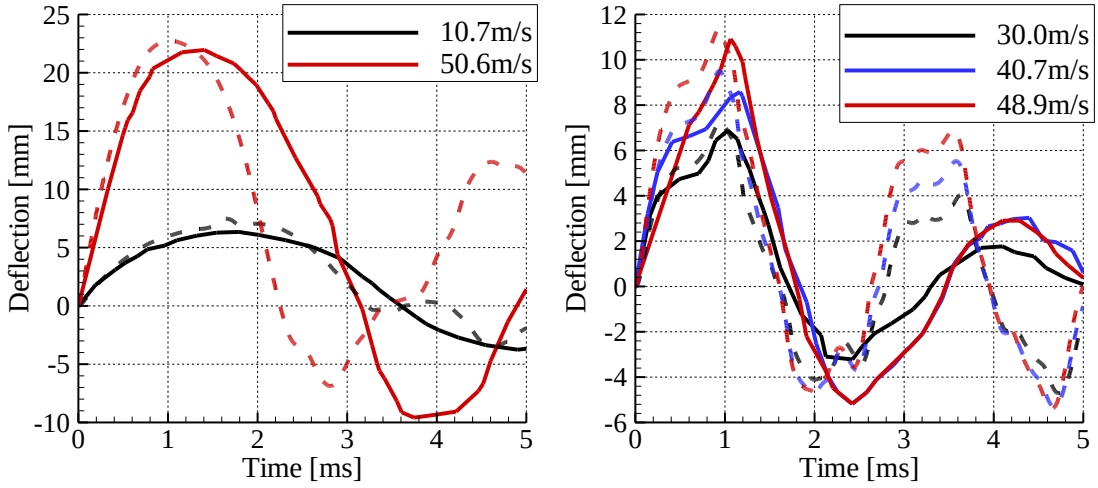

Fig.1–11: Time histories of the experimental (solid curves) and the computed (dashed curves) deflections of the centers of the back face of the PC plates of thickness 5.85 mm (left) and 12.32 mm (right).

The time periods of the first three modes of free vibrations of the 5.85 mm and the 12.32 mm thick clamped PC plates are 1.32, 1.60, 2.35 ms, and 0.66, 0.80, 1.12 ms, respectively. Comparing these with the time histories of the deflection of the plates shown above, we see that there is no clear correlation between the time periods of free vibration and time periods of the contact force histories.

1.5.3 Impact of Laminated Plates

We now study transient deformations of 12.7×12.7 cm² clamped PMMA/Adhesive/PC laminated plate impacted at normal incidence by a 28.5 g 1-cm diameter hemispherical nosed steel cylinder at either 12 m/s or 22 m/s. Using the notation of Fig.1–1, we set $h_1 = h_3 = 1.5875$ mm, and $h_2 = 0.635$ mm for the adhesive interlayer. Thus the top PMMA and the bottom PC layer have the same thickness. This configuration was used by Stenzler [63] in his experiments.

Time histories of the experimental [63] and computed reaction force for the plates bonded with the DFA4700 and the IM800A adhesives are displayed in Fig.1–12 and the deviations between the two sets of results are summarized in Table 1–4.

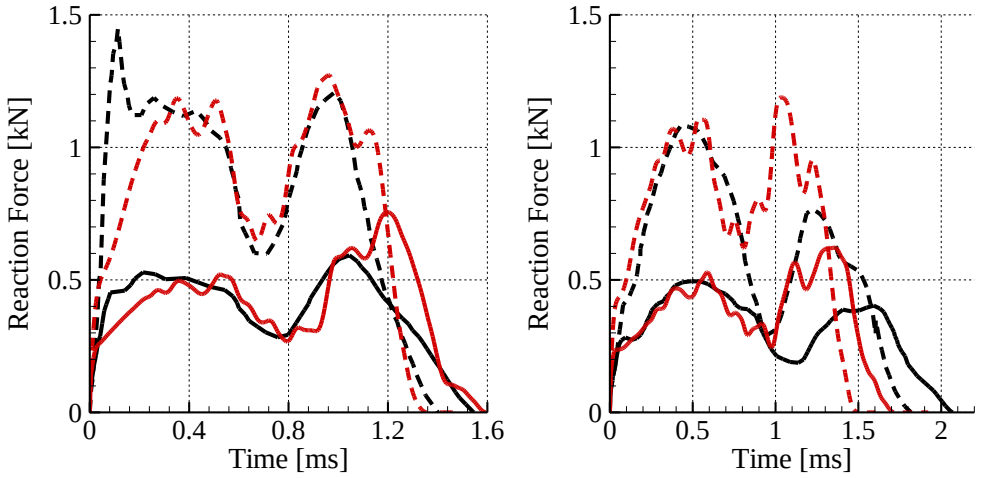

Fig.1–12: Experimental (dark curves) and computed (red curves) reaction force time histories for the PMMA/DFA4700/PC (left) and the PMMA/IM800A/PC (right) plates impacted at 12 m/s (dashed curves) and 22 m/s (solid curves).

The time periods of the first four modes of free vibrations of the clamped laminated plates are 0.82, 0.96, and 1.34 ms (two modes) for the plate with the DFA4700 interlayer, and 0.97, 1.03, and 1.43 ms (two modes) for the IM800A adhesive. Therefore we can see that for both plates the drop in the reaction force coincides with the time period of the 1st mode, the second peak to that of the 2nd mode, and the contact termination with that of the 3rd period.

Plate	12 m/s impact velocity	22 m/s impact velocity
PMMA-DFA4700-PC	0.26	0.23
PMMA-IM800A-PC	0.46	0.43

Table 1–4: L^2-norm of the difference between the experimental and the computed reaction force vs. time curves.

We note that the computed and the experimental time histories of the reaction force for the PMMA/DFA4700/PC laminate are close to each other except for small times for the 22 m/s impact speed and around 1.2 ms for the 12 m/s impact speed. The large local differences between the two curves give L^2-norm deviations of about 25%. However, the numerically computed results for the PMMA/IM800A/PC laminate differ noticeably from the corresponding test findings for times beyond the time of the first peak in the reaction force. In particular the second spike in the computed reaction force at $t \approx 1.1$ ms is not found in test results. The qualitative shape of the reaction force history curve (two peaks separated by a drop) is consistent with the experimental results of Wu and Chang [57] and to the corresponding simulations by Her and Liang [81] who used ANSYS/LS-DYNA (these results were obtained for low-velocity impact of graphite/epoxy composites). Moreover we notice that the maximum

value reached by the reaction force is nearly proportional to the impact velocity, which agrees with the observations of Her and Liang [81].

The characteristics of the computed crack patterns in the PMMA plate are compared with those found experimentally in Table 1–5. In Fig.1–13 we have exhibited the crack patterns on the back surface of the PMMA plate obtained for the impact speed of 12 m/s, and in Fig.1–14 and Fig.1–15 we have depicted the experimental and the computed post-impact failure of the PMMA plate. These two sets of results are in good agreement with each other for the four impact scenarios studied. One can conclude from these results that the adhesive significantly affects the fracture of the PMMA plate since a change in the adhesive material noticeably alters the fracture induced in the PMMA plate. The evolution with time of the failed and hence the deleted region in the PMMA plate is also exhibited in Fig.1–15. Whereas in the simulations, a cavity is developed in the PMMA plate, in tests this material is severely deformed and its mechanical properties severely degraded but it is not removed from the plate.

Impact velocity [m/s]	Interlayer material	Experimental	Computed
12	DFA4700	No damaged material at the impact site 5 cracks, length 4~7 mm	No damaged material at the impact site 4 cracks, length 10~11mm
12	IM800A	No damaged material at the impact site 5 cracks, length 14~17 mm	No damaged material at the impact site 4 cracks, length 12~13mm
22	DFA4700	Diameter of damaged zone at the impact site = 5 mm 7 cracks, length 11~12 mm	Diameter of damaged zone at the impact site = 6 mm 8~9 cracks, length 10~11 mm
22	IM800A	Diameter of damaged zone at the impact site = 5 mm 6 cracks, length 22~28 mm	Diameter of damaged zone at the impact site = 7 mm 8 cracks, length 31~33mm

Table 1–5: Comparison of the experimental and the computed fracture patterns on the back surface of the PMMA plate for the PMMA/DFA4700/PC and the PMMA/IM800A/PC laminates.

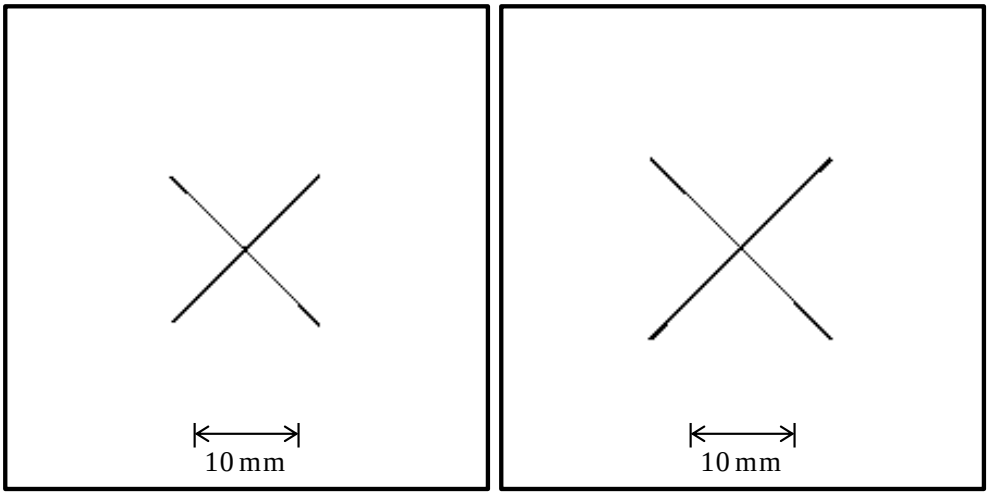

Fig.1–13: Computed fracture patterns on the back surface of the PMMA plates of the PMMA/DFA4700/PC (left) and the PMMA/IM800A/PC (right) laminates for 12m/s impact speed.

(a)

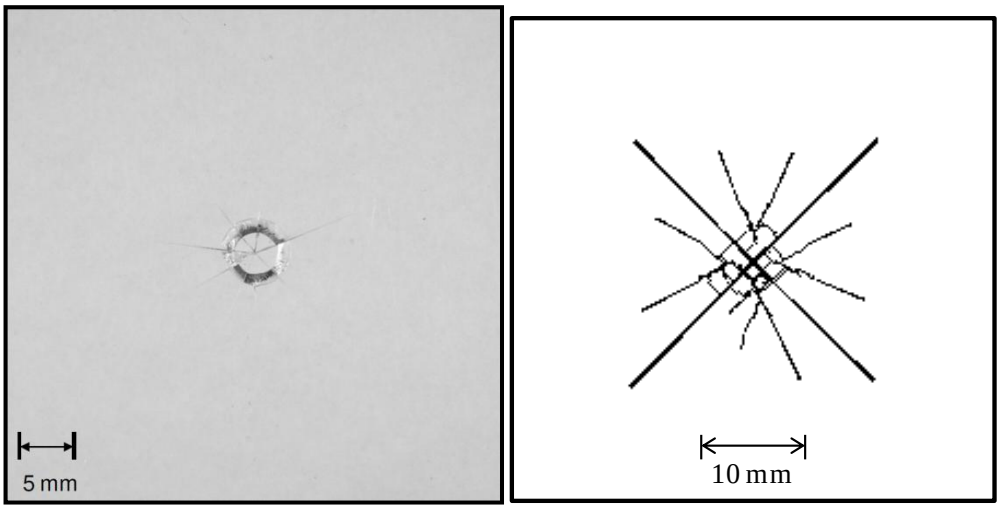

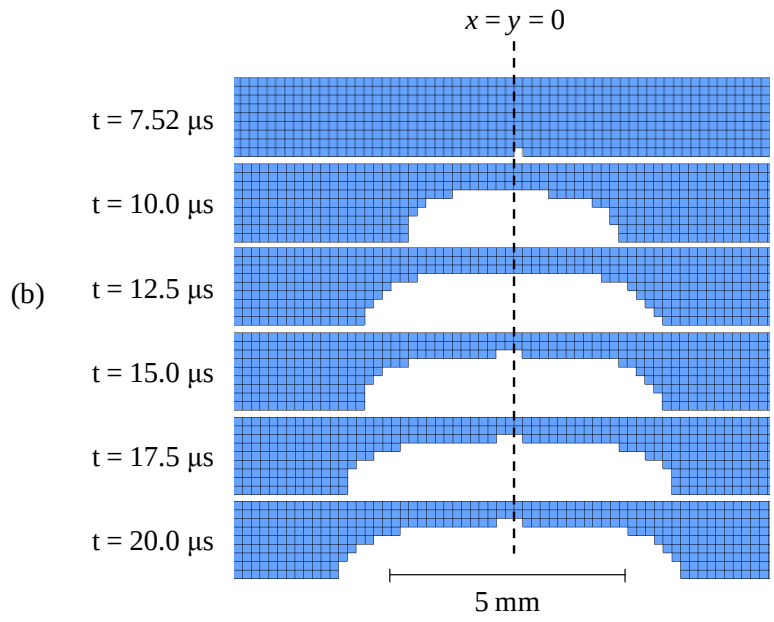

Fig.1–14: Details of the experimental [63] (left) and the computed (right) fracture pattern on the back surface of the PMMA plate of the PMMA/DFA4700/PC laminate for 22 m/s impact speed.
(a): view orthogonal to $\mathbf{e}_z$ after impact.
(b): view normal to $(\mathbf{e}_x + \mathbf{e}_y)$ (since the main cracks form along the diagonals) for the PMMA plate at various times.

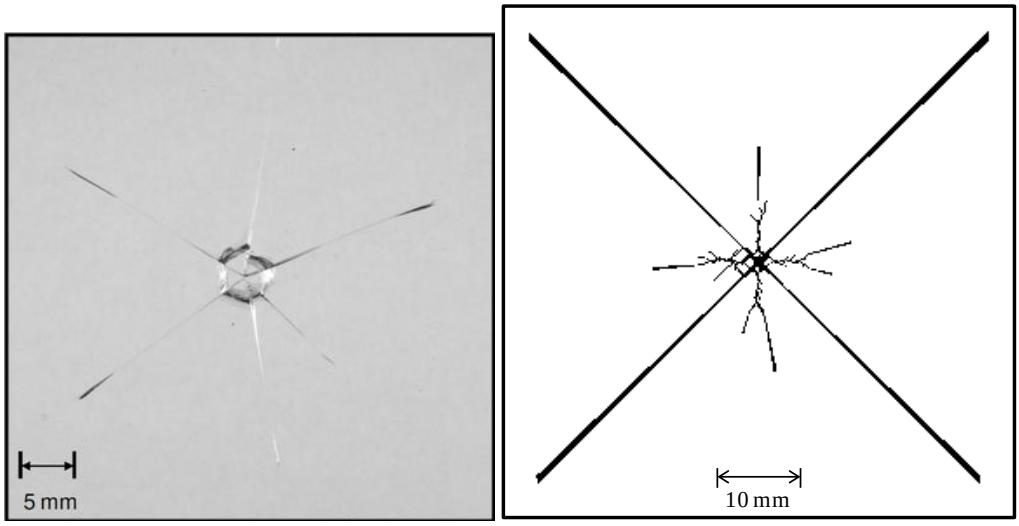

Fig.1–15: (Top) Details of the experimental [63] (left) and the computed (right) fracture pattern on the back surface of the PMMA plate for the PMMA/IM800A/PC laminate for the impact speed of 22 m/s.

The energy balance at the instant of separation of the impactor from the laminates is given in Table 1–6. For the laminate using the DFA4700 (IM800A) this time equals ~1.6 (1.8) ms and ~1.4 (1.6) ms, respectively, for 12 m/s and 22 m/s impact speeds.

Adhesive material of the laminated plate:		**DFA4700**		**IM800A**	
Impact velocity		**12 m/s**	**22 m/s**	**12 m/s**	**22 m/s**
INITIAL IMPACTOR KINETIC ENERGY		**2.041**	**6.860**	**2.041**	**6.860**
Impactor Kinetic energy		**1.603**	**5.123**	**1.629**	**4.992**
Plate kinetic energy		**0.185**	**0.264**	**0.179**	**0.357**
PMMA		0.078	0.101	0.076	0.139
adhesive		0.029	0.61	0.027	0.081
PC		0.078	0.102	0.076	0.137
Elastic energy of the plate		**0.109**	**0.336**	**0.092**	**0.471**
PMMA		0.039	0.096	0.039	0.151
adhesive		0.031	0.068	0.026	0.147
PC		0.038	0.172	0.028	0.173
Dissipation by plasticity, softening and viscosity		**0.133**	**0.894**	**0.111**	**0.789**
PMMA	plasticity	0.000	0.003	0.000	0.001
	softening	0.005	0.007	0.005	0.007
adhesive	viscosity	0.001	0.004	0.000	0.000
PC	plasticity	0.121	0.871	0.102	0.771
	softening	0.005	0.010	0.004	0.010
Dissipation due to cracking/failure		**0.020**	**0.154**	**0.030**	**0.279**
PMMA		0.020	0.154	0.030	0.279
adhesive		0.000	0.000	0.000	0.000
PC		0.000	0.000	0.000	0.000
Dissipation by delamination		**0.000**	**0.001**	**0.000**	**0.001**
PMMA–adhesive interface		0.000	0.001	0.000	0.001
PC–adhesive interface		0.000	0.000	0.000	0.000
Remaining energy (elastic and kinetic)		**1.897**	**5.722**	**1.900**	**5.820**
Energy dissipation		**0.153**	**1.049**	**0.142**	**1.069**
TOTAL		**2.049**	**6.771**	**2.041**	**6.889**
Variation w.r.t. initial energy		**+0.42%**	**-1.29 %**	**+0.02%**	**+0.43%**

Table 1–6: Energy analysis of the impact of the laminates. Energies are given in Joules.

Values of different energies listed in the Table indicate that the main energy dissipation mechanisms are plastic deformations of the PC plate and the energy dissipated due to cracking (element deletion) of the PMMA plate. Since the PMMA is brittle, it is not surprising that its plastic deformations are negligible. The only material which partially failed in the simulations is the PMMA. The failure criteria for the other materials were not met at any point in their domains. The energy dissipated due to viscous deformations of the adhesives is small, which is consistent with the large relaxation times (β^{-1}~1s) of the DFA4700 and the IM800A as compared to the impact duration (~1ms) considered. The delamination at the adhesive interfaces dissipated a negligible amount of energy. For the lowest impact velocity, the dissipation due to the softening of the PMMA and the PC materials contributed to about 7% of the total energy dissipation.

By comparing results depicted in Fig.1–14 and Fig.1–15, and considering the energy dissipated due to cracking of the PMMA plate listed in Table 6, we conclude that choosing a softer – in terms of the instantaneous modulus – adhesive interlayer (IM800A over DFA4700) induces longer cracks and hence larger energy dissipation due to failure of the impacted front PMMA layer but decreases the energy dissipated due to plastic deformations of the PC layer. In order to relate this to the stress wave reflections introduced by the acoustic impedance mismatch at the PMMA/adhesive and the adhesive/PC interfaces,

we consider their 1-D deformations and linear elastic response. The acoustic impedance of the PMMA, DFA4700 and IM800A are, respectively, ~ 2.3, 0.11 and 0.077 $mg.mm^{-2}\mu s^{-1}$. Therefore, in this approximation, 9% of the stress wave amplitude coming from the PMMA material and reaching the PMMA/DFA4700 interface will be transmitted to the DFA4700 interlayer, while only 6% will be transmitted for the PMMA/IM800A interface. Since the rest of the stress wave is reflected, stresses in the PMMA layer induce more damage with the IM800A adhesive. This also explains, at least partially, the lower energy dissipation in the PC layer with the IM800A rather than the DFA4700 as the adhesive. In Fig.1–16, we have exhibited fringe plots of the larger of the effective plastic strain in the α and the β phases at the bottom surface of the PC plate, and in a plane orthogonal to the plate edge. It is clear that larger surface area of the PC plate is more severely plastically deformed for the DFA4700 adhesive as compared to that for the IM800A adhesive.

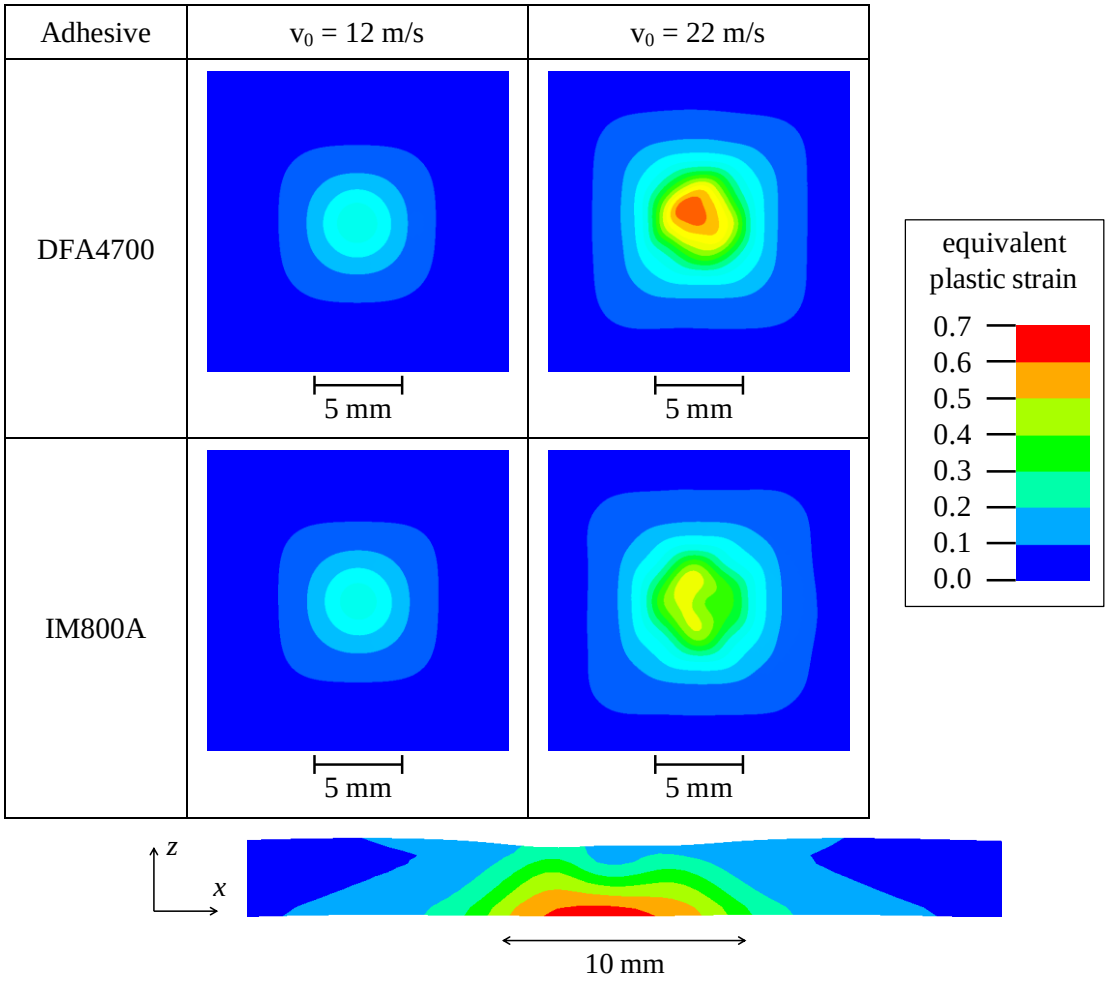

Fig.1–16: For the impact of PMMA/adhesive/PC plate at 22m/s, fringe plots in the PC layer of the computed equivalent plastic strain on the back surface (top) and for the PMMA/DFA4700/PC laminate in a plane orthogonal to the edge of the plate and passing through its center (bottom).

Time histories of the in-plane lengths of the computed cracks on the back surface of the PMMA layer in the two laminates for impact speeds of 12 and 22 m/s are plotted in Fig.1–17 and Fig.1–18, respectively.

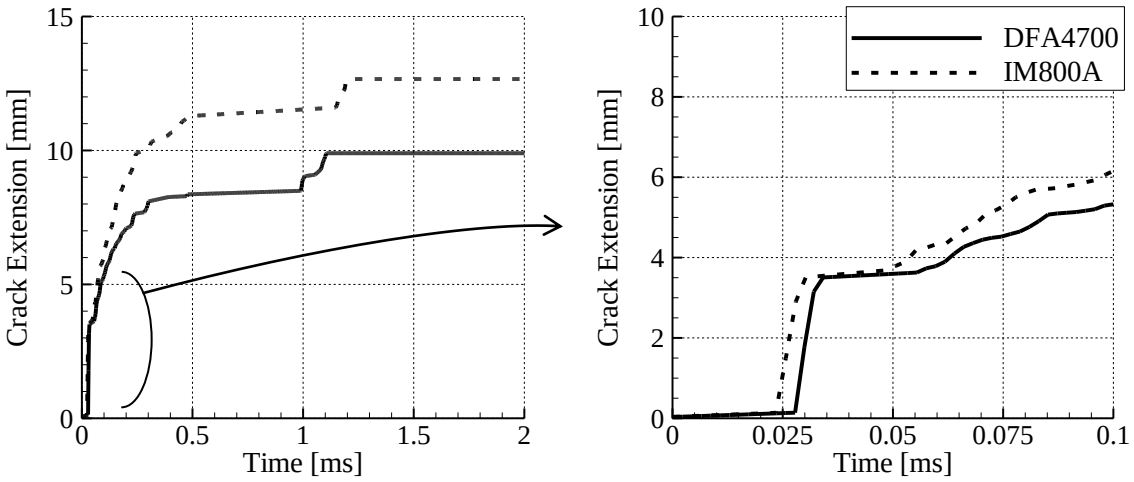

Fig.1–17: Radial lengths of the cracks in the PMMA plate bonded with DFA4700 and IM800A adhesives and impacted at 12 m/s.
The Fig. on the right is a magnified view of that on the left for small times.

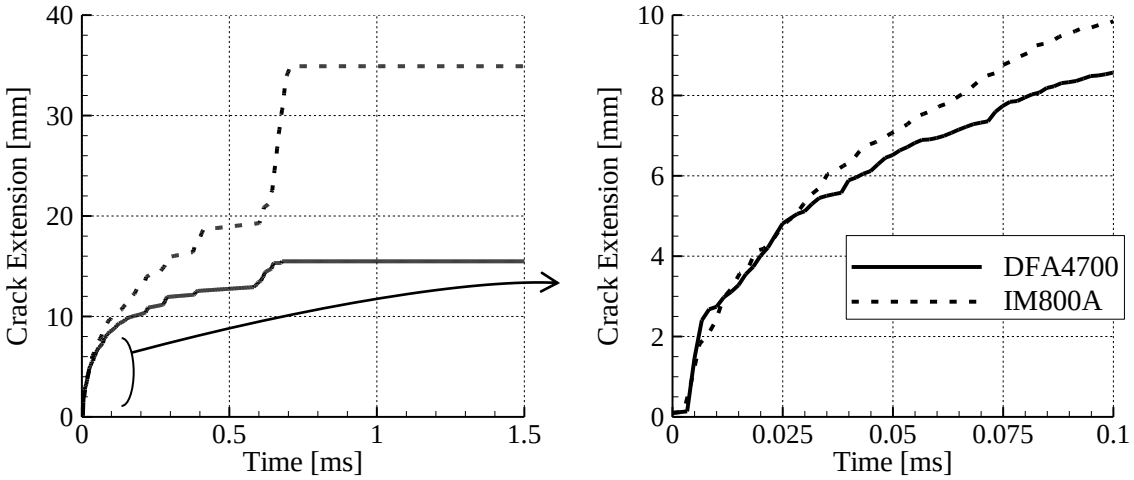

Fig.1–18: Radial lengths of the cracks in the PMMA plate bonded with DFA4700 and IM800A adhesives impacted at 22 m/s.
The Fig. on the right is a magnified view of that on the left for small times.

Plate	12 m/s impact speed	22 m/s impact speed
PMMA/DFA4700/PC	28.6 μs (1687/s, 141 MPa)	7.39 μs (2319/s, 142 MPa)
PMMA/IM800A/PC	24.4 μs (1095/s, 141 MPa)	7.51 μs (2213/s, 142 MPa)

Table 1–7: Computed times of crack initiation (first element deletion), corresponding strain rates and the maximum principal stress in parentheses at the crack initiation sites.
The temperature rise at these times was insignificant.

The length of a radial crack increases rapidly in the early formation phase (25μs-35μs for the 12 m/s impact speed, 5μs-15μs for the 22 m/s impact speed) and the crack speed reaches a peak value of 1.0 mm/μs (1 km/s) for the four cases investigated. For 5000/s strain rate (which is typical for impact problems) and 300K temperature the speed of an elastic wave in the PMMA is about 2.5 mm/μs and the Rayleigh wave speed is 1.19 mm/μs. Thus the maximum crack speed is 40% of the elastic wave speed and 84% of the Rayleigh wave speed. The crack initiation times and the corresponding values of the maximum principal stress and the strain rate at the crack initiation site are given in Table 1–7. The maximum principal stress in the PMMA at the time of crack initiation is essentially the same for the four cases studied, and the strain rate for the 12 m/s impact speed is about 40% less for the IM800A adhesive than that for the DFA4700 adhesive. Also, the crack initiates 4μs earlier with the IM800A interlayer than that with the DFA4700 adhesive. For the higher impact speed of 22 m/s, the crack initiation times, the maximum principal stress and the strain rates are essentially the same for the two adhesives.

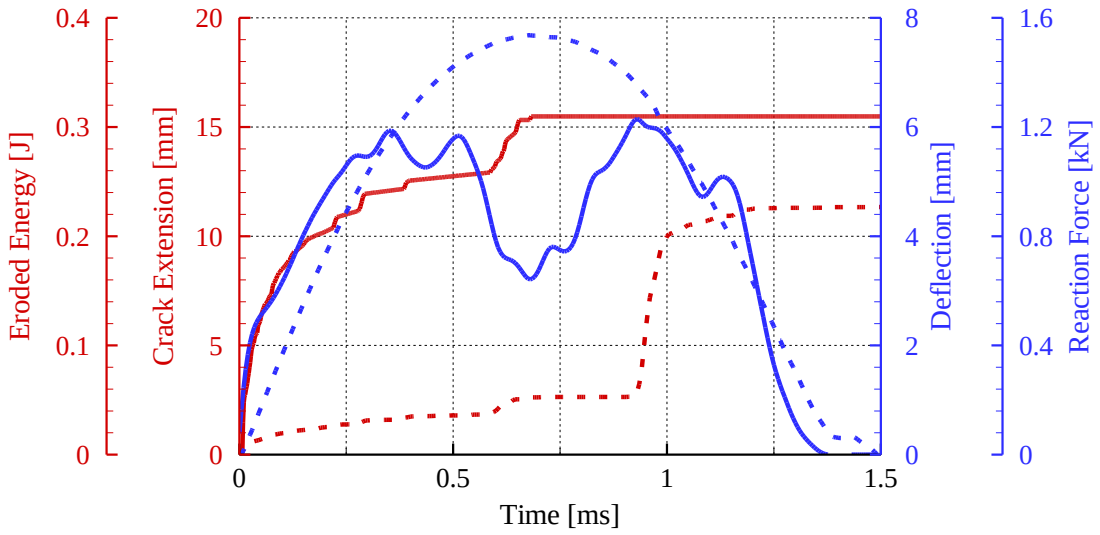

Fig.1–19: Time histories of the crack length, eroded energy, reaction force, and the laminate deflection for the 22 m/s impact of the PMMA/DFA4700/PC laminate.
Red curve, solid for crack extension and dashed for eroded energy; Blue curve, solid for reaction force and dashed for deflection.

The reaction force, the energy dissipation, the deflection (measured at the center of the back face of the PC layer) and the in-plane extension of the cracks in the PMMA are plotted against time in Fig.1–19. More than 75% of the erosion energy is not due to the elongation of radial cracks but due to the formation of the "secondary cracks", i.e., to the formation of smaller cracks and to the damage induced at the impact site (e.g., see Fig.1–20 in which crack patterns at t = 0.8 and 1.0 ms are exhibited). This is because the number of elements that fail due to ductile failure (Johnson-Cook damage criterion) increases with time and more energy/volume is dissipated due to the ductile failure than that due to the brittle failure. We also notice that the drop in the reaction force (at ~0.7 ms) occurs when the plate deflection is the maximum. At this time, the radial cracks have reached their maximum length. There is almost no energy eroded subsequent to the reaction force decreasing to 0.65 kN at t = ~0.7 ms as shown by the eroded energy reaching a plateau between 0.65 ms and 0.90 ms. The majority of the energy erosion occurs during the

spring back phase of the plate (reloading corresponding to the second peak of the reaction force, and return to the 0 deflection position).

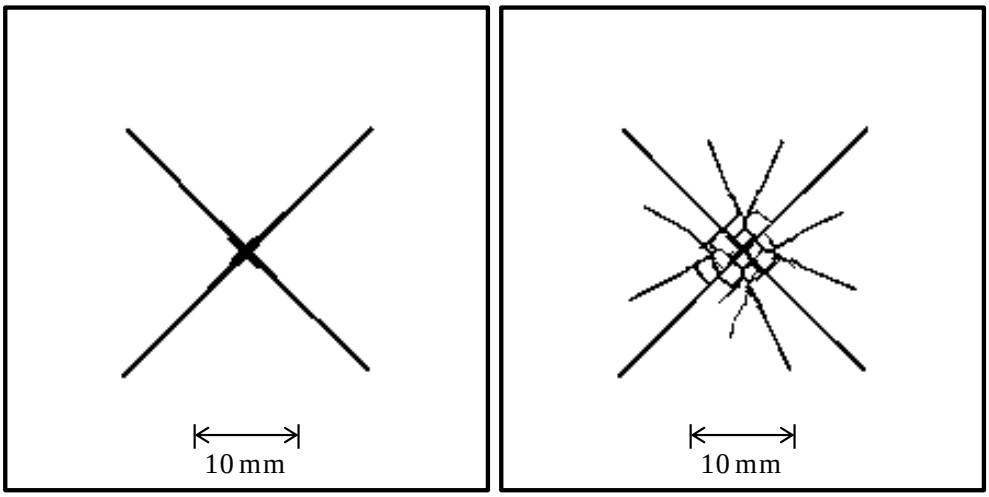

Fig.1–20: Details of the crack patterns in the PMMA plate of the PMMA/DFA4700/PC laminate impacted at 22 m/s at t = 0.8 ms (left) and t = 1.0 ms (right).

1.6 Summary and Discussion

We have analyzed by the FEM transient deformations of PMMA/DFA4700/PC and PMMA/IM800A/PC laminates impacted at normal incidence by a 28.5 g hemispherical nosed steel cylinder translating at 12 m/s and 22 m/s. The computed results are found to reasonably agree with the corresponding experimental ones. These simulations confirm the "sacrificial" role of the front PMMA plate. Results computed by enhancing the failure stress of the PMMA by 15% induced less damage in the impacted face of the PMMA in the PMMA/DFA4700/PC laminate but increased by 20% damage at the center of the rear face of the PC plate. Hence plastic deformations and failure of the impacted PMMA plate dissipate energy and protect the rear plate of the assembly.

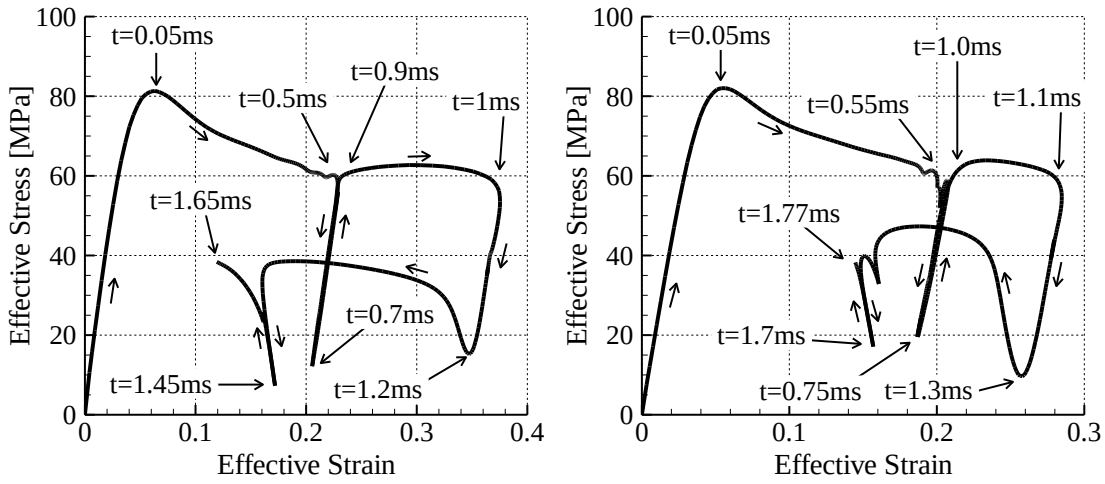

Fig.1–21: Effective stress vs. effective strain curves at the point located at the center of the rear surface of the PC layer of the PMMA/DFA4700/PC (left) and PMMA/IM800A/PC (right) panels impacted at 22 m/s.

In Fig.1–21 are plotted the equivalent stress $\hat{\sigma} = \sqrt{\frac{3}{2}\boldsymbol{\sigma}' : \boldsymbol{\sigma}'}$ against the effective strain $\hat{\varepsilon} = \sqrt{\frac{2}{3}\boldsymbol{\varepsilon}' : \boldsymbol{\varepsilon}'}$ at the center of the back surface of the PC layer (where the damage is maximum). Here $\boldsymbol{\sigma}'$ is the deviatoric part of the Cauchy stress tensor and $\boldsymbol{\varepsilon}'$ the deviatoric part of the Hencky strain tensor. The stress-strain curves for the PMMA/DFA4700/PC and the PMMA/IM800A/PC laminates are qualitatively similar, but the times corresponding to various features of the curves and magnitudes of the stresses and strains differ quantitatively. In both cases the yield stress of PC – about 80 MPa – is reached 50 μs after contact initiation. This initial phase of elastic deformation is followed by softening of the PC material that lasts until 0.5 (0.55) ms for the laminates with the DFA4700 (IM800A) adhesive. These times correspond to the first peak in the time-history of the reaction force, see Fig.1–12, and with the initiation of elastic unloading of the PC during which the effective stress drops to nearly one-fourth (one-third) of its original value for the DF4700 (IMA800A) adhesive. The subsequent increase of the contact force corresponds to the elastic re-loading of the PC material. The PC deforms then plastically until the effective strain reaches its maximum value. Then there is elastic unloading of the PC followed by an increase in the effective stress while the effective strain decreases. This corresponds to switching from tensile to compressive deformations of the PC as made clear by the two non-zero in-plane principal stresses plotted in Fig.1–22, the 3rd out-of-plane principal stress is zero. The maximum effective strain at the point in the PC layer and the transition from tensile to compressive deformations occurs during the second peak of the reaction force. It is clear from these plots that the evolution of stresses and strains in the PC is unaffected by the initiation and propagation of cracks in the PMMA layer.

The dominant stress component in the adhesives at points more than 5 mm in-plane distance from the interlayer centroid is the shear stress σ_{rz}. Its time history for the two laminates is plotted in Fig.1–23 for the impact speed of 22 m/s. This stress component was found to be the dominant one by examining stress components at different points on the mid-plane of the adhesive layer. Therefore, the adhesive deforms mostly in shear suggesting thereby that it is mainly loaded by the relative radial sliding of the PMMA and the PC layers. However, at the centroid of the adhesive interlayer the pressure is greater than the effective

stress implying that near the center of impact the adhesive transmits normal tractions mainly due to the high value of the hydrodynamic pressure.

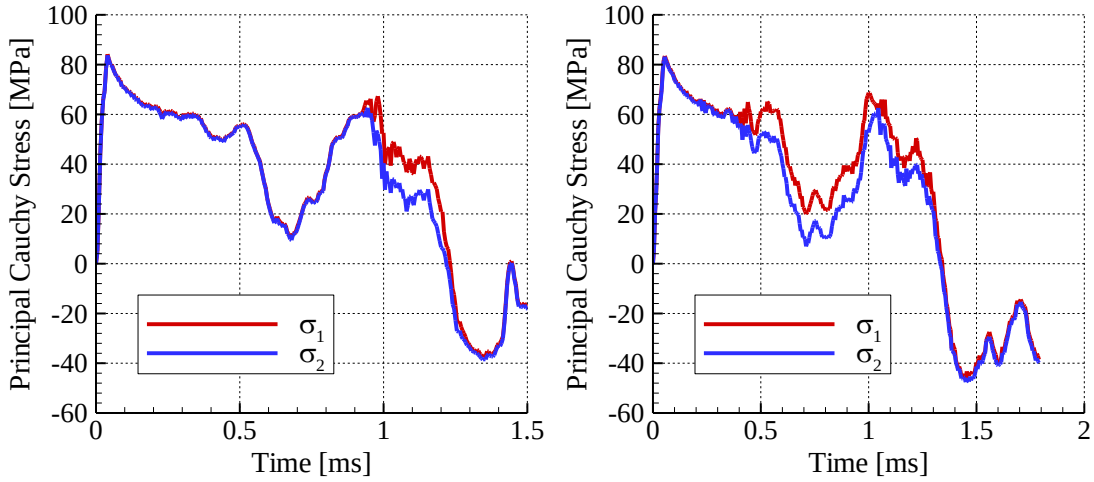

Fig.1–22: Time histories of the in-plane principal stresses σ_1 and σ_2 (with $\sigma_1 \geq \sigma_2$) at the center of the rear surface of the PC plate of the PMMA/DFA4700/PC (left) and PMMA/IM800A/PC (right) laminates impacted at 22m/s.
The out-of-plane principal stress is zero since the surface is traction free.

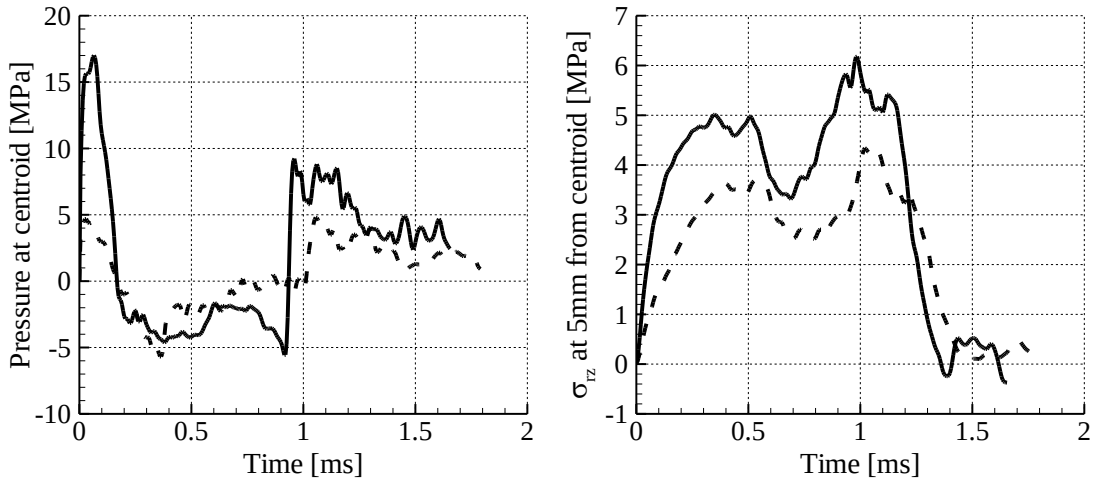

Fig.1–23: Time history of the pressure at the adhesive centroid and dominant stress component at 5 mm in-plane offset from the adhesive centroid for the PMMA/DFA4700/PC (solid curves) and PMMA/IM800A/PC (dashed curves) laminates impacted at 22 m/s.

The deformed shape of the PC layer is plotted in Fig.1–24 for the 22m/s impact speed and the PMMA/DFA4700/PC laminate. The maximum deflection, 7.57 mm, of the plate occurs at its center at 0.68 ms. It is interesting to observe that the sides of the plate initially have a negative deflection, i.e., that they have an upward displacement. This agrees with the experimental results of Stenzler [63].

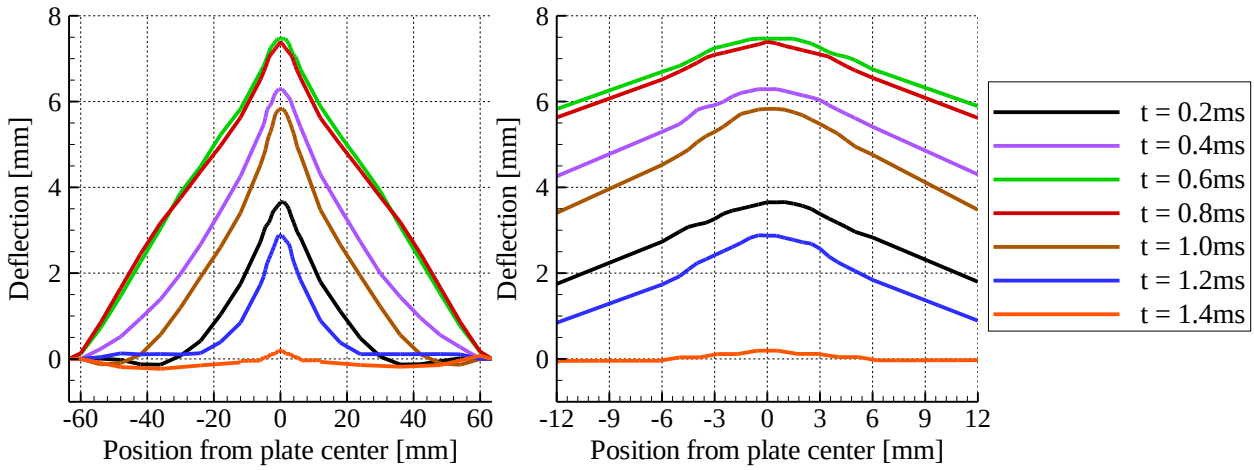

Fig.1–24: Deformed shapes of the back surface of the PC plate of the PMMA/DFA4700/PC laminate impacted at 22 m/s.
The right Fig. is a blown up view of the deformed central region of the plate.

The main energy dissipation mechanisms have been identified and quantified. While the viscous deformations of the adhesive interlayers do not contribute significantly to the energy dissipated during the impact process, the plastic deformations of the PC material and the cracking of the PMMA materials are responsible for more than 90% of the energy dissipated. The energy dissipated by softening of the PMMA and the PC due to temperature rise had a small contribution. The energy dissipated due to delamination at the interfaces was also miniscule.

Factors such as values of material parameters, failure criteria, delamination criteria, constitutive relations (material models) for the PMMA, the PC and the adhesives, and the boundary conditions affect computed results. No single paper in the literature provides a complete set of material data in order to compute results. Algorithms employed in the computational model such as the numerical integration with respect to time of the coupled nonlinear ordinary differential equations, element deletion algorithm, and the FE mesh size and the gradation of elements in the FE mesh introduce dissipation and errors in the computed solution. Of course, the test data is not necessarily exactly reproducible. It is an arduous task to quantify error introduced by each factor/parameter in a complex system such as the one analyzed here. Nevertheless the model enables one to delineate details of deformations in each component of the system, and identify dominant sources of energy dissipation.

1.7 Conclusions

We have developed a mathematical and a computational model to study finite transient deformations of a laminated plate impacted at normal incidence by a hemispherical nosed steel cylinder. The PMMA and the PC have been modeled as thermo-elasto-visco-plastic materials and the adhesive as a viscoelastic material. Failure of each material and of the interface between two distinct materials has been considered. Values of material parameters have been determined by using test data available in the literature. The user defined subroutine for modeling the PMMA and the PC have been implemented in the commercial software, LS-DYNA.

During the impact of the PMMA/DFA4700/PC and PMMA/IM800A/PC laminates the time history of the reaction force experienced by the impactor has two dominant peaks before dropping to zero when the impactor separates from the laminate. Whereas the computational model predicts reasonably well the portion of the reaction force time history until the first peak and the maximum deflection of the laminate, the reaction force beyond the first peak and hence the time of separation between the impactor and the laminate are not well predicted. The dominant source of energy dissipation is the plastic deformation in the PC back plate rather than the cracking of the front PMMA plate. The time of rapid drop in the reaction force corresponds to that of the maximum deflection of the plate, and at this time the radial cracks in the PMMA have reached their maximum in-plane extension. The majority of the eroded energy occurs during the rebound of the laminate to the zero deflection position. The mechanical properties of the adhesive significantly influence both the time when cracks in the PMMA initiate, the damage zone in the PMMA plate developed around the impact site, and the lengths and the number of cracks. An adhesive with a small value of instantaneous Young's modulus will result in more damage to the front layer due to the greater impedance mismatch between the PMMA and the adhesive, and will protect the rear PC layer more effectively in the sense that there will be less damage induced in it due to plastic deformations.

1.8 Acknowledgments

This research was sponsored by the Army Research Laboratory and was accomplished under Cooperative Agreement Number W911NF-06-2-0014. The views and conclusions contained in this document are those of the authors and should not be interpreted as representing the official policies, either expressed or implied, of the Army Research Laboratory or the U.S. Government. The U.S. Government is authorized to reproduce and distribute reprints for Government purposes notwithstanding any copyright notation hereon.

References

[1] J. Radin, W. Goldsmith, Normal Projectile Penetration and Perforation of Layered Targets, Int J Impact Eng, 7 (1988) 229-259.
[2] J. Sands, P. Patel, P. Dehmer, A. Hsieh, Protecting the Future Force: Transparent Materials Safeguard the Army's Vision, AMTIAC Quarterly, 8, (2004).
[3] S. Rabinowitz, I. Ward, J. Parry, The effect of hydrostatic pressure on the shear yield behaviour of polymers, J Mater Sci, 5 (1970) 29-39.
[4] R. Duckett, S. Rabinowitz, I. Ward, The strain-rate, temperature and pressure dependence of yield of isotropic poly (methylmethacrylate) and poly (ethylene terephthalate), J Mater Sci, 5 (1970) 909-915.
[5] E.M. Arruda, M.C. Boyce, R. Jayachandran, Effects of Strain-Rate, Temperature and Thermomechanical Coupling on the Finite Strain Deformation of Glassy-Polymers, Mech Mater, 19 (1995) 193-212.
[6] A.D. Mulliken, M.C. Boyce, Mechanics of the rate-dependent elastic-plastic deformation of glassy polymers from low to high strain rates, Int J Solids Struct, 43 (2006) 1331-1356.
[7] C.R. Siviour, S.M. Walley, W.G. Proud, J.E. Field, The high strain rate compressive behaviour of polycarbonate and polyvinylidene difluoride, Polymer, 46 (2005) 12546-12555.
[8] P. Moy, T. Weerasooriya, A. Hsieh, W. Chen, Strain rate response of a polycarbonate under uniaxial compression, in: Proceedings of the SEM Conference on Experimental Mechanics, 2003.
[9] J. Richeton, S. Ahzi, L. Daridon, Y. Remond, A formulation of the cooperative model for the yield stress of amorphous polymers for a wide range of strain rates and temperatures, Polymer, 46 (2005) 6035-6043.
[10] J. Richeton, G. Schlatter, K.S. Vecchio, Y. Remond, S. Ahzi, A unified model for stiffness modulus of amorphous polymers across transition temperatures and strain rates, Polymer, 46 (2005) 8194-8201.
[11] J. Richeton, S. Ahzi, K.S. Vecchio, F.C. Jiang, R.R. Adharapurapu, Influence of temperature and strain rate on the mechanical behavior of three amorphous polymers: Characterization and modeling of the compressive yield stress, Int J Solids Struct, 43 (2006) 2318-2335.
[12] D. Rittel, N. Eliash, J.L. Halary, Hysteretic heating of modified poly(methylmethacrylate), Polymer, 44 (2003) 2817-2822.
[13] D. Rittel, An investigation of the heat generated during cyclic loading of two glassy polymers. Part I: Experimental, Mech Mater, 32 (2000) 131-147.
[14] D. Rittel, Y. Rabin, An investigation of the heat generated during cyclic loading of two glassy polymers. Part II: Thermal analysis, Mech Mater, 32 (2000) 149-159.
[15] E. Schmachtenberg, M. Glissmann, M. Brinkmann, Modelling the dynamic material behaviour of thermoplastics in the FEA, J Polym Eng, 26 (2006) 245-258.
[16] J. Richeton, S. Ahzi, K.S. Vecchio, F.C. Jiang, A. Makradi, Modeling and validation of the large deformation inelastic response of amorphous polymers over a wide range of temperatures and strain rates, Int J Solids Struct, 44 (2007) 7938-7954.
[17] T. Tervoort, R. Smit, W. Brekelmans, L.E. Govaert, A constitutive equation for the elasto-viscoplastic deformation of glassy polymers, Mechanics of Time-Dependent Materials, 1 (1997) 269-291.
[18] C.P. Buckley, D.C. Jones, Glass-Rubber Constitutive Model for Amorphous Polymers near the Glass-Transition, Polymer, 36 (1995) 3301-3312.
[19] J.A. Alvarado-Contreras, M.A. Polak, A. Penlidis, Constitutive Modeling of Damage Evolution in Semicrystalline Polyethylene, J Eng Mater-T Asme, 132 (2010).
[20] M.C. Boyce, D.M. Parks, A.S. Argon, Large Inelastic Deformation of Glassy-Polymers .1. Rate Dependent Constitutive Model, Mech Mater, 7 (1988) 15-33.
[21] A.G. Varghese, R.C. Batra, Constitutive equations for thermomechanical deformations of glassy polymers, Int J Solids Struct, 46 (2009) 4079-4094.
[22] A.G. Varghese, R.C. Batra, Strain localization in polycarbonates deformed at high strain rates, J Polym Eng, 31 (2011) 495-519.

[23] E.Z. Lajtai, B.J. Carter, M.L. Ayari, Criteria for Brittle-Fracture in Compression, Eng Fract Mech, 37 (1990) 59-74.
[24] H. Saghafi, M.R. Ayatollahi, M. Sistaninia, A modified MTS criterion (MMTS) for mixed-mode fracture toughness assessment of brittle materials, Mat Sci Eng a-Struct, 527 (2010) 5624-5630.
[25] A. Seweryn, Brittle-Fracture Criterion for Structures with Sharp Notches, Eng Fract Mech, 47 (1994) 673-681.
[26] A. Seweryn, A. Lukaszewicz, Verification of brittle fracture criteria for elements with V-shaped notches, Eng Fract Mech, 69 (2002) 1487-1510.
[27] N. Vandenberghe, R. Vermorel, E. Villermaux, Star-Shaped Crack Pattern of Broken Windows, Physical review letters, 110 (2013) 174302.
[28] J.M. Schultz, Microstructural Aspects of Failure in Semicrystalline Polymers, Polym Eng Sci, 24 (1984) 770-785.
[29] F. Zairi, M. Nait-Abdelaziz, J.M. Gloaguen, J.M. Lefebvre, Modelling of the elasto-viscoplastic damage behaviour of glassy polymers, Int J Plasticity, 24 (2008) 945-965.
[30] M.R. Ayatollahi, M.R.M. Aliha, M.M. Hassani, Mixed mode brittle fracture in PMMA - An experimental study using SCB specimens, Mat Sci Eng a-Struct, 417 (2006) 348-356.
[31] P.W. Beaumont, R.J. Young, Failure of brittle polymers by slow crack growth, J Mater Sci, 10 (1975) 1334-1342.
[32] H. Wada, M. Seika, C.A. Calder, T.C. Kennedy, Measurement of Impact Fracture-Toughness for Pmma with Single-Point Bending Test Using an Air Gun, Eng Fract Mech, 46 (1993) 715-719.
[33] G. Marshall, J. Williams, C. Turner, Fracture toughness and absorbed energy measurements in impact tests on brittle materials, J Mater Sci, 8 (1973) 949-956.
[34] P. Moy, T. Weerasooriya, W. Chen, A. Hsieh, Dynamic stress-strain response and failure behavior of PMMA, in, ASME, 2003.
[35] T. Weerasooriya, P. Moy, D. Casem, M. Cheng, W. Chen, Fracture toughness for PMMA as a function of loading rate, in: Proceedings of the 2006 SEM Annual Conference on Experimental Mechanics, June, 2006, pp. 5-7.
[36] F.C. Chang, L.H. Chu, Coexistence of Ductile, Semi-Ductile, and Brittle Fractures of Polycarbonate, J Appl Polym Sci, 44 (1992) 1615-1623.
[37] N. Mills, The mechanism of brittle fracture in notched impact tests on polycarbonate, J Mater Sci, 11 (1976) 363-375.
[38] R. Fraser, I. Ward, The impact fracture behaviour of notched specimens of polycarbonate, J Mater Sci, 12 (1977) 459-468.
[39] G. Allen, D. Morley, T. Williams, The impact strength of polycarbonate, J Mater Sci, 8 (1973) 1449-1452.
[40] D. Rittel, R. Levin, H. Maigre, On dynamic crack initiation in polycarbonate under mixed-mode loading, Mech Res Commun, 24 (1997) 57-64.
[41] D. Rittel, R. Levin, Mode-mixity and dynamic failure mode transitions in polycarbonate, Mech Mater, 30 (1998) 197-216.
[42] D.R. Curran, D.A. Shockey, L. Seaman, Dynamic fracture criteria for a polycarbonate, Journal of Applied Physics, 44 (1973) 4025-4038.
[43] E. Plati, J. Williams, Effect of temperature on the impact fracture toughness of polymers, Polymer, 16 (1975) 915-920.
[44] E. Plati, J. Williams, The determination of the fracture parameters for polymers in impact, Polymer Engineering & Science, 15 (1975) 470-477.
[45] G.C. Adams, R.G. Bender, B.A. Crouch, J.G. Williams, Impact Fracture-Toughness Tests on Polymers, Polym Eng Sci, 30 (1990) 241-248.
[46] S. Ogihara, T. Ishigure, A. Kobayashi, Study on impact perforation fracture mechanism in PMMA, J Mater Sci Lett, 17 (1998) 691-692.
[47] N.A. Fleck, W.J. Stronge, J.H. Liu, High Strain-Rate Shear Response of Polycarbonate and Polymethyl Methacrylate, P Roy Soc Lond a Mat, 429 (1990) 459-&.

[48] I. Livingstone, M. Richards, R. Clegg, Numerical and experimental investigation of ballistic performance of transparent armour systems, in: Lightweight Armour System Symposium, LASS, 1999.
[49] M. Richards, R. Clegg, S. Howlett, Ballistic performance assessment of glass laminates through experimental and numerical investigation, in: Proceedings of the 18th International Symposium on Ballistics, 1999, pp. 1123-1130.
[50] P.M. Kelly, Lightweight transparent armour systems for combat eyewear, in: the Proceedings of the 19th International Symposium of Balllistics, Interlaken, Switzerland, 2001, pp. 7-11.
[51] K. Kihara, H. Isono, H. Yamabe, T. Sugibayashi, A study and evaluation of the shear strength of adhesive layers subjected to impact loads, Int J Adhes Adhes, 23 (2003) 253-259.
[52] Y.M. Tsai, Y.T. Chen, Transition of Hertzian Fracture to Flexure Fracture Produced in Glass Plates by Impact, Eng Fract Mech, 18 (1983) 1185-1190.
[53] C. Fountzoulas, J. Sands, G. Gilde, P. Patel, Modeling of Defects in Transparent Ceramics for Improving Military Armor, in, DTIC Document, 2009.
[54] G.A. Gilde, P.J. Patel, A.J. Hsieh, Improved Low-Cost Multi-Hit Transparent Armor, in, Army Research Lab Aberdeen Proving Ground MD Weapons and Materials Research Directorate, 2006.
[55] R.H. Zee, C.J. Wang, A. Mount, B.Z. Jang, C.Y. Hsieh, Ballistic Response of Polymer Composites, Polym Composite, 12 (1991) 196-202.
[56] N. Tarim, F. Findik, H. Uzun, Ballistic impact performance of composite structures, Compos Struct, 56 (2002) 13-20.
[57] H.Y.T. Wu, F.K. Chang, Transient Dynamic Analysis of Laminated Composite Plates Subjected to Transverse Impact, Comput Struct, 31 (1989) 453-466.
[58] V. Tita, J. de Carvalho, D. Vandepitte, Failure analysis of low velocity impact on thin composite laminates: Experimental and numerical approaches, Compos Struct, 83 (2008) 413-428.
[59] A.N. Palazotto, E.J. Herup, L.N.B. Gummadi, Finite element analysis of low-velocity impact on composite sandwich plates, Compos Struct, 49 (2000) 209-227.
[60] S.S. Cheon, T.S. Lim, D.G. Lee, Impact energy absorption characteristics of glass fiber hybrid composites, Compos Struct, 46 (1999) 267-278.
[61] R.C. Batra, G. Gopinath, J.Q. Zheng, Damage and failure in low energy impact of fiber-reinforced polymeric composite laminates, Compos Struct, 94 (2012) 540-547.
[62] J.S. Stenzler, N. Goulbourne, Impact mechanics of transparent multi-layered polymer composites, in: Society for Experimental Mechanics-SEM Annual Conference and Exposition on Experimental and Applied Mechanics, 2009, pp. V3.
[63] J.S. Stenzler, Impact mechanics of PMMA/PC multi-laminates with soft polymer interlayers, in, University Libraries, Virginia Polytechnic Institute and State University,, Blacksburg, VA., 2009.
[64] W. Zhang, S.A. Tekalur, L. Huynh, Impact Behavior and Dynamic Failure of PMMA and PC Plates, in: Dynamic Behavior of Materials, Volume 1, Springer, 2011, pp. 93-104.
[65] S.A. Tekalur, W. Zhang, L. Huynh, Dynamic Failure of Monolithic and Layered PMMA and PC Plates, (2010).
[66] C.A. Gunnarsson, B. Ziemski, T. Weerasooriya, P. Moy, Deformation and Failure of Polycarbonate during Impact as a Function of Thickness, in: Proceedings of the 2009 International Congress and Exposition on Experimental Mechanics and Applied Mechanics, 2009.
[67] C.A. Gunnarsson, T. Weerasooriya, P. Moy, Impact Response of PC/PMMA Composites, in: Dynamic Behavior of Materials, Volume 1, Springer, 2011, pp. 195-209.
[68] A.M. Stickle, P.H. Schultz, Exploring the role of shear in oblique impacts: A comparison of experimental and numerical results for planar targets, Int J Impact Eng, 38 (2011) 527-534.
[69] E. Kröner, Allgemeine kontinuumstheorie der versetzungen und eigenspannungen, Archive for Rational Mechanics and Analysis, 4 (1959) 273-334.
[70] E.H. Lee, Elastic-plastic deformation at finite strains, Stanford University, Divsion of Engineering Mechanics, 1968.
[71] A.D. Mulliken, Mechanics of amorphous polymers and polymer nanocomposites during high rate deformation, in, Massachusetts Institute of Technology, 2006, pp. 290 p.

[72] R.W. Ogden, Non-linear elastic deformations, Courier Dover Publications, 1997.
[73] R.M. Christensen, A Non-Linear Theory of Viscoelasticity for Application to Elastomers, J Appl Mech-T Asme, 47 (1980) 762-768.
[74] C. Rankin, Application of linear finite elements to finite strain using corotation, in: AIAA Paper AIAA-2006-1751, 47th AIAA Structures, Structural Dynamics and Materials Conference, May, 2006.
[75] F. Folgar, Advanced Aliphatic Polyurethane Resins for High Durability and Superior Ballistic Performance Laminated Glass, in: 22nd International Symposium on Ballistics, DESTech Publications, Inc., Vancouver BC, Canada, 2005, pp. 908-916
[76] N. MacAloney, A. Bujanda, R. Jensen, N. Goulbourne, Viscoelastic characterization of aliphatic polyurethane interlayers, in, DTIC Document, 2007.
[77] A4700 Dureflex® Optical Aliphatic Polyether Polyurethane Grade, in: D. Urethane (Ed.), 2006.
[78] S. Gerlach, M. Fiolka, A. Matzenmiller, Modelling and analysis of adhesively bonded joints with interface elements for crash analysis, in: LS-DYNA Anwenderforum, Bamberg, 2005.
[79] J.E. Pickett, J.A. Suriano, S.T. Rice, X. Li, Weatherable multilayer articles and method for their preparation, in, Google Patents, 2003.
[80] S.M.R. Khalili, M. Soroush, A. Davar, O. Rahmani, Finite element modeling of low-velocity impact on laminated composite plates and cylindrical shells, Compos Struct, 93 (2011) 1363-1375.
[81] S.C. Her, Y.C. Liang, The finite element analysis of composite laminates and shell structures subjected to low velocity impact, Compos Struct, 66 (2004) 277-285.

2 Low Velocity Impact of Flat and Doubly Curved Polycarbonate Panels

G. O. Antoine and R. C. Batra*
Department of Biomedical Engineering and Mechanics, M/C 0219
Virginia Polytechnic Institute and State University
Blacksburg, VA 24061, USA
Email: antoineg@vt.edu; rbatra@vt.edu
*Corresponding author; Tel: 540-231-6051; Fax: 540-231-4574

This chapter has been prepared for submission to a refereed journal.

2.1 Abstract

We study three-dimensional finite transient deformations of polycarbonate (PC) panels impacted at low velocity by a hemispherical nosed rigid cylinder using the commercial finite element software LS-DYNA with a thermo-elasto-visco-plastic material model for the PC incorporated in it as a user defined subroutine. The implementation of the user defined subroutine has been verified by comparing analytical and numerical solutions of simple initial-boundary-value problems. The mathematical model of the low velocity impact problem has been validated by comparing the computed and the experimental results for the maximum deflection and time histories of the centroidal deflection. It is found that the initial slope of the reaction force between the impactor and the panel vs. the centroidal deflection for a curved panel can be nearly 20 times that for the flat panel of the same thickness as the curved panel. For the impact velocity considered it is found that the maximum effective plastic strain in the PC shell near the center of impact strongly depends on the panel curvature. Furthermore, the effect of the panel curvature on stresses and strains developed in the panel is delineated. This information should be useful to designers of impact resistant transparent panels such as an airplane canopy, automobile windshield and goggles.

Key Words: Impact, Flat and curved panels, Finite element analysis, Thermo-elasto-viscoplastic material

2.2 Introduction

Polymers are composed of long chains of monomers while a metal is generally a polycrystalline material. This difference in the microstructure usually influences their thermo-mechanical response to applied loads. Polymers generally exhibit strong strain-rate dependence and are widely used as transparent armor because of their high specific impact performance, e.g., see Radin and Goldsmith [1]. Sands et al. [2] have reported that polycarbonates (PCs) have better specific impact resistance than most glasses. A lightweight transparent PC panel is subjected to low velocity impact when either a stone hits a windshield of a car or when police use curved panels to protect themselves from rocks thrown at them by a crowd of people during riots. Mathematical and computational models that can reliably predict the response of these panels to low velocity impact will help improve upon their design and possibly reduce their weight.

Deformations of PC have been experimentally studied at different strain rates and temperatures in uniaxial compression/tension and simple shear [3-11]. The test results have demonstrated that a PC material initially deforms elastically and exhibits strain softening subsequent to yielding that is followed by strain hardening at large strains. Moreover, increasing the temperature decreases the yield stress and increases the yield strain of the PC, while increasing the strain rate has the opposite effect. Young's

modulus (initial elastic modulus) of the material increases with an increase in the strain rate but decreases with rise in the temperature. Furthermore, the PC material can undergo large plastic deformations before failure. The energy dissipated due to plastic deformations is partially converted into heat for low [12, 13] and high strain rates [14]. For high strain rate deformations of PC samples, and assuming adiabatic heating of the material, Rittel [14] introduced two parameters β_{diff} and β_{int} relating the rate of heating to the plastic working, and the accumulated heating to the total plastic work, respectively. He found that for strain rates greater than 5000/s, β_{int} varies between 0.4 and 1, while β_{diff} can be 2.5 (larger than 1), which he attributed to the conversion of the elastic energy into heat during the softening regime.

Different constitutive equations (or material models) for the mechanical response of the PC have been proposed [5, 15-17]. They usually model the nonlinear elastic response of the PC with a Langevin spring and the visco-elasto-plastic response by using spring-dashpot systems modified to account for large deformations. Here we adopt the phenomenological model developed by Mulliken and Boyce [5] and modified by Varghese and Batra [18, 19] to account for effects of temperature rise due to adiabatic heating. This model incorporates strain-rate and temperature dependence of material properties. We note that the model proposed by Mulliken and Boyce [5] was recently extended to very high strain rates ($>10^4$/s) by Safari et al. [20]. However, this extension is not included here because we learned of it after having completed most of the work, and strain rates anticipated to occur in the PC plate at low velocity impact are considerably less than 10^4/s. Moreover, damage and failure of the PC material are not considered for the low-velocity impact problems studied here. We investigate the effect of curvature on the impact response of monolithic PC panels of different thicknesses.

The effect of curvature on the impact response of laminates has been studied both experimentally [21, 22] and numerically [23-28]. In References [21, 22], curved sandwich panels with aluminum face sheets and aluminum foam core of fixed radius of curvature subjected to blast loads were tested. The panel geometries used in [21, 22] are comparable to each other: In Ref. [21] (Ref. [22]) the edge length is 0.4 m (0.31 m), the aluminum face sheets have thicknesses between 0.5 and 1.6 mm (0.5 and 1.0 mm), the foam core thickness varies between 10 and 30 mm (10 mm), and the ratio of the curved edge length, L, to the radius of curvature, R, varies between 1.33 and 0.67 (0.62 and 1.24). It is found that the curvature of the sandwich panels changes the deformation regimes (bending becomes more important for curved panels) [21] and decreases the blast resistance of the panel [22]. The decrease in the blast resistance is attributed to the larger area of deformation of flat plates which enables them to absorb more energy. In References [24, 25] a semi-analytical approach is used to analyze deformations of curved graphite-epoxy laminates. The load applied at the laminate center increases with time to about 40 kN in 2 ms. In Ref. [25] a doubly curved laminate of equal radii of curvature is impacted at 2.5 m/s by a 330 g steel hemispherical-nosed cylinder. In [24] the ratio of the arc length to its curvature ranges between 0 and 2, while it varies between 0.33 and 1 in [25]. It is found in these two works that the curvature degraded the impact performance of the laminate, since the maximum in-plane strain induced at the shell centroid increased with an increase in the shell curvature [24]. However, the peak contact force between the impactor and the laminate increased with an increase in the curvature of the shell [25]. Transient deformations of curved panels have been analyzed by the finite element method (FEM) in Refs. [23, 26-28] for which geometries, boundary conditions and impact conditions are summarized in Table 2–1. For these problems, the impact energies varied between 0.329 and 11.2 J and the composites were modeled as linear elastic materials.

Ref.	Sample size [mm]	Materials	Boundary conditions	Curvature	Impactor
[23]	80×80×2.54	carbon-fiber-reinforced plastic	simply supported	single with L/R = 1.6, 0.8, 0.08	m=2.92 g v=15 m/s
[26]	25.4×25.4×2.54	graphite/epoxy	simply supported or clamped	single or double with L/R = 0.2, 0.1, 0.01	m=8.44 g v=30 m/s
[27]	140×140×3.35	glass/epoxy	clamped	single with L/R = 1.37, 0.27	m=14.175 g v=39.7 m/s
	149×149×1.7	graphite/epoxy	free	single with L/R = 1.192	m=38.87 g v=1.70 m/s
[28]	228.6×127×2.032	graphite/epoxy	clamped	single with L/R = 4.54, 0.14	m=1.134 kg v=1.89 m/s

Table 2–1: Geometries and impact conditions for curved shells studied in Refs. [23, 26-28] by the FEM.

Results presented in Ref. [26] suggest that the curvature does not significantly change the time history of the contact force between the plate/shell and the impactor; in particular the maximum contact force is the same for the flat plate and the singly and the doubly curved panels. However, other works report that the shell curvature increases the maximum contact force due to the enhanced bending stiffness of curved panels [23, 25, 27, 28]. Furthermore, a larger area is delaminated in curved panels than that in flat plates [23] and for similar impact conditions the panel curvature decreases the impact duration [24, 27]. We have not found in the open literature similar studies for curved PC panels.

Here we numerically investigate the effect of positive and negative curvature on the static indentation and the low-velocity impact response of PC panels with L/R varying between 0 and 2. The objectives of the study are to ascertain the effect of curvature on the contact force between the panels and the impactor and on the stresses, strains and plastic deformations developed. A major difference between the current work and most works summarized above is that the PC material can undergo large plastic deformations whereas the glass/epoxy composite fails at very small strains and deformations are generally elastic.

The rest of the paper is organized as follows. We formulate the initial-boundary-value problem in Section 2.3, and describe the corresponding computational model in Section 2.4. Results for the low velocity impact of flat and curved PC panels and their comparisons with the test data available in the literature are presented and discussed in Section 2.5. Conclusions from this work are summarized in Section 2.6.

2.3 Mathematical Model

A schematic sketch of the problem studied is exhibited in Fig.2–1. Either a flat or a curved monolithic PC panel of sides L_1 and L_2 and thickness h clamped on all four edges is impacted at normal incidence by a steel cylinder with a hemispherical nose of diameter d. We describe deformations of the panel by using rectangular Cartesian coordinate axes with the origin at the centroid of the top face of the panel, the positive x-axis pointing to the right and the positive z-axis pointing upwards.

In the Lagrangian description of motion transient deformations of the panel are governed by the following conversation laws.

$$\begin{aligned} &\text{mass}: && \rho J = \rho_0 \\ &\text{linear momentum}: && \rho_0 \dot{\mathbf{v}} = \hat{\nabla} \cdot \mathbf{T} \\ &\text{moment of momentum}: && \mathbf{T} \cdot \mathbf{F}^{\mathrm{T}} = \mathbf{F} \cdot \mathbf{T}^{\mathrm{T}} \end{aligned} \tag{2–1}$$

Here ρ and ρ_0 are mass densities in the current and the reference configurations, respectively, $J = \det(\mathbf{F})$, $\mathbf{F} = \partial \mathbf{x} / \partial \mathbf{X}$ is the deformation gradient that maps a material point from the reference position $\mathbf{X}$ to its current location $\mathbf{x}$, a superimposed dot indicates the material time derivative, $\mathbf{v}$ is the velocity of a material point, $\mathbf{T}$ is the first Piola-Kirchhoff stress tensor related to the Cauchy stress tensor $\boldsymbol{\sigma}$ by $\mathbf{T} = J\, \boldsymbol{\sigma} \cdot \mathbf{F}^{-\mathrm{T}}$, and $(\hat{\nabla} \cdot)$ is the divergence operator with respect to $\mathbf{X}$.

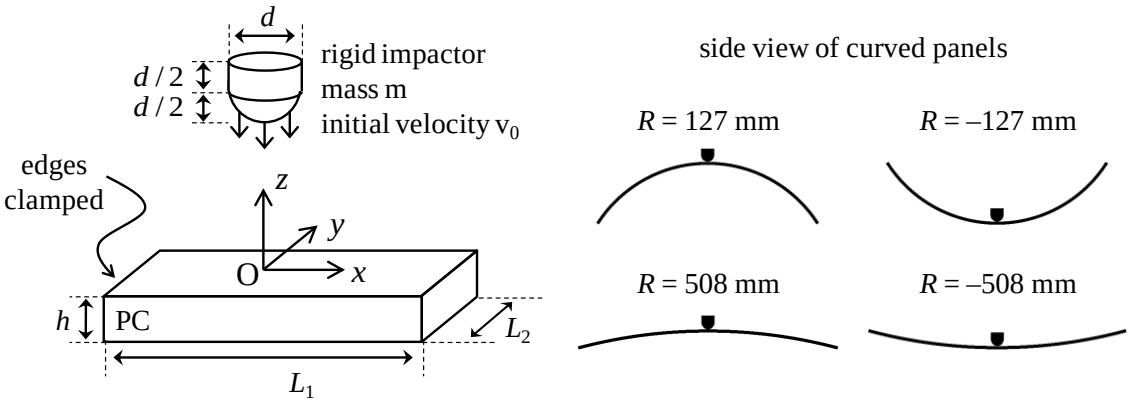

Fig.2–1: Sketch of the impact problem studied.

For impact speeds studied here deformations of the steel impactor are assumed to be negligible as compared to those of the PC panel and are thus neglected. The impactor is taken to be a rigid hemispherical-nosed cylinder, and have only translational motion that is governed by

$$\dot{\mathbf{p}} = \mathbf{f} \tag{2–2}$$

where $\mathbf{p}$ equals the linear momentum and $\mathbf{f}$ the resultant force acting on the impactor. For transient problems involving low to moderate impact speeds, Khalili et al. [29] have shown that assuming the impactor to be rigid reduces the computation time with minor effects on the numerical results.

At points on a clamped edge, the three displacement components are set equal to zero. At a free surface, the surface tractions vanish. On the smooth contact surface between the impactor and the panel, we apply the following continuity conditions.

$$\begin{aligned} &\text{normal velocity}: && [\![\dot{\mathbf{u}}]\!] \cdot \mathbf{n} = 0 \\ &\text{normal traction}: && [\![\mathbf{t}]\!] \cdot \mathbf{n} = 0 \\ &\text{tangential traction}: && \mathbf{t} \times \mathbf{n} = \mathbf{0} \end{aligned} \tag{2–3}$$

Here double brackets enclosing a variable indicate the jump in it across the contact surface, $\mathbf{n}$ is a unit normal to the contact surface, $\mathbf{u}$ the displacement field, $\dot{\mathbf{u}}$ the velocity field, $\mathbf{t}$ the traction vector, and the symbol $\times$ denotes the cross product between two vectors. These conditions imply that there is no

interpenetration between the impactor and the PC panel. At a point on the contact surface, the normal component of displacement and surface traction is continuous, and the tangential traction vanishes.

At t = 0, the panel is at rest, stress free, at the uniform temperature of 300 K, and the moving impactor just contacts the top surface of the panel.

The thermo-elasto-visco-plastic response of the PC is modeled by the Mulliken and Boyce [5] constitutive relation with the modifications suggested by Varghese and Batra [18]. It is briefly described in the Appendix for easy reference. For problems studied herein temperature rise is small and thermal effects can be neglected. When the magnitude of the axial stress is plotted against the magnitude of the axial strain, the stress-strain curves for the PC in uniaxial tension and compression are different, and the yield stress in tension is smaller than that in compression, see Fig.2–2. Thus even in pure bending of a straight beam deformations of the PC layer will in general be not symmetric about the beam midsurface. For low impact velocities considered herein we assume that there is no damage induced and the PC does not fail.

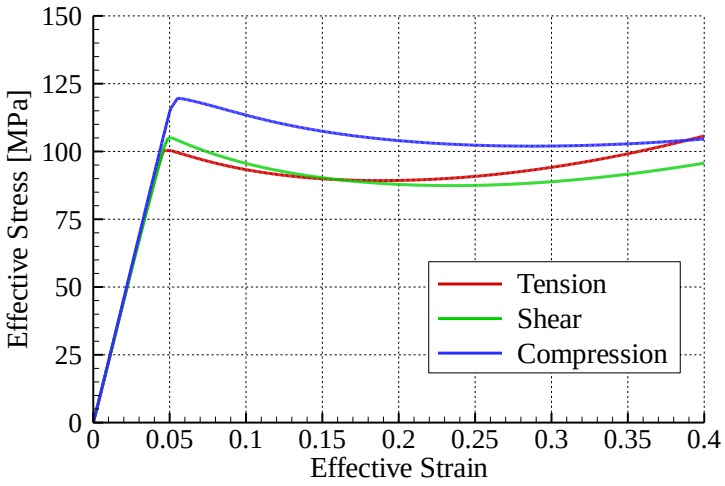

Fig.2–2: Effective stress as a function of the effective strain for uniaxial tension, simple shear and uniaxial compression of the PC at 5000/s strain rate.

2.4 Computational Model

We use the commercial FE software LS-DYNA in which the constitutive relation for the PC has been implemented as a user-defined subroutine written in FORTRAN. The verification of the implementation has been described by Varghese and Batra [18].

Khalili et al. [29] have analyzed an impact problem using different shell elements, integration schemes and FE meshes. They found that an "unstructured" FE mesh gave better convergence rate versus computational cost than a structured FE mesh. Here we use a FE mesh consisting of 8-node brick elements with one point integration rule for evaluating element matrices and the Belytschko-Bindeman hourglass control algorithm. For a sample problem, the energy of hourglass modes of deformation was found to be less than 5% of the total strain energy of deformations.

We analyzed a quasistatic Hertz contact problem with LS-DYNA by considerably increasing the mass density of the PC to ensure that we were correctly using the code. We studied the indentation by a 50 mm diameter rigid sphere of a 160 mm thick and 500 mm diameter cylindrical plate with edges and bottom face clamped and made of an isotropic linear elastic material with Young's modulus E = 10 GPa and Poisson's ratio ν = 0.25. We used as reference the Hertz solution for the contact force between the rigid indenter and a semi-infinite linear elastic half space. The analytical and the computed reaction forces are plotted in Fig.2–3 as a function of the indentation depth. One can see that for indentation depth less than 1 mm the deviation between the two sets of results is less than 5%. We note that the initial large difference is due to the numerical noise when the contact force is very small.

For each impact problem studied, results were computed with at least two FE meshes. The FE mesh A was uniformly refined to obtain a finer FE mesh B having at least 30% more nodes than those in mesh A. The process was repeated till the maximum reaction force and the energy dissipation computed with the two successive FE meshes differed by less than 10%. We have included in the Appendix a typical FE mesh used in the analysis and how it was generated.

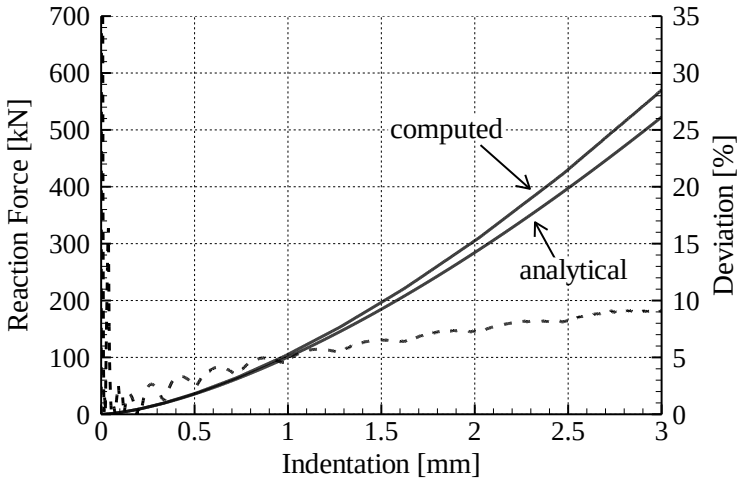

Fig.2–3: Analytical and computed reaction forces (solid lines) and the % difference between them (dashed line) as a function of the indentation.

2.5 Results and Discussion

2.5.1 Impact of flat plates

2.5.1.1 Validation of the model

We have simulated test configurations of Gunnarsson et al. [30, 31] and Gunnarsson et al. [32] who used the digital image correlation technique to experimentally measure deflection of the back face of clamped 254 mm square PC plates of thickness varying between 3 and 12.32 mm as they were impacted by a 104 g impactor at speeds ranging from 10 to 50 m/s. In [32] the authors provide the time-history of the deflection of the center of the rear face of 3, 4.45, 5.85, 9.27 and 12.32 mm thick panels, while in [30] they give deformed profiles of the rear face of the 5.60 mm thick panel. The measured and the computed maximum deflections listed in Table 2–2 reveal that the largest difference, 10.3%, between them is for the

12.32 mm thick panel impacted at 40 m/s. The impact speeds given in the Table are approximate values since the same impact velocity could not be used for plates of different thicknesses.

Panel thickness [mm]	Approximate Impact velocity [m/s]				
	10	20	30	40	50
	Experimental (computed) maximum deflection in mm, and % difference between the two values				
3.00	13.2 (13.0) [-1.5]	16.1 (17.1) [6.2]			
4.45	9.4 (9.0) [–4.3]	12.9 (13.1) [1.6]			
5.85	6.5 (7.1) [9.2]	10.9 (10.2) [-6.4]	15.2 (14.8) [-2.6]	19.2 (19.0) [-1.0]	22.0 (22.7) [3.2]
9.27			10.2 (10.4) [2.0]	11.3 (12.1) [7.1]	14.0 (14.8) [5.7]
12.32			6.9 (7.3) [5.8]	8.7 (9.6) [10.3]	10.7 (11.3) [5.6]

Table 2–2: Comparison of the experimental [32] and the computed maximum deflections of the centroid of the back surface of clamped PC plates.

We have exhibited in Fig.2–4 the computed and the experimental [32] time histories of the maximum deflections of the 4.45 and the 12.32 mm thick plates for different impact speeds. The two time histories agree well with each other during the initial rising portion for the five problems studied. For the 12.32 mm thick plate and impact speeds of 30, 40.7 and 48.9 m/s, the computed and the experimental time histories of the maximum deflection are close to each other even when the deflection is decreasing but that is not the case for the 4.45 mm thick panel impacted at 10.5 and 19.1 m/s.

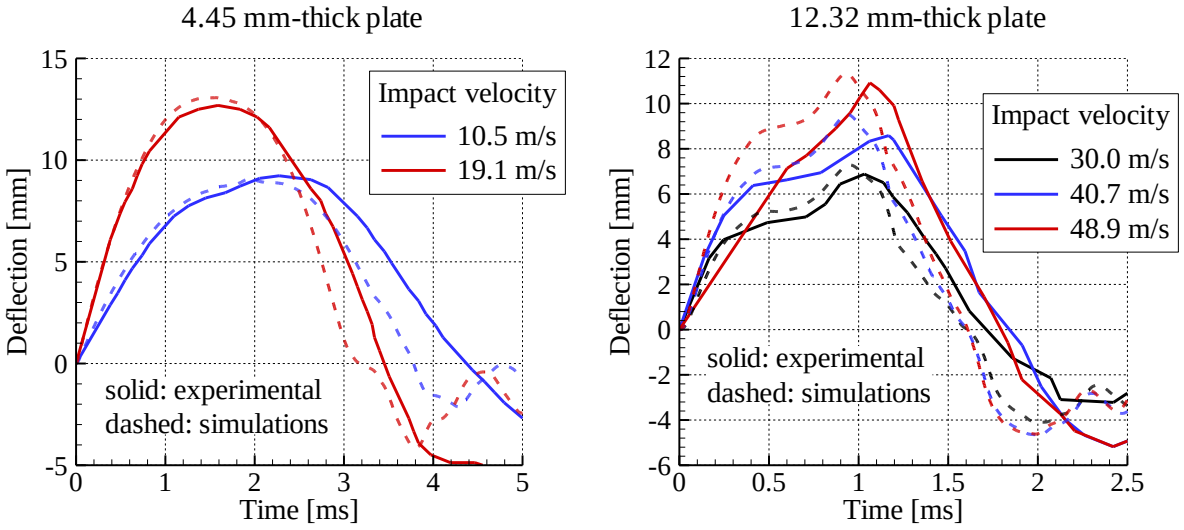

Fig.2–4: Time histories of the deflection (experimental data from [32]) of the centroid of the back surface of two panels for different impact velocities.

The experimentally observed and the computed deformed shapes, at different times, of the central portion of the rear face of 5.60 mm thick panels impacted at 30.5 m/s are shown in Fig.2–5 .The comparisons between the deformed shapes at the other impact speeds are similar to this one and are not exhibited. The

computed maximum deflection at the plate centroid is a little more than the corresponding experimental one for the first three times but a little less for the latter two time instants considered. Overall, the computed deformed shapes are close to the corresponding experimental ones at each one of the five times.

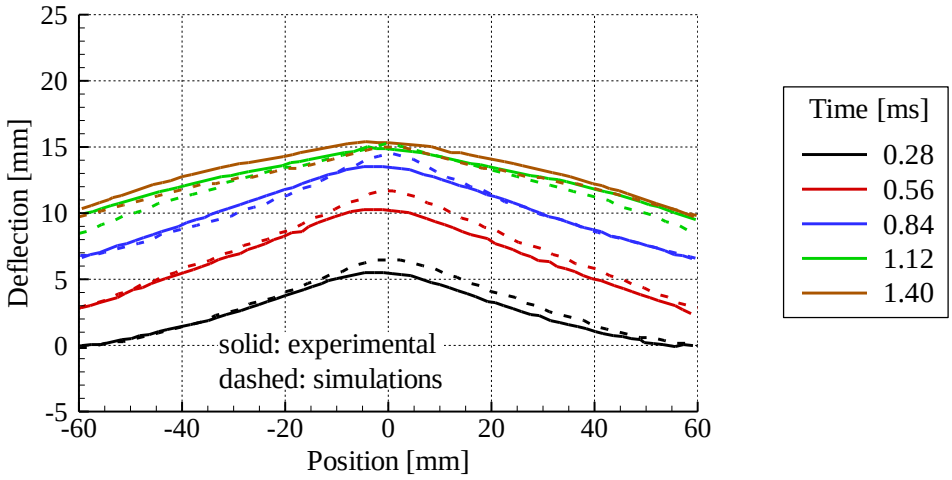

Fig.2–5: Deformed shapes at different times of the back surface of the 5.60 mm thick PC panel impacted at 30.5 m/s. Experimental data from [30].

2.5.1.2 Effect of plate thickness for 30.0 m/s impact speed

We have numerically simulated deformations of 3, 4.45, 5.85, 9.27 and 12.32 mm thick 254 mm square clamped flat plates impacted by the rigid cylinder (mass 104 g, nose radius 6.35 mm) imparting to the panel kinetic energy and linear momentum of 20.8 J and 2.08 N·s, respectively.

In order to ascertain dominant deformation modes in the impacted plates, we define the overall average axial stress at a point T_{axial} and its through-the-thickness average $T_{\text{axial,avg}}$ by

$$\hat{T}_{\text{axial}} = \left[\left(\frac{\mathbf{F}^{-\text{T}} \cdot \mathbf{N}}{\left\| \mathbf{F}^{-\text{T}} \cdot \mathbf{N} \right\|} \right)^{\text{T}} \cdot \mathbf{T} \cdot \mathbf{N} \right] \quad , \quad T_{\text{axial}} = \frac{1}{t_f} \int_{t=0}^{t_f} \hat{T}_{\text{axial}} dt \quad , \quad T_{\text{axial,avg}} = \frac{1}{h} \int_{Z=-h}^{0} T_{\text{axial}} dZ \qquad (2\text{–}4)$$

Here T_{axial} is the axial stress at a point averaged over time from the beginning of impact till the time t_f when the impactor finally separates from the plate and not the time when the plate comes to rest and **N** a unit vector normal to the local cross section in the undeformed configuration and pointing towards the panel center. Thus the value of t_f varies with the plate thickness and the impact speed. Values of t_f listed in Fig. 5 equal 3.02, 2.78, 2.6, 2.1 and 1.74 ms, respectively, for the 3, 4.45, 5.85, 9.27 and 12.32 mm thick plates. That is, t_f monotonically decreases with an increase in the plate thickness.

The $T_{\text{axial,avg}}$ equals the value of T_{axial} averaged over a transverse normal to the midsurface of the panel in the reference configuration, and is related to the through-the-thickness averaged stretching of the panel.

We note that both T_{axial} and $T_{\text{axial,avg}}$ give the time-averaged values rather than the instantaneous values at a point. The difference between values of T_{axial} at points of intersection of a transverse normal to the panel midsurface with its top and the bottom surfaces is related to the local bending of the panel; a negative value of this difference will imply that on the average points on the transverse normal have experienced either bending or compressive deformations, and a positive value will suggest that they have experienced stretching deformations since the panel is deformed concave upwards. Because of the difference in the yield stress of the PC in tension and compression, the foregoing statement is approximately valid. The variations with the *x*-coordinate along the centroidal axis of $T_{\text{axial,avg}}$ and the difference in the values of T_{axial} at corresponding points on the top and the bottom surfaces are shown in Fig.2–6 for 30 m/s impact speed and the five thickness values. These results evince that in the 3 mm thick plate the average axial stress is tensile, and is much higher than that in the thicker plates implying that stretching deformations are dominant in the thin plate. This is further confirmed by the relatively small difference between values of the axial stress on the top and the bottom surfaces of the plate (cf Fig.2–6 right). In the 5.85, 9.27 and 12.32 mm thick plates, $T_{\text{axial,avg}}$ is negative or compressive near the center of impact (cf. Fig.2–6 left). It becomes positive at points situated at least 4, 4.5 and 10 mm away from the panel center.

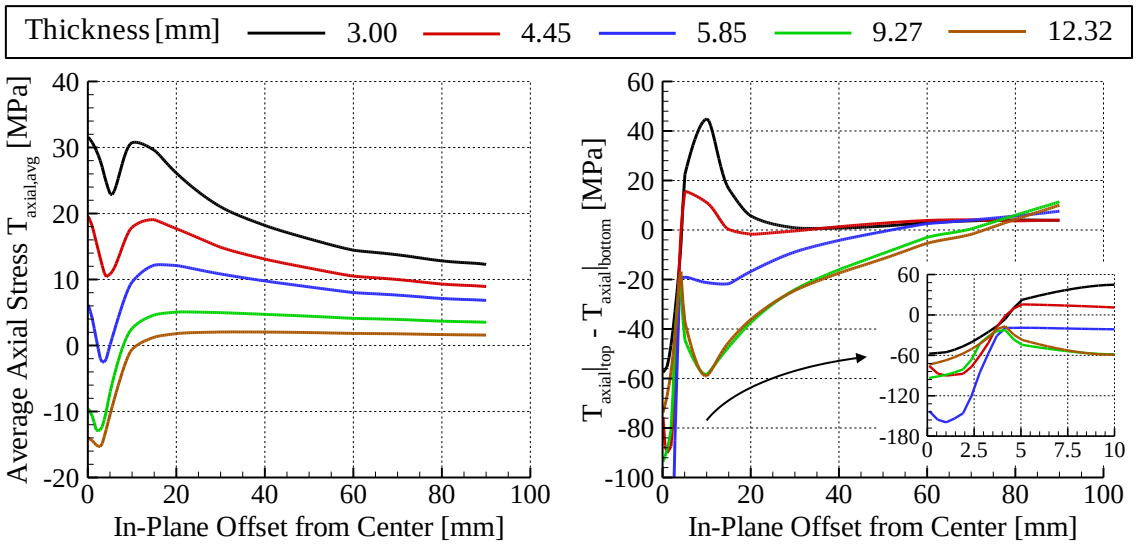

Fig.2–6: Average axial stress and difference between the average axial stress on the top and the bottom surfaces as a function of the *x*-coordinate along the centroidal axis for impact at 30 m/s of panels of different thicknesses.

The central portions of the final deformed cross-sections of plates impacted at 30 m/s including fringe plots of the effective plastic strain are exhibited in Fig.2–7. It is clear that deformations of the 3 mm thick plate are quite different from those of the thicker plates, plastic deformations are highly localized near the impacted point, and the maximum effective plastic strain in the 3 mm thick panel is more than twice of that in the 12.32 mm thick panel. For each plate, strains are not symmetric about the midsurface due to stretching deformations and the difference in the yield stress in tension and compression for the PC.

However, the difference in the effective plastic strains is much more than that due to the difference in the yield stresses. Whereas the 12.32 mm thick plate has noticeable plastic strains around the impact point and near the top surface, the other four plates have more plastic deformations in the same general region near the bottom surface. The impactor stays in contact with the 3 and the 4.45 mm thick panels throughout their ½ cycle of motion, it loses contact for the 5.85, 9.27 and 12.32 thick panels before they revert back to the position of zero deflection. The deformed regions of plates under the impactor have larger slopes near the crater edges for the thinnest plate than that for the thickest plate studied which is possibly due to the higher elastic flexural rigidity of a thick plate. Except for the 12.32 mm thick panel, the other four plates are not quite flat when they revert back to the position of zero centroidal deflection.

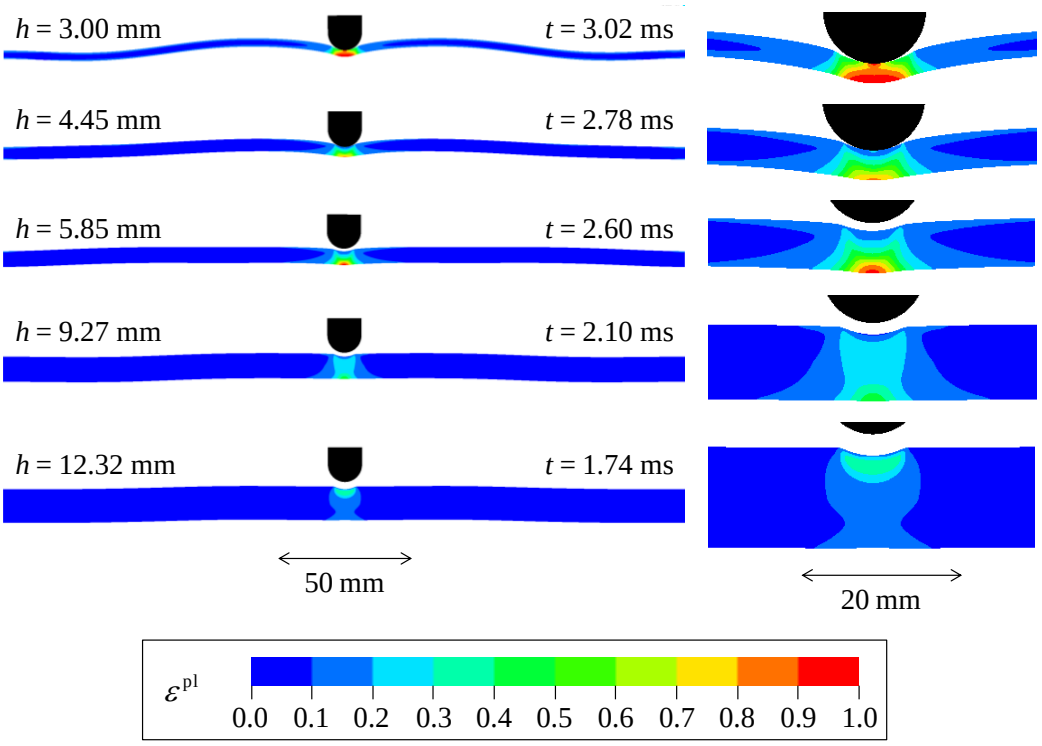

Fig.2–7: Fringe plots of the effective plastic strain in the deformed configurations corresponding to times when plates first revert back to the zero deflection position.

For impact speed of 30 m/s time histories of strain energies of elastic deformations, kinetic energies, the contact force and the total energy dissipated due to plastic deformations and material softening are plotted in Fig.2–8. The final time corresponds to the instant of complete separation between the impactor and the plate and has been denoted above by t_f. The elastic and the kinetic energy time histories of the 5 plates are qualitatively similar to each other. The energy dissipated in the thickest plate is highest even though the maximum effective plastic strain induced in it is small because more material has been deformed plastically. The elastic (first peak in the kinetic energy) energy of the thinnest plate attains its maximum value at 1.5 ms (1 ms) whereas the corresponding time for the thickest plate is 0.7 ms (0.5 ms). Since the plates are undergoing forced vibrations, these times need not be related to time periods of their free vibrations. We note that the maximum values of the elastic energy for the five plates are about the same but those of the maximum kinetic energy monotonically decrease with a decrease in the plate thickness.

Note that the minimum value of the kinetic energy does not equal zero since the velocity vectors differ from point to point. For each one of the five plates, the time of the maximum elastic energy nearly coincides with that of the first minimum in the kinetic energy of the panel, and the energy dissipated due to plastic deformations at these times is about 10% of the initial kinetic energy of the impactor. At time t_f, the energy dissipated equals 9.5 (45.7% of the initial kinetic energy of the impactor) , 7.5 (36.1%), 11 (52.9%), 13.5 (64.9%) and 13 J (62.5%), respectively, for the 3, 4.45, 5.85, 9.27 and 12.32 mm thick plates, and is not a monotonic function of the plate thickness. We recall that the initial kinetic energy of the impactor equals 20.8 J. Computations were not continued till the plate came to rest.

The maximum value of the reaction force between the impactor and the PC panel increases with an increase in the plate thickness. The contact force time histories for the 9.27 and the 12.32 mm thick plates differ qualitatively from those for plates of the other three thicknesses. For the thinner plates, once the contact between the impactor and the plate is lost, they stay separated but for the 9.27 and the 12.32 mm thick plates the contact stops after 0.8 and 0.65 ms, respectively, and is then reestablished before the separation becomes final. The peak contact force for the 9.27 and the 12.32 mm thick plates is more than that for the thinner plates, and the value of the 2nd peak contact force is higher than that of the 1st one. The times of the 2nd peaks in the contact force seem to correspond to those of the 2nd peaks in the kinetic energy time histories, however, there is no such correlation in the times of the 1st peaks in the contact force and the kinetic energy.

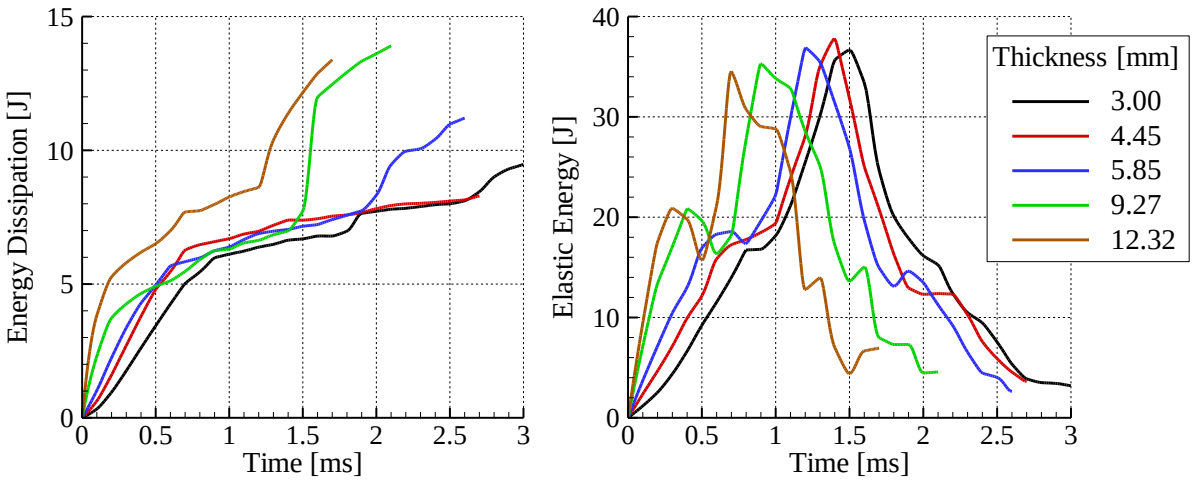

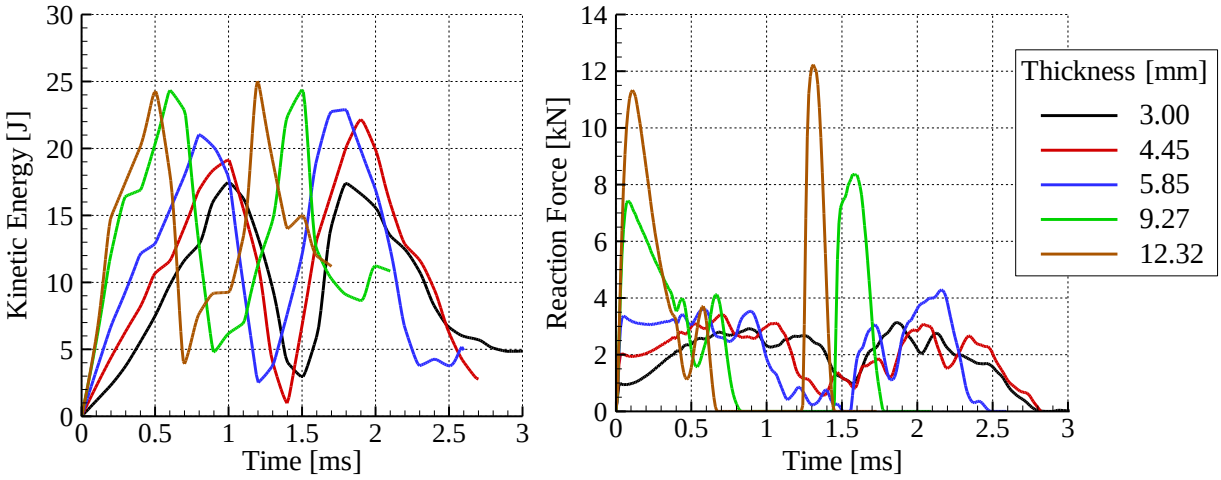

Fig.2–8: Time histories of the strain energy, the kinetic energy, the energy dissipated, and the contact force of plates of different thicknesses impacted at 30 m/s.

We define the axial stretch λ_{i_0} as the eigenvalue of the left Cauchy-Green tensor **B** corresponding to the eigenvector of **B** nearest to the deformed image of the vector **N** which in the undeformed configuration is tangent to the mid-plane of the panel and points towards the center of the panel. That is,

$$i_0 = \max_i \left| \left(\frac{\mathbf{F}^{-\mathrm{T}} \cdot \mathbf{N}}{\left\| \mathbf{F}^{-\mathrm{T}} \cdot \mathbf{N} \right\|} \right) \cdot \mathbf{v}_i \right| \quad \text{with} \quad \mathbf{V} = \sqrt{\mathbf{B}} = \sqrt{\mathbf{F} \cdot \mathbf{F}^{\mathrm{T}}} = \sum_{i=1}^{3} \left(\lambda_i \mathbf{v}_i \otimes \mathbf{v}_i \right) \quad , \quad \left\| \mathbf{v}_i \right\| = 1 \tag{2–5}$$

This definition is motivated by the expectation that at least one eigenvector of **B** is tangent to the mid-plane of the deformed panel. For all problems studied here, it was found that $_{i_0} > 0.9$. Thus the vectors $\mathbf{v}_i$ and the vector into which $\mathbf{N}$ is deformed were always nearly collinear. With **n** denoting a unit vector into which **N** is deformed, the axial stretch along **n** is given by the square root of **n.Bn**. However, the unit vector **n** may not be normal to the centroidal axis of the deformed plate. One could potentially plot the square root of **N.CN** along the Z-axis in the undeformed configuration. Here **C** is the right Cauchy-Green tensor. Whereas tensors **B** and **C** have the same eigenvalues, their eigenvectors are directions of principal stretches in the deformed and the deformed configurations, respectively. The value of λ_{i_0} approximately represents the axial stretch at a point in the deformed configuration.

The value of the axial stretch λ_{i_0} less (greater) than 1 implies that the length of the line element decreases (increases) after deformation, and λ_{i_0} = 1 means that there is zero axial strain. For the 5.85 mm thick plate we have depicted in Fig.2–9 the axial stress $\hat{T}_{\text{axial}}$ (see Eq.(2–4)) and the axial stretch λ_{i_0} versus the in-plane distance from the plate center (measured in the undeformed configuration) on the top (Z = 0), the mid (Z = -*h*/2) and the bottom (Z = -*h*) surfaces at the time when the impactor just separates from the panel. It is clear that a very small portion of the plate near the top surface is compressed and the rest of the region is stretched. The axial elongation is dominant near the bottom central part of the plate and

even the midsurface is stretched. Thus stretching deformations dominate those due to bending. Near the clamped edge, the bottom (top) surface is in compression (tension) signifying that the plate is bent concave down. The portion of the plate located at least 40 mm away from the Z-axis has undergone bending deformations. In the portion of the plate for which 7mm < Z < 40 mm, the maximum tensile axial stress is generally less than the magnitude of the axial compressive stress even though the axial elongation of the top surface is more than the axial contraction of the bottom surface. In the central portion the top surface is in compression and the bottom surface in tension. Points on the midsurface have experienced contraction. Thus deformations of the plate are quite complicated.

In Fig.2–10 we have plotted through-the-thickness variation of the axial stress $\hat{T}_{\text{axial}}$ and the axial stretch λ_{i_0} on the line passing through the plate centroid that also passes through the center of impact at times corresponding to those given in Fig.2–7. Note that the initial Z- coordinates are normalized with respect to the plate thickness, thus zero corresponds to the top face of the plate and -1 to the bottom one. For the 3, 4.45 and 5.85 mm thick plates, only a very small portion near the top surface is compressed, and most points including that on the midsurface experience axial tension. For the 9.27 and 12.32 mm thick plates, all points on this line experience axial tension. Thus according to the classical definition of the neutral surface (i.e., the surface on which the length of a line element remains unchanged) there is no such surface for the 9.27 and the 12.32 mm thick plates. The resultant axial force can be computed by integrating $\hat{T}_{\text{axial}}$ over the thickness. We thus see that the axial force for plates of all thicknesses considered is compressive implying that both bending moment and axial force act on an infinitesimal cross-section since we have not integrated along either the X- or the Y-direction. For each plate points where the axial stress equals zero do not coincide with those where the axial stretch equals 1.

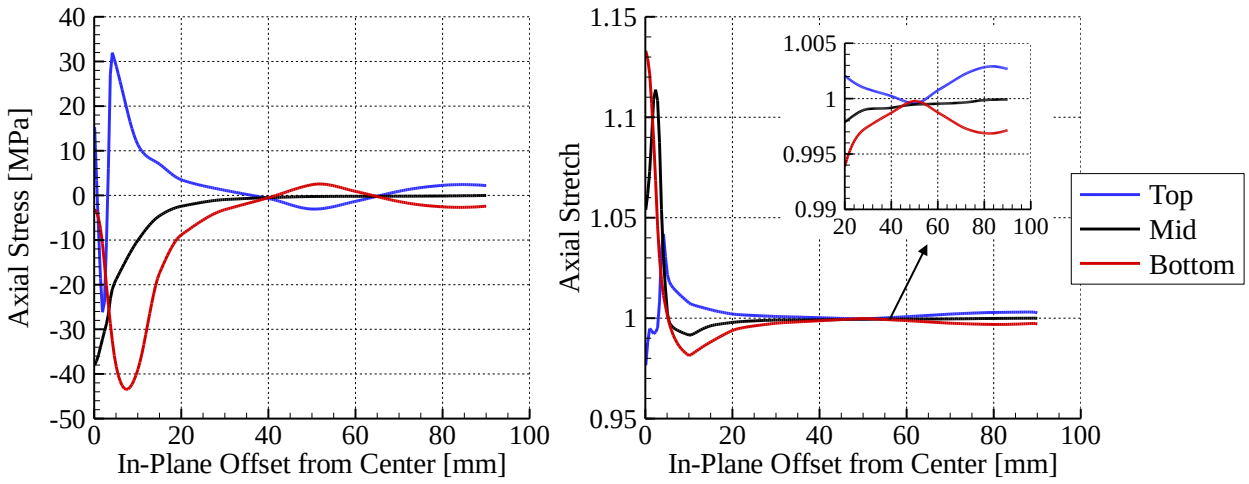

Fig.2–9: Axial stress and axial stretch as a function of the distance from the plate center at the top, mid-plane and bottom of the 5.85 mm thick PC plate for 30 m/s impact velocity at the time t_f = 2.60 ms.

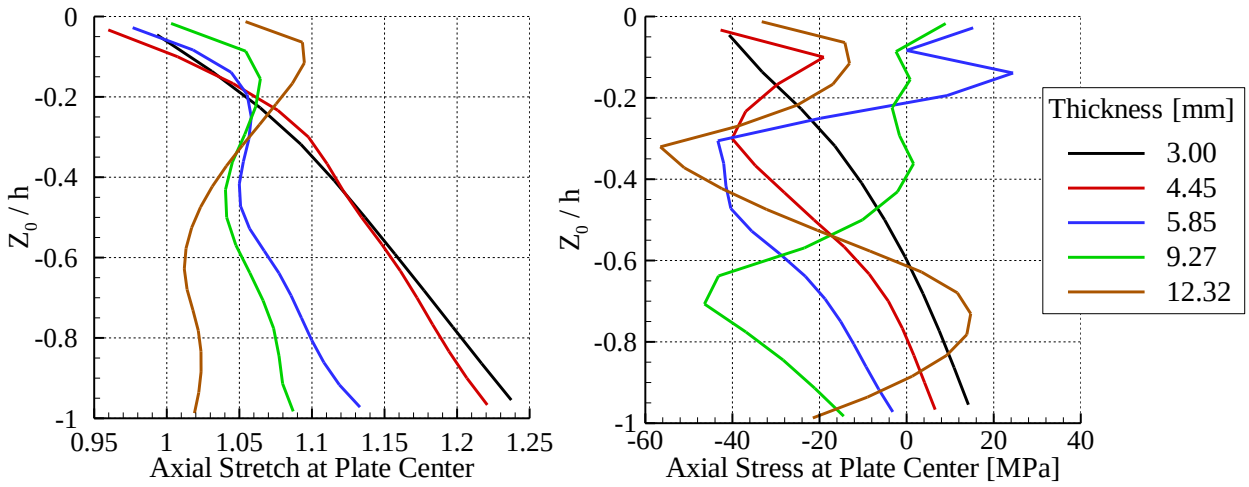

Fig.2–10: Through-the-thickness variation of the axial stress and the axial stretch on the centroidal axis for the 3, 4.45, 5.85, 9.27 and 12.32 mm thick PC plates and 30 m/s impact velocity at the times t_f of Fig.2–7.

2.5.1.3 Effect of impact velocity for 5.85 mm plate thickness

In this subsection we study and compare results for impacts of the 5.85 mm thick PC plates by 104 g hemispherical-nosed impactor of radius 6.35 mm. The impact speeds considered are 10, 20, 30, 40 and 50 m/s.

In Fig.2–11 we have plotted the variations along the centroidal x-axis of the T_{axial} and the $T_{\text{axial,avg}}$ as defined in Eq.(2–4). With an increase in the impact speed the value of the average axial stress T_{axial} at points more than 10 mm away from the plate center is qualitatively unchanged but increases with an increase in the impact speed. At the plate center the sign of T_{axial} changes from negative to positive when the impact speed is increased from 20 to 30 m/s.

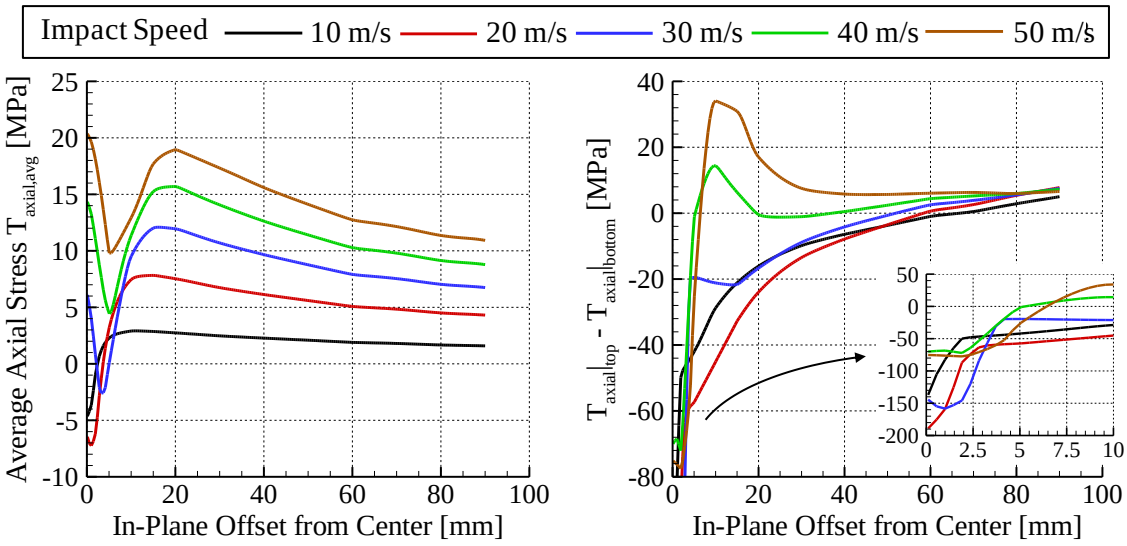

Fig.2–11: Average axial stress and difference between the average axial stress on the top and the bottom surfaces as a function of the *x*-coordinate along the centroidal axis for impact of 5.85 mm thick panels at different speeds.

For each impact speed we have exhibited in Fig.2–12 the spatial distribution of the effective plastic strain on a plane section perpendicular to a plate edge and passing through the plate centroid. It is clear that plastic strains are localized in a narrow region near the plate center and as expected the size of the plastically deformed region as well as the maximum effective plastic strain increase with an increase in the impact speed. The maximum effective plastic strain equals 0.23, 0.50, 0.94, 1.2 and 1.4, respectively, for 10, 20, 30, 40 and 50 m/s impact speed which shows that it is not proportional to the initial kinetic energy of the impactor. The largest values of the effective plastic strain occur at points near the bottom face of the plate and effective plastic strains on the top face of the plate are generally much smaller than those at corresponding points on the bottom face of the plate. How much of this difference is due to the magnitude of the yield stress of the PC being smaller in tension than that in compression remains to be investigated.

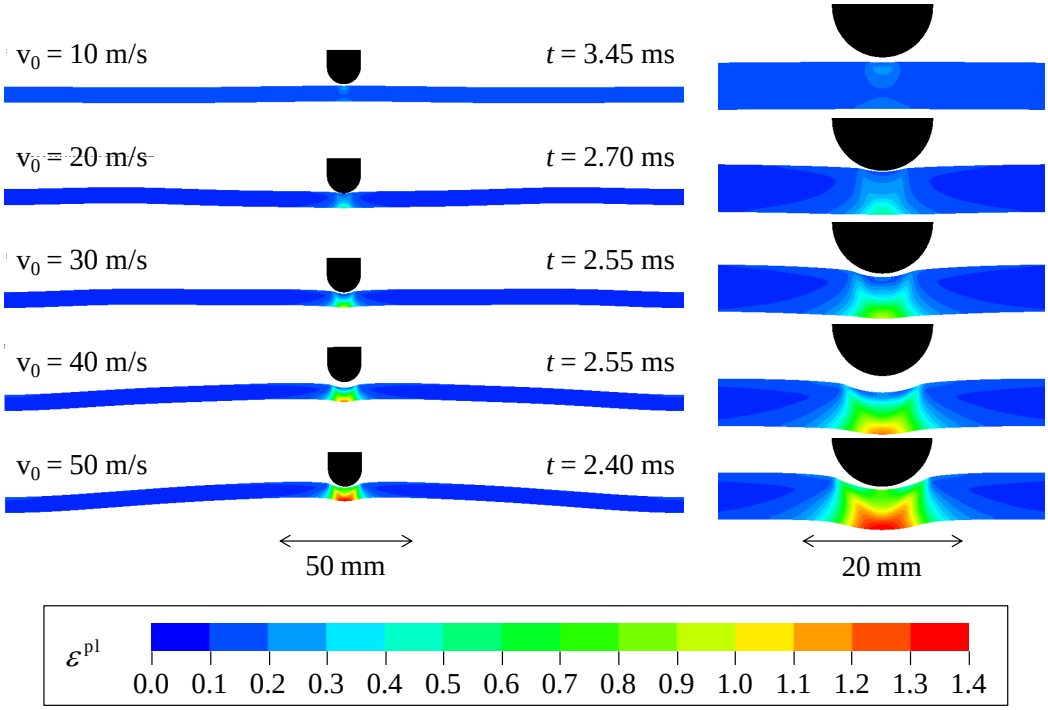

Fig.2–12: Fringe plots of the effective plastic strain in the deformed configurations at the times of separation between the 5.85 mm thick plate and the impactor. The times of separation are also listed in the Fig.

The time histories of the kinetic, the elastic and the dissipated energies of the plates normalized by the initial kinetic energy of the impactor, and of the reaction force between the impactor and the plate are depicted in Fig.2–13. With an increase in the impact speed, a larger portion of the initial kinetic energy of the impactor is used to plastically deform the plate, and the time of separation of the impactor from the plate monotonically decreases with an increase in the impact speed. The times of the initial peaks in the elastic and the kinetic energies monotonically decrease with an increase in the kinetic energy of the impactor. The qualitative nature of these plots remains unaffected by the impact speed. The maximum value of the reaction force is nearly proportional to the impact speed which agrees with the results of Her and Liang [26].

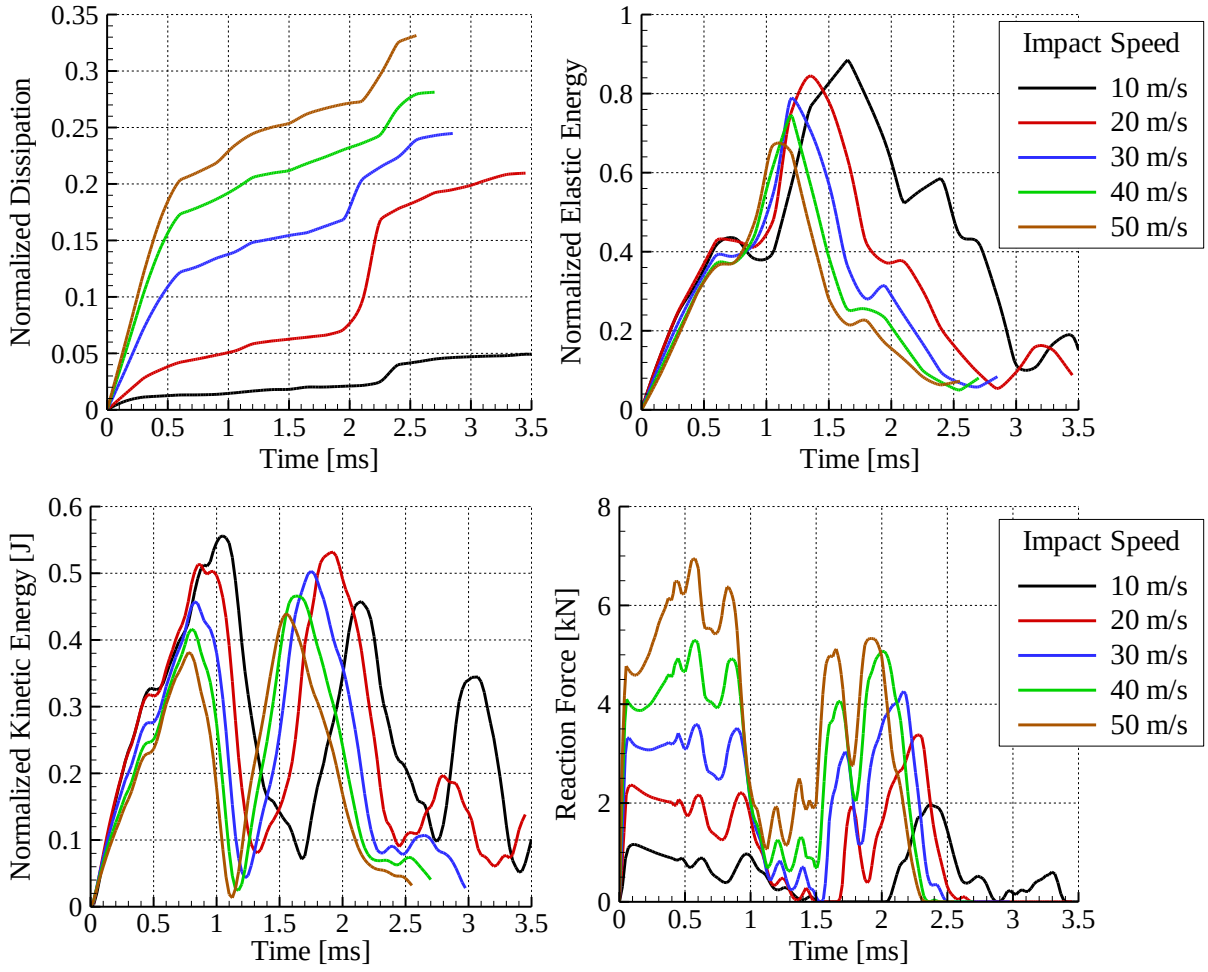

Fig.2–13: Time histories of the normalized strain energy, the normalized kinetic energy, the normalized energy dissipated, and the contact force for the 5.85 mm thick plate for different impacts speeds. Energies are normalized with the initial kinetic energy of the impactor.

Similar to the results plotted in Fig.2–10 we have exhibited in Fig.2–14 and in Fig.2–15 the axial stress and the axial stretch as a function of the distance from the plate center for the impact speed of 50 m/s, and through-the-thickness distribution of the axial stress and the axial stretch for different impact speeds. We see that far from the plate center the magnitude of the axial stress on the mid surface is much smaller than that on the top and the bottom surfaces which have opposite signs, indicating there the dominance of bending deformations. Close to the plate center, points on the top, the mid and the bottom surface are axially stretched. However, at 10 mm from the plate center points on the top surface are axially stretched and those on the mid and the bottom surfaces are axially compressed.

Through-the-thickness variations of the axial stretch for impact speeds of 20, 30, 40 and 50 m/s are quite different from that for the impact speed of 10 m/s. Except for the impact speed of 10 m/s, axial lines at all points except those close to the top surface have been elongated as indicated by values of the axial stretch greater than 1. For the impact speed of 10 m/s, axial line elements at several points on the cnetroidal axis have not experienced either much elongation or noticeable contraction. The axial elongation at the plate

bottom surface monotonically increases with an increase in the impact speed. For each impact speed, the resultant axial force on an infinitesimal area is negative, and points where the axial stress vanishes do not coincide with those where the axial stretch equals 1.

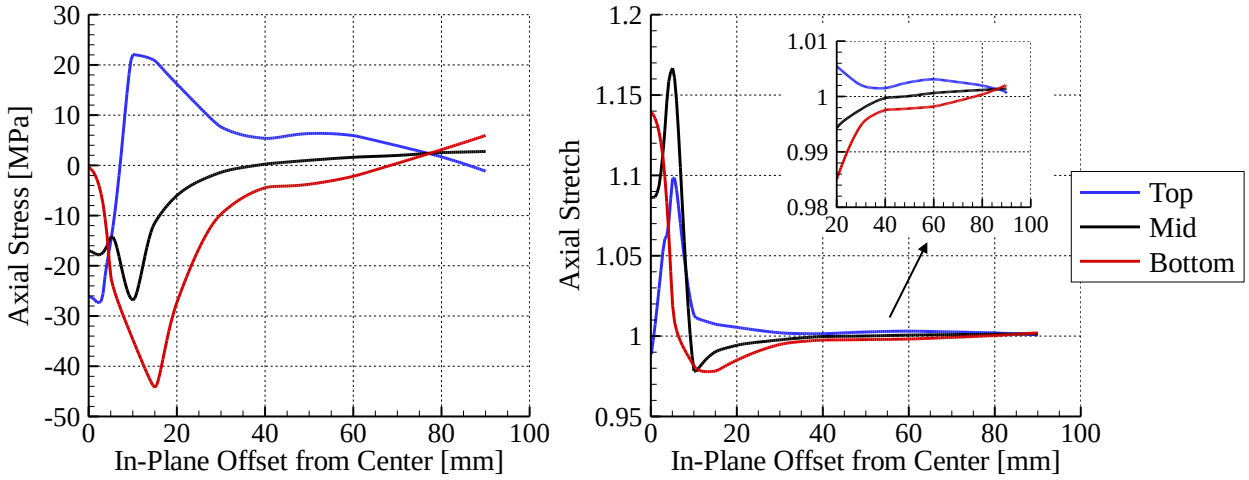

Fig.2–14: Axial stress and axial stretch as a function of the distance from the plate center at the top, mid-plane and bottom of the PC plate for 50 m/s impact velocity and at the final time t_f = 2.40 ms.

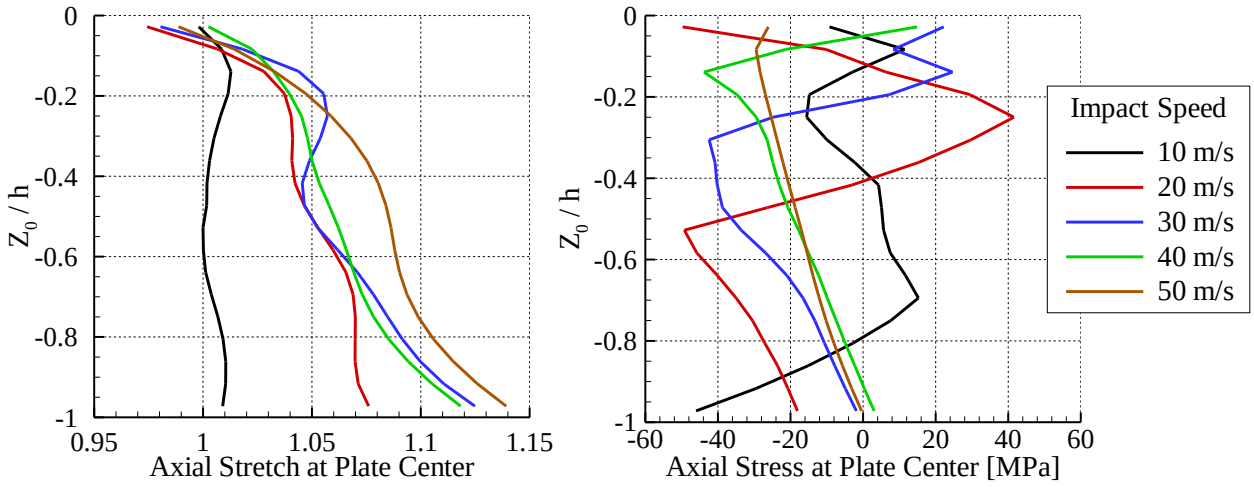

Fig.2–15: Axial stress and axial stretch at the plate center as a function of the initial Z position for 10, 20, 30, 40 and 50 m/s impact velocities at the times t_f of Fig.2–12.

2.5.2 Curved panels

In order to study the effect of the curvature on the impact response of clamped panels, we consider 254 × 254 mm panels of different thicknesses having equal principal radii, R = –127, –254, –508, ±∞ (flat plate), 508, 254 and 127 mm.

2.5.2.1 Quasi-static indentation

For a cylindrical impactor of nose radius 6.35 mm (see Fig.2–1) we have plotted in Fig.2–16 the computed contact force as a function of the quasi-static indentation depth. Quasistatic deformations were simulated by increasing the mass density of the panel material so that the time for an elastic wave to propagate to the panel edge was nearly 1/1000 of the final time of the computed deformation. The kinetic energy of the panel equaled less than 1% of its total strain energy of deformations for material properties at the strain rate of 0.001/s thereby ensuring that deformations analyzed were quasistatic.

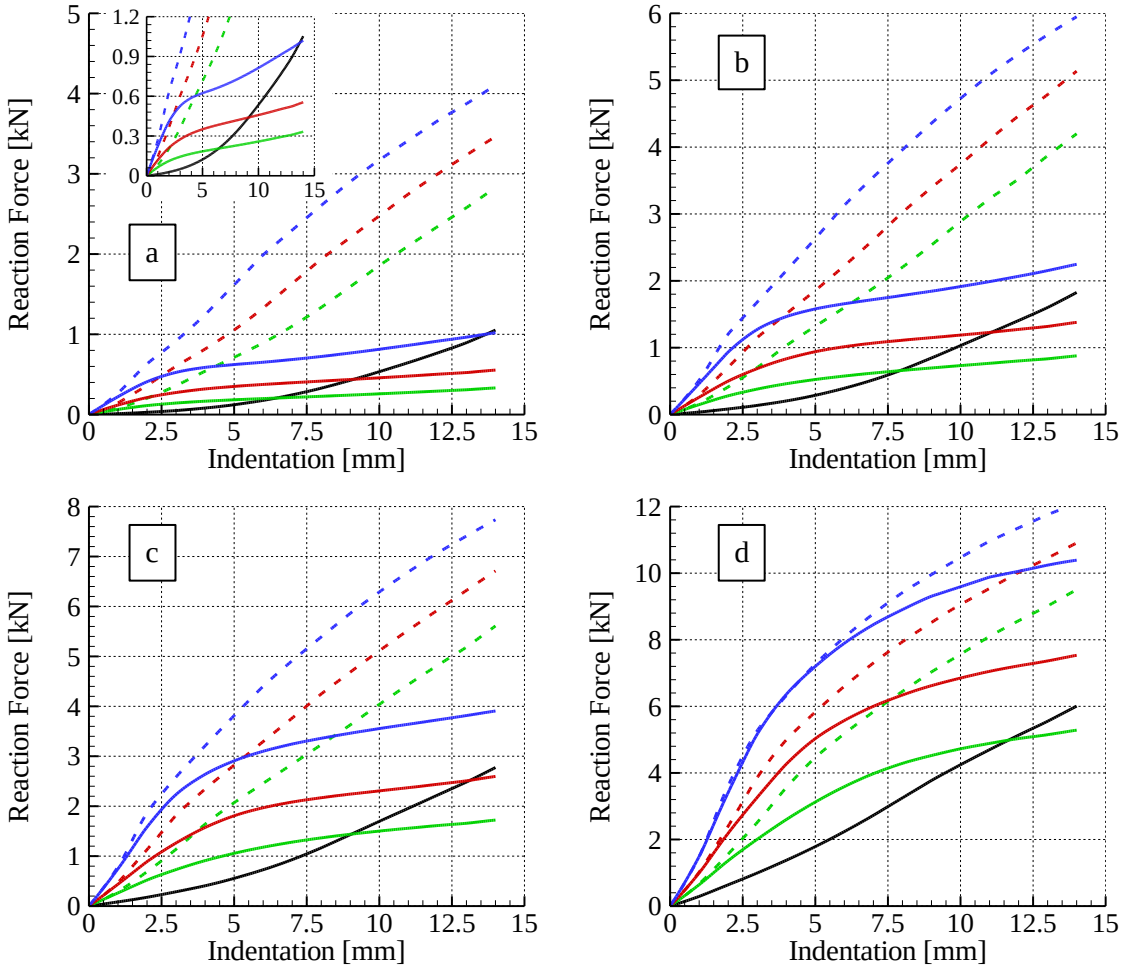

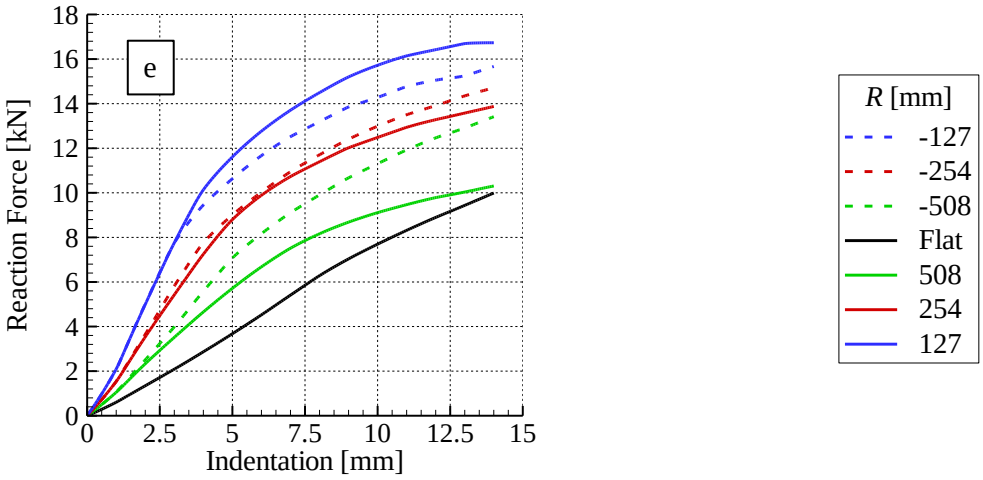

Fig.2–16: Contact force vs. indentation for the (a) 3.00, (b) 4.45, (c) 5.85, (d) 9.27 and (e) 12.32 mm thick panels of different radii of curvature.

Plate thickness [mm]	Radius of curvature R [mm]						
	–127	–254	–508	$\pm\infty$	508	254	127
3.00	0.27	0.36	0.081	0.011	0.064	0.12	0.22
4.45	0.51	0.29	0.17	0.038	0.15	0.26	0.46
5.85	0.79	0.47	0.29	0.084	0.26	0.44	0.75
9.27	1.5	1.0	0.67	0.29	0.64	1.0	1.5
12.32	2.1	1.5	1.1	0.60	1.0	1.5	2.1

Table 2–3: Initial stiffness of curved panels in kN/mm.

We have listed in Table 2–3 values of the initial stiffness, i.e., slope of the contact force vs. the indentation depth curves for the 5 values of the plate thickness. These results evince that the initial resistance to indentation of a panel increases with an increase in the panel curvature for plates with both positive (concave down) and negative (concave up) curvatures. These results qualitatively agree with those of Kim et al. [23] and Lin and Lee [27]. However, the variation of the contact force with the indentation for thin panels is qualitatively and quantitatively different for panels of positive and negative curvature. For panels of negative curvature the contact force is nearly proportional to the indentation, while the tangent stiffness for the positively curved panels decreases with an increase in the indentation. For the 3 mm thick panels and the 12.5 mm indentation, the contact force for the panel with $R > 0$ is nearly 4 to 8 times that of the panel of negative curvature but having the same magnitude of R. For thicker panels, however, the effect of the sign of the curvature is small and the magnitude of the curvature determines the response of the plate. For example, the initial tangent stiffness of the 5.85 (length of side/thickness = 43.4), 9.27 and the 12.32 mm thick panels listed in Table 2–3 is nearly the same for positive and negative values of R. Thus the effect of the sign of curvature on the initial stiffness becomes negligible for aspect ratios less than 43.

In order to investigate the effect of curvature on the stretching/bending of the panel we use the variable T_{axial} defined by Eq.(2–4) with the difference that the time averaging is replaced by averaging over the indentation depth. For a curved panel the vector **N** is orthogonal to the local cross section and points towards the panel center. The mean value of T_{axial} through the thickness measures the local stretching of the panel while the difference between its values at the top and the bottom of the panel for the same initial arc length is related to the local bending of the panel. Variations with the initial arc length, r, of T_{axial} and the difference in its values at corresponding points on the top and the bottom surfaces are shown in Fig.2–17a-e for the 3, 4.45, 5.85, 9.27 and 12.32 mm thick panels. It is clear that both the panel thickness and the panel curvature influence bending and stretching deformations at a point. For R < 0, values of $T_{axial,avg}$ at r = 0 decrease with an increase in the panel thickness. Bending deformations dominate only in a very small region near the center of a panel. In general, values of $T_{axial,avg}$ do not vary monotonically with a change in the plate curvature. We recall that the panel material is modeled as thermo-elasto-visco-plastic and thermal effects are nonexistent for quasistatic deformations. Because of the possibility of noticeable plastic deformations induced the present results cannot be directly compared with those for elastically deformed panels.

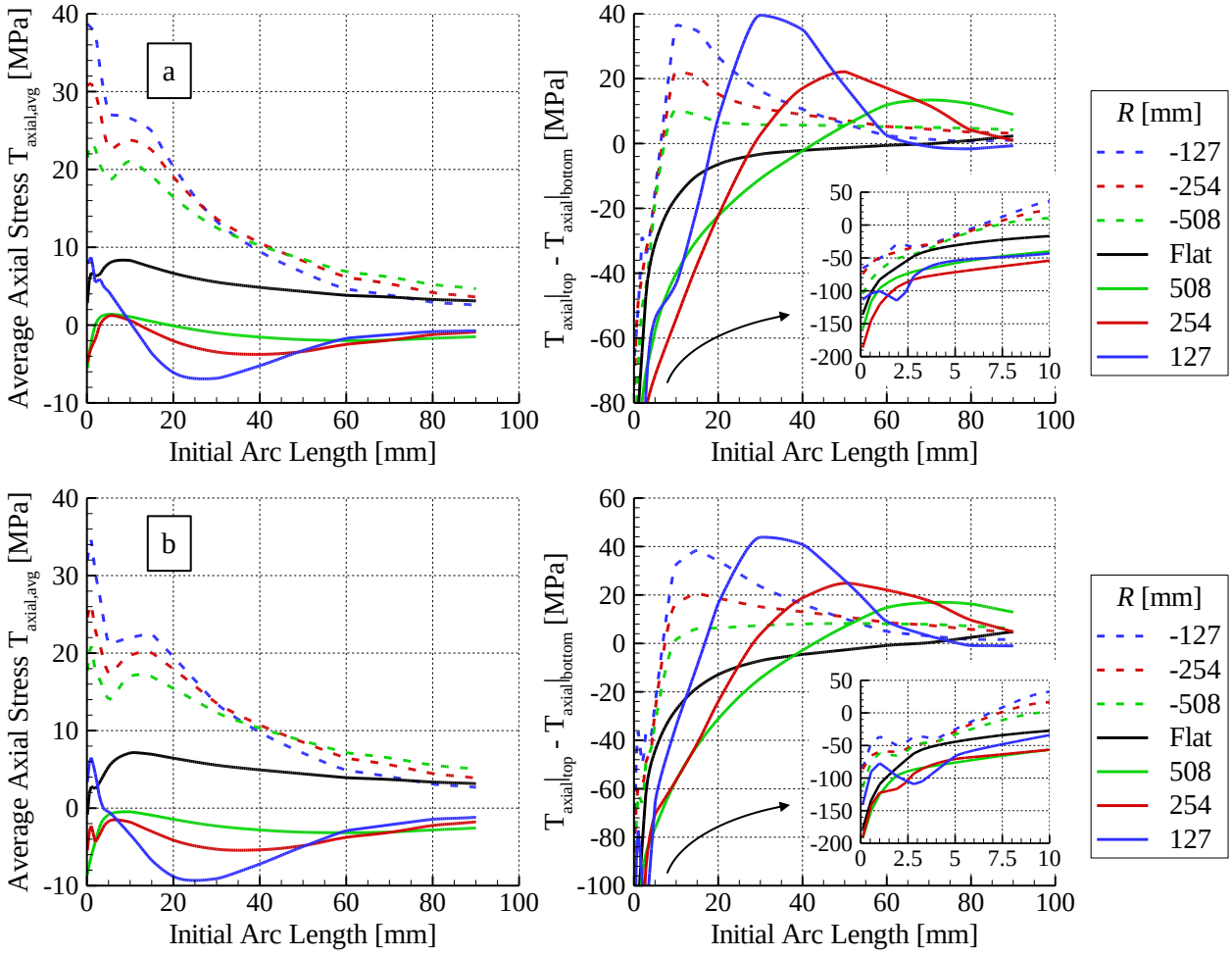

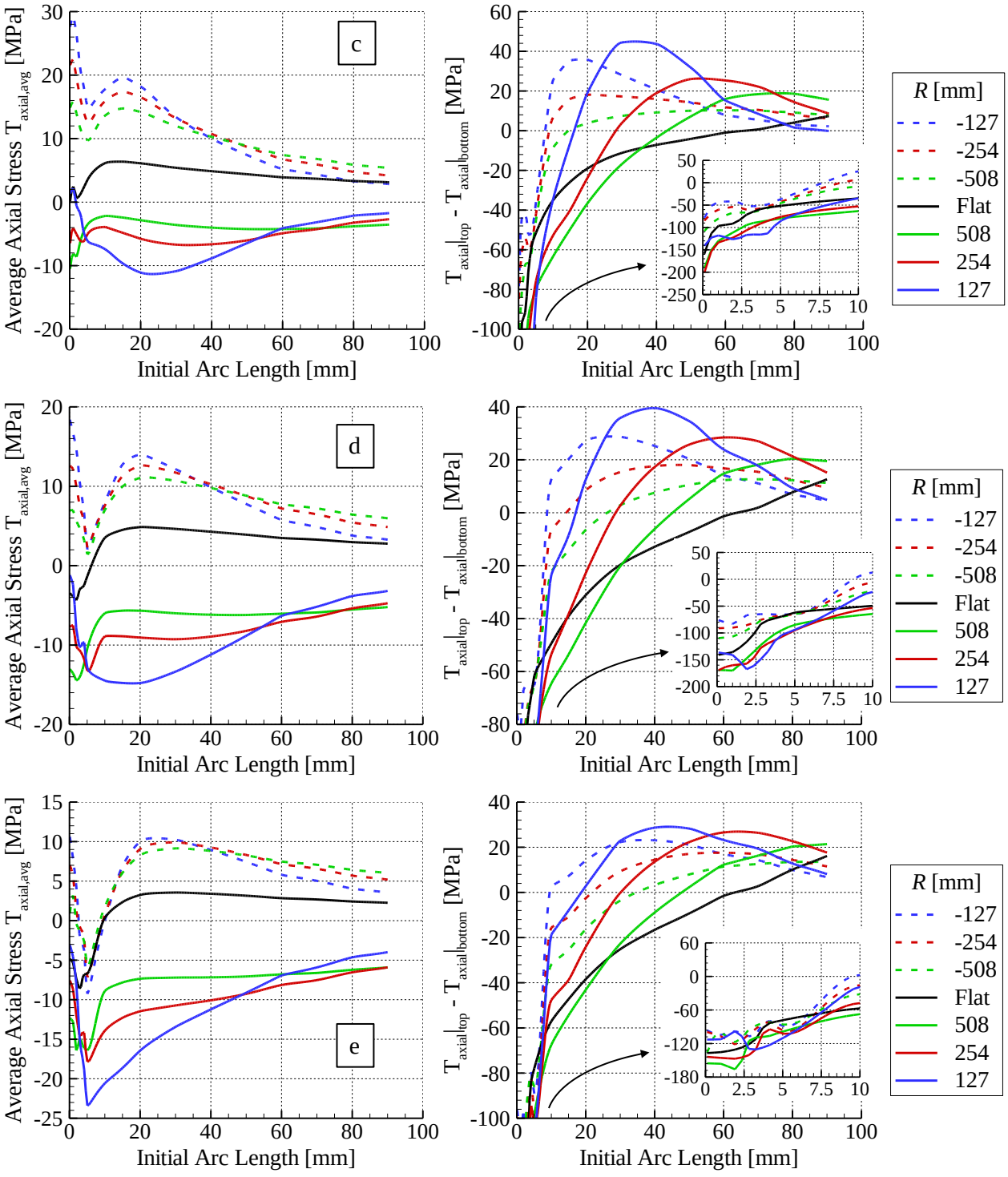

Fig.2–17: Average axial stress and the difference between the axial stress on the top and on the bottom surfaces of the (a) 3.00, (b) 4.45, (c) 5.85, (d) 9.27 and (e) 12.32 mm thick panels as a function of the initial arc length (measured from the panel center).

2.5.2.2 Impact at 20 m/s

2.5.2.2.1 Panels 3 mm thick

For different values of *R* time histories of the reaction force between the 3 mm thick panel and the 105 g hemispherical nosed cylindrical impactor traveling at 20 m/s are presented in Fig.2–18. These results have been plotted till the time when the impactor finally separates from the panel. Whereas the time histories are quite smooth for panels with R < 0, they have high frequency components for panels with R > 0. For R < 0, the contact duration for R = 127 mm is between that for R = 254 and 508 mm. For R = 254 mm, variations in the contact force during the time of contact are much smaller than those for other values of R. It seems that the contact duration is related to the panel static bending stiffness (Fig.2–16) as the panel with the highest value of the initial slope of the reaction force vs. the indentation curve has the shortest impact duration. Below we provide additional information on how the panel curvature affects its deformations.

Fringe plots of the effective plastic strain distribution on a cross-section passing through the panel centroid when the impactor finally loses contact with it are depicted in Fig.2–19. These results suggest that the impact responses of panels with the positive and the negative curvatures are noticeably different. Curiously enough the effective plastic strain distribution in the flat plate is qualitatively similar to that in the panel with R = 127 mm rather than that in the panel with R = 508 mm. The panel with R = 254 mm has the least plastically deformed region, and the maximum effective plastic strain in it is smaller than that in the other six panels. The panel with R = - 127 mm has the largest plastically deformed region with the maximum effective plastic strain of about 1.4.

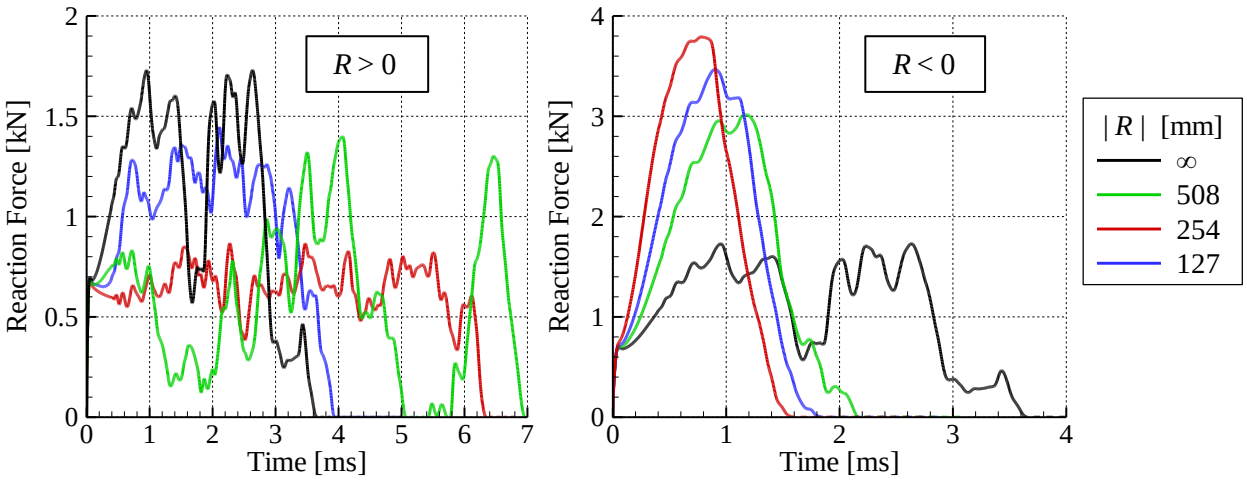

Fig.2–18: Time histories of the contact force for 3 mm thick panels of different curvatures impacted at 20 m/s.

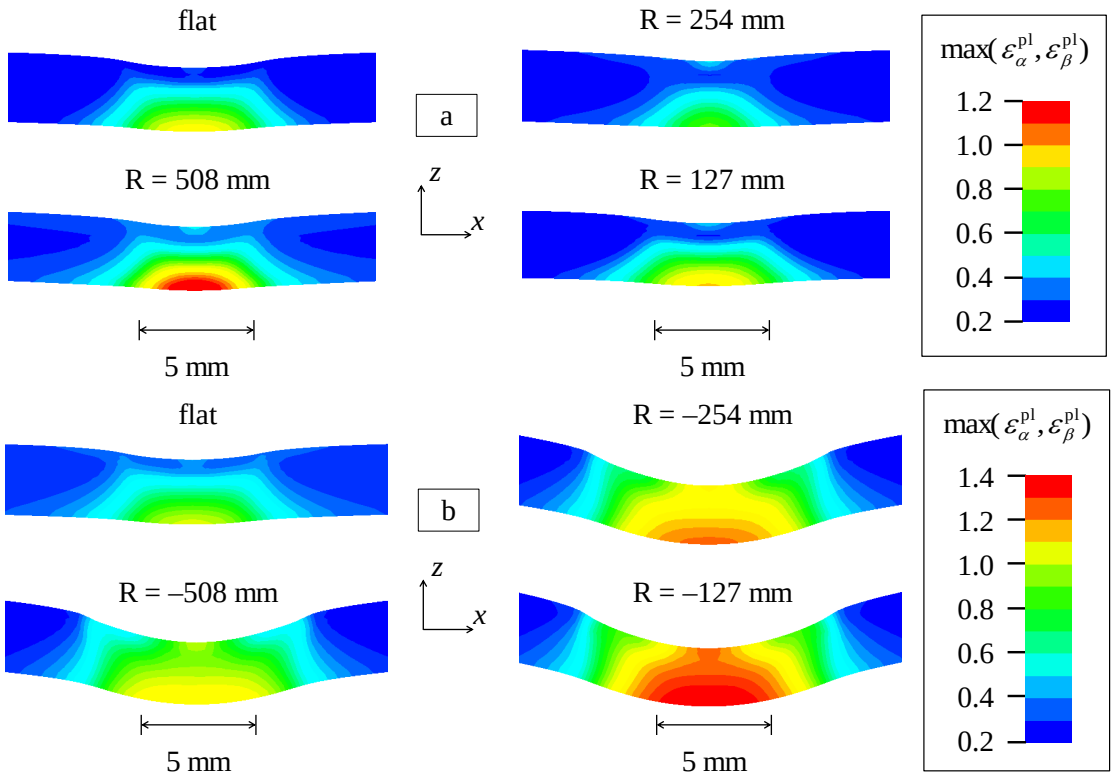

Fig.2–19: Fringe plots of the effective plastic strain in the central region of a cross-section passing through the centroid of the 3 mm thick panels with (a) R > 0, and (b) R < 0.

Time histories of the total energy dissipated due to plastic deformations and material softening during the impact of the 3 mm thick panels are exhibited in Fig.2–20. For panels with R < 0 the energy dissipation decreases with the increase in the magnitude of R, the energy dissipated is consistent with the plastic strain distribution in the neighborhood of the impact area shown in Fig.2–19, and the energy dissipated is significantly more than that for panels with R > 0. Results for the flat plate are close to those of panels with R > 0 and are generally closer to those of the panel with R = 127 mm

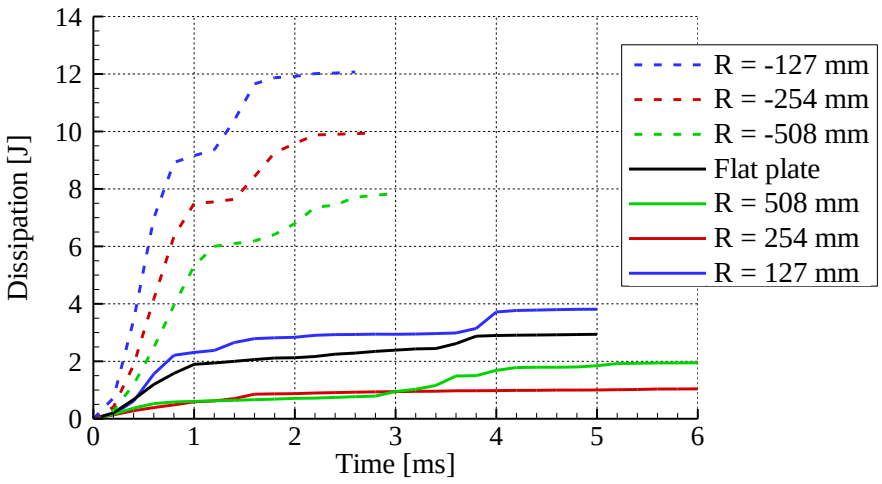

Fig.2–20: Time histories of the energy dissipation for 3 mm thick panels of different curvatures for impacts at 20 m/s.

The results are less intuitive for the panels with R > 0 because the energy dissipated in the panel with R = 127 mm is more than that in the panel with R = 508 mm since the largest plastic strains occur in the later panel. However, these results can be explained by examining the distribution of the energy dissipation density on the bottom surface and through the thickness of the panels with R = 508 and 127 mm, and evinced in Fig.2–21.

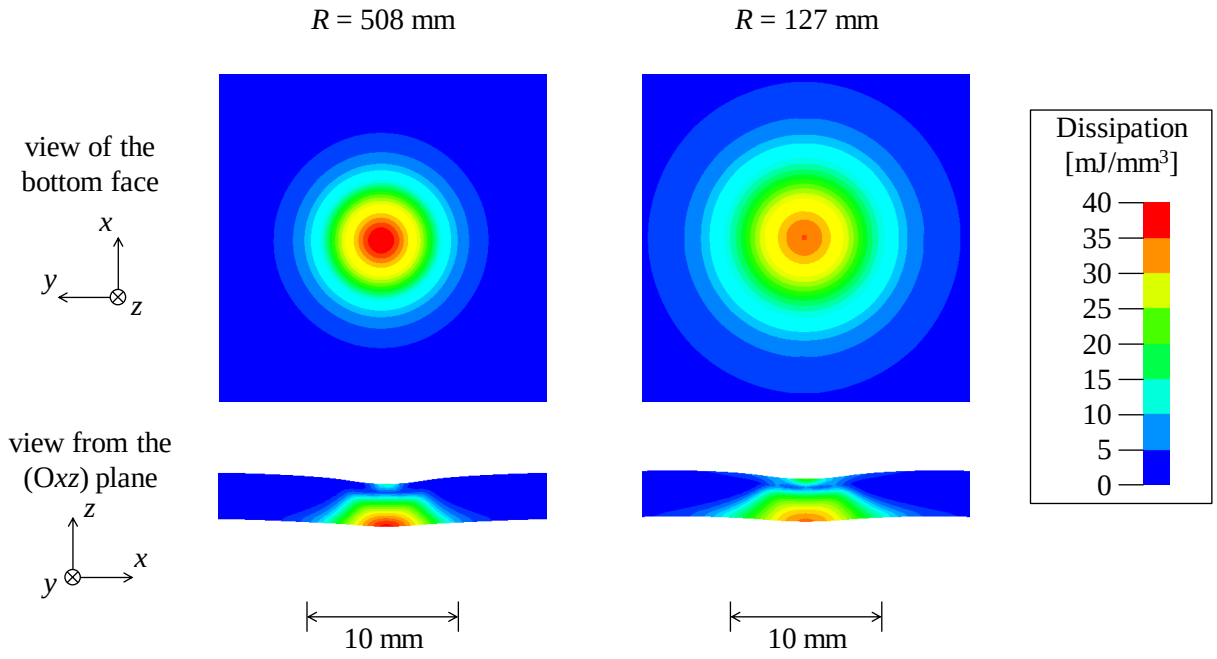

Fig.2–21: Fringe plots of the energy dissipation density on the back surface and through the thickness of panels with R = 508 and 127 mm.

It is clear that the magnitude of the energy dissipation density is larger at the center of the back face of the panel with R = 508 mm, but the dissipation density on the top surface of the panel as well as at a few mm

away from the panel center is less than that for the panel with R = 127 mm. It explains the larger total energy dissipated despite the smaller value of the maximum effective plastic strain induced in the panel of R = 127 mm. In order to further corroborate this observation we introduce the function

$$f(r) = \int_{t=0}^{t_f} \left[\int_{\Omega(r)} \left(\dot{W}_\alpha^{\text{e,soft}} + \dot{W}_\beta^{\text{e,soft}} + J\boldsymbol{\sigma}_\alpha : \tilde{\mathbf{D}}_\alpha^{\text{p}} + J\boldsymbol{\sigma}_\beta : \tilde{\mathbf{D}}_\beta^{\text{p}} \right) dV_0 \right] dt \qquad (2\text{–}6)$$

where $\Omega(r)$ is the portion of the panel that is located inside the cylinder $X^2 + Y^2 = r^2$ in the undeformed configuration. The function f measures the amount of energy dissipated in the portion of the panel initially (at time t = 0) located within a distance r from the axis $X = Y = 0$ of impact. In Eq. (9) terms appearing on the right-hand side represent the energy dissipated due to softening and plastic deformations, and t_f is the time when the impactor finally separates from the panel. Since the volume over which f is computed varies with r, values of the function f will vary even if the integrand is a constant. Thus one expects f to be essentially zero at r = 0. Values of f versus the radius r are plotted in Fig.2–22 for two curved panels with R = 127 and 508 mm. These plots reveal that the energy dissipated near the center of impact is about the same for the two panels, and the larger energy dissipation in the panel with R = 127 mm is mainly due to the higher value of the energy dissipated in the region located at distance between 3 and 10 mm from the center of impact. This explains the counter-intuitive result that larger plastic strains near the center of the panel do not necessarily imply larger energy dissipation. Whereas there is energy dissipated in the region with r > 50 mm for the flat plate and in the curved panel of R = 508 mm, there is essentially no energy dissipated in this region for the panel with R = 127 mm.

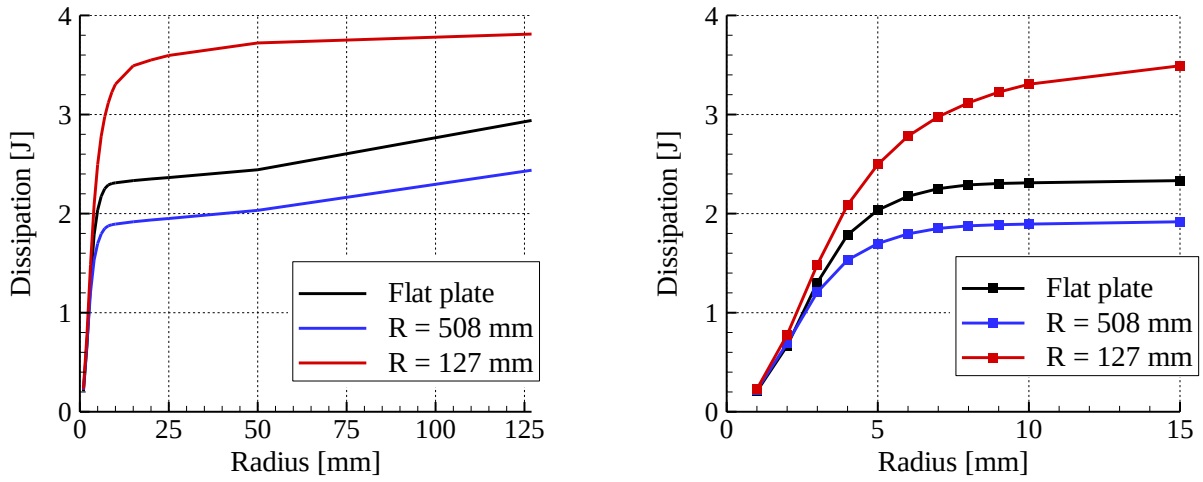

Fig.2–22: Variation of the function $f(r)$ with the radius for the flat and the curved panels of R = 127 and 508 mm. The Fig. on the right is a blow-up of that on the left for small values of r.

2.5.2.2.2 Panels of different thicknesses

Variations with r of T_{axial} are shown in Fig.2–23a-e for the 3, 4.45, 5.85, 9.27 and 12.32 mm thick panels. We recall that T_{axial} measures the local stretching of the panel while the difference between its values at the top and the bottom surfaces of the panel for the same initial arc length is related to the local bending.

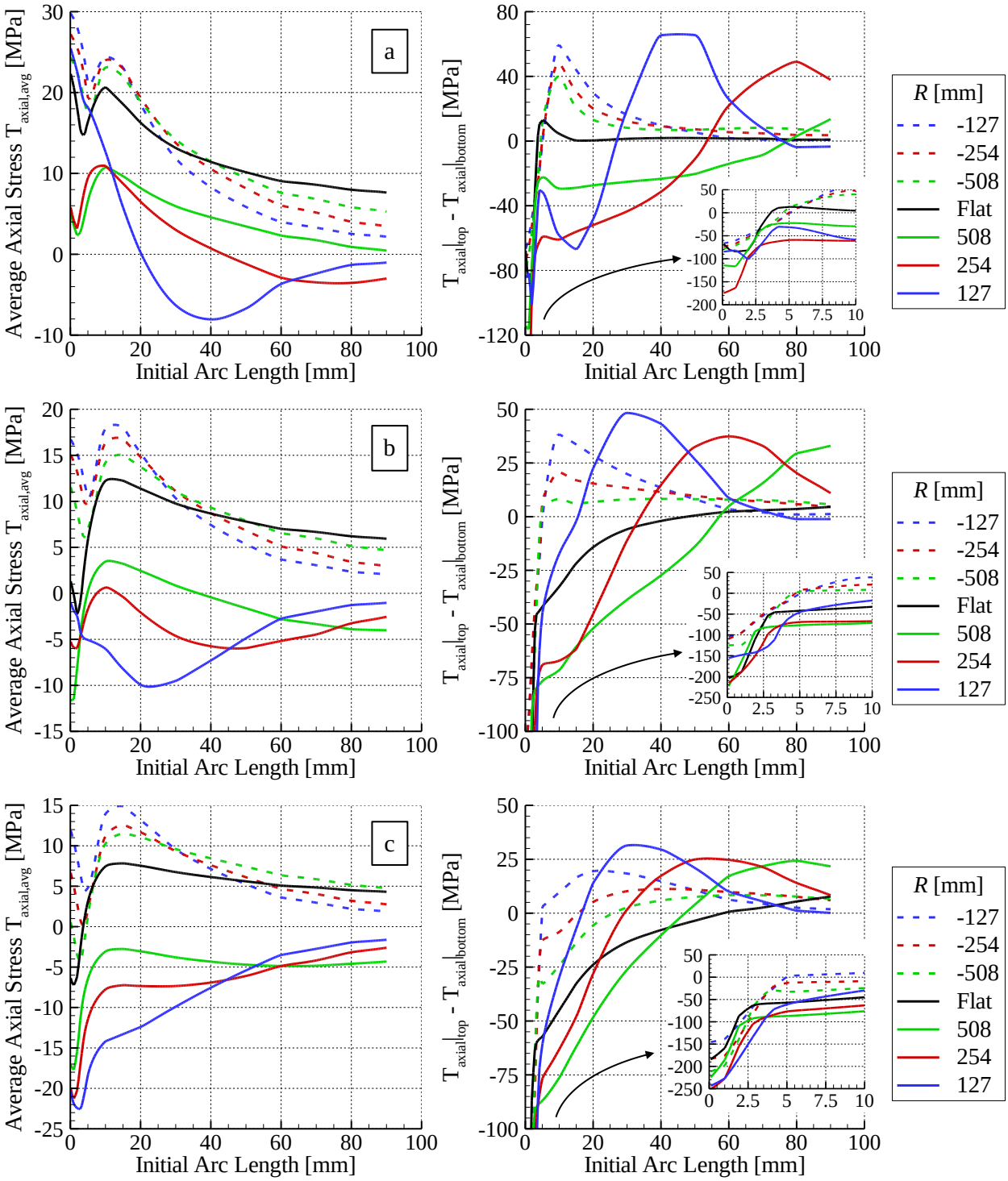
a
b
c
Average Axial Stress $T_{axial,avg}$ [MPa]
$T_{axial|top}$ - $T_{axial|bottom}$ [MPa]
Initial Arc Length [mm]
R [mm]
-127
-254
-508
Flat
508
254
127

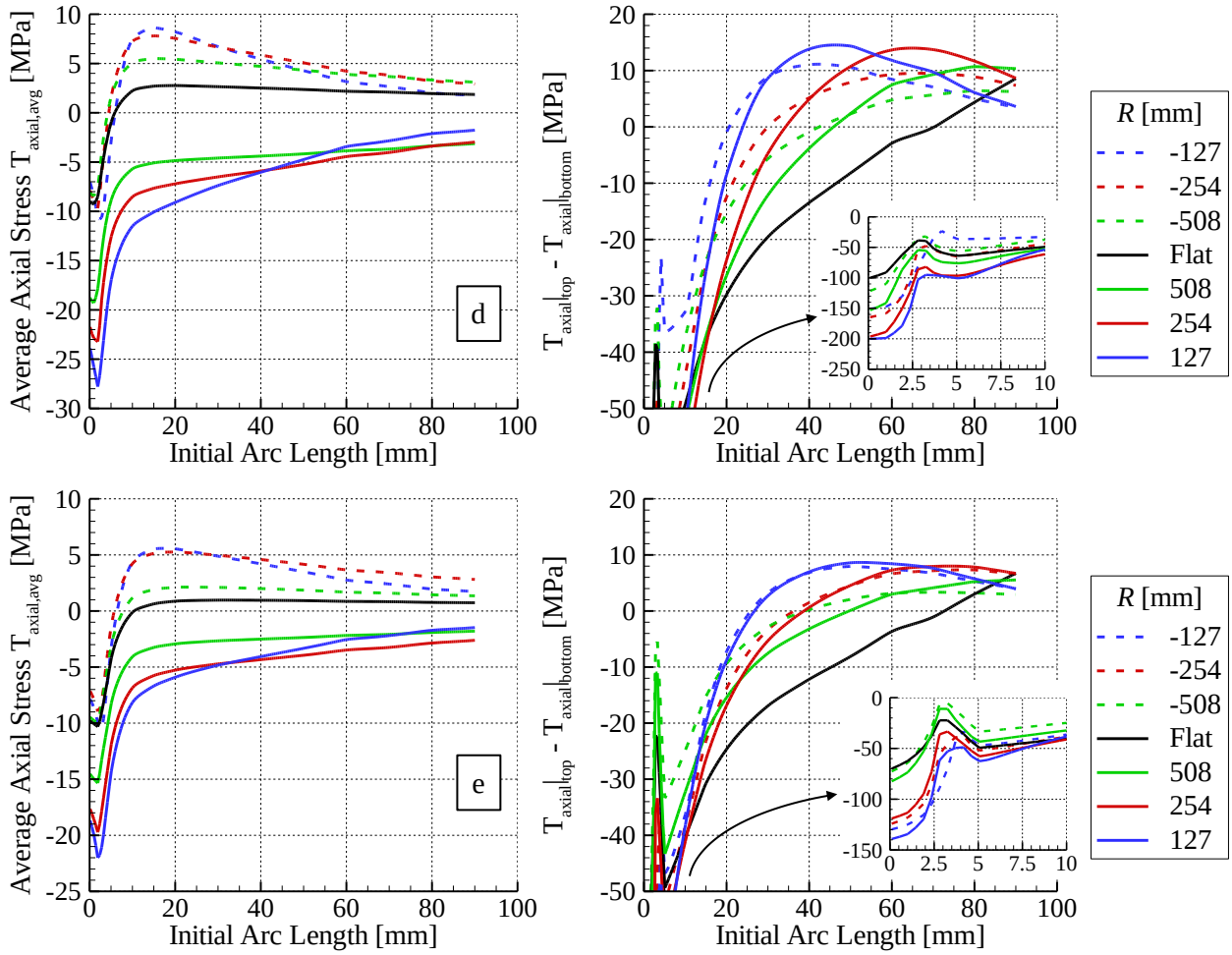

Fig.2–23: Average axial stress and the difference between the axial stress on the top and on the bottom surfaces of the (a) 3 mm, (b) 4.45 mm and (c) 5.85 mm thick panels as a function of the initial arc length (measured from the panel center).

It is evident from the results plotted in Fig.2–23 that the curvature of the panel strongly influences the average stress $T_{axial;avg}$. The negative (positive) curvature increases (decreases) the tensile axial stress near the center of the contact area. For panels with negative (positive) curvature the average axial stress near the panel edges is compressive (tensile). Results for the flat plate are qualitatively similar to those for a panel of positive curvature. For the 3 and the 4.45 mm thick panels the stress distributions for R = 127 mm are quite different from those in panels with R = 254 and 508 mm in the sense that the average tensile axial stress near the center is much larger and drops rapidly to become larger in compression for arc length in the reference configuration of more than 10 mm. Results plotted in Fig.2–23 (right) suggest than bending effects are more dominant in panels with positive curvatures. We notice in particular that for the thickest panels (9.27 and 12.32 mm) the sign of the curvature has negligible influence on the bending of the plate while it has a major impact on the average axial stress $T_{axial,avg}$. This is further elucidated upon below by additional results provided for the 12.32 mm thick panels.

For the 12.32 mm thick panels of various curvatures and 20 m/s impact speed the post-impact contours of the effective plastic strain are depicted in Fig.2–24 at times when the impactor definitely separates from

the panels. The largest values of the effective plastic strain occur in the flat panel. Overall the effective plastic strains developed in the 12.32 thick panels are much smaller than those in the 3 mm thick panels. While negative curvatures considerably degraded performances of the 3 mm thick panels it is not the case for the 12.32 mm thick panels. Fringe plots of Fig.2–24 indicate that the largest effective plastic strains do not occur at points on the rear face of the panels (which is the case for the 3 mm thick panel for which fringe plots are depicted in Fig.2–19) and that the regions of noticeable effective plastic strains are narrow (about the same radius as that of the impactor) and about 5 mm deep.

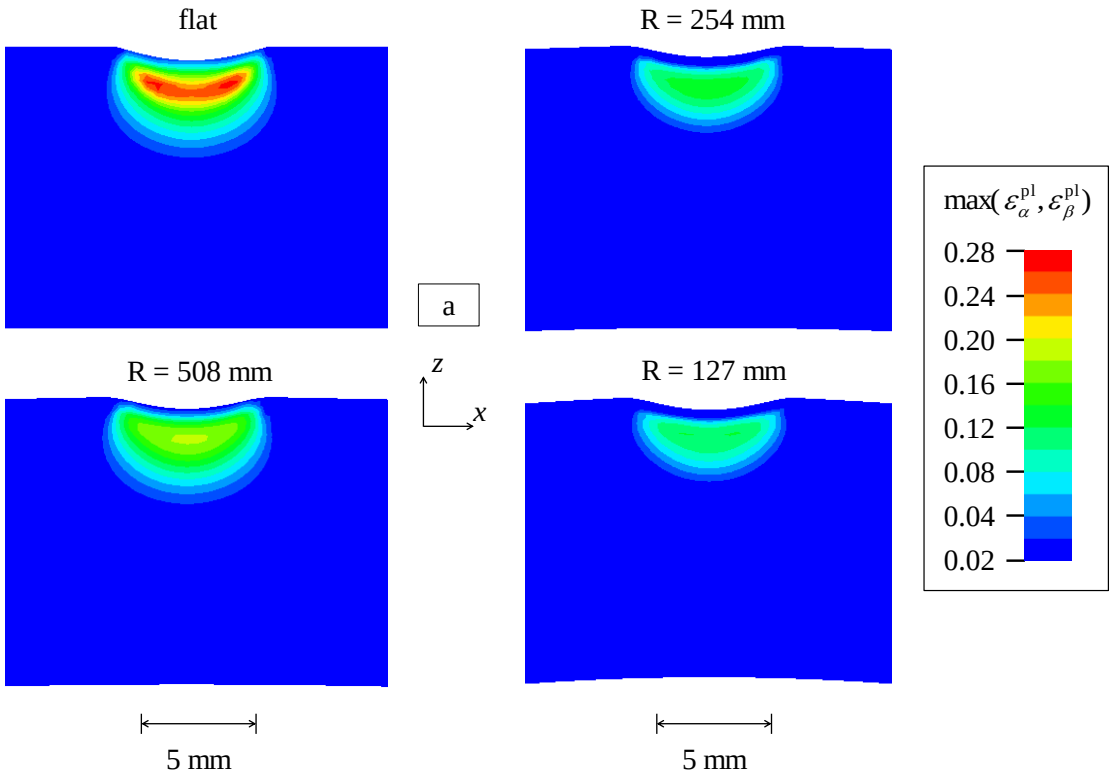

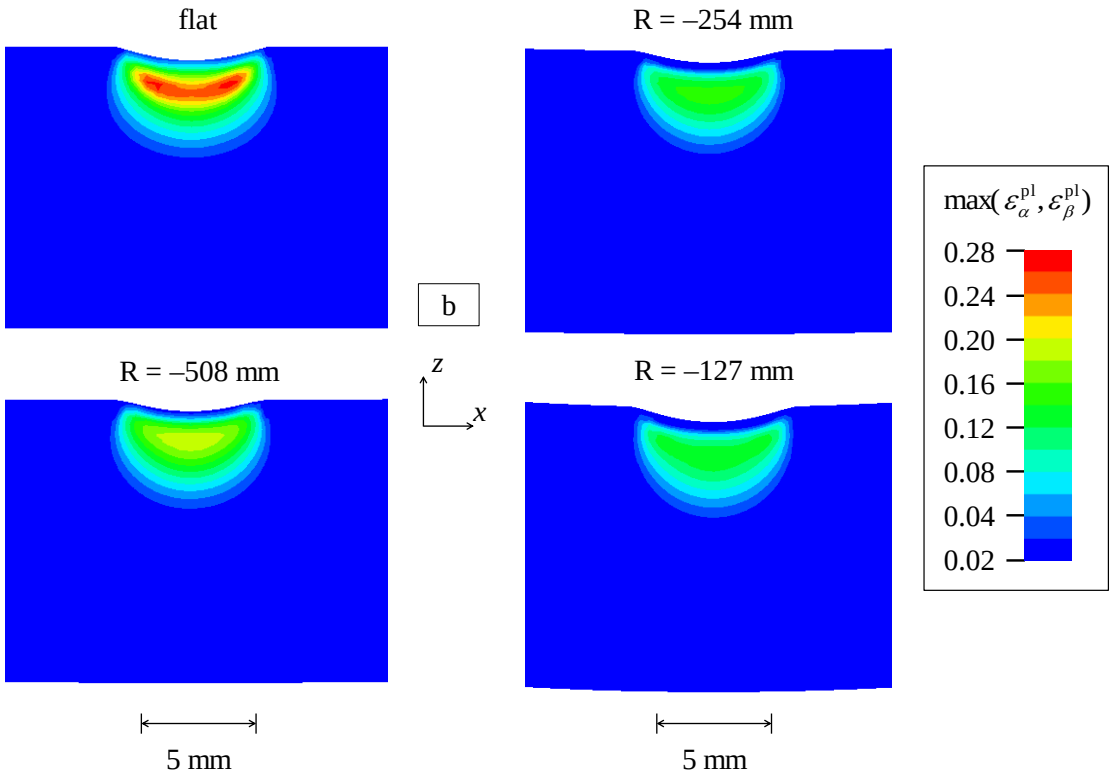

Fig.2–24: Fringe plots of the effective plastic strain in the central region of a cross-section passing through the centroid of the 12.32 mm thick panels with (a) R > 0, and (b) R < 0.

We have exhibited in Fig.2–25a,b the axial stress and the axial stretch as a function of the distance from the plate center for the 3 and the 12.32 mm thick panels with the radius of curvature, R = ∞, 127 mm and -127 mm . In Fig.2–26 we have plotted through-the-thickness variations of the axial stress and the axial stretch on the centroidal axis. In these Figures, the curves for panels with R=∞ (i.e., flat), 127 mm and -127 mm correspond to t = 3.6 (1.5), 3.8 (0.68), and 1.6 (0.65) ms for the 3.00 (12.32) mm thick plate, respectively. For the 3 mm thick flat plate, the axial stress is tensile on a significant portion of the central region at points on the top surface and compressive at points on the mid- and the bottom surfaces. The signs of the axial stress reverses from tensile to compressive at points situated more than 40 mm from the centroidal axis. Except for the magnitudes the qualitative distribution of axial stresses remains the same. The plate with R = 127 mm has the maximum magnitude of the compressive axial stress, the plate with R = ∞ has a higher value of the maximum tensile stress than the plates with R = 127 and - 127 mm. For the plate with R = -127 mm, the central portion of the mid-surface that has large values of the axial stretch extends further out than that for plates with the other two values of R. A small central region of the top surface for the two plates with R = ∞ and 127 mm is compressed. However, for the plate with R = -127 mm, the entire top surface has values of the axial stretch larger than one with the maximum value occurring at a point situated about 8 mm from the centroidal axis. Thus the plate curvature influences whether the central portion of the plate surrounding the central axis is compressed or stretched and the maximum magnitude of the axial stretch induced there.

Referring to Fig.2–25, we see that for the 12.32 mm thick flat plate, the axial stress at points on the bottom, the mid- and the top surface that are quite close to the centroidal axis is tensile. However, as one

moves away from the centroidal axis, it becomes compressive at points on the top surface, zero at points on the midsurface but stays tensile at points on the bottom surface. For the curved plate with R = - 127 mm, the axial stress is compressive at all points on the mid and the bottom surfaces but on the top surface it switches from tensile at points close to the centroidal axis to compressive at points located about 6 mm away from the centroidal axis. When R = 127 mm, the axial stress at all points on the top and the mid-surfaces is tensile and that on the bottom surface is compressive at points near the centroidal axis but tensile at points at least 20 mm away from this axis. The maximum magnitude of the axial stress is for the plate with R = 127 mm, and occurs at a point 2 mm away from the centroidal axis. Thus the distribution of the axial stress on the three surfaces strongly depends upon the plate curvature. The axial strains (= (axial stretch – 1)) are small at all points with the maximum axial strain equaling about 6.5%, and it occurs at points located about 3 mm from the centroidal axis. The maximum axial strain is higher in the plate with R = - 127 mm than that in the flat plate. Thus the plate that has the maximum axial tensile stress developed in it does not have the maximum axial tensile strain.

The through-the-thickness variation of the axial stretch plotted in Fig.2–26 for the 3 mm thick plate are quite different, both qualitatively and quantitatively from those for the 12.32 mm thick plate. In the 12.32 mm thick plate with R = -127, ∞ and 127 mm, there is practically no axial strain in the bottom $1/4^{th}$ of the plate near the centroidal axis, with the remaining portion having tensile axial strain. The maximum value of the axial strain occurs at points nearly $1/10^{th}$ plate thickness below the top surface. In the thin plate with R = -127, ∞ and 127 mm, the axial strain is tensile through most of the plate thickness and is compressive at points near the top surface for plates with R = ∞ and 127 mm. The through-the-thickness axial stress distribution is smoother in the 12.32 mm thick plate for the three values of R and in the 3 mm thick curved plate with R = 127 mm than that in the 3 mm thick plate with R = ∞ and -127 mm. The integral of the axial stress over the plate thickness has a negative value, except for the 3 mm thick plate with R = -127 mm. Thus there is a resultant axial force and a bending moment acting on both thin and thick plates for all three values of R.

We note that the yield stress of the PC in uniaxial tension is about 23% less than that in uniaxial compression. Quantifying its effect on plate's deformations is rather arduous and has not been attempted here.

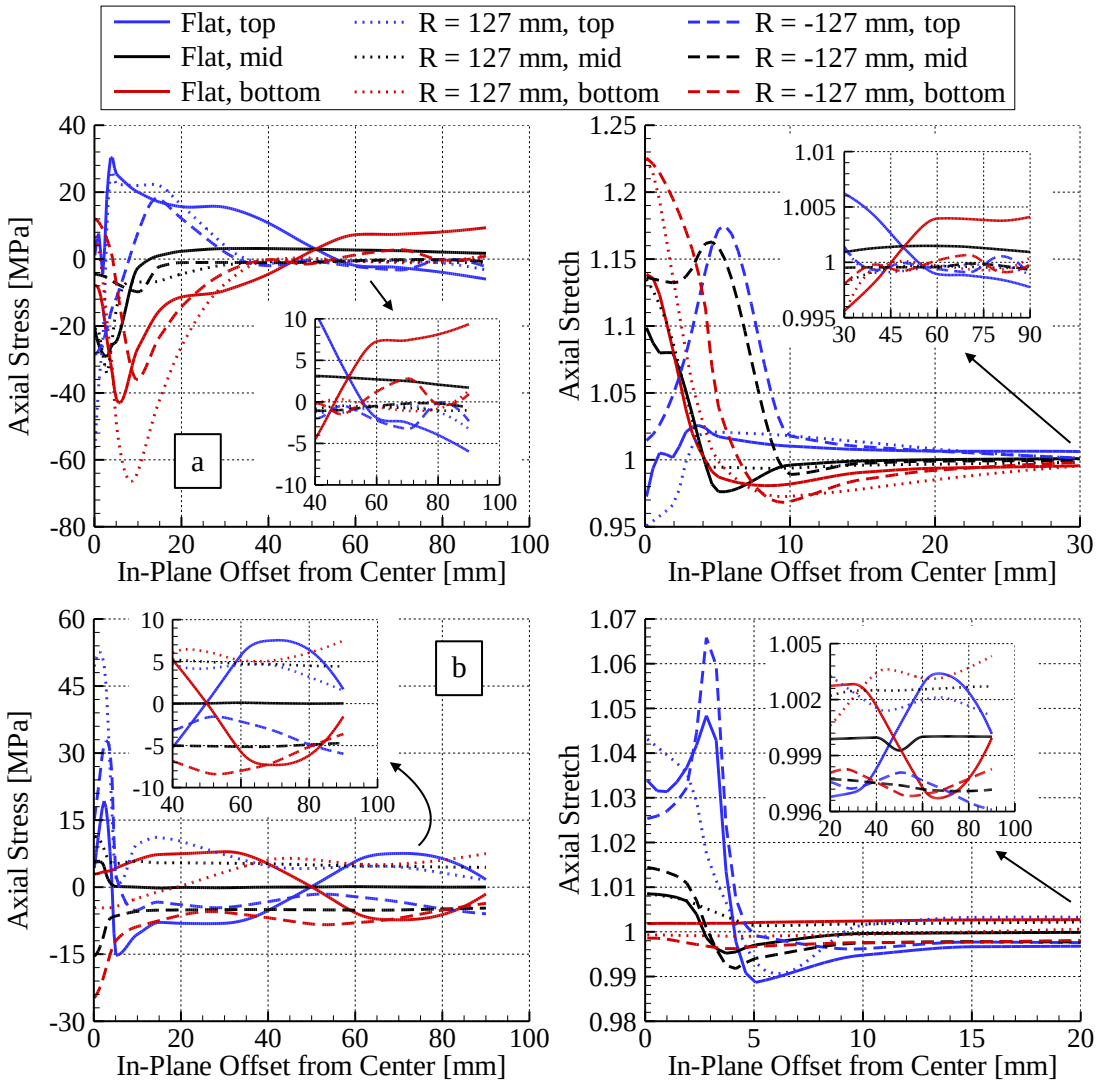

Fig.2–25: Axial stress and axial stretch as a function of the distance from the plate center at the top, mid-plane and bottom of the (a) 3.00 mm and (b) 12.32 mm thick PC plates for 50 m/s impact velocity when the impactor separates from the plate.

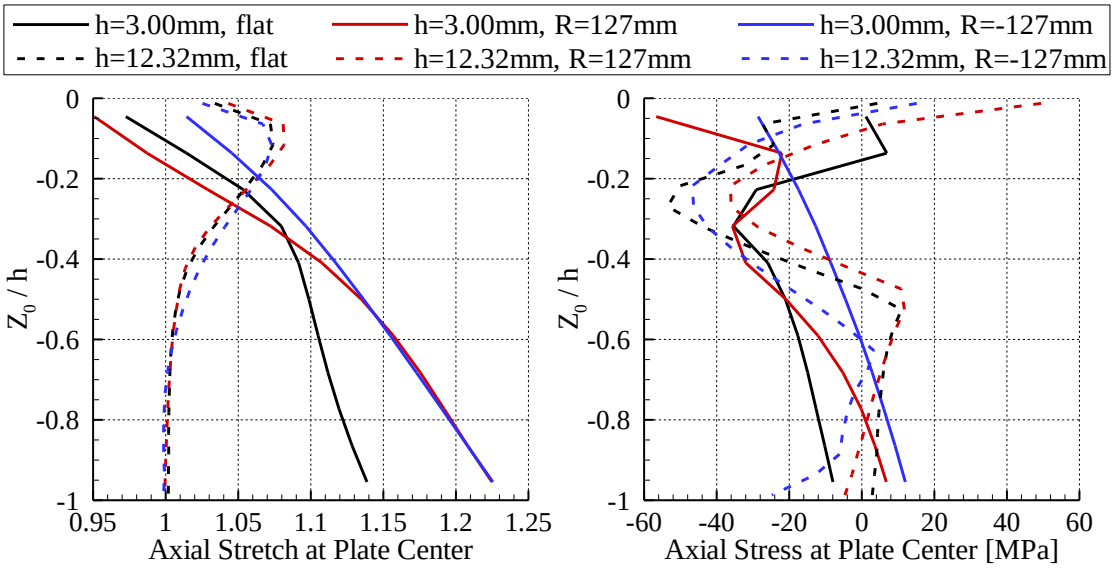

Fig.2–26: Through the thickness variations of the axial stress and the axial stretch on the transverse normal passing through the plate centroid for 20 m/s impact velocity at the time when the impactor separates from the plate.

2.6 Conclusions

We have analyzed by the finite element method transient large deformations of flat and curved polycarbonate (PC) panels of five different thicknesses impacted at normal incidence at the center by a 104 g hemispherical nosed steel cylinder moving with a maximum speed of 30 m/s. The PC has been modeled as thermo-elasto-visco-plastic, and the steel cylinder as rigid. The peak computed deflections of the clamped square panels agree well with their corresponding experimental values, and the maximum difference between the two values is found to be 10.3% for the 12.32 mm thick flat plate. For quasistatic indentation, the initial slope of the force versus the indentation depth curve of a panel is found to decrease with an increase in the magnitude of the radius R of curvature irrespective of the sign of the curvature. For the 3 (12.32) mm thick panel the ratio of this slope for the panel with R = 127 mm to that of the flat plate is 20 (3.5). For the 3 mm thick curved panel impacted at 20 m/s, the plastically deformed region in the flat plate is close in size to that of the plate with R = 127 mm rather than that in the plate with R = 508 mm. The energy dissipated due to plastic deformations and material softening in the flat plate is between those for plates with R = 127 and 508 mm, and the energy dissipated in plates of negative curvature is noticeably more than that in the corresponding plate of positive curvature. However, the energy dissipation density at the center of the back surface of the plate with R = 508 mm is higher than that in the panel with R = 127 mm. The effective plastic strains developed in the 12.32 thick panels are much smaller than those in the corresponding 3 mm thick panels. Whereas negative curvatures noticeably degrade performances of the 3 mm thick panels it is not so for the 12.32 mm thick panels. Furthermore, unlike that in the 3 mm thick panels, significant effective plastic strains do not occur at points on the rear face of the panels, and the maximum effective plastic strain is induced in the flat plate. The computed results suggest that bending becomes more important relative to in-plane stretching/compression of the panels with an increase in the panel thickness. The panel thickness at which the transition from stretching dominance to bending dominance occurs is left for a future study.

2.7 Acknowledgements

This research was sponsored by the Army Research Laboratory and was accomplished under Cooperative Agreement Number W911NF-06-2-0014. The views and conclusions contained in this document are those of the authors and should not be interpreted as representing the official policies, either expressed or implied, of the Army Research Laboratory or the U.S. Government. The U.S. Government is authorized to reproduce and distribute reprints for Government purposes notwithstanding any copyright notation hereon.

Appendix A

A.1 Material model for the PC

We assume that the total Cauchy stress tensor $\boldsymbol{\sigma}$ at a material point equals the sum of contributions from three phases, namely B, α and β, i.e., $\boldsymbol{\sigma} = \boldsymbol{\sigma}_{\mathrm{B}} + \boldsymbol{\sigma}_{\alpha} + \boldsymbol{\sigma}_{\beta}$. The three phases coexist at a material point and have the same value of the deformation gradient **F**. The phase B behaves like a non-linear elastic Langevin spring for which

$$\boldsymbol{\sigma}_{\mathrm{B}} = \frac{C_{\mathrm{R}}}{3}\frac{\sqrt{N_l}}{\lambda^{\mathrm{p}}} L^{-1}\left(\frac{\lambda^{\mathrm{p}}}{\sqrt{N_l}}\right)\overline{\mathbf{B}}'_{\mathrm{B}} \tag{A–1}$$

Here $\boldsymbol{\sigma}_{\mathrm{B}}$ is the Cauchy stress tensor, $\overline{\mathbf{B}}'_{\mathrm{B}}$ the deviatoric part of $\overline{\mathbf{B}}_{\mathrm{B}} = (J)^{-2/3}\mathbf{F}\mathbf{F}^{\mathrm{T}}$, $\lambda^{\mathrm{p}} = \sqrt{\mathrm{tr}\left(\overline{\mathbf{B}}_{\mathrm{B}}\right)/3}$ a measure of stretch, $\mathrm{tr}()$ the trace operator, L^{-1} the inverse of the Langevin function defined by $L(\beta) \equiv \coth\beta - 1/\beta$, N_l the limiting stretch, $C_{\mathrm{R}} \equiv n_{\mathrm{R}} k\theta$ the rubbery modulus, θ the temperature in Kelvin, k Boltzmann's constant, and n_{R} a material parameter.

The other two phases, α and β, are modeled with the same constitutive equation but with different values of material parameters. For each phase the deformation gradient **F** is decomposed into elastic and plastic parts, e.g., see Kroner [33] and Lee [34]:

$$\mathbf{F} = \mathbf{F}^{\mathrm{e}}_{\alpha}\mathbf{F}^{\mathrm{p}}_{\alpha} = \mathbf{F}^{\mathrm{e}}_{\beta}\mathbf{F}^{\mathrm{p}}_{\beta} \tag{A–2}$$

Neither $\mathbf{F}^{\mathrm{e}}_{\alpha}$, $\mathbf{F}^{\mathrm{e}}_{\beta}$ nor $\mathbf{F}^{\mathrm{p}}_{\alpha}$, $\mathbf{F}^{\mathrm{p}}_{\beta}$ is gradient of a vector field. The plastic deformation gradients $\mathbf{F}^{\mathrm{p}}_{\alpha}$ and $\mathbf{F}^{\mathrm{p}}_{\beta}$ map a material point in the reference configuration to a material point in the intermediate configuration obtained after elastically unloading the current configuration to a stress-free state.

The rate of the plastic deformation gradient in phases α and β is given by

$$\dot{\mathbf{F}}^{\mathrm{p}}_{\alpha} = \mathbf{F}^{\mathrm{e}\,-1}_{\alpha}\widetilde{\mathbf{D}}^{\mathrm{p}}_{\alpha}\mathbf{F} \quad , \quad \dot{\mathbf{F}}^{\mathrm{p}}_{\beta} = \mathbf{F}^{\mathrm{e}\,-1}_{\beta}\widetilde{\mathbf{D}}^{\mathrm{p}}_{\beta}\mathbf{F} \tag{A–3}$$

where $\widetilde{\mathbf{D}}^{\mathrm{p}}_{i}$ is the plastic strain rate tensor in phase i ($i = \alpha, \beta$), and it has been assumed that the plastic spin tensors in phases α and β identically vanish. We note that $\widetilde{\mathbf{D}}^{\mathrm{p}}_{i}$ does *not* equal the symmetric part of the velocity gradient (with respect of **x**) of phase i.

The Hencky elastic strain tensors of phases α and β are defined as

$$\boldsymbol{\varepsilon}^{\mathrm{e}}_{\alpha} = \ln\left(\sqrt{\mathbf{F}^{\mathrm{e}}_{\alpha}\mathbf{F}^{\mathrm{e}\,\mathrm{T}}_{\alpha}}\right) \quad , \quad \boldsymbol{\varepsilon}^{\mathrm{e}}_{\beta} = \ln\left(\sqrt{\mathbf{F}^{\mathrm{e}}_{\beta}\mathbf{F}^{\mathrm{e}\,\mathrm{T}}_{\beta}}\right) \tag{A–4}$$

and the corresponding Cauchy stress tensors are given by

$$\boldsymbol{\sigma}_\alpha = \frac{1}{J}\left[2\mu_\alpha \boldsymbol{\varepsilon}^{\mathrm{e}}_\alpha + \lambda_\alpha \mathrm{tr}(\boldsymbol{\varepsilon}^{\mathrm{e}}_\alpha)\boldsymbol{\delta}\right] \quad , \quad \boldsymbol{\sigma}_\beta = \frac{1}{J}\left[2\mu_\beta \boldsymbol{\varepsilon}^{\mathrm{e}}_\beta + \lambda_\beta \mathrm{tr}(\boldsymbol{\varepsilon}^{\mathrm{e}}_\beta)\boldsymbol{\delta}\right] \tag{A–5}$$

where Young's moduli of phases α and β of PC and consequently Lame's constants, λ and μ, are temperature and strain-rate dependent. They partly capture the temperature and the strain-rate dependence of the material response while Poisson's ratio is taken to be constant. Using test data given in the Appendix of Mulliken's thesis [6], we compute the temperature and the strain-rate dependence of Young's moduli of PC. These results are depicted in Fig.A–1 and imply that the total Young's modulus of each material increases with an increase in the strain-rate and decreases with a rise in the temperature.

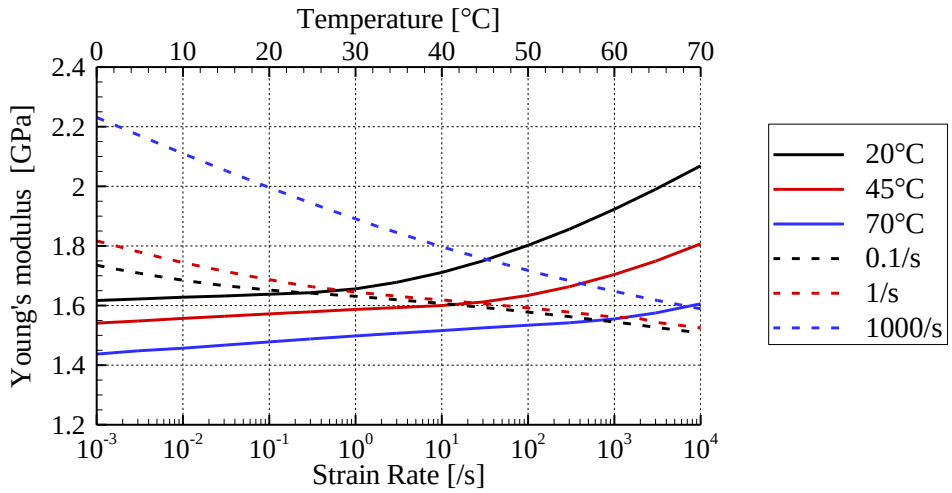

Fig.A–1: Variation with the strain rate and temperature of the total Young's modulus (E_α+E_β) of the PC.

We note that Eq.(A–5) is valid for finite deformations and accounts for all geometric nonlinearities.

The plastic strain rates are assumed to be coaxial with the deviatoric Cauchy stress tensors in their respective phases, that is,

$$\tilde{\mathbf{D}}^{\mathrm{p}}_\alpha = \dot{\gamma}^{\mathrm{p}}_\alpha \frac{\boldsymbol{\sigma}'_\alpha}{\left|\boldsymbol{\sigma}'_\alpha\right|} \quad , \quad \tilde{\mathbf{D}}^{\mathrm{p}}_\beta = \dot{\gamma}^{\mathrm{p}}_\beta \frac{\boldsymbol{\sigma}'_\beta}{\left|\boldsymbol{\sigma}'_\beta\right|} \tag{A–6}$$

where $\boldsymbol{\sigma}'_i$ (i = α, β) is the deviatoric part of the Cauchy stress in phase i, $\left|\boldsymbol{\sigma}'_i\right| = \sqrt{\mathrm{tr}(\boldsymbol{\sigma}'_i\boldsymbol{\sigma}'_i)}$ is the magnitude of $\boldsymbol{\sigma}'_i$, and $\dot{\gamma}^{\mathrm{p}}_i$ is the effective plastic strain rate in phase i. This equation implies that $\mathrm{tr}(\tilde{\mathbf{D}}^{\mathrm{p}}_i) = 0$.

The effective plastic strain rates in α and β phases are given by

$$\dot{\gamma}^{\mathrm{p}}_i = \dot{\gamma}^{\mathrm{p}}_{0i} \exp\left[-\frac{\Delta G_i}{k\theta}\left(1 - \frac{\tau_i}{t_i \hat{s}_i + \alpha^{\mathrm{p}}_i p}\right)\right] \quad , \quad i = \alpha, \beta \tag{A–7}$$

where $\dot{\gamma}_{0i}^{\mathrm{p}}$ ($i = \alpha, \beta$) is the pre-exponential factor, ΔG_i the activation energy, $p = -\mathrm{tr}(\boldsymbol{\sigma})/3$ the pressure, $\tau_i = \sqrt{0.5\mathrm{tr}\left(\boldsymbol{\sigma}_i^{'}\boldsymbol{\sigma}_i^{'}\right)}$ the effective stress, α_i^{p} the pressure coefficient, $\hat{s}_i = 0.077\mu_i/(1-\nu_i)$ the athermal shear strength, ν_i Poisson's ratio, k Boltzmann's constant, and t_i an internal variable that evolves with plastic deformations. The variable $\hat{s}_i$ is function of μ_i and is, therefore, temperature and strain-rate dependent. Since no yield surface is postulated plastic deformations always occur. The evolution of internal variable t_i in phases α and β is given by

$$\dot{t}_i = \frac{h_i}{\hat{s}_i^0}\left(1 - \frac{t_i}{t_i^{\mathrm{ss}}}\right)\dot{\gamma}_i^{\mathrm{p}} \quad , \quad i = \alpha, \beta \tag{A–8}$$

where t_i^{ss} and h_i are softening parameters, and $\hat{s}_i^0$ is the reference value of $\hat{s}_i$ given by the reference values of μ_i and ν_i. Eq. (11) implies that the internal variable t_i remains constant for elastic deformations.

We postulate that the energy dissipated during plastic deformations in the α and β phases is converted into heat, that is

$$\dot{Q} = J \cdot \left(\boldsymbol{\sigma}_\alpha : \tilde{\mathbf{D}}_\alpha^{\mathrm{p}} + \boldsymbol{\sigma}_\beta : \tilde{\mathbf{D}}_\beta^{\mathrm{p}}\right) \tag{A–9}$$

where $\dot{Q}$ is the heat generated per unit volume in the reference configuration. It is assumed that heating is mostly adiabatic for the impact problems studied here because there is not enough time for the heat to be conducted away, and neglecting heat conduction facilitates numerical integration of the governing differential equations. Thus the temperature rise is given by

$$\rho_0 c\dot{\theta} = \dot{Q} \tag{A–10}$$

where c is the specific heat of either the PC.

We refer the reader to Mulliken's thesis [6], Mulliken and Boyce [5] and Varghese and Batra [18] for the determination of values of material parameters from the test data for the PC that are given in Table A–1, and for the comparison of the computed and experimental axial stress vs. axial strain curves.

	Phase α	Phase β	Phase B	Common
v_i	0.38	0.38		
$\dot{\gamma}_{0i}^{\mathrm{p}}$ [/s]	2.94×10^{16}	3.39×10^{5}		
ΔG_i [J]	3.744×10^{-19}	3.769×10^{-20}		
α_i^{p}	0.168	0.245		
h_i [MPa]	125	400		
t_i^{ss}	0.33	2.00		
C_{R} at 300K [MPa]			35.0	
N_l			12.25	
c [J/(g·K)]				1.20
ρ [g/cm^3]				1.20
E [GPa] at 300K, 5000/s	1.678	0.344		

Table A–1: Values of material parameters for the PC.

A.2 FE Mesh

An example with a very coarse mesh is shown in Fig.2–28 with dimensions of specimens used in experiments conducted by Gunnarsson et al. [30-32].

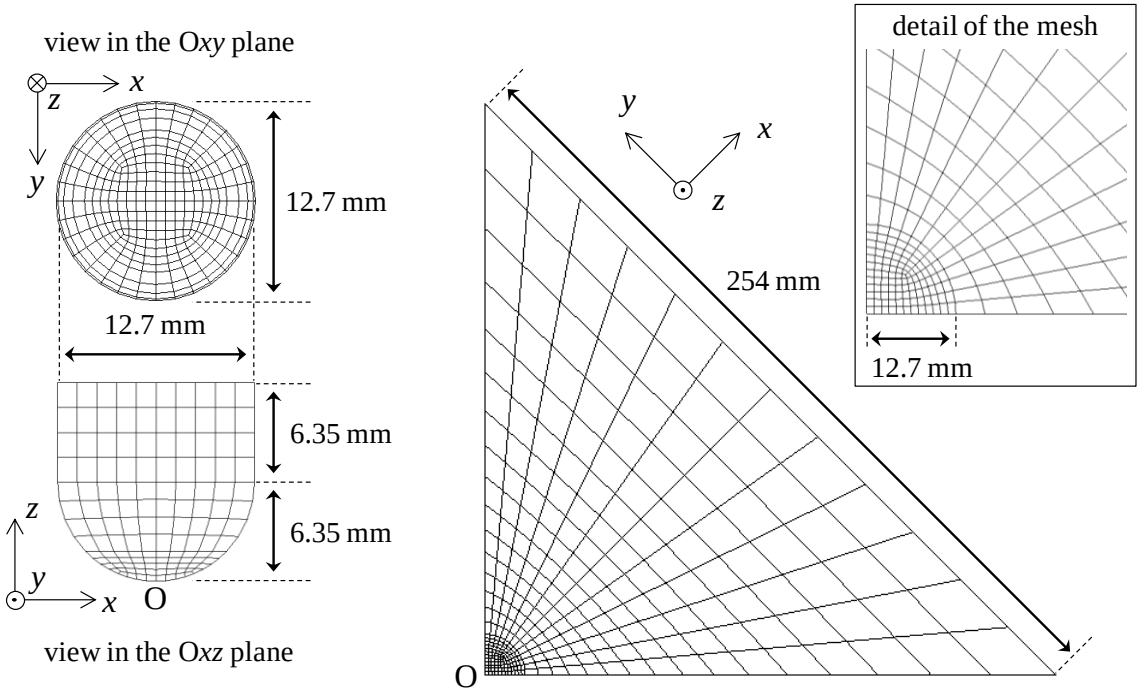

Fig.A–2: Coarse mesh for the impactor and the square plate (much finer meshes were used for the simulations).

The pattern of the FE mesh in the *xy*-plane is obtained by partitioning the plate along its diagonals. Then each of the four quarters of the plate is partitioned by a 12.7-mm radius circle centered at the point of impact. Each quarter of the circumference of the circle, the part of each one of the four diagonals that are within the circle, and each edge of the plate are discretized with 38 uniform elements. The outer part of the plate diagonals, i.e., the part located more than 12.7-mm from the plate center, is divided into 48 segments of different lengths so that the ratio of the length of the smallest segment – located near the circle – to that of the largest segment – located at the corner – equals 20. Each layer has 11628 elements, and 11, 15, 18, 29 and 39 layers are used for the 3.0-mm, 4.45-mm, 5.85-mm, 9.27-mm and 12.32-mm thick PC plates, respectively.

The FE mesh for the impactor near the contact region was refined until the element size there was comparable to that of elements at the plate center. The rest of the impactor was discretized with a coarse mesh. The FE mesh for the impactor has 8576 elements.

References

[1] J. Radin, W. Goldsmith, Normal Projectile Penetration and Perforation of Layered Targets, Int J Impact Eng, 7 (1988) 229-259.
[2] J. Sands, P. Patel, P. Dehmer, A. Hsieh, Protecting the Future Force: Transparent Materials Safeguard the Army's Vision, AMTIAC Quarterly, 8, (2004).
[3] C.R. Siviour, S.M. Walley, W.G. Proud, J.E. Field, The high strain rate compressive behaviour of polycarbonate and polyvinylidene difluoride, Polymer, 46 (2005) 12546-12555.
[4] P. Moy, T. Weerasooriya, A. Hsieh, W. Chen, Strain rate response of a polycarbonate under uniaxial compression, in: Proceedings of the SEM Conference on Experimental Mechanics, 2003.
[5] A.D. Mulliken, M.C. Boyce, Mechanics of the rate-dependent elastic-plastic deformation of glassy polymers from low to high strain rates, Int J Solids Struct, 43 (2006) 1331-1356.
[6] A.D. Mulliken, Mechanics of amorphous polymers and polymer nanocomposites during high rate deformation, in, Massachusetts Institute of Technology, 2006, pp. 290 p.
[7] J. Richeton, S. Ahzi, L. Daridon, Y. Remond, A formulation of the cooperative model for the yield stress of amorphous polymers for a wide range of strain rates and temperatures, Polymer, 46 (2005) 6035-6043.
[8] J. Richeton, G. Schlatter, K.S. Vecchio, Y. Remond, S. Ahzi, A unified model for stiffness modulus of amorphous polymers across transition temperatures and strain rates, Polymer, 46 (2005) 8194-8201.
[9] J. Richeton, S. Ahzi, K.S. Vecchio, F.C. Jiang, R.R. Adharapurapu, Influence of temperature and strain rate on the mechanical behavior of three amorphous polymers: Characterization and modeling of the compressive yield stress, Int J Solids Struct, 43 (2006) 2318-2335.
[10] N.A. Fleck, W.J. Stronge, J.H. Liu, High Strain-Rate Shear Response of Polycarbonate and Polymethyl Methacrylate, P Roy Soc Lond a Mat, 429 (1990) 459-&.
[11] K.R. Ramakrishnan, Low Velocity Impact Behaviour of Unreinforced Bi-layer Plastic Laminates, in, Australian Defence Force Academy, 2009.
[12] D. Rittel, An investigation of the heat generated during cyclic loading of two glassy polymers. Part I: Experimental, Mech Mater, 32 (2000) 131-147.
[13] D. Rittel, Y. Rabin, An investigation of the heat generated during cyclic loading of two glassy polymers. Part II: Thermal analysis, Mech Mater, 32 (2000) 149-159.
[14] D. Rittel, On the conversion of plastic work to heat during high strain rate deformation of glassy polymers, Mech Mater, 31 (1999) 131-139.
[15] J. Richeton, S. Ahzi, K.S. Vecchio, F.C. Jiang, A. Makradi, Modeling and validation of the large deformation inelastic response of amorphous polymers over a wide range of temperatures and strain rates, Int J Solids Struct, 44 (2007) 7938-7954.
[16] T. Tervoort, R. Smit, W. Brekelmans, L.E. Govaert, A constitutive equation for the elasto-viscoplastic deformation of glassy polymers, Mechanics of Time-Dependent Materials, 1 (1997) 269-291.
[17] M.C. Boyce, D.M. Parks, A.S. Argon, Large Inelastic Deformation of Glassy-Polymers .1. Rate Dependent Constitutive Model, Mech Mater, 7 (1988) 15-33.
[18] A.G. Varghese, R.C. Batra, Constitutive equations for thermomechanical deformations of glassy polymers, Int J Solids Struct, 46 (2009) 4079-4094.
[19] A.G. Varghese, R.C. Batra, Strain localization in polycarbonates deformed at high strain rates, J Polym Eng, 31 (2011) 495-519.
[20] K.H. Safari, J. Zamani, F.J. Ferreira, R.M. Guedes, Constitutive modeling of polycarbonate during high strain rate deformation, Polym Eng Sci, 53 (2013) 752-761.
[21] J.H. Shen, G.X. Lu, Z.H. Wang, L.M. Zhao, Experiments on curved sandwich panels under blast loading, Int J Impact Eng, 37 (2010) 960-970.
[22] L. Jing, Z. Wang, V. Shim, L. Zhao, An experimental study of the dynamic response of cylindrical sandwich shells with metallic foam cores subjected to blast loading, Int J Impact Eng, (2014).
[23] S.J. Kim, N.S. Goo, T.W. Kim, The effect of curvature on the dynamic response and impact-induced damage in composite laminates, Compos Sci Technol, 57 (1997) 763-773.

[24] R.L. Ramkumar, Y.R. Thakar, Dynamic-Response of Curved Laminated Plates Subjected to Low Velocity Impact, J Eng Mater-T Asme, 109 (1987) 67-71.
[25] S.M.R. Khalili, A. Ardali, Low-velocity impact response of doubly curved symmetric cross-ply laminated panel with embedded SMA wires, Compos Struct, 105 (2013) 216-226.
[26] S.C. Her, Y.C. Liang, The finite element analysis of composite laminates and shell structures subjected to low velocity impact, Compos Struct, 66 (2004) 277-285.
[27] H.J. Lin, Y.J. Lee, On the Inelastic Impact of Composite Laminated Plate and Shell Structures, Compos Struct, 14 (1990) 89-111.
[28] Z. Leylek, M.L. Scott, S. Georgiadis, R.S. Thomson, Computer modelling of impact on curved fibre composite panels, Compos Struct, 47 (1999) 789-796.
[29] S.M.R. Khalili, M. Soroush, A. Davar, O. Rahmani, Finite element modeling of low-velocity impact on laminated composite plates and cylindrical shells, Compos Struct, 93 (2011) 1363-1375.
[30] C.A. Gunnarsson, T. Weerasooriya, P. Moy, Measurement of Transient Full-Field, Out-of-Plane Back Surface Displacements of Polycarbonate during Impact, in: Proceedings of the 2008 International Congress and Exposition on Experimental Mechanics and Applied Mechanics, 2008.
[31] C.A. Gunnarsson, T. Weerasooriya, P. Moy, Impact Response of PC/PMMA Composites, in: Dynamic Behavior of Materials, Volume 1, Springer, 2011, pp. 195-209.
[32] C.A. Gunnarsson, B. Ziemski, T. Weerasooriya, P. Moy, Deformation and Failure of Polycarbonate during Impact as a Function of Thickness, in: Proceedings of the 2009 International Congress and Exposition on Experimental Mechanics and Applied Mechanics, 2009.
[33] E. Kröner, Allgemeine kontinuumstheorie der versetzungen und eigenspannungen, Archive for Rational Mechanics and Analysis, 4 (1959) 273-334.
[34] E.H. Lee, Elastic-plastic deformation at finite strains, Journal of Applied Mechanics, 36 (1969) 1-6.

3 Constitutive Relations and Parameter Estimation for Finite Deformations of Viscoelastic Adhesives

G. O. Antoine and R. C. Batra*
Department of Engineering Science and Mechanics, M/C 0219
Virginia Polytechnic Institute and State University
Blacksburg, VA 24061, USA
Email: antoineg@vt.edu; rbatra@vt.edu
*Corresponding author; Tel: 540-231-6051; Fax: 540-231-4574

This chapter has been prepared for submission to a refereed journal.

3.1 Abstract

We propose a constitutive relation for finite deformations of nearly incompressible isotropic viscoelastic rubbery adhesives assuming that the Cauchy stress tensor can be written as the sum of elastic and viscoelastic parts. The former is derived from a stored energy function and the latter from a hereditary type integral. Using Ogden's expression for the strain energy density and the Prony series for the viscoelastic shear modulus, values of material parameters are estimated by using experimental data for uniaxial tensile and compressive cyclic deformations at different constant engineering axial strain rates. It is found that values of material parameters using the loading part of the 1st cycle, the complete first cycle and the complete two loading cycles are quite different. Furthermore, the constitutive relation with values of material parameters determined from the monotonic loading during the 1st cycle of deformations cannot well predict even deformations during the unloading portion of the 1st cycle. The developed constitutive relation is used to study low velocity impact of polymethylmethacrylate/adhesive/polycarbonate laminate. The three sets of values of material parameters for the adhesive seem to have a negligible effect on the overall deformations of the laminate. It is attributed to the fact that peak strain rates in the severely deforming regions are large and the corresponding stresses are essentially unaffected by the long time response of the adhesive.

Key Words: Viscoelasticity, finite deformations, constitutive equations, parameter estimation, low-velocity impact

3.2 Introduction

Thermoplastic polyurethanes (TPUs) are a class of polymers composed of soft and hard segments which form a two-phase microstructure (e.g., see Hepburn [1], Cooper et al. [2], Sanchez-Adsuar and Martin-Martinez [3], Yi et al. [4]). The soft segments account for the high extension and elastic recovery while the hard segments provide high modulus and strength (Petrovic and Ferguson [5]). The TPUs often exhibit a strain-rate and temperature dependent response to mechanical deformations. The viscous response is related to relative sliding of a molecule with respect to its neighbors (Budinski and Budinski [6]). It is quite challenging to model the large strain viscoelastic response of the TPUs.

The high elasticity, flexibility, resistance to abrasion and impact and the ease in processing TPUs have significantly increased their applications in diverse areas. Their use as bonding interlayers in structures subjected to impact and blast loading is believed to increase the survivability of structures. In particular,

Tasdemirci and Hall [7] have shown that the choice of an adhesive interlayer influences the damage induced in a structure subjected to impact. They used a split Hopkinson pressure bar and numerical simulations to study the response of an alumina ceramic/adhesive/glass-epoxy laminate to an incident compressive stress wave. Considering the damage induced in the glass-epoxy plate as the critical parameter for impact resistance they concluded that the low acoustic impedance of the bonding interlayer reduced the damage induced in the back plate since it transmits less stress from the front layer to the back plate. We note that constituents of a structure subjected to impact loads usually undergo large strains and varying strain rates. Thus the study of the response of TPUs for large strains and over a wide range of strain-rates (e.g., 10^{-3} to 10^{3}/s) is fundamental to understanding the dynamic response of structures using TPUs, and is of great engineering relevance.

Kinhara et al. [8] experimentally measured the impact shear strength of an electro-conductive material and an epoxy resin and performed finite element (FE) simulations to determine the maximum shear stress in the sample at fracture. They concluded that the maximum shear stress equals the impact shear strength of the adhesive. Boyce et al. [4] experimentally found that the representative polyurethanes considered in their study transitioned from rubbery-like behavior at strain rate of 10^{-3} to leathery/glassy-like behavior at strain rates of 10^{3}/s. Similar results were obtained by Sarva et al. [9] who investigated the response of a polyurea and a polyurethane ("PU2") for compressive strain rates between 10^{-3} to 10^{4}/s. They found that at room temperature the behavior of the PU2 transitioned from rubbery at strain rates of ~0.002/s to leathery at 0.1/s and to glassy at strain rates $>10^{3}$/s.

Numerical simulations are being increasingly used to replace physical experiments since they reduce time, cost, and materials. They also provide details of deformations in the interior of a structure not easily accessible through experimental measurements. This requires reliable constitutive equations for all materials used in a structure including the TPUs. Challenges in modeling the response of TPUs include large deformations, strain-rate and temperature-dependence of their response. The elastic response of incompressible hyperelastic rubbers has been investigated by Rivlin [10], Ericksen[11] and Ogden [12] amongst others. The Mooney-Rivlin material model and the empirical strain-energy density function proposed by Ogden [12] have been implemented in many commercial software. Arruda and Boyce [13] proposed an eight-chain network model in which the material is assumed to be an assembly of cubic material particles each containing eight chains originating from the cube centroid and ending at its vertices. Using Langevin's work on chains they developed a temperature-dependent strain energy density potential with a small number of material parameters. Coleman and Noll [14] employed concepts of materials with fading memory and developed a hereditary type constitutive relation for finite deformations of viscoelastic materials. Christensen [15] expressed these constitutive relations as convolution integrals involving a relaxation moduli and the time rate of the Green-St. Venant strain tensor, and showed that the relaxation moduli can be determined with a set of simple tests (simple shear, creep). Qi and Boyce [16] relying on the works of Boyce et al. [17, 18] assumed that the response of a TPU is the sum of a non-linear elastic contribution modeled with a Langevin spring and a viscoelastoplastic stress (nonlinear spring-dashpot system) capturing the rate-dependent response of the material with both contributions being temperature dependent. They showed that this model predicts well the response of a TPU specimen under tensile and compressive cyclic loadings at strain rates from 0.01/s to 0.1/s.

A challenging and somewhat unresolved issue is that of finding values of material parameters and what portion of the test data to use. This is compounded by the observation that most experiments are conducted at constant nominal strain rates whereas the material response depends upon the current or the true strain rate. Here we assume that the viscoelastic response of a TPU can be modeled as the sum of two terms – elastic represented by Ogden's form of the strain energy density function and viscous represented by a hereditary type integral of the type employed by Christensen. Of course, the hereditary type integral also includes the instantaneous elastic response of the material. We then use the uniaxial deformations test data at constant engineering axial strain rate for the first loading, the first complete cycle of loading and unloading, and the first two loading and unloading cycles to find values of material parameters appearing in the assumed constitutive relation. The time delay between the two cycles is also considered. The number of material parameters in the constitutive relation needed to reasonably well replicate the experimental uniaxial stress – uniaxial strain curves varies with the amount of test data employed. This constitutive relation has been implemented in the commercial software, LSDYNA, and used to study the low velocity impact response of a PMMA/adhesive/PC laminate which is similar to the work of Antoine and Batra [19]. Here, the acronyms PMMA and PC stand for poly-methyl-methacrylate and polycarbonate, respectively.

3.3 Constitutive Relations

We assume that a TPU can be modeled as an isotropic, viscoelastic and nearly incompressible material. A one-dimensional mechanical analog of the material model described in this section is shown in Fig.3–1.

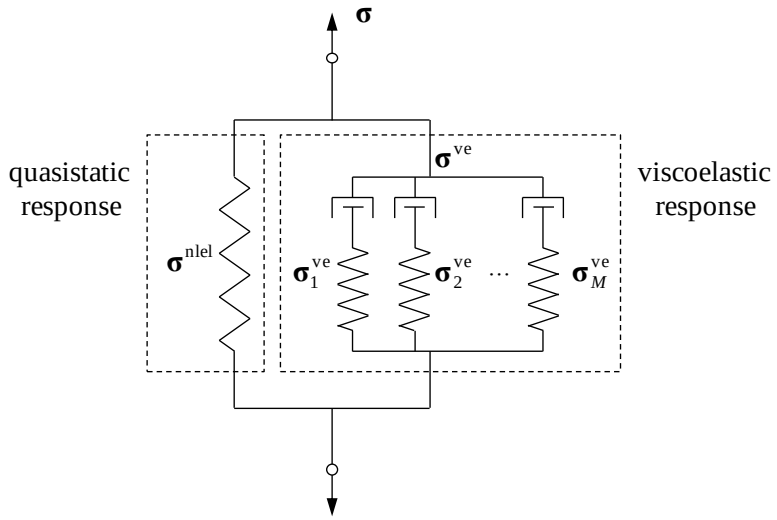

Fig.3–1: One-dimensional rheological analog interpretation of the material model.

The total response of the material consists of a nonlinear spring ($\boldsymbol{\sigma}^{\text{nlel}}$) accounting for the quasi-static (very low strain rate) elastic response of the material and the viscoelastic response ($\boldsymbol{\sigma}^{\text{ve}}$) modeled with a Maxwell ladder (Prony series). The kinematic constraint of incompressibility of the material requires an additional contribution in the form of a pressure term where the pressure p is a Lagrange multiplier and cannot be found from deformations of the material but is determined by solving an initial- boundary-value

problem in which normal tractions must be prescribed on a part of the boundary of the body. Thus the total Cauchy stress $\boldsymbol{\sigma}$ at a material point is expressed as

$$\boldsymbol{\sigma} = \boldsymbol{\sigma}^{\text{nlel}} + \boldsymbol{\sigma}^{\text{ve}} - p\,\mathbf{I} \tag{3–1}$$

where $\mathbf{I}$ is the identity tensor.

We assume that the material is hyperelastic. For the strain energy density potential *W*, we use the following form proposed by Ogden [20].

$$W = \sum_{n=1}^{N} \frac{\mu_n}{\alpha_n}\left(\lambda_1^{\alpha_n} + \lambda_2^{\alpha_n} + \lambda_3^{\alpha_n} - 3\right) \tag{3–2}$$

In Eq. (3–2) *N* is an integer, $\{\mu_n\}_{n=1,\ldots,N}$ and $\{\alpha_n\}_{n=1,\ldots,N}$ are material parameters, and $\{\lambda_i\}_{i=1,2,3}$ are principal stretches satisfying the incompressibility constraint $\lambda_1 \lambda_2 \lambda_3 = 1$.

In order to motivate the choice of the constitutive equation for the viscoelastic response of the material, we consider a one-dimensional linear Maxwell model sketched in Fig.3–2.

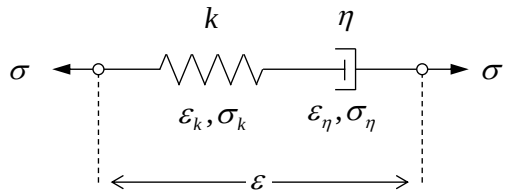

Fig.3–2: One-dimensional Maxwell model.

Thus

$$\begin{cases} \sigma = \sigma_k = \sigma_\eta \quad , \quad \varepsilon = \varepsilon_k + \varepsilon_\eta \\ \sigma_\eta = \eta\,\dot{\varepsilon}_\eta \quad , \quad \sigma_k = k\,\varepsilon_k \end{cases} \tag{3–3}$$

where *k* is the spring constant, σ the axial stress, ε the axial strain, η the viscosity and a superimposed dot indicates the material time derivative. Equations (3–3) give

$$\dot{\sigma} = k\,\dot{\varepsilon} - \frac{k}{\eta}\,\sigma \tag{3–4}$$

Motivated by Eq. (3–4) the viscoelastic response $\boldsymbol{\sigma}^{\text{ve}}$ of the material for three-dimensional deformations is modeled with the following Prony series:

$$\boldsymbol{\sigma}^{\text{ve}} = \sum_{m=1}^{M} \boldsymbol{\sigma}_m^{\text{ve}} \quad , \quad \begin{cases} \overset{\bullet}{\boldsymbol{\sigma}}_m^{\text{ve}} = 2G_m \mathbf{D} - \beta_m \boldsymbol{\sigma}_m^{\text{ve}} \\ \boldsymbol{\sigma}_m^{\text{ve}}\big|_{t=0} = \mathbf{0} \end{cases} \tag{3–5}$$

In Eq. (3–5), $\overset{\bullet}{\boldsymbol{\sigma}}_m^{\text{ve}}$ is the Green-Naghdi [21] objective rate-of-stress tensor, **D** the deviatoric part of the strain-rate tensor, G_m and β_m are material parameters that can be thought of as shear moduli and decay constants, respectively, and M is an integer. We note that Eq. (3–5) accounts for geometric nonlinearities, is materially objective, is valid for finite deformations, and **D** does not equal the time rate of a strain tensor unless the present configuration is taken as the reference configuration, e.g. see [22].

The energy dissipated per unit volume, $E^{\text{visc,ve}}$, during finite deformations of the material obeying Eq. (3–5) is given by

$$E^{\text{visc,ve}} = \int_t \left[\sum_{m=1}^{M} \left(\frac{\beta_m}{2G_m} \boldsymbol{\sigma}_m^{\text{ve}} : \boldsymbol{\sigma}_m^{\text{ve}} \right) dt \right] \tag{3–6}$$

where $\boldsymbol{\sigma}_m^{\text{ve}} : \boldsymbol{\sigma}_m^{\text{ve}}$ denotes inner product of second order tensors $\boldsymbol{\sigma}_m^{\text{ve}}$ and $\boldsymbol{\sigma}_m^{\text{ve}}$. Equation (3–6) is derived in the Appendix.

3.4 Values of the Material Parameters

Of special interest here are cyclic uniaxial tension or compression tests since viscoelastic materials exhibit hysteresis and the area between the loading and the unloading curves is related to the energy dissipated due to viscous deformations of the material. These tests are displacement-controlled and are often performed at constant engineering strain rate by clamping one end of the sample and prescribing a constant velocity at the other end. For finite deformations the difference between the engineering strain rate and the true strain rate cannot be neglected. Accordingly, we present relations giving the axial Cauchy stress (or true stress) as a function of the axial stretch and the engineering axial strain rate for the first and the second loading-unloading cycles of a cyclic test performed at a constant engineering strain rate for a material obeying the constitutive relations (3–1) with W and $\boldsymbol{\sigma}^{\text{ve}}$ given by equations (3–2) and (3–5), respectively. The derivation of these expressions is given in the Appendix where expressions for the 3rd and the 4th loading-unloading cycles are also given.

We use the following notation: σ^{True} is the true axial stress, λ the axial stretch, $\dot{\varepsilon}^{\text{Eng}}$ the constant engineering strain rate (taken positive for both loading and unloading), λ_I^{p} and λ_{II}^{p} the maximum axial stretch of the 1st and the 2nd cycle, respectively, and Δt is the delay time between the end of the 1st cycle and the beginning of the 2nd cycle. We introduce functions $I_{\text{load}}\left(\dot{\varepsilon}^{\text{Eng}}, G, \beta, \lambda\right)$ and $I_{\text{unload}}\left(\dot{\varepsilon}^{\text{Eng}}, G, \beta, \lambda_0, \lambda\right)$ defined as

$$I_{\text{load}}\left(\dot{\varepsilon}^{\text{Eng}}, G, \beta, \lambda\right) = 3G \exp\left(-\frac{\beta\lambda}{\dot{\varepsilon}^{\text{Eng}}}\right)\left[\text{Ei}\left(\frac{\beta\lambda}{\dot{\varepsilon}^{\text{Eng}}}\right) - \text{Ei}\left(\frac{\beta}{\dot{\varepsilon}^{\text{Eng}}}\right)\right] \tag{3–7a}$$

$$I_{\text{unload}}\left(\dot{\varepsilon}^{\text{Eng}}, G, \beta, \lambda_0, \lambda\right) = 3G \exp\left(\frac{\beta\lambda}{\dot{\varepsilon}^{\text{Eng}}}\right)\left[\text{Ei}\left(-\frac{\beta\lambda}{\dot{\varepsilon}^{\text{Eng}}}\right) - \text{Ei}\left(-\frac{\beta\lambda_0}{\dot{\varepsilon}^{\text{Eng}}}\right)\right] \tag{3–7b}$$

where $\text{Ei}(x) = -\int_{\xi=-x}^{+\infty} \frac{e^{-\xi}}{\xi} d\xi$ and the integral is understood as the Cauchy principal value due to the singularity of the integrand at $\xi = 0$.

For an incompressible material, expressions giving the true axial stress as a function of the axial stretch and the engineering strain rate without explicit reference to time are listed below.

- 1st cycle, loading:

$$\sigma_{I,\text{load}}^{\text{True}}(\lambda) = \sum_{n=1}^{N} \mu_n \left(\lambda^{\alpha_n} - \lambda^{-\alpha_n/2}\right) + \sum_{m=1}^{M} 3G_m \exp\left(-\frac{\beta_m\lambda}{\dot{\varepsilon}^{\text{Eng}}}\right)\left[\text{Ei}\left(\frac{\beta_m\lambda}{\dot{\varepsilon}^{\text{Eng}}}\right) - \text{Ei}\left(\frac{\beta_m}{\dot{\varepsilon}^{\text{Eng}}}\right)\right] \tag{3–8}$$

- 1st cycle, unloading:

$$\begin{aligned}\sigma_{I,\text{unload}}^{\text{True}}(\lambda) = &\sum_{n=1}^{N} \mu_n \left(\lambda^{\alpha_n} - \lambda^{-\alpha_n/2}\right) \\ &+ \sum_{m=1}^{M} 3G_m \exp\left(-\beta_m \frac{2\lambda_I^{\text{p}} - \lambda}{\dot{\varepsilon}^{\text{Eng}}}\right)\left[\text{Ei}\left(\frac{\beta_m\lambda_I^{\text{p}}}{\dot{\varepsilon}^{\text{Eng}}}\right) - \text{Ei}\left(\frac{\beta_m}{\dot{\varepsilon}^{\text{Eng}}}\right)\right] \\ &+ \sum_{m=1}^{M} 3G_m \exp\left(\frac{\beta_m\lambda}{\dot{\varepsilon}^{\text{Eng}}}\right)\left[\text{Ei}\left(-\frac{\beta_m\lambda}{\dot{\varepsilon}^{\text{Eng}}}\right) - \text{Ei}\left(-\frac{\beta_m\lambda_I^{\text{p}}}{\dot{\varepsilon}^{\text{Eng}}}\right)\right]\end{aligned} \tag{3–9}$$

- 2nd cycle, loading:

$$\begin{aligned}\sigma_{II,\text{load}}^{\text{True}}(\lambda) = &\sum_{n=1}^{N} \mu_n \left(\lambda^{\alpha_n} - \lambda^{-\alpha_n/2}\right) \\ &+ \sum_{m=1}^{M} \exp\left(-\beta_m\left(\Delta t + \frac{\lambda + \lambda_I^{\text{p}} - 2}{\dot{\varepsilon}^{\text{Eng}}}\right)\right) I_{\text{load}}\left(\dot{\varepsilon}^{\text{Eng}}, G_m, \beta_m, \lambda_I^{\text{p}}\right) \\ &+ \sum_{m=1}^{M} \exp\left(-\beta_m\left(\Delta t + \frac{\lambda - 1}{\dot{\varepsilon}^{\text{Eng}}}\right)\right) I_{\text{unload}}\left(\dot{\varepsilon}^{\text{Eng}}, G_m, \beta_m, \lambda_I^{\text{p}}, 1\right) \\ &+ \sum_{m=1}^{M} I_{\text{load}}\left(\dot{\varepsilon}^{\text{Eng}}, G_m, \beta_m, \lambda\right)\end{aligned} \tag{3–10}$$

- 2nd cycle, unloading:

$$
\begin{aligned}
\sigma^{\text{True}}_{II,\text{unload}}(\lambda) = & \sum_{n=1}^{N} \mu_n \left(\lambda^{\alpha_n} - \lambda^{-\alpha_n/2} \right) \\
& + \sum_{m=1}^{M} \exp\left(-\beta_m \left(\Delta t + \frac{\lambda_I^{\text{p}} + 2\lambda_{II}^{\text{p}} - 2 - \lambda}{\dot{\varepsilon}^{\text{Eng}}} \right) \right) I_{\text{load}}\left(\dot{\varepsilon}^{\text{Eng}}, G_m, \beta_m, \lambda_I^{\text{p}} \right) \\
& + \sum_{m=1}^{M} \exp\left(-\beta_m \left(\Delta t + \frac{2\lambda_{II}^{\text{p}} - 1 - \lambda}{\dot{\varepsilon}^{\text{Eng}}} \right) \right) I_{\text{unload}}\left(\dot{\varepsilon}^{\text{Eng}}, G_m, \beta_m, \lambda_I^{\text{p}}, 1 \right) \\
& + \sum_{m=1}^{M} \exp\left(-\beta_m \frac{\lambda_{II}^{\text{p}} - \lambda}{\dot{\varepsilon}^{\text{Eng}}} \right) I_{\text{load}}\left(\dot{\varepsilon}^{\text{Eng}}, G_m, \beta_m, \lambda_{II}^{\text{p}} \right) \\
& + \sum_{m=1}^{M} I_{\text{unload}}\left(\dot{\varepsilon}^{\text{Eng}}, G_m, \beta_m, \lambda_{II}^{\text{p}}, \lambda \right)
\end{aligned}
\tag{3–11}
$$

For monotonic uniaxial compression the axial stress can be found from Eq. (3–8) by substituting a negative value for the constant engineering strain rate.

3.5 Materials and Experimental Data

The two model adhesives considered in this work are the transparent TPUs DFA4700 (Dureflex® A4700) and IM800A (INTER Materials 800A). Stenzler [23] has provided test data for these two materials for uniaxial tests summarized in Table 3–1. For the cyclic tensile tests, the materials were deformed up to a prescribed strain, then unloaded to zero strain, and allowed to relax for Δt =30 s between the cycles. The peak engineering strains of the cyclic tests were gradually increased from 1 for the first cycle to 4 for the 4th cycle.

Type of test	strain rate $\dot{\varepsilon}^{\text{Eng}}$ [/s]	Number of cycles	Amplitude
monotonic compression	-0.001	/	$\varepsilon^{\text{Eng}}_{\text{min}}$ = -0.2
monotonic tension	5.0	/	$\varepsilon^{\text{Eng}}_{\text{max}}$ = 1
cyclic tension	0.01, 0.1, 0.5	4	$\varepsilon^{\text{Eng}}_{\text{max}}$ = 1, 2, 3, 4
cyclic tension	1.0	1	$\varepsilon^{\text{Eng}}_{\text{max}}$ = 1

Table 3–1: Test conditions for data available for DFA4700 and IM800A (Stenzler [23]).

3.5.1 Method and Results

The material parameters to be determined are the number N of terms in the Ogden potential and the corresponding parameters $\{\mu_n\}_{1\le n\le N}$ and $\{\alpha_n\}_{1\le n\le N}$, and the number M of terms in the Prony series and the corresponding shear moduli $\{G_m\}_{1\le m\le M}$ and decay constants $\{\beta_m\}_{1\le m\le M}$. Values of N and M are progressively increased until the deviation in the L²- norm between the experimental stress-strain curve

considered and the corresponding model prediction (equations (3–8) to (3–11)) is less than 15%. The procedure is applied three times for successively larger test data.

For case 1 we only consider the monotonic compression (-0.001/s) and tension (5/s) tests, and the loading portion of the first cycle of the cyclic tensile tests at all strain rates (0.01/s, 0.1/s, 0.5/s). For case 2 we consider the complete first cycle of the cyclic tests in addition to the data included for case 1. For case 3 we consider the data for the first two complete cycles.

The optimal set of parameters is searched using MATHEMATICA and the "FindFit" function. The functions listed in the equations (3–8),(3–9),(3–10) and (3–11) are written for assumed values of N and M and a least-square fit of the stress predictions with the corresponding experimental curves is performed. The values of N and M are gradually increased till the L^2- norm of the deviation is less than 15%. *When the 3rd cycle was included in the fitting no value of N and M could be found to achieve the desired deviation*. Accordingly, we discuss results obtained with only 2 cycles of loading/unloading. Moreover, no acceptable fit could be found for the DFA4700 when the second cycle was included. Deviations of about 25% are persistent despite increasing values of N and M. We will present here the results obtained for N = 1 and M = 5. Using stress, strain and strain-rate relations other than those given by equations (3–8), (3–9), (3–10) and (3–11) was not investigated.

Values of material parameters for cases 1, 2 and 3 found using the above-mentioned procedure are listed in Table 3–2 for the DFA4700 and the IM800A.

Experimental data considered	Experimental data considered for the 3 cases					
	case 1		**case 2**		**case 3**	
compression	✓		✓		✓	
cycle 1, loading	✓		✓		✓	
cycle 1 , unloading	×		✓		✓	
cycle 2	×		×		✓	
	Optimal values of the material parameters for the DFA4700					
	μ_n [MPa]	α_n	μ_n [MPa]	α_n	μ_n [MPa]	α_n
$N = 1$	0.8716	2.340	6.958e-3	7.954	0.03046	5.381
$N = 2$	-0.2815	-6.698	-0.3318	-6.047		
	G_m [MPa]	β_m [/s]	G_m [MPa]	β_m [/s]	G_m [MPa]	β_m [/s]
$M = 1$	2.571	8.086	1.189	3.750e-3	1.732	1.037e-3
$M = 2$	0.9873	0.4183	0.8255	0.5305	0.6344	0.1652
$M = 3$			2.661	6.136	1.24	0.5783
$M = 4$					0.0881	4.2933
$M = 5$					1.740	5.316
	Optimal values of the material parameters for the IM800A					
	μ_n [MPa]	α_n	μ_n [MPa]	α_n	μ_n [MPa]	α_n
$N = 1$	2.044	1.562	1.363	1.664	0.05349	4.229
$N = 2$			-0.09025	-6.642		
	G_m [MPa]	β_m [/s]	G_m [MPa]	β_m [/s]	G_m [MPa]	β_m [/s]
$M = 1$	0.2691	0.9391	0.2480	0.02602	1.496	7.162e-4
$M = 2$			0.3587	2.974	0.2875	0.1404
$M = 3$					0.3168	0.9253

Table 3–2: Values of material parameters for the DFA4700 and the IM800A TPUs.

The percentage deviations between the experimental data and the model prediction are given in Table 3–3. For cases 1 and 2 the deviations between the model predictions and the experimental results not included in the least-square fit are large. In particular, more than 200% deviation is observed for DFA4700 between predictions of the second tensile cycle and the results of case 2 while smaller deviations are obtained with case 1. *Thus one cannot hope to correctly predict the experimental data not included in finding optimal values of the material parameters, and that improving the agreement with the first complete deformation cycle does not imply that the agreement with the second cycle is also improved.*

Stress-stretch curve	Strain rate $\dot{\varepsilon}^{\text{Eng}}$	DFA4700			IM800A		
		case 1	case 2	case 3	case 1	case 2	case 3
compression	-0.001/s	12.2	10.2	16.1	9.52	3.92	7.82
tension cycle 1 loading	0.01/s	7.01	10.7	24.0	3.17	4.53	12.6
tension cycle 1 unloading		*27.0*	4.61	20.3	*15.1*	2.56	10.1
tension cycle 2 loading		*32.1*	*142*	16.0	*7.85*	*9.65*	10.3
tension cycle 2 unloading		*88.3*	*223*	18.1	*40.9*	*36.3*	8.98
tension cycle 1 loading	0.1/s	2.52	5.64	12.6	3.00	4.68	8.14
tension cycle 1 unloading		*19.3*	12.9	18.6	*8.25*	5.56	6.93
tension cycle 2 loading		*20.2*	*125*	12.5	*3.70*	*5.13*	8.19
tension cycle 2 unloading		*75.8*	*218*	25.3	*31.5*	*33.4*	14.0
tension cycle 1 loading	0.5/s	3.39	6.74	12.0	1.25	2.14	3.71
tension cycle 1 unloading		*18.0*	9.92	15.5	*4.35*	2.54	6.14
tension cycle 2 loading		*20.2*	*79*	17.7	*5.82*	*3.69*	5.71
tension cycle 2 unloading		*55.4*	*160*	22.7	*20.4*	*25.7*	12.3
tension cycle 1 loading	1.0/s	3.65	6.31	10.7	4.00	3.48	7.49
tension cycle 1 unloading		*14.7*	*8.26*	14.6	*8.38*	*3.27*	7.79
tension	5.0/s	2.26	*2.35*	4.79	3.33	*2.64*	5.67

Table 3–3: Percentage deviations in L^2-norm between the experimental and the predicted stress, stretch, strain-rate curves. Numbers are in italics when the experimental data was not considered for the least-squares fit.

For small strains the instantaneous Young's modulus E_0 of the material is given by

$$E_0 = \frac{3}{2}\sum_{n=1}^{N}\mu_n\alpha_n + \sum_{m=1}^{M}3G_m \tag{3–12}$$

where the first term on the right-hand side is due to the contribution from $\boldsymbol{\sigma}^{\text{nlel}}$ derived from W, and the second term corresponds to the contribution from $\boldsymbol{\sigma}^{\text{ve}}$. In Fig.3–3 we have exhibited contributions from the elastic and the viscoelastic responses to the initial instantaneous Young's modulus of the DFA4700 and the IM800A materials. It is clear from the results that when test data from more cycles are considered to find values of material parameters the contribution from the elastic part of the constitutive relation to the initial shear modulus decreases. The decrease is especially large for cases 2 and 3 for which test data for complete cycle 1, and complete first two cycles is considered for finding values of material parameters. One should note that the contribution to the stress from $\boldsymbol{\sigma}^{\text{nlel}}$ is not negligible at large strains since the hardening parameters $\underline{\alpha_n}$ have large values. The results depicted in Fig.3–3 follow from the observation that if more cycles are considered and consequently the final time of the test becomes large a part of the response that was initially considered nonlinear elastic has more time to relax and gets incorporated into the viscoelastic response via additional terms in the Prony series that have small decay constants (i.e., large relaxation times).

In Fig.3–4 and Fig.3–5 we have plotted the tangent Young's modulus for uniaxial tension or compression (computed as

$\partial\sigma^{\text{True}}_{I,\text{load}}\big/\partial\lambda$ with different values of $\dot{\varepsilon}^{\text{Eng}}$ (= $\dot{\lambda}$) and λ) as a function of the axial stretch λ for different strain rates. The highest strain rate considered is 10^3/s since curves for higher strain rates would be superimposed. It is interesting to note that for low strain rates, the tangent Young's modulus initially decreases with a change in the value of the axial stretch from 1 or equivalently small axial strains. However, this is not the case for axial engineering strain rates higher than 10 /s. Also, the tangent modulus at a constant engineering strain rate is a function of the stretch. Even for small strains, the tangent modulus is a different function of the magnitude of the axial strain for compressive and tensile deformations except for large values of the axial strain rate.

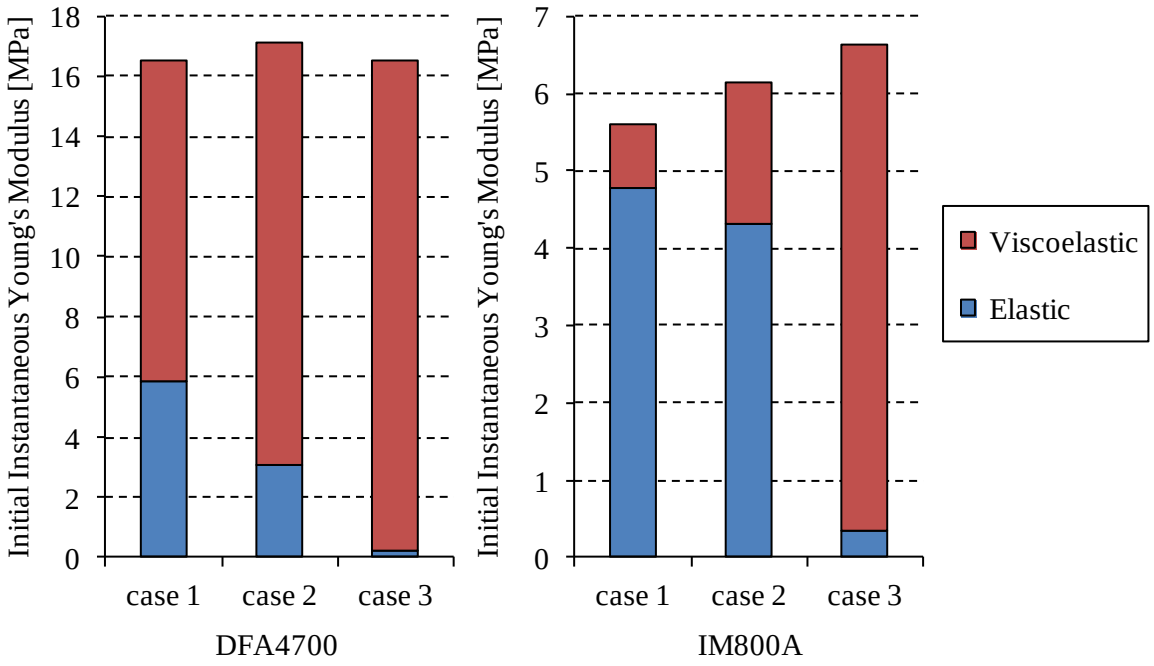

Fig.3–3: Contributions to the small-strain instantaneous Young's modulus from the elastic and the viscoelastic parts of the constitutive relation.

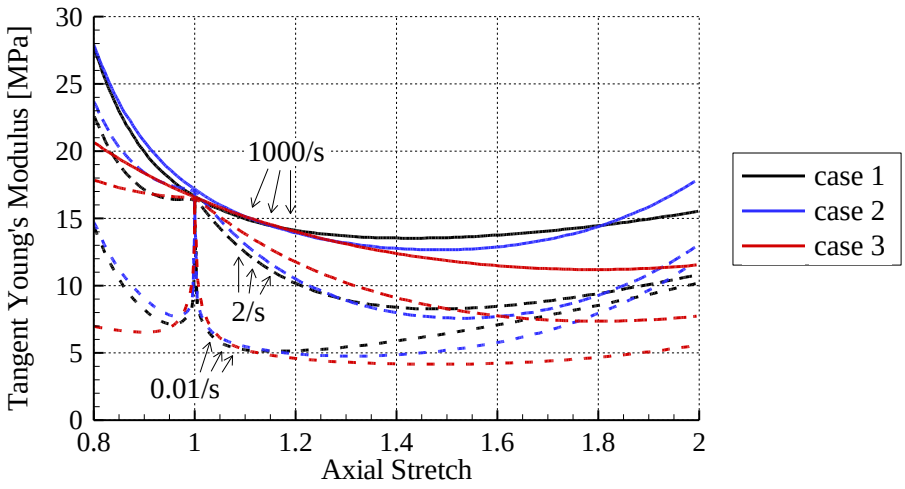

Fig.3–4: Predicted tangent modulus as a function of the axial stretch for the DFA4700 material.

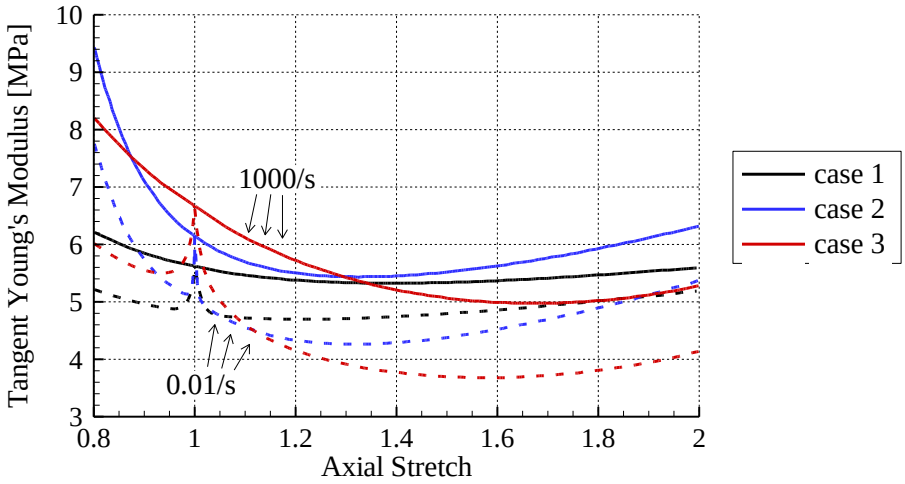

Fig.3–5: Predicted tangent modulus as a function of the axial stretch for the IM800A material.

In Fig.3–6 we have exhibited the tangent Young's modulus in uniaxial tension $\partial\sigma^{\text{True}}_{I,\text{load}}\big/\partial\lambda$ for λ=1.1 as a function of the strain rate of the deformation $\dot{\varepsilon}^{\text{Eng}}=\dot{\lambda}$ and for the different fitting methods used. The choice λ=1.1 is motivated by the large change in the value of the predicted tangent moduli for this value of stretch (see Fig.3–4 and Fig.3–5). These plots clearly show that the strain-rate sensitivity of the proposed

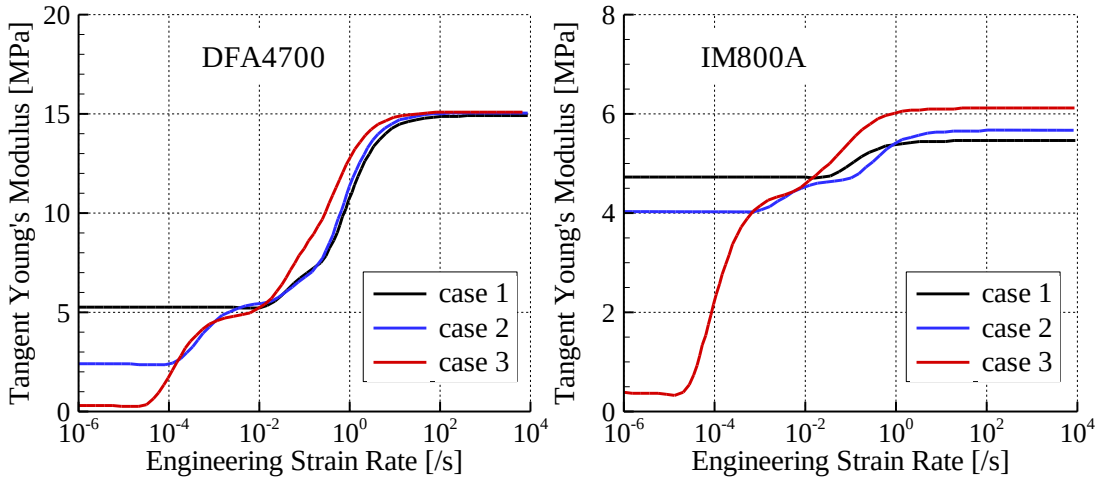

Fig.3–6: Predicted tangent modulus at 10% engineering strain (λ =1.1) as a function of the engineering strain rate $\dot{\varepsilon}^{\mathrm{Eng}} = \dot{\lambda}$.

constitutive relation increases when data for more loading cycles are considered in finding values of material parameters. One should note that the range of strain rates in the experimental data used for the three cases is not the same (-0.001/s in compression, 0.01 to 5/s in tension). The high strain rate stiffness of the materials is much less affected by the fitting method than its low strain rate response. This is because terms with small decay constants are added to the Prony series when more deformation cycles are included.

The experimental stress-axial stretch curves are given, respectively, in Fig.3–7and Fig.3–8 for the DFA4700 and the IM800A materials as well as the corresponding model predictions for the three methods of finding values of material parameters.

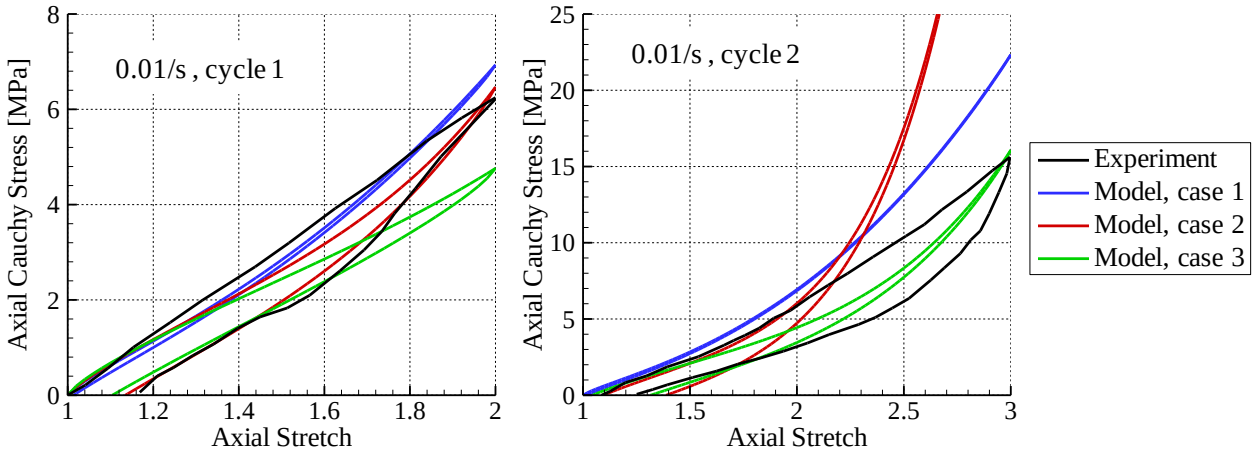

Fig.3–7: Experimental and predicted true axial stress as a function of the axial stretch for cyclic tensile deformations of DFA4700 at 0.01/s.

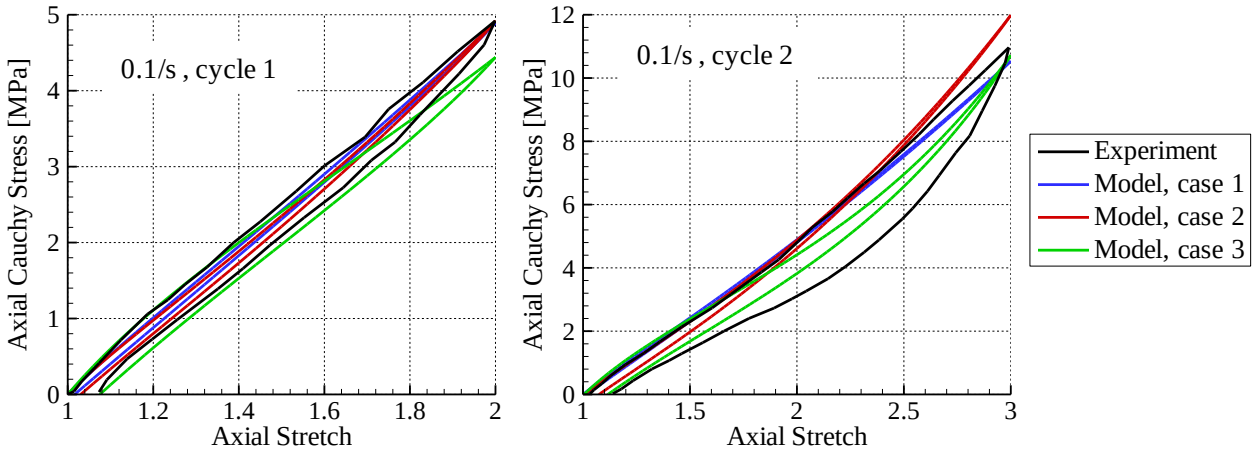

Fig.3–8: Experimental and predicted true axial stress as a function of the axial stretch for cyclic tensile deformations of IM800A at 0.1/s.

The statement made earlier that the agreement between the model predictions and the experimental results for the second deformation cycle is not necessarily improved by including data from the unloading part of the first cycle (case 2 compared to case 1) is obvious from results depicted in Fig.3–7. Moreover, we see that predictions of model 1 exhibit a very small hysteresis since the curves corresponding to loading and unloading are almost superimposed. We also note that the blue curves (case 1) are in close agreement with the loading part of the first cycle while they don't capture the unloading part and the second cycle. Similar remarks hold for the IM800A adhesive (Fig.3–8). We see that for both adhesives the agreement between the green curves (case 3) and the experimental data for the second deformation cycle is not very good, and in particular the area within the hysteresis loop (which is related to the energy dissipation) is underestimated. This is a limitation of the proposed constitutive relation since no values of material parameters could be found that improved the correlation between the test data and the model predictions for cyclic loading.

3.5.2 Loss and Storage Moduli

To find expressions for the storage and the loss moduli as a function of the frequency of the deformation we first derive an expression for the axial stress as a function of the axial strain for small strains which are typical of DMA experiments. We linearize Eq. (3–61) of the Appendix for small strains for which there is no distinction between the true and the engineering strains, strain rates and stresses, and obtain the following axial stress–axial strain relation:

$$\sigma(t)=\left(\sum_{n=1}^{N}\frac{3}{2}\mu_n\alpha_n\right)\varepsilon(t)+\sum_{m=1}^{M}\sigma_m(t)\quad,\quad \sigma_m(t)=3G_m\int_{\tau=0}^{t}e^{-\beta_m(t-\tau)}\dot{\varepsilon}(\tau)d\tau \tag{3–13}$$

Equation $(3–13)_2$ is equivalent to the following differential equation:

$$\dot{\sigma}_m(t)=3G_m\dot{\varepsilon}(t)-\beta_m\sigma_m(t) \tag{3–14}$$

In terms of complex variables indicated below by a superimposed hat, we define the complex axial strain $\bar{\varepsilon}$ and the complex axial stresses $\bar{\sigma}$ and $\bar{\sigma}_m$ as

$$\begin{aligned} \varepsilon(t) &= \mathrm{Re}\big(\bar{\varepsilon}(t)\big) \quad , \quad \bar{\varepsilon}(t) = \hat{\varepsilon}\, e^{i\omega t} \\ \sigma(t) &= \mathrm{Re}\big(\bar{\sigma}(t)\big) \quad , \quad \bar{\sigma}(t) = \hat{\sigma}\, e^{i\omega t} \\ \sigma_m(t) &= \mathrm{Re}\big(\bar{\sigma}_m(t)\big) \quad , \quad \bar{\sigma}_m(t) = \hat{\sigma}_m\, e^{i\omega t} \end{aligned} \tag{3–15}$$

By substituting from Eq. (3–15) into Eq. (3–14) we obtain the following relation between $\hat{\sigma}_m$ and $\hat{\varepsilon}$ featuring the loss and the storage moduli, $E'_m(i\omega)$ and $E''_m(i\omega)$, corresponding to the m^{th} term of the Prony series:

$$\hat{\sigma}_m = E'_m(i\omega)\,\hat{\varepsilon} + iE''_m(i\omega)\,\hat{\varepsilon} \quad , \quad E'_m(i\omega) = \frac{3G_m}{1+\big(\beta_m/\omega\big)^2} \quad , \quad E''_m(i\omega) = \frac{3G_m}{\frac{\beta_m}{\omega}+\frac{\omega}{\beta_m}} \tag{3–16}$$

Equations (3–13), (3–14), (3–15) and (3–16) give

$$\hat{\sigma} = E'(i\omega)\,\hat{\varepsilon} + iE''(i\omega)\,\hat{\varepsilon} \quad \text{with} \quad \begin{cases} E'(i\omega) = \displaystyle\sum_{n=1}^{N} \frac{3}{2}\mu_n\alpha_n + \sum_{m=1}^{M} \frac{3G_m}{1+\big(\beta_m/\omega\big)^2} \\ E''(i\omega) = \displaystyle\sum_{m=1}^{M} \frac{3G_m}{\frac{\beta_m}{\omega}+\frac{\omega}{\beta_m}} \end{cases} \tag{3–17}$$

In Fig.3–9 we have depicted the storage modulus and $\tan(\delta) = E''/E'$ as a function of the angular frequency ω of the deformation for the two materials and for different methods of finding values of the material parameters described above. Note that the shear storage and loss moduli $G'(i\omega)$ and $G''(i\omega)$ are related to Young's storage and loss moduli $E'(i\omega)$ and $E''(i\omega)$ by $G'(i\omega) = E'(i\omega)/\big(2(1+\nu)\big) = E'(i\omega)/3$ and $G''(i\omega) = E''(i\omega)/3$ since the materials are incompressible and the deformations are small.

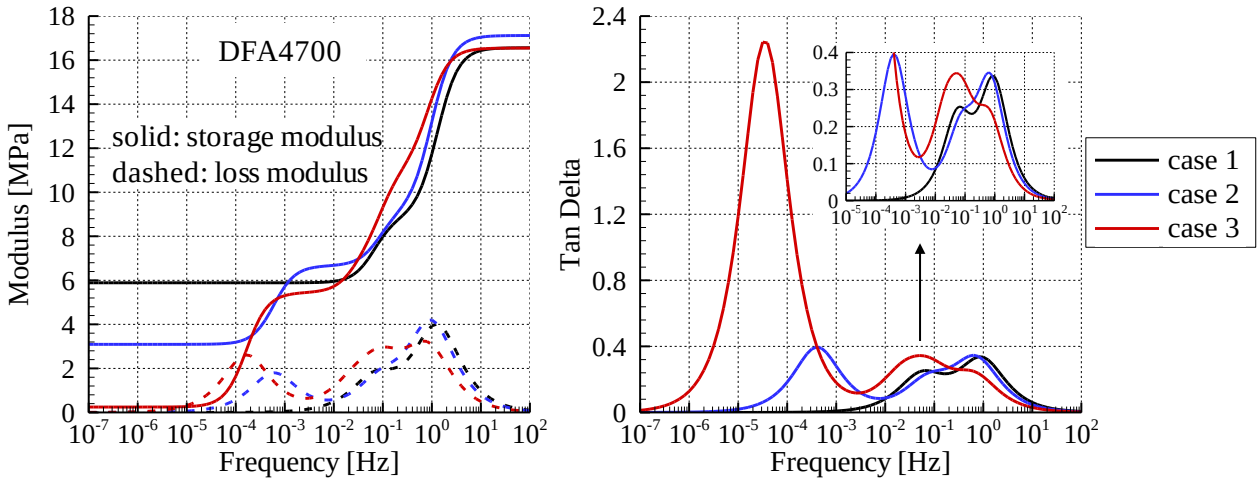

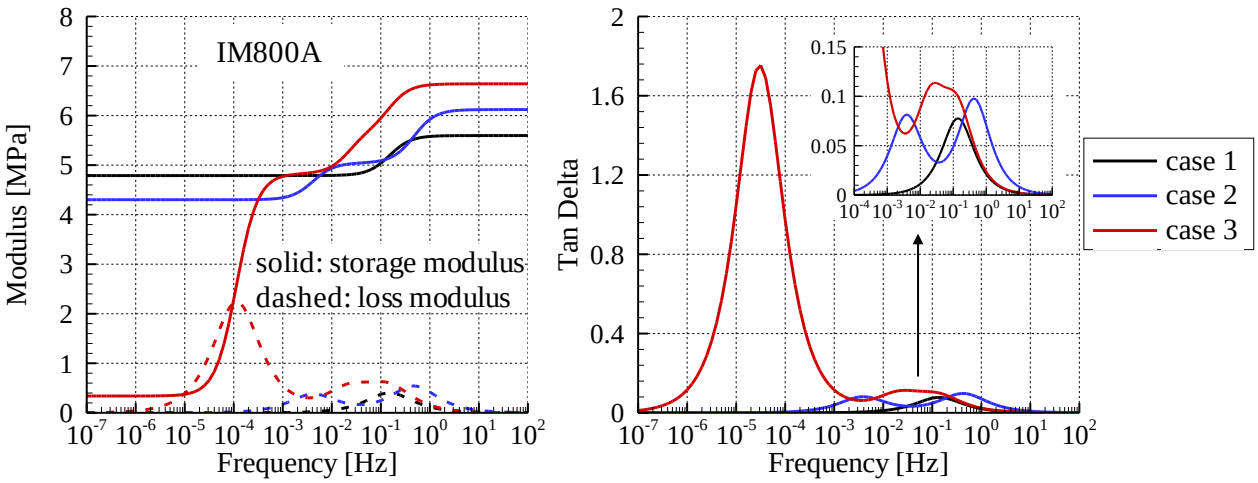

Fig.3–9: Storage modulus, loss modulus and tangent delta as a function of the frequency $f = \omega/(2\pi)$ for uniaxial deformations. Note that the frequency is plotted by using the logarithmic scale.

For the DFA4700 the model predicted values of the storage and the loss moduli for f > 10 Hz and cases 1, 2 and 3 do not show any significant differences. The storage modulus predicted at high frequencies for case 2 is about 17.2 MPa while it is 16.6 MPa for the two other cases considered (3.6% difference). For the IM800A adhesive and f >10 Hz the predicted values of the storage moduli vary between 5.60 MPa (case 1) and 6.64 MPa (case 3), which gives a difference of approximately 19%. Besides these observations the largest difference in the predictions is the following: the consideration of the first unloading and of the second complete deformation cycle in the data used to find values of material parameters causes a large difference in the very low strain-rate (<10^{-4} Hz) response of the material. This is true for both materials, and for DFA4700 (IM800A) the predicted storage modulus at very low strain-rates is 5.88 MPa (4.79 MPa) in case 1, 3.11 MPa (4.31 MPa) in case 2 and 0.23 MPa (0.343 MPa) in case 3. This gives a factor of 25 and 14 between the quasi-static storage moduli of cases 1 and 3 for the DFA4700 and the IM800A, respectively. Moreover, we notice that for both adhesives values of material parameters found in case 3 introduce a very large peak in the value of the tangent delta at low strain rates since the tangent delta is greater than one for some frequencies, which means that at those frequencies the loss modulus is greater than the storage modulus. Since the storage modulus at very low strain-rates is the small strain Young's modulus of the nonlinear elastic response of the material (see Eq. (3–17) when $\omega \to 0$) this is consistent with the remarks made for results shown in Fig.3–3.

Stenzler [23] performed DMA of DFA4700 and IM800A samples at 1 Hz for temperatures between -150 and +100 °C. From the experimental results one can read the tan(δ) at room temperature (assumed to be 20±5°C) for imposed cyclic deformation at 1 Hz. These values are compared to the corresponding model predictions in Table 3–4.

Material	Experimental tan(δ)	Predicted tan(δ)		
		case 1	case 2	case 3
DFA4700	0.37±0.04	0.34	0.32	0.22
IM800A	0.11±0.02	0.021	0.071	0.023

Table 3–4: Comparison of experimental and predicted values of tan(δ) at room temperature (20±5°C) and 1 Hz loading rate.

With the material parameters found in cases 1 and 2 the predicted value of tan(δ) for the DFA4700 is comparable to the experimental value. However, in case 3 the predicted value is about 40% smaller than that obtained from the DMA data. For the IM800A adhesive the predicted values are far smaller than the experimental ones in all three cases. We note that the experimental tan(δ) of the IM800A is quite small and corresponds to a 6.3±1.1° phase difference between the prescribed stress and the measured strain.

When test data for case 3 is used to find values of material parameters, the constitutive relation shows the most rate sensitivity and the predicted tan(δ) for 1 Hz at room temperature is smaller than that found for cases 1 and 2. This is because most of the strain-rate dependency for case 3 occurs at very low frequencies because in Fig.3–9 the peak in the value of tan(δ) occurs at 10^{-5}~10^{-4} Hz frequencies. These results suggest that by improving the agreement between the model predictions and the experimental data for the second cycle of deformations the model predictions for the first deformation cycles are worsened. A large part of the viscoelastic response of the material is attributed to very small relaxation times which results in smaller value of tan(δ) at room temperature and 1 Hz frequency. These remarks are also valid for the IM800A material even though the tan(δ) for it has small values.

3.5.3 Shear Response

We note that simple shear deformations, the orthogonal matrix R in the polar decomposition of the deformation gradient F is not identity as it is for uniaxial deformations. Thus, the analysis of the viscoelastic part of the stress-strain curve becomes more interesting. Simple shear deformations in the *xy* – plane are described by

$$x = X + \gamma Y \quad , \quad y = Y \quad , \quad z = Z \tag{3–18}$$

where lower (upper) case letters correspond to the position of a material point in the current (reference) configuration, and the shear strain γ is given by $\gamma = \dot{\gamma} t$ with $\dot{\gamma}$ being the constant strain rate. The condition $\sigma_{zz} = 0$ is used to determine the hydrostatic pressure. Since $\sigma_{zx} = \sigma_{zy} = 0$, the deformation is plane-stress. The differential equation giving the shear stress σ_{xy} as a function of γ and $\dot{\gamma}$ is integrated numerically using the "NDSolve" function of MATHEMATICA (see the appendix for more details). The tangent shear modulus calculated as $\partial \sigma_{xy} / \partial \gamma$ is plotted as a function of the shear strain γ for different values of $\dot{\gamma}$ in Fig.3–10 for the DFA4700 and in Fig.3–11 for the IM800A.

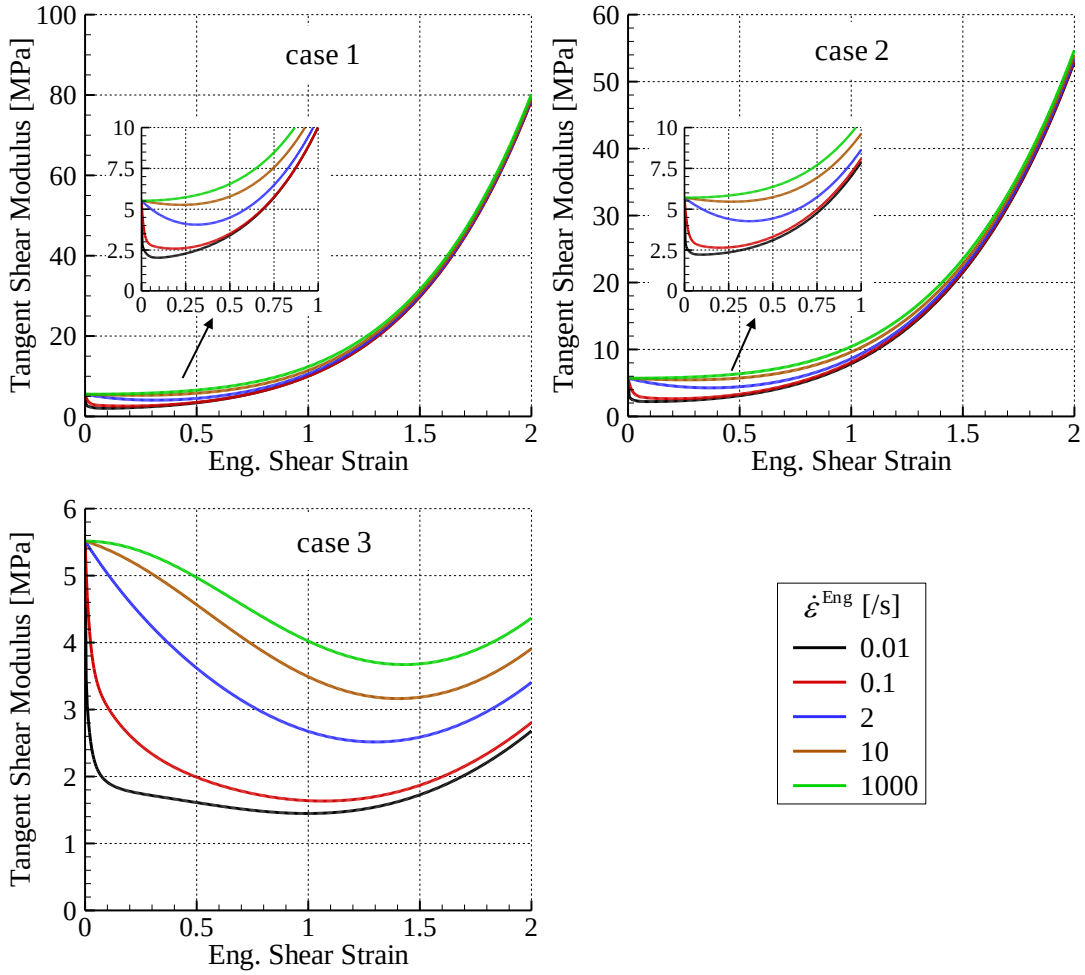

Fig.3–10: Predicted tangent shear modulus for simple shear deformations of the DFA4700 material.

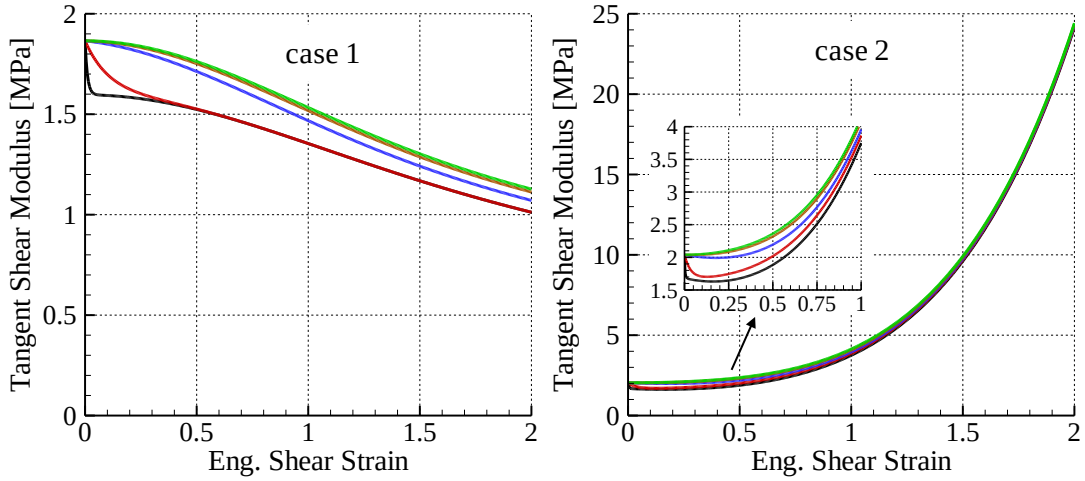

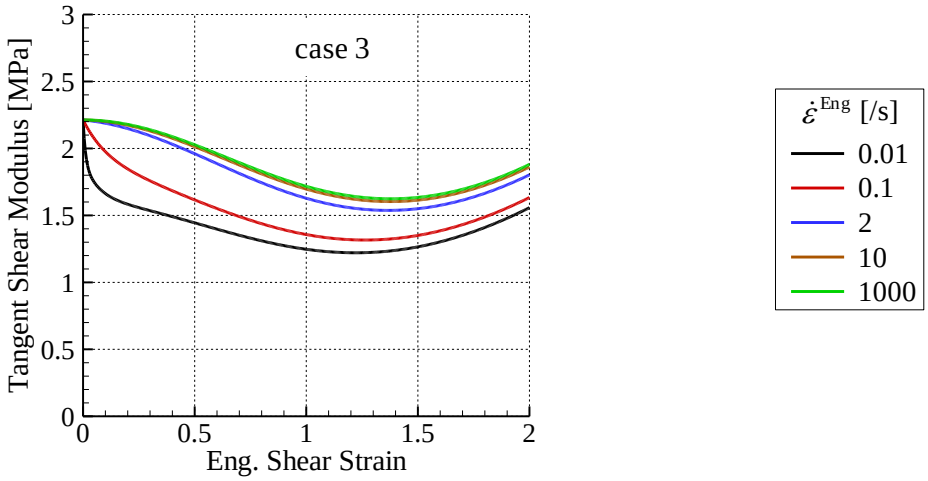

Fig.3–11: Predicted tangent shear modulus for simple shear deformations of the IM800A material.

For cases 1 and 2 of the DFA4700 and case 2 of the IM800A – for which there are terms with negative exponents in the strain energy density function W – one can observe that the tangent shear modulus becomes very large at large strains while it remains quite small for the other cases. It is clear that the strain-rate dependency of the DFA4700 material is stronger than that of the IM800A, which is consistent with the results in uniaxial deformation.

The tangent shear modulus is strain rate dependent even for cases 1 and 2 (see insets in the figure) but the scale of the y-axis is so large that it is not obvious in the plots of all of the data. We note that for cases 1 and 2 the tangent shear modulus at high strains has most of the contribution from the nonlinear elastic part of the stress-strain curve which is strain-rate independent. However, for case 3 the contribution to the tangent shear modulus from nonlinear elastic deformations is small which explains the much lower value of the tangent modulus at high strains. Therefore it appears that having data for shear deformations of adhesives at large shear strains (even for only one strain rate) is essential for capturing the shear response of the adhesive since the latter is strongly affected by the stored energy function *W*. However, we note that the deformation field given by Eq. (3–18) cannot be easily used in experiments since it leads to non-zero tractions on the material faces orthogonal to the Y-axis in the undeformed configuration, while in a shear lap test (for instance) those boundaries would be free (and the deformation non-uniform). Another possibility is to study the Couette flow between two cylinders.

3.5.4 Discussion of the Constitutive Relations

The proposed constitutive relation does not account for irreversible processes that can take place during large deformations of TPUs such as rearrangement of molecular networks (see [16]), since when the material is unloaded and $t \to \infty$ the material completely "forgets" its deformation history as contributions from the Prony series vanish and the material retrieves its original shape. The temperature dependence of material parameters and the relaxation times has not been considered. The latter could be incorporated via the William-Landel-Ferry equation, e.g., see [24], and assuming that the stored energy function also depends upon the temperature change. These factors may explain why the model cannot well capture the second deformation cycle of the DFA4700 and IM800A. Furthermore, one should compare predictions from the constitutive relation with test data for other types (especially, 3-dimensional) of deformation that

have not been used to find values of material parameters. However, this has not been done because of the lack of availability of the test data in the open literature.

Ideally one should consider test data under a variety of loading conditions to find values of material parameters. However, it is not possible since testing materials under controlled conditions and accurately measuring stresses and strains is rather difficult.

The considerable deviation remaining between the predictions and the experimental data of the second deformation cycles in Fig.3–7 and Fig.3–8 are a limitation of the model. Several different initial points (i.e. sets of values) have been used for the least square fitting of the material parameters but all of them eventually yielded values reported in Table 3–2 of the manuscript (or sets of values giving a worse agreement with experimental data). We have not been able to find in the open literature a paper that compares model predictions and test results for one or more cycles of deformations for a viscoelastic material.

For strain-rates varying from 10^{-3} to 10^{3}/s, one probably needs a nonlinear dependence of the Cauchy stress upon the strain-rate tensor. One could potentially include dependence of the Cauchy stress upon $\mathbf{D}^2$, $\mathbf{D}^3$, 2nd invariant of $\mathbf{D}$ and third invariant of $\mathbf{D}$ with the resulting increase in the number of material parameters. Whether or not it will improve correlation between test results and model predictions remains to be explored.

We believe that the constitutive relations is applicable for general 3-dimensional deformations of rubberlike materials as similar material models have been used for analyzing finite deformations, e.g., see [15, 24].

3.6 Application: Simulations of Low-velocity Impact of Laminate

The constitutive equations presented above have been implemented in the explicit commercial FE software LS-DYNA as a user-defined subroutine. The quasi-static response of the material is computed from the deformation gradient to avoid writing the corresponding constitutive equation in a rate form. For a perfectly incompressible material the pressure term is a Lagrange multiplier and cannot be determined from deformations of the material (e.g., see Batra [22]). However for numerical work, the kinematic constraint of incompressibility is often relaxed and the pressure is simulated by penalizing volumetric strains (e.g., see Simo and Taylor [25]). Alternatively, one can use a mixed formulation in which the pressure is an unknown variable and is determined as a part of the solution of the problem, e.g. see [24]. A mechanical analog of the former approach is depicted in Fig.3–12. Thus

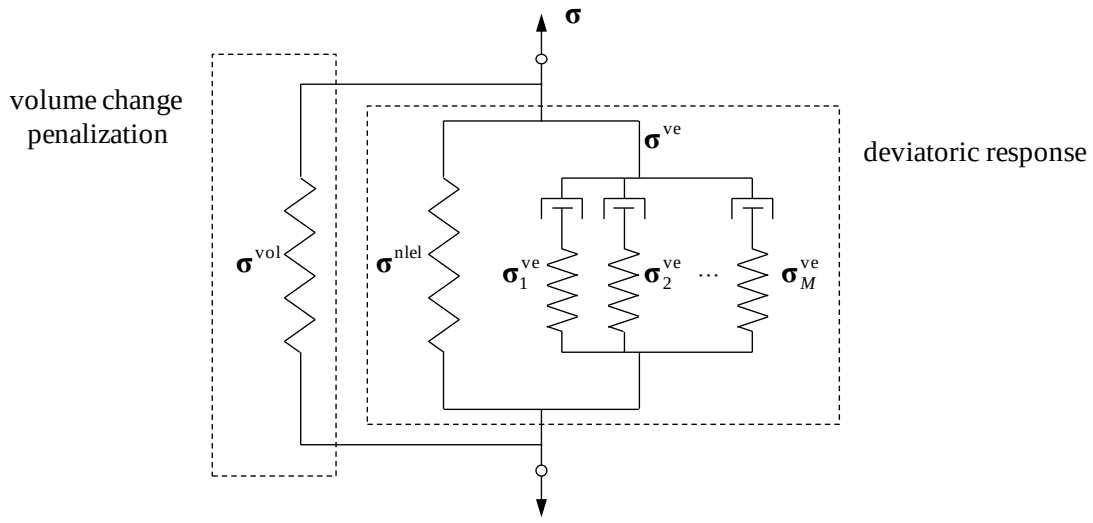

Fig.3–12: One-dimensional rheological analog interpretation of the constitutive relation for an incompressible material.

$$\boldsymbol{\sigma} = \boldsymbol{\sigma}^{\text{nlel}} + \boldsymbol{\sigma}^{\text{ve}} + \boldsymbol{\sigma}^{\text{vol}} \tag{3–19}$$

The Cauchy stress $\boldsymbol{\sigma}^{\text{nlel}}$ is found from the following modified strain energy density function

$$W = \sum_{n=1}^{N} \frac{\mu_n}{\alpha_n}\left(\tilde{\lambda}_1^{\alpha_n} + \tilde{\lambda}_2^{\alpha_n} + \tilde{\lambda}_3^{\alpha_n} - 3\right) \quad \text{where} \quad \tilde{\lambda}_i = \frac{\lambda_i}{\left(\lambda_1\lambda_2\lambda_3\right)^{1/3}}, i = 1,2,3 \tag{3–20}$$

The Cauchy stress $\boldsymbol{\sigma}^{\text{vol}}$ is derived from the strain energy density potential W^{vol} defined in Eq. (3–21) where J is the Jacobian of the deformation gradient.

$$W^{\text{vol}} = K\left(J - 1 - \ln(J)\right) \tag{3–21}$$

The value of the bulk modulus K must be much greater than that of the shear modulus of the material. In the present work, unless otherwise specified, the value of K has been determined by assuming that the initial Poisson's ratio (at zero strain) of the nearly incompressible materials equals 0.4995.

Viscous deformations of the material are assumed to depend only on the deviatoric part $\mathbf{D}^{\text{dev}}$ of the strain rate tensor.

$$\boldsymbol{\sigma}^{\text{ve}} = \sum_{m=1}^{M} \boldsymbol{\sigma}_m^{\text{ve}} \quad , \quad \begin{cases} \overset{\bullet}{\boldsymbol{\sigma}}_m^{\text{ve}} = 2G_m\mathbf{D}^{\text{dev}} - \beta_m\boldsymbol{\sigma}_m^{\text{ve}} \\ \boldsymbol{\sigma}_m^{\text{ve}}\big|_{t=0} = \mathbf{0} \end{cases} \tag{3–22}$$

The energy dissipated per unit current volume due to viscous effects $E^{\text{visc,ve}}$ is calculated at each time step in the user defined material subroutine, and the total energy dissipated due to viscous deformations is obtained by integrating over the deformed volume (i.e., by summing elemental contributions).

The impact problem studied here, shown schematically in Fig.3–13, is the same as that analyzed by Antoine and Batra [19] where a complete description of the problem, the mathematical model, and details of the computational work are described. The difference between that work and the one reported here is in the constitutive relations of the DFA4700 and the IM800A and values of material parameters. Here results have been computed for the three sets of test data used to find values of material parameters for the two adhesives.

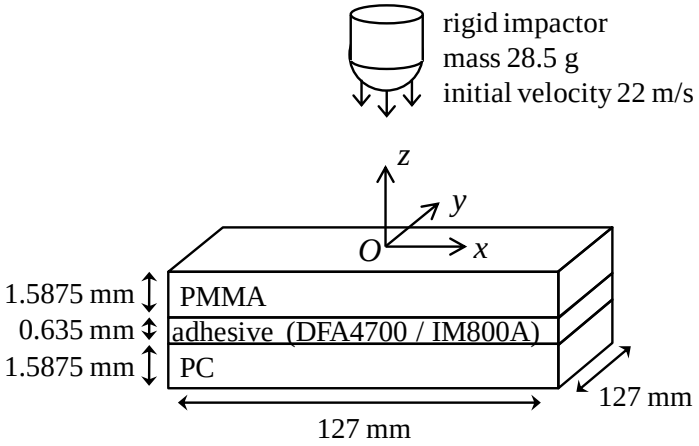

Fig.3–13: Schematic sketch of the impact problem studied

For the sake of completeness, we give a brief description of the material model for the PC and the PMMA. The same set of constitutive equations is used for the two materials, only values of the material parameters differ. We assume that the Cauchy stress $\boldsymbol{\sigma}$ is the sum of a nonlinear elastic contribution $\boldsymbol{\sigma}_{\mathrm{B}}$ (restoring force from phase B) and of two viscoelastoplastic contributions $\boldsymbol{\sigma}_{\alpha}$ and $\boldsymbol{\sigma}_{\beta}$ (from phases α and β), i.e., $\boldsymbol{\sigma} = \boldsymbol{\sigma}_{\mathrm{B}} + \boldsymbol{\sigma}_{\alpha} + \boldsymbol{\sigma}_{\beta}$. The contribution of phase B is

$$\boldsymbol{\sigma}_{\mathrm{B}} = \frac{C_{\mathrm{R}}}{3}\frac{\sqrt{N_l}}{\lambda^{\mathrm{p}}} L^{-1}\left(\frac{\lambda^{\mathrm{p}}}{\sqrt{N_l}}\right)\overline{\mathbf{B}}'_{\mathrm{B}} \tag{3–23}$$

Here $\overline{\mathbf{B}}'_{\mathrm{B}}$ is the deviatoric part of $\overline{\mathbf{B}}_{\mathrm{B}} = (J)^{-2/3}\mathbf{F}\mathbf{F}^{\mathrm{T}}$, $\lambda^{\mathrm{p}} = \sqrt{\mathrm{tr}\left(\overline{\mathbf{B}}_{\mathrm{B}}\right)/3}$, L^{-1} is the inverse of the Langevin function $L(\beta) \equiv \coth\beta - 1/\beta$, N_l is the limiting stretch, $C_{\mathrm{R}} \equiv n_{\mathrm{R}} k\theta$, θ is the temperature in Kelvin, k is Boltzmann's constant and n_{R} a material parameter.

The constitutive equations of the two other phases α and β rely on the decomposition of the deformation gradient into elastic and plastic parts, e.g., see Kroner [26] and Lee [27]:

$$\mathbf{F} = \mathbf{F}^{\mathrm{e}}_{\alpha}\mathbf{F}^{\mathrm{p}}_{\alpha} = \mathbf{F}^{\mathrm{e}}_{\beta}\mathbf{F}^{\mathrm{p}}_{\beta} \tag{3–24}$$

The rate of the plastic deformation gradient is given by

$$\dot{\mathbf{F}}_{\alpha}^{\mathrm{p}} = \mathbf{F}_{\alpha}^{\mathrm{e}\,-1}\widetilde{\mathbf{D}}_{\alpha}^{\mathrm{p}}\mathbf{F} \quad , \quad \dot{\mathbf{F}}_{\beta}^{\mathrm{p}} = \mathbf{F}_{\beta}^{\mathrm{e}\,-1}\widetilde{\mathbf{D}}_{\beta}^{\mathrm{p}}\mathbf{F} \,, \tag{3–25}$$

where $\widetilde{\mathbf{D}}_{i}^{\mathrm{p}}$ is the plastic stain-rate tensor in phase $i = \alpha, \beta$ (it has been assumed that the plastic spin tensors are identically zero).

The Hencky elastic strain tensor and the Cauchy stress tensor in phase $i = \alpha, \beta$ are given by

$$\boldsymbol{\varepsilon}_{i}^{\mathrm{e}} = \ln\left(\sqrt{\mathbf{F}_{i}^{\mathrm{e}}\mathbf{F}_{i}^{\mathrm{e}\,\mathrm{T}}}\right) \quad , \quad \boldsymbol{\sigma}_{i} = \frac{1}{\det(\mathbf{F}_{i}^{\mathrm{e}})}\left[2\mu_{i}\boldsymbol{\varepsilon}_{i}^{\mathrm{e}} + \lambda_{i}\,\mathrm{tr}(\boldsymbol{\varepsilon}_{i}^{\mathrm{e}})\boldsymbol{\delta}\right] \tag{3–26}$$

The plastic rate-of-strain tensors in phases α and β are collinear with the deviatoric Cauchy stress tensor of their respective phases and have magnitude $\dot{\gamma}_{i}^{\mathrm{p}}$ given by

$$\dot{\gamma}_{i}^{\mathrm{p}} = \dot{\gamma}_{0i}^{\mathrm{p}} \exp\left[-\frac{\Delta G_{i}}{k\theta}\left(1 - \frac{\tau_{i}}{t_{i}\hat{s}_{i} + \alpha_{i}^{\mathrm{p}}\, p}\right)\right] \tag{3–27}$$

Here $\dot{\gamma}_{0i}^{\mathrm{p}}$, ΔG_{i}, α_{i}^{p} are material parameters, $\tau_{i} = \sqrt{0.5\,\mathrm{tr}\left(\boldsymbol{\sigma}_{i}^{'}\boldsymbol{\sigma}_{i}^{'}\right)}$, $\hat{s}_{i} = 0.077\mu_{i}/(1-\nu_{i})$ where ν_{i} is Poisson's ratio of phase $i = \alpha, \beta$, $p = -\,\mathrm{tr}(\boldsymbol{\sigma})/3$, t_{i} is an internal variable whose initial value is one and whose evolution is described by

$$\dot{t}_{i} = \frac{h_{i}}{\hat{s}_{i}^{0}}\left(1 - \frac{t_{i}}{t_{i}^{\mathrm{ss}}}\right)\dot{\gamma}_{i}^{\mathrm{p}} \tag{3–28}$$

The energy dissipated by plastic deformations is converted into heat and deformations are assumed to be adiabatic (which is a reasonable assumption for impact problems) resulting in equation (27) for the rate of change of temperature, $\dot{\theta}$.

$$\rho_{0} c\dot{\theta} = \dot{Q} = J \cdot \left(\boldsymbol{\sigma}_{\alpha} : \widetilde{\mathbf{D}}_{\alpha}^{\mathrm{p}} + \boldsymbol{\sigma}_{\beta} : \widetilde{\mathbf{D}}_{\beta}^{\mathrm{p}}\right) \tag{3–29}$$

In Eq.(3–29) c is the specific heat of the material, and ρ_{0} the initial mass density.

Values of material parameters and approximate values of Young's moduli of phases α and β are given in Table 3–5 for the PC and in Table 3–6 for the PMMA.

	Phase α	Phase β	Phase B	Common
v_i	0.38	0.38		
$\dot{\gamma}_{0i}^{\mathrm{p}}$ [/s]	2.94×10^{16}	3.39×10^{5}		
ΔG_i [J]	3.744×10^{-19}	3.769×10^{-20}		
α_i^{p}	0.168	0.245		
h_i [MPa]	125	400		
t_i^{ss}	0.33	2.00		
C_{R} at 300K [MPa]			35.0	
N_l			12.25	
c [J/(g·K)]				1.20
ρ [g/cm^3]				1.20
E [GPa] at 300K, 5000/s	1.678	0.344		

Table 3–5: Values of material parameters for the PC.

	Phase α	Phase β	Phase B	Common
v_i	0.35	0.35		
$\dot{\gamma}_{0i}^{\mathrm{p}}$ [/s]	6.95×10^{219}	1.77×10^{3}		
ΔG_i [J]	5.528×10^{-18}	6.036×10^{-20}		
α_i^{p}	0.260	0.260		
h_i [MPa]	200	500		
t_i^{ss}	0.73	0.45		
C_{R} at 300K [MPa]			14.0	
N_l			2.10	
c [J/(g·K)]				1.46
ρ [g/cm^3]				1.14
E [GPa] at 300K, 5000/s	2.604	1.748		

Table 3–6: Values of material parameters for the PMMA.

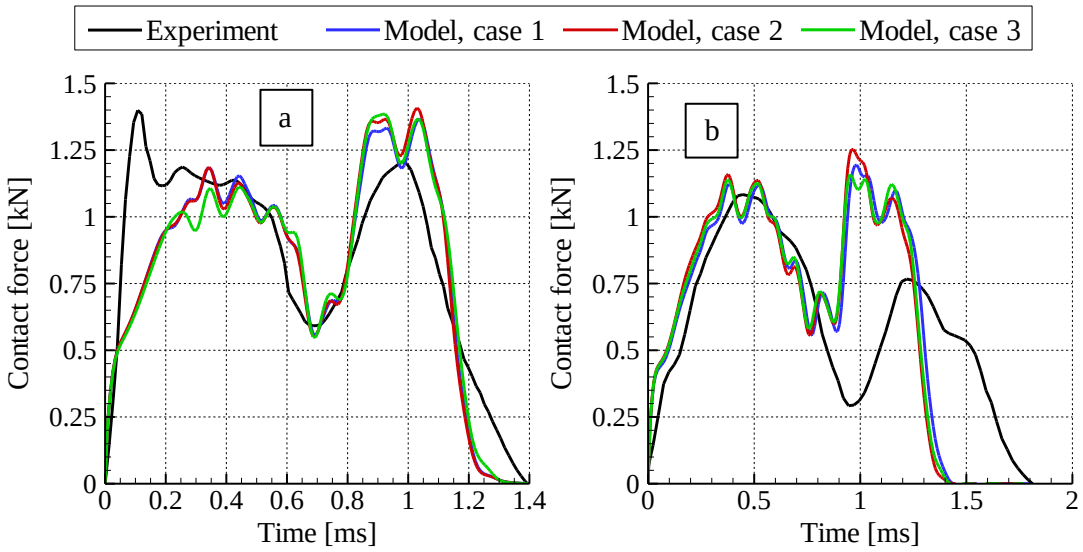

Fig.3–14: Time histories of the experimental [23] and the computed contact force for the impact of the (a) PMMA/DFA4700/PC and (b) PMMA/IM800A/PC plates.

In Fig.3–14 are depicted time histories of the contact force for the normal incidence impact of the clamped PMMA/DFA4700/PC and the PMMA/IM800A/PC plates at 22 m/s by a 28.5 g hemispherical-nosed impactor. The closeness of the numerical results for the three sets of values of material parameters is consistent with those depicted in Fig.3–6 which shows that the response of the interlayer material at high strain rates (which are typical of the impact problem) is essentially independent of the method used to find values of material parameters. We now comment on the experimental value of the peak contact force at 0.1 ms. For each laminate and the impact velocity Stenzler [23] conducted three tests but gave only one curve ("Representative force and displacement traces are given for each interlayer and velocity" [23]). For the PMMA/DFA4700/PC assembly and 22m/s impact velocity he did not mention if the peak in the contact force at 0.1 ms was present in all three experiments. Stenzler [23] provided in the appendix of his thesis a summary of the characteristics of the reaction force history. There in the column "1st force peak" and row "PMMA/DFA4700/PC, 22.7 m/s" is written 1.14 kN, which does not correspond to the peak value of 1.4 kN at 0.1 ms shown in the Fig. but to the value of the contact force at about 0.3 ms. It thus appears that this peak in the contact force did not occur in all of the three tests.

The post-impact fracture patterns in the PMMA layer are shown in Fig.3–15 (Fig.3–16) for plates with the DFA4700 (the IM800A) interlayer.

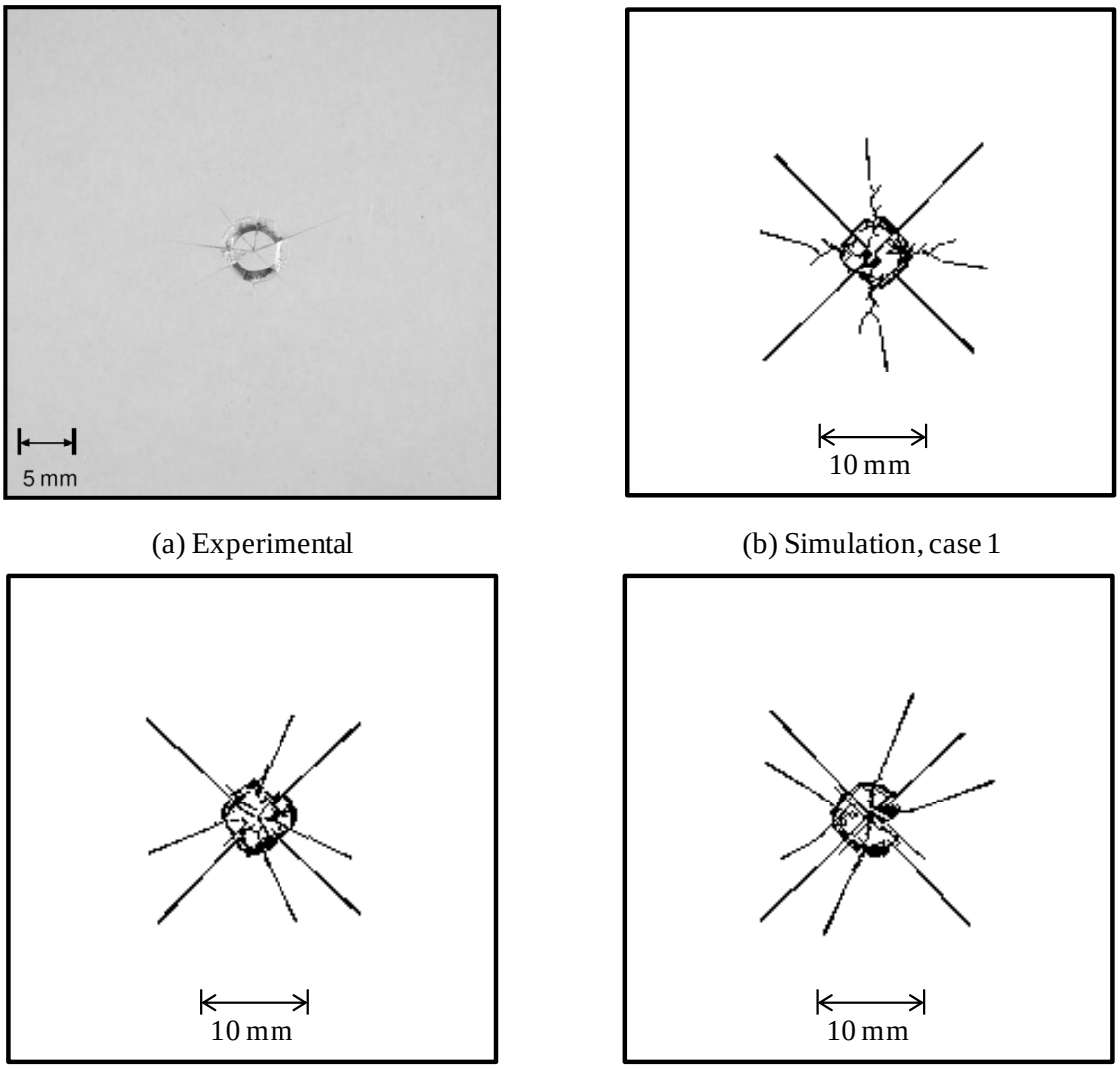

(a) Experimental

(b) Simulation, case 1

(c) Simulation, case 2

(d) Simulation, case 3

Fig.3–15: (a) Experimental (from Stenzler [23]) and simulated (b,c,d) post-impact crack patterns in the PMMA layer of the PMMA/DFA4700/PC assembly impacted at 22 m/s. The three sets of material parameters for the DFA4700 interlayer are used in the simulations.

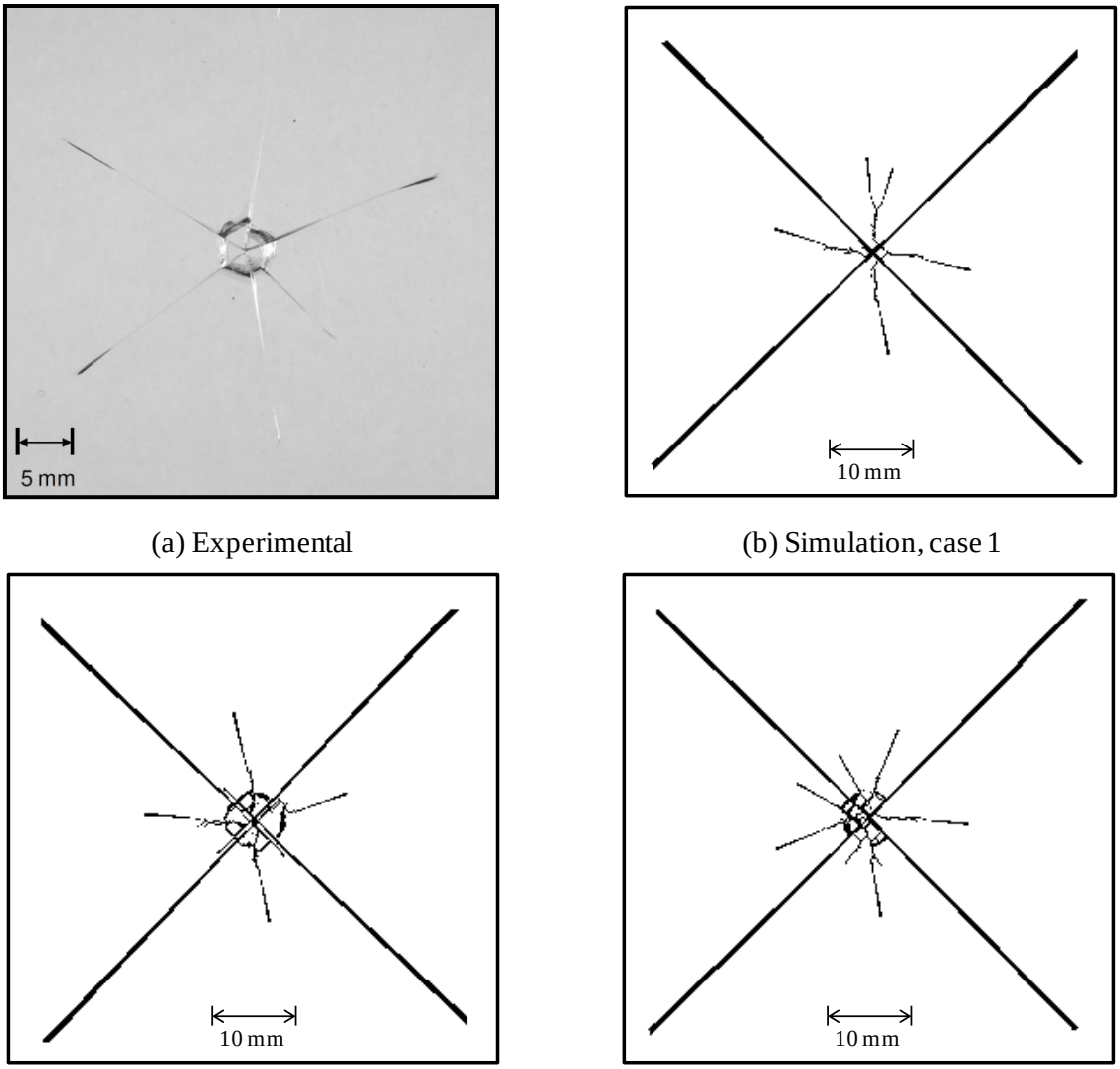

(a) Experimental (b) Simulation, case 1

(c) Simulation, case 2 (d) Simulation, case 3

Fig.3–16: (a) Experimental (from Stenzler [23]) and simulated (b,c,d) post-impact crack patterns in the PMMA layer of the PMMA/IM800A/PC assembly impacted at 22 m/s. The three sets of material parameters for the DFA4700 interlayer are used in the simulations.

The fracture patterns are qualitatively and quantitatively similar for cases 1, 2 and 3 for both adhesives. We observe that the circular-shaped cracks near the center of impact in the PMMA layers have essentially the same radii, except for the IM800A adhesive and case 1 in which no such pattern formed. Moreover, the in-plane extension of cracks is the same as also evidenced by the time histories of the computed maximum in-plane extension of a crack in the PMMA plate provided in Fig.3–17. We note that no such experimental data are available.

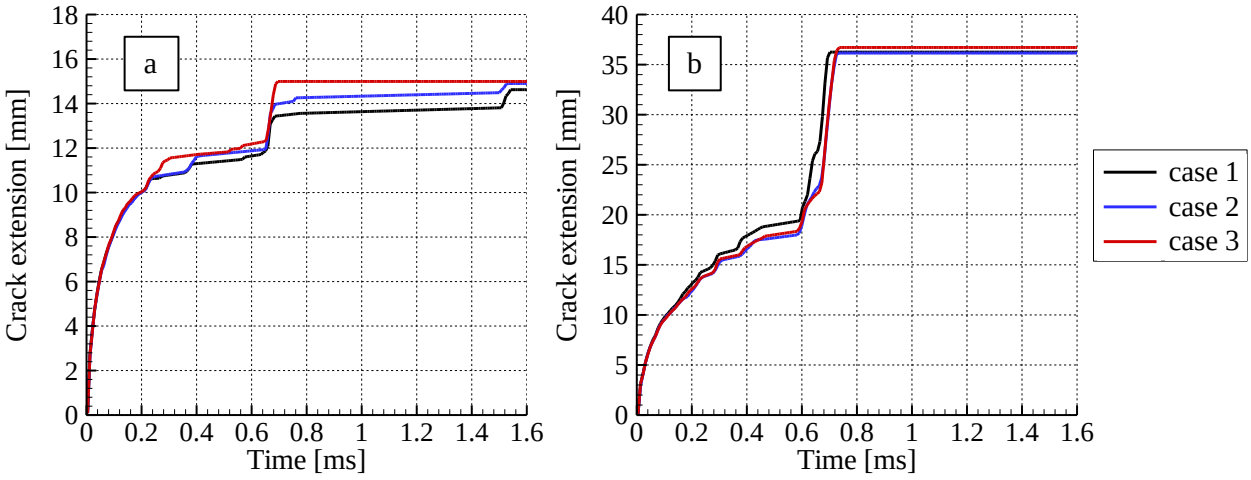

Fig.3–17: Time histories of the in-plane extension of cracks formed in the PMMA layer for the normal impact of the (a) PMMA/DFA4700/PC, and (b) PMMA/IM800A/PC plates.

The principal sources of energy dissipation for the impact problem are the "eroded energy" due to the material failure and the subsequent crack formation in the PMMA layer, the energy due to plastic deformations of the PMMA and the PC layers, and the energy of viscous deformations of the adhesive interlayer. Their values in mJ are listed in Table 3–7. We note that the kinetic and the strain energies of the PMMA, the PC and the adhesive layers are not listed in the Table. The energy dissipated due to viscous deformations of the adhesive is a miniscule part of the kinetic energy of the impactor. For the DFA4700 (IM800A) the choice of the set of material parameters for the adhesive used in the simulations induces a variation in the energy dissipated due to cracking of the PMMA layer of about 11% (19%). The energy dissipated due to plastic deformations of the PC layer varies by about 10% (4%) for the laminate using DFA4700 (IM800A). As expected values of material parameters for the adhesive noticeably influence the energy dissipated due to viscous deformations of the adhesive interlayer. However, energies dissipated due to deformations of the adhesive are negligible as compared to that due to plastic deformations of the PC layer. The energy dissipated due to cracking and plastic deformations of the PMMA layer is approximately one-fourth of that due to plastic deformations of the PC layer.

For the three sets of values of material parameters for the two adhesives contours of the plastic strain on the back face of the PC layer are not much affected either qualitatively or quantitatively, as shown in Fig.3–18 and Fig.3–19.

	PMMA/DFA4700/PC plate			PMMA/IM800A/PC plate		
	case 1	case 2	case 3	case 1	case 2	case 3
Initial kinetic energy of impactor	6900	6900	6900	6900	6900	6900
Final kinetic energy of impactor	4620	4640	4620	4830	4730	4760
Energy due to cracking of PMMA	210	189	195	238	280	261
Energy of plastic deformations of the PMMA	18.1	18.9	20.3	29.5	21.3	26.4
Energy due to viscous deformations of the adhesive	6.33	4.92	3.43	0.288	0.965	0.318
Energy of plastic deformations of the PC	794	846	867	817	785	810
Total energy dissipated	1028	1059	1086	1085	1087	1098

Table 3–7: Impact energy and sources of energy dissipation for the impact of the laminated plates. Energies are given in [mJ].

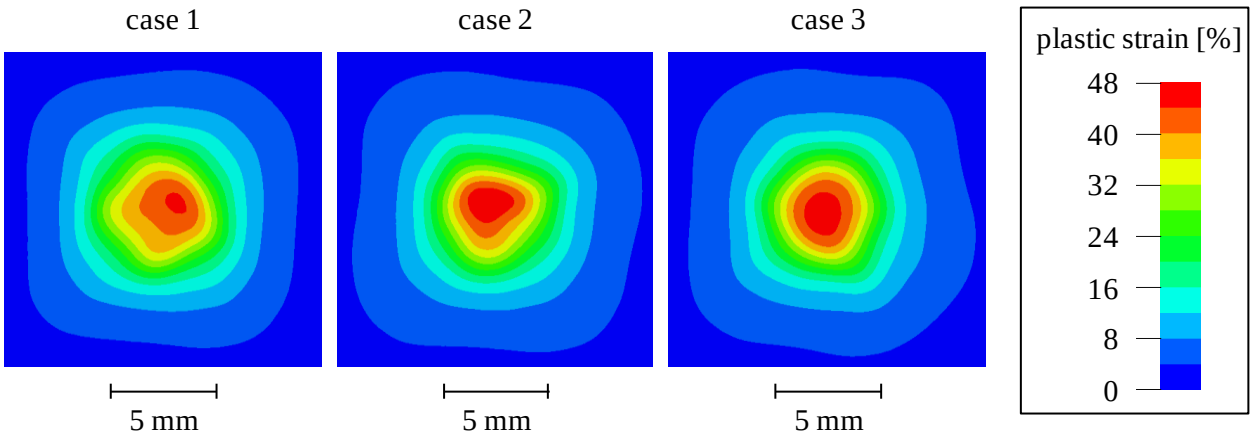

Fig.3–18: Fringe plots of the effective plastic strain near the center of the back surface of the PC layer of the PMMA/DFA4700/PC laminate.

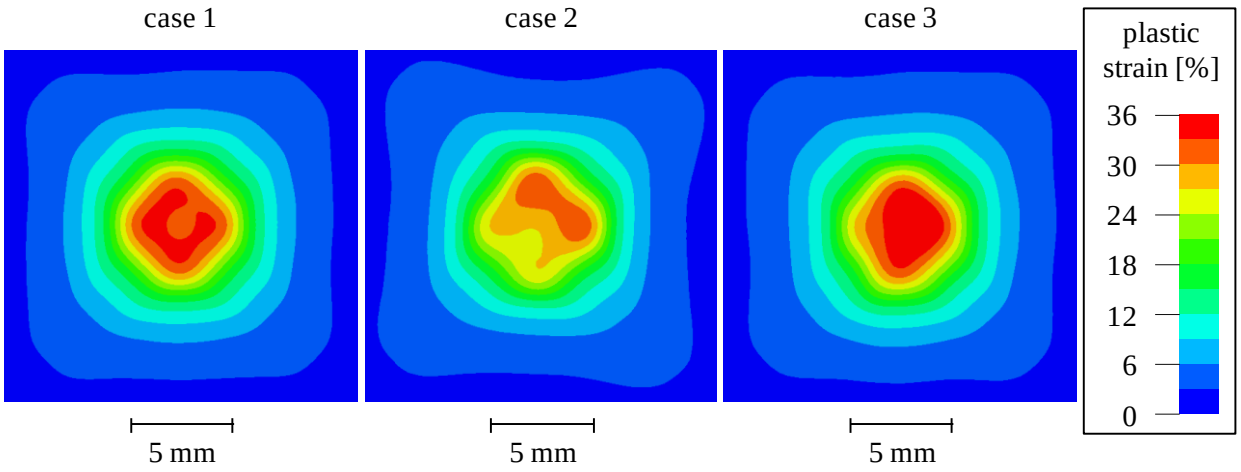

Fig.3–19: Fringe plots of the effective plastic strain near the center of the back surface of the PC layer of the PMMA/IM800A/PC laminate.

The results given in Table 3–7 imply that the energy due to viscous dissipation does not increase between cases 1 and 3, which seems to contradict results included in Fig.3–3 that indicate that the viscoelastic contribution to the instantaneous elastic response of the materials increases. In order to investigate this further, we assume that relaxation effects are negligible (i.e., $\left\|2G_m\mathbf{D}^{\text{dev}}\right\| >> \left\|\beta_m\boldsymbol{\sigma}_m^{\text{ve}}\right\|$ for all m, deformations are isochoric (i.e., $J = 1$), and rotation effects are negligible (i.e., the deformation gradient $\mathbf{F}$ is nearly symmetric). These assumptions imply that $\boldsymbol{\sigma}_m^{\text{ve}} \approx 2G_m\boldsymbol{\varepsilon}^{\text{dev}}$, where $\boldsymbol{\varepsilon}^{\text{dev}}$ is the deviatoric part of the Hencky strain tensor. In this approximation the energy dissipated per unit volume by the m^{th} term of the Prony series, $E_m^{\text{visc,ve}}$, is given by

$$E_m^{\text{visc,ve}} = \int_t \left[\frac{\beta_m}{2G_m} 2G_m\boldsymbol{\varepsilon}^{\text{dev}} : 2G_m\boldsymbol{\varepsilon}^{\text{dev}}\right] dt = 2G_m\beta_m \int_t \boldsymbol{\varepsilon}^{\text{dev}} : \boldsymbol{\varepsilon}^{\text{dev}} dt = 3G_m\beta_m \int_t \bar{\varepsilon}^2 dt \tag{3–30}$$

where $\bar{\varepsilon} = \sqrt{\frac{2}{3}\boldsymbol{\varepsilon}^{\text{dev}} : \boldsymbol{\varepsilon}^{\text{dev}}}$ is the effective strain.

To ensure that Eq. (3–30) gives reasonably good estimate of the energy dissipated due to viscous effects, we compare at the final time of impact simulation the normalized total dissipation

$$\hat{E}_m^{\text{visc,ve}} = \sqrt{\frac{1}{3V_0 t_f G_m \beta_m} \int_{V_0} \left[E_m^{\text{visc,ve}}\Big|_{t=t_f}\right] dV_0} \tag{3–31}$$

obtained by using the actual dissipation calculated during the simulation, and its approximation

$$\hat{\varepsilon} = \sqrt{\frac{1}{V_0 t_f} \int_{V_0} \left[\int_{t=0}^{t_f} \bar{\varepsilon}^2 dt\right] dV_0} \tag{3–32}$$

calculated during the post-processing of results. The values given in Table 3–8 clearly indicate that the approximate expression listed in Eq. (3–30) gives a very good estimate of the energy dissipated due to viscous effects. Moreover, one can see that the average strain $\hat{\varepsilon}$ is essentially the same for the three sets of values of material parameters.

PMMA/DFA4700/PC	case 1	$\hat{\varepsilon}$	0.0845
		$\hat{E}_1^{visc,ve}$	0.0829 (+1.9%)
		$\hat{E}_2^{visc,ve}$	0.0832 (+1.6%)
	case 2	$\hat{\varepsilon}$	0.0841
		$\hat{E}_1^{visc,ve}$	0.0827 (+1.7%)
		$\hat{E}_2^{visc,ve}$	0.0827 (+1.7%)
		$\hat{E}_3^{visc,ve}$	0.0824 (+2.0%)
	case 3	$\hat{\varepsilon}$	0.0887
		$\hat{E}_1^{visc,ve}$	0.0874 (+1.5%)
		$\hat{E}_2^{visc,ve}$	0.0874 (+1.5%)
		$\hat{E}_3^{visc,ve}$	0.0874 (+1.5%)
		$\hat{E}_4^{visc,ve}$	0.0872 (+1.7%)
		$\hat{E}_5^{visc,ve}$	0.0872 (+1.8%)
PMMA/IM800A/PC	case 1	$\hat{\varepsilon}$	0.161
		$\hat{E}_1^{visc,ve}$	0.152 (+5.9%)
	case 2	$\hat{\varepsilon}$	0.144
		$\hat{E}_1^{visc,ve}$	0.136 (+5.9%)
		$\hat{E}_2^{visc,ve}$	0.136 (+6.0%)
	case 3	$\hat{\varepsilon}$	0.138
		$\hat{E}_1^{visc,ve}$	0.139 (–0.4%)
		$\hat{E}_2^{visc,ve}$	0.139 (–0.4%)
		$\hat{E}_3^{visc,ve}$	0.139 (–0.3%)

Table 3–8: Normalized energy dissipations found by using equations (3–6) and (3–30). Deviations between $\hat{E}_m^{visc,ve}$'s and $\hat{\varepsilon}$ are given in parentheses (using the $\hat{E}_m^{visc,ve}$'s as reference values).

We now use the approximate expression of Eq. (3–30) to explain that the viscous dissipation can decrease even if the viscoelastic contribution to the response of the material increases. Since values of $\hat{\varepsilon}$ given in Table 3–8 are virtually independent of the choice of the set of material parameters, the term $\int_t \bar{\varepsilon}^2 dt$ in

Eq.(3–30) is the same for cases 1, 2 and 3 at the corresponding locations in the PMMA, the adhesive and the PC and times. Rewriting Eq.(3–30) as

$$E^{\text{visc,ve}} = \sum_{m=1}^{M}\left[3G_m\beta_m\int_t \bar{\varepsilon}^{\,2}dt\right] = \int_t \bar{\varepsilon}^{\,2}dt\sum_{m=1}^{M}\left[3G_m\beta_m\right] \tag{3–33}$$

we see that the term $E^{\text{visc,ve}}\Big/\sum_{m=1}^{M}3G_m\beta_m$ is nearly the same for the three data sets. This is confirmed by the total normalized viscous dissipation $\widetilde{E}^{\text{visc,ve}} = \left[\int_{V_0} E^{\text{visc,ve}}dV_0\right]\Big/\left[t_f V_0\sum_{m=1}^{M}3G_m\beta_m\right]$ (we added the $t_f V_0$ term to obtain a dimensionless number) plotted in Fig.3–20.

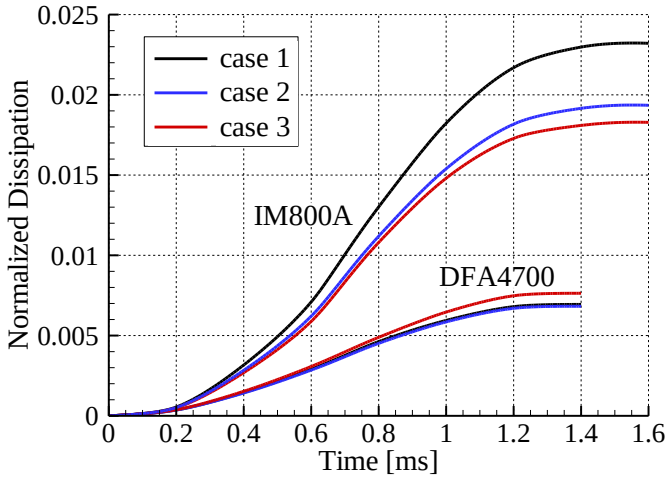

Fig.3–20: For values of material parameters corresponding to cases 1, 2 and 3, the normalized total energy $\widetilde{E}^{\text{visc,ve}}$ due to viscous deformations as function of time for the impact of PMMA/adhesive/PC plates with either DFA4700 or IM800A as adhesive.

The curves in Fig.3–20 are close to each other for the DFA4700 while for the IM800A the black curve is quantitatively different from the other two (20% difference at the final time). It follows from Eq. (3–30) that the energy dissipated due to viscous effects is proportional to $\sum_{m=1}^{M}G_m\beta_m$. Thus even though $\sum_{m=1}^{M}G_m$ is larger in case 3 as compared to that in the other two cases, it does not imply that $\sum_{m=1}^{M}G_m\beta_m$ is also larger. The decrease in the relaxation times β_m is so large that it more than compensates for the increase in the value of G_m's and energy dissipated decreases. This explains why the IM800A with the set of material parameters for case 3 has less energy dissipated due to viscous deformations than that for values of material parameters for case 1. While the total viscoelastic contribution to the response is more important in case 3 the reduction by several orders of magnitude of some decay constants β_m results in a

decrease in the energy dissipated. We note that the curves corresponding to the DFA4700 adhesive are below those corresponding to the IM800A adhesive which is related to the higher stiffness of the DFA4700 material and the consequent lower strains.

3.7 Conclusions

We have considered a simple constitutive equation for finite deformations of viscoelastic adhesives at different strain rates. For uniaxial tensile and compressive deformations at constant engineering axial strain rates, equations for the true axial stress have been derived as functions of the axial stretch and the axial stretch rate. Experimental data for uniaxial tests performed at constant engineering strain rates has been used to find values of material parameters for two adhesives, the DFA4700 and the more compliant IM800A. It is shown that depending upon the data used for monotonic loading, one cycle of loading and unloading, and two cycles of loading and unloading, values of material parameters are quite different. The tangent modulus at given values of the axial stretch and the axial stretch rate depends upon the data used to find values of material parameters. Thus even for uniaxial deformations one cannot correctly predict the experimental data not included in finding optimal values of the material parameters, and that improving the agreement with the first complete deformation cycle does not imply that the agreement with the second cycle is also improved. The validity of the constitutive relations for 3-dimensional deformations of the adhesive cannot be ascertained due to the nonexistence of the test data in the open literature. Values of the tangent modulus in simple shear deformations have been plotted as functions of the shear strain and the shear strain rate.

The constitutive equation has been implemented in the commercial finite element software LS-DYNA and used to analyze transient deformations of a laminated plate impacted at low velocity by a rigid hemi-spherical nosed impactor. We found that the energy dissipated by viscous deformations of the adhesive interlayers decreased when more deformation cycles were included to find values of material parameters for the adhesive materials. However, the energy dissipated due to viscous deformations of the adhesive is miniscule relative to the kinetic energy of the impactor and the energy dissipated due to plastic deformations of the PC layer and cracking of the PMMA layer. Furthermore, it is found that plastic deformations of the PC layer, the fracture of the PMMA layer and the total energy dissipated are not sensitive to the values of material parameters used for the interlayer for the impact problem studied. This is due to the fact that using larger set of test data for finding values of the material parameters for the adhesive significantly affected their predicted low strain-rate response without impacting much their high strain-rate response.

3.8 Acknowledgments

This research was sponsored by the Army Research Laboratory and was accomplished under Cooperative Agreement Number W911NF-06-2-0014. The views and conclusions contained in this document are those of the authors and should not be interpreted as representing the official policies, either expressed or implied, of the Army Research Laboratory or the U.S. Government. The U.S. Government is authorized to reproduce and distribute reprints for Government purposes notwithstanding any copyright notation hereon.

Appendix B

B.1 Constitutive Relation for Viscoelastic Materials

We assume that the deformation gradient $\mathbf{F}$ and the strain-rate tensor $\mathbf{D}$ are given with respect to the global rectangular Cartesian coordinates axes.

In order to determine the contribution $\boldsymbol{\sigma}^{\text{nlel}}$ to the total Cauchy stress tensor $\boldsymbol{\sigma}$ we first find the eigensystem (i.e., eigenvectors $\{\mathbf{b}_i\}_{i=1,2,3}$ and eigenvalues $\{\beta_i\}_{i=1,2,3}$) of the left Cauchy-Green tensor $\mathbf{B}$:

$$\mathbf{B} = \mathbf{F}\cdot\mathbf{F}^{\mathrm{T}} = \sum_{i=1}^{3} \eta_i \left|\mathbf{b}_i\right\rangle\left\langle\mathbf{b}_i\right| \tag{B–1}$$

where $\left|\mathbf{b}_i\right\rangle\left\langle\mathbf{b}_j\right|$ denotes the tensor product between vectors $\mathbf{b}_i$ and $\mathbf{b}_j$. The principal stretches $\{\lambda_i\}_{i=1,2,3}$ are related to the eigenvalues $\{\beta_i\}_{i=1,2,3}$ by $\lambda_i = \sqrt{\beta_i}$, i=1, 2, 3. The Cauchy stress for the nonlinear elastic deformations can thus be written as [23]

$$\boldsymbol{\sigma}^{\text{nlel}} = \frac{1}{J}\sum_{i=1}^{3}\lambda_i\frac{\partial W}{\partial\lambda_i}\left|\mathbf{b}_i\right\rangle\left\langle\mathbf{b}_i\right| = \frac{1}{\lambda_1\lambda_2\lambda_3}\sum_{i=1}^{3}\sum_{n=1}^{N}\mu_n\left[\tilde{\lambda}_i^{\alpha_n} - \frac{1}{3}\left(\tilde{\lambda}_1^{\alpha_n} + \tilde{\lambda}_2^{\alpha_n} + \tilde{\lambda}_3^{\alpha_n}\right)\right]\left|\mathbf{b}_i\right\rangle\left\langle\mathbf{b}_i\right| \tag{B–2}$$

where $\tilde{\lambda}_i = \lambda_i \big/ \left(\lambda_1\lambda_2\lambda_3\right)^{1/3}$.

The Green-Naghdi stress rate requires that the rotation matrix $\mathbf{R}$ in the polar decomposition of the deformation gradient $\mathbf{F}$ be known. It is found from the relation

$$\mathbf{R} = \left(\sum_{i=1}^{3}\frac{1}{\lambda_i}\left|\mathbf{b}_i\right\rangle\left\langle\mathbf{b}_i\right|\right)\cdot\mathbf{F} \tag{B–3}$$

Thus the constitutive relation (5) for the viscoelastic contribution can be written as

$$\frac{d}{dt}\left[\mathbf{R}^{\mathrm{T}}\cdot\boldsymbol{\sigma}_m^{\text{ve}}\cdot\mathbf{R}\right] = 2G_m\mathbf{R}^{\mathrm{T}}\cdot\mathbf{D}^{\text{dev}}\cdot\mathbf{R} - \beta_m\mathbf{R}^{\mathrm{T}}\cdot\boldsymbol{\sigma}_m^{\text{ve}}\cdot\mathbf{R} \tag{B–4}$$

Introducing $\hat{\boldsymbol{\sigma}}_m^{\text{ve}} = \mathbf{R}^{\mathrm{T}}\cdot\boldsymbol{\sigma}_m^{\text{ve}}\cdot\mathbf{R}$ and $\hat{\mathbf{D}}^{\text{dev}} = \mathbf{R}^{\mathrm{T}}\cdot\mathbf{D}^{\text{dev}}\cdot\mathbf{R}$, the contribution of the m^{th} term of the Prony series $\boldsymbol{\sigma}_m^{\text{ve}}$ to the total Cauchy stress tensor can be incrementally updated according to

$$\boldsymbol{\sigma}_m^{\text{ve}}\Big|_{t+\Delta t} = \left(\mathbf{R}\big|_{t+\Delta t}\right)\cdot\left(\hat{\boldsymbol{\sigma}}_m^{\text{ve}}\Big|_{t+\Delta t}\right)\cdot\left(\mathbf{R}\big|_{t+\Delta t}\right)^{\mathrm{T}} \quad , \quad \hat{\boldsymbol{\sigma}}_m^{\text{ve}}\Big|_{t+\Delta t} = \hat{\boldsymbol{\sigma}}_m^{\text{ve}}\Big|_{t} + \left(2G_m\left(\hat{\mathbf{D}}^{\text{dev}}\Big|_{t+\Delta t}\right) - \beta_m\left(\hat{\boldsymbol{\sigma}}_m^{\text{ve}}\Big|_{t}\right)\right)\Delta t \tag{B–5}$$

In order to find the pressure for an incompressible material, the volume change is penalized by adding a contribution derived from the strain energy density function $W^{\text{vol}} = K\big(J - 1 - \ln(J)\big)$ which results in adding the contribution $\boldsymbol{\sigma}^{\text{vol}}$ to the total Cauchy stress of the material where

$$\boldsymbol{\sigma}^{\text{vol}} = K\left(1 - \frac{1}{J}\right)\mathbf{I} = K\left(1 - \frac{1}{\lambda_1\lambda_2\lambda_3}\right)\mathbf{I} \tag{B–6}$$

In equation (35) $\mathbf{I}$ is the identity tensor, and the bulk modulus K is given by

$$K = \frac{2(1+\nu)}{3(1-2\nu)}\left[\frac{1}{2}\sum_{n=1}^{N}\mu_n\alpha_n + \sum_{m=1}^{M}G_m\right] \tag{B–7}$$

where ν is Poisson's ratio of the material at zero strain.

B.2 Viscous Dissipation

We additively decompose the deviatoric strain-rate tensor into elastic and viscous parts:

$$\mathbf{D}^{\text{dev}} = \mathbf{D}_m^{\text{el}} + \mathbf{D}_m^{\text{visc}} \tag{B–8}$$

The constitutive relation (5) of the viscoelastic contribution can then be rewritten as

$$\overset{\bullet}{\boldsymbol{\sigma}}_m^{\text{ve}} = 2G_m\mathbf{D}^{\text{dev}} - \beta_m\boldsymbol{\sigma}_m^{\text{ve}} = 2G_m\left(\mathbf{D}^{\text{dev}} - \frac{\beta_m}{2G_m}\boldsymbol{\sigma}_m^{\text{ve}}\right) = 2G_m\mathbf{D}_m^{\text{el}} \tag{B–9}$$

where we have set

$$\mathbf{D}_m^{\text{visc}} = \frac{\beta_m}{2G_m}\boldsymbol{\sigma}_m^{\text{ve}} \tag{B–10}$$

which is valid for both incompressible and nearly incompressible materials. For an incompressible material, $\mathbf{D}^{\text{dev}} = \mathbf{D}$.

For an incompressible material the rate of internal energy (work done to deform the material) per unit volume in the reference configuration equals $J\,\boldsymbol{\sigma}:\mathbf{D} = \boldsymbol{\sigma}:\mathbf{D}^{\text{dev}}$ and

$$\boldsymbol{\sigma}:\mathbf{D}^{\text{dev}} = \left(\boldsymbol{\sigma}^{\text{nlel}} + \sum_{m=1}^{M}\boldsymbol{\sigma}_m^{\text{ve}} - p\,\mathbf{I}\right):\mathbf{D}^{\text{dev}} \tag{B–11a}$$

$$= \dot{W} + \sum_{m=1}^{M}\boldsymbol{\sigma}_m^{\text{ve}}:\mathbf{D}_m^{\text{el}} + \sum_{m=1}^{M}\boldsymbol{\sigma}_m^{\text{ve}}:\mathbf{D}_m^{\text{visc}} - p\,\text{tr}(\mathbf{D}^{\text{dev}}) \tag{B–11b}$$

Since $\text{tr}(\mathbf{D}^{\text{dev}}) = 0$, Eq. (B–11b) can be rewritten as

$$\boldsymbol{\sigma}:\mathbf{D}^{\text{dev}} = \dot{W} + \sum_{m=1}^{M}\boldsymbol{\sigma}_m^{\text{ve}}:\mathbf{D}_m^{\text{el}} + \sum_{m=1}^{M}\boldsymbol{\sigma}_m^{\text{ve}}:\mathbf{D}_m^{\text{visc}} \quad \text{(B–12a)}$$

$$= \dot{W} + \dot{E}^{\text{el,ve}} + \dot{E}^{\text{visc,ve}} \quad \text{(B–12b)}$$

$\dot{W}$ is the rate of energy of the nonlinear elastic contribution, $\dot{E}^{\text{el,ve}}$ is the rate of elastic energy of the viscoelastic contribution and $\dot{E}^{\text{visc,ve}}$ is the rate of energy dissipated due to viscous deformations. We can use Eq. (B–10) to obtain the following expression for the energy per unit volume dissipated due to viscous deformations.

$$E^{\text{visc,ve}} = \int_t \left[\sum_{m=1}^{M} \left(\frac{\beta_m}{2G_m} \boldsymbol{\sigma}_m^{\text{ve}} : \boldsymbol{\sigma}_m^{\text{ve}} \right) dt \right] \quad \text{(B–13)}$$

For a nearly incompressible material, the rate of internal energy (work done to deform the material) per unit volume in the reference configuration is $J\,\boldsymbol{\sigma}:\mathbf{D}$ and

$$J\,\boldsymbol{\sigma}:\mathbf{D} = J\left(\boldsymbol{\sigma}^{\text{nlel}} + \boldsymbol{\sigma}^{\text{vol}} + \sum_{m=1}^{M}\boldsymbol{\sigma}_m^{\text{ve}}\right):\mathbf{D} \quad \text{(B–14a)}$$

$$= \dot{W} + \dot{W}^{\text{vol}} + J\sum_{m=1}^{M}\boldsymbol{\sigma}_m^{\text{ve}}:\mathbf{D}_m^{\text{el}} + J\sum_{m=1}^{M}\boldsymbol{\sigma}_m^{\text{ve}}:\mathbf{D}_m^{\text{visc}} + J\sum_{m=1}^{M}\boldsymbol{\sigma}_m^{\text{ve}}:\left(\mathbf{D}-\mathbf{D}^{\text{dev}}\right) \quad \text{(B–14b)}$$

In order to prove that $\boldsymbol{\sigma}_m^{\text{ve}}:\left(\mathbf{D}-\mathbf{D}^{\text{dev}}\right)=0$, we start with $\mathbf{D}-\mathbf{D}^{\text{dev}} = \frac{1}{3}\text{tr}\left(\mathbf{D}\right)\mathbf{I}$, and simplify Eq. (B–14b) by noticing that

$$\boldsymbol{\sigma}_m^{\text{ve}}:\left(\mathbf{D}-\mathbf{D}^{\text{dev}}\right) = \text{tr}\left(\boldsymbol{\sigma}_m^{\text{ve}}\cdot\frac{1}{3}\text{tr}\left(\mathbf{D}\right)\mathbf{I}\right) = \frac{1}{3}\text{tr}\left(\boldsymbol{\sigma}_m^{\text{ve}}\right)\text{tr}\left(\mathbf{D}\right) \quad \text{(B–15)}$$

We apply the trace operator to the constitutive relation (B–9) which uses the Green-Naghdi stress-rate and obtain

$$\text{tr}\left(\mathbf{R}\cdot\frac{d}{dt}\left[\mathbf{R}^{\text{T}}\cdot\boldsymbol{\sigma}_m^{\text{ve}}\cdot\mathbf{R}\right]\cdot\mathbf{R}^{\text{T}}\right) = 2G_m\text{tr}\left(\mathbf{D}^{\text{dev}}\right) - \beta_m\text{tr}\left(\boldsymbol{\sigma}_m^{\text{ve}}\right) \quad \text{(B–16)}$$

Eq. (B–16b) can be simplified and used with $\boldsymbol{\sigma}_m^{\text{ve}}\big|_{t=0} = \mathbf{0}$ to give the differential equation and the initial condition:

$$\frac{d}{dt}\left[\text{tr}\left(\boldsymbol{\sigma}_m^{\text{ve}}\right)\right] = -\beta_m\text{tr}\left(\boldsymbol{\sigma}_m^{\text{ve}}\right) \quad , \quad \text{tr}\left(\boldsymbol{\sigma}_m^{\text{ve}}\right)\big|_{t=0} = 0 \quad \text{(B–17)}$$

It follows from equations(B–17) that $\text{tr}\left(\boldsymbol{\sigma}_m^{\text{ve}}\right)=0$ at all times which leads to the simplified expression:

$$J\,\boldsymbol{\sigma}:\mathbf{D} \;=\; \dot{W} \;+\; \dot{W}^{\mathrm{vol}} \;+\; J\sum_{m=1}^{M}\boldsymbol{\sigma}_m^{\mathrm{ve}}:\mathbf{D}_m^{\mathrm{el}} \;+\; J\sum_{m=1}^{M}\boldsymbol{\sigma}_m^{\mathrm{ve}}:\mathbf{D}_m^{\mathrm{visc}} \qquad \text{(B–18a)}$$

$$= \dot{W} + \dot{W}^{\mathrm{vol}} + \dot{E}^{\mathrm{el,ve}} + \dot{E}^{\mathrm{visc,ve}} \qquad \text{(B–18b)}$$

Here $\dot{W}$ is the rate of elastic energy of the deviatoric nonlinear elastic contribution, $\dot{W}^{\mathrm{vol}}$ is the rate of elastic energy due to the volumetric strain, $\dot{E}^{\mathrm{el,ve}}$ is the rate of elastic energy of the viscoelastic contribution and $\dot{E}^{\mathrm{visc,ve}}$ is the rate of energy dissipated by viscous deformations. Using Eq. (B–10)we get the following expression for the energy per unit undeformed volume dissipated due to viscous deformations:

$$E^{\mathrm{visc,ve}} = \int_t \left[J\sum_{m=1}^{M}\left(\frac{\beta_m}{2G_m}\boldsymbol{\sigma}_m^{\mathrm{ve}}:\boldsymbol{\sigma}_m^{\mathrm{ve}} \right) dt \right] \qquad \text{(B–19)}$$

B.3 Stress-Strain Relations for Cyclic Tensile Tests

We recall the notations: $\mathbf{F}$ is the deformation gradient, λ the axial stretch, λ_{T} the transverse stretch, $\varepsilon^{\mathrm{True}}$ the true axial strain, $\varepsilon^{\mathrm{Eng}}$ the engineering axial strain, $\dot{\varepsilon}^{\mathrm{Eng}}$ the engineering axial strain rate of the test, and λ_I^{p}, $\lambda_{II}^{\mathrm{p}}$, $\lambda_{III}^{\mathrm{p}}$ and $\lambda_{IV}^{\mathrm{p}}$ are the peak axial stretches reached during cycles 1, 2, 3 and 4, respectively. We will use σ^{True} for the true (or Cauchy) axial stress and σ^{Eng} for the engineering axial stress.

B.3.1 Constitutive Relations for Incompressible Material under Uniaxial Loading

Since test data is available for large strains we need to distinguish between engineering and true (or logarithmic) strains and strain rates. The engineering strain $\varepsilon^{\mathrm{Eng}}$ and the engineering stress σ^{Eng} are related to $\varepsilon^{\mathrm{True}}$ and σ^{True} by

$$\varepsilon^{\mathrm{True}} = \ln\left(1+\varepsilon^{\mathrm{Eng}}\right) = \ln(\lambda) \quad , \quad \sigma^{\mathrm{True}} = \left(1+\varepsilon^{\mathrm{Eng}}\right)\sigma^{\mathrm{Eng}} = \lambda\sigma^{\mathrm{Eng}} \qquad \text{(B–20)}$$

With a proper choice of the coordinate system, we have

$$\mathbf{F} = \begin{pmatrix} \lambda & & \\ & \lambda_{\mathrm{T}} & \\ & & \lambda_{\mathrm{T}} \end{pmatrix} \qquad \text{(B–21)}$$

and since its determinant is one we have $\lambda_{\mathrm{T}} = \lambda^{-1/2}$. It is clear from Eq.(B–21) that the rotation matrix in the polar decomposition of $\mathbf{F}$ is the identity matrix at all times. Therefore, in the fixed frame of the experiment, the constitutive equations for the viscoelastic contribution can be simplified to give

$$\frac{d\boldsymbol{\sigma}_m^{\text{ve}}}{dt} = 2G_m\mathbf{D} - \beta_m\boldsymbol{\sigma}_m^{\text{ve}} \quad , \quad \boldsymbol{\sigma}_m^{\text{ve}}\Big|_{t=0} = 0 \tag{B–22}$$

where we have used $\mathbf{D} = \mathbf{D}^{\text{dev}}$. The solution of Eq. (B–22) is the convolution integral

$$\boldsymbol{\sigma}_m^{\text{ve}} = 2G_m \int_{\tau=0}^{t} e^{-\beta_m(t-\tau)}\mathbf{D}(\tau)d\tau \tag{B–23}$$

where the strain-rate tensor $\mathbf{D}$ is given by

$$\mathbf{D} = \frac{1}{2}\left(\dot{\mathbf{F}}\mathbf{F}^{-1} + \mathbf{F}^{-\text{T}}\dot{\mathbf{F}}^{\text{T}}\right) = \frac{\dot{\lambda}}{\lambda}\begin{pmatrix} 1 & & \\ & -1/2 & \\ & & -1/2 \end{pmatrix} \tag{B–24}$$

The quasi-static or elastic contribution to the material response is:

$$\boldsymbol{\sigma}^{\text{nlel}} = \sum_{n=1}^{N}\mu_n\begin{pmatrix} \lambda^{\alpha_n} & & \\ & \lambda_{\text{T}}^{\alpha_n} & \\ & & \lambda_{\text{T}}^{\alpha_n} \end{pmatrix} = \sum_{n=1}^{N}\mu_n\begin{pmatrix} \lambda^{\alpha_n} & & \\ & \lambda^{-\alpha_n/2} & \\ & & \lambda^{-\alpha_n/2} \end{pmatrix} \tag{B–25}$$

Using equations (B–23) and (B–25) we obtain the stress-strain relation

$$\boldsymbol{\sigma} = -p\mathbf{I} + \sum_{n=1}^{N}\mu_n\begin{pmatrix} \lambda^{\alpha_n} & & \\ & \lambda^{-\alpha_n/2} & \\ & & \lambda^{-\alpha_n/2} \end{pmatrix} + \left[\sum_{m=1}^{M} 2G_m \int_{\tau=0}^{t} e^{-\beta_m(t-\tau)}\frac{\dot{\lambda}}{\lambda}\Big|_{\tau} d\tau\right]\begin{pmatrix} 1 & & \\ & -1/2 & \\ & & -1/2 \end{pmatrix} \tag{B–26}$$

To find the pressure p we use the condition that the lateral faces of the body are traction-free, i.e., $\sigma_{22}(=\sigma_{33}) = 0$, and therefore

$$p = \sum_{n=1}^{N}\mu_n\lambda^{-\alpha_n/2} - \frac{1}{2}\sum_{m=1}^{M} 2G_m \int_{\tau=0}^{t} e^{-\beta_m(t-\tau)}\frac{\dot{\lambda}}{\lambda}\Big|_{\tau} d\tau \tag{B–27}$$

Thus the axial stress $\sigma^{\text{True}} = \sigma_{11}$ is given by

$$\sigma^{\text{True}} = \sum_{n=1}^{N}\mu_n\left(\lambda^{\alpha_n} - \lambda^{-\alpha_n/2}\right) + \sum_{m=1}^{M} 3G_m \int_{\tau=0}^{t} e^{-\beta_m(t-\tau)}\frac{\dot{\lambda}}{\lambda}\Big|_{\tau} d\tau \tag{B–28}$$

B.3.2 Cauchy Stress as Function of Axial Stretch for Deformations at Constant Engineering Strain Rate

We use here the convention that $\dot{\varepsilon}^{\mathrm{Eng}}$ is positive for the cyclic tensile tests in both loading and unloading. It represents the global engineering strain rate of the test and not the actual strain rate at which the material deforms. For the uniaxial compression test $\dot{\varepsilon}^{\mathrm{Eng}}$ is negative. We will now give recursive relations that can be used to find the axial stress-axial stretch relations for an arbitrary number of cycles.

We introduce the exponential integral function Ei defined by $\mathrm{Ei}(x) = -\int_{\xi=-x}^{+\infty} \frac{e^{-\xi}}{\xi} d\xi$ where the integral is understood as the Cauchy principal value due to the singularity of the integrand at 0.

- 1st cycle, loading

During the loading part of the first cycle, we have $\dot{\lambda} = \dot{\varepsilon}^{\mathrm{Eng}}$ (constant), and $\lambda = 1 + t\dot{\varepsilon}^{\mathrm{Eng}}$. Thus the convolution integral in Eq. (B–28) can be simplified to

$$\sigma_{I,\mathrm{load}}^{\mathrm{True}}(\lambda) = \sum_{n=1}^{N} \mu_n \left(\lambda^{\alpha_n} - \lambda^{-\alpha_n/2}\right) + \sum_{m=1}^{M} 3G_m \int_{\tau=0}^{t} e^{-\beta_m (t-\tau)} \frac{\dot{\varepsilon}^{\mathrm{Eng}}}{1+\tau\,\dot{\varepsilon}^{\mathrm{Eng}}} d\tau \tag{B–29}$$

The time and the axial stretch are related by $t = (\lambda - 1)/\dot{\varepsilon}^{\mathrm{Eng}}$, and we introduce for later use the function

$$I_{\mathrm{load}}\left(\dot{\varepsilon}^{\mathrm{Eng}}, G, \beta, \lambda\right) = 3G \int_{\tau=0}^{(\lambda-1)/\dot{\varepsilon}^{\mathrm{Eng}}} \exp\left(-\beta\left(\frac{\lambda-1}{\dot{\varepsilon}^{\mathrm{Eng}}} - \tau\right)\right) \frac{\dot{\varepsilon}^{\mathrm{Eng}}}{1+\tau\,\dot{\varepsilon}^{\mathrm{Eng}}} d\tau \tag{B–30a}$$

$$= 3G \exp\left(-\frac{\beta\lambda}{\dot{\varepsilon}^{Eng}}\right)\left[\mathrm{Ei}\left(\frac{\beta\lambda}{\dot{\varepsilon}^{Eng}}\right) - \mathrm{Ei}\left(\frac{\beta}{\dot{\varepsilon}^{Eng}}\right)\right] \tag{B–30b}$$

Thus the axial stress as a function of the axial stretch is given by

$$\sigma_{I,\mathrm{load}}^{\mathrm{True}}(\lambda) = \sum_{n=1}^{N} \mu_n \left(\lambda^{\alpha_n} - \lambda^{-\alpha_n/2}\right) + \sum_{m=1}^{M} I_{\mathrm{load}}\left(\dot{\varepsilon}^{\mathrm{Eng}}, G_m, \beta_m, \lambda\right) \tag{B–31a}$$

$$= \sum_{n=1}^{N} \mu_n \left(\lambda^{\alpha_n} - \lambda^{-\alpha_n/2}\right) + \sum_{m=1}^{M} 3G_m \exp\left(-\frac{\beta_m\lambda}{\dot{\varepsilon}^{Eng}}\right)\left[\mathrm{Ei}\left(\frac{\beta_m\lambda}{\dot{\varepsilon}^{Eng}}\right) - \mathrm{Ei}\left(\frac{\beta_m}{\dot{\varepsilon}^{Eng}}\right)\right] \tag{B–31b}$$

which does not explicitly depend upon time.

- 1st cycle, unloading

The end time of the loading phase of the first cycle is given by $t_I^{\mathrm{p}} = (\lambda_I^{\mathrm{p}} - 1)/\dot{\varepsilon}^{\mathrm{Eng}}$. To obtain the expression for the stress in the unloading phase, we first note that

$$\int_{\tau=0}^{t} e^{-\beta_m(t-\tau)} \frac{\dot{\lambda}}{\lambda}\bigg|_{\tau} d\tau = \int_{\tau=0}^{t_I^{\mathrm{p}}} e^{-\beta_m(t-\tau)} \frac{\dot{\lambda}}{\lambda}\bigg|_{\tau} d\tau + \int_{\tau=t_I^{\mathrm{p}}}^{t} e^{-\beta_m(t-\tau)} \frac{\dot{\lambda}}{\lambda}\bigg|_{\tau} d\tau \quad \text{(B–32a)}$$

$$= e^{-\beta_m\left(t-t_I^{\mathrm{p}}\right)} \int_{\tau=0}^{t_I^{\mathrm{p}}} e^{-\beta_m\left(t_I^{\mathrm{p}}-\tau\right)} \frac{\dot{\lambda}}{\lambda}\bigg|_{\tau} d\tau + \int_{\xi=0}^{t-t_I^{\mathrm{p}}} e^{-\beta_m\left(\left(t-t_I^{\mathrm{p}}\right)-\xi\right)} \frac{\dot{\lambda}}{\lambda}\bigg|_{t_I^{\mathrm{p}}+\xi} d\tau \quad \text{(B–32b)}$$

Between t_I^{p} and t (unloading) we have $\dot{\lambda} = -\dot{\varepsilon}^{\mathrm{Eng}}$ and $\lambda = \lambda_I^{\mathrm{p}} - (\xi - t_I^{\mathrm{p}})\dot{\varepsilon}^{\mathrm{Eng}}$, which leads to

$$\int_{\xi=0}^{t-t_I^{\mathrm{p}}} e^{-\beta_m\left(\left(t-t_I^{\mathrm{p}}\right)-\xi\right)} \frac{\dot{\lambda}}{\lambda}\bigg|_{t_I^{\mathrm{p}}+\xi} d\tau = \int_{\xi=0}^{t-t_I^{\mathrm{p}}} e^{-\beta_m\left(\left(t-t_I^{\mathrm{p}}\right)-\xi\right)} \frac{-\dot{\varepsilon}^{\mathrm{Eng}}}{\lambda_I^{\mathrm{p}} - \xi\ \dot{\varepsilon}^{\mathrm{Eng}}} d\tau \quad \text{(B–33)}$$

In terms of the function

$$I_{\mathrm{unload}}\left(\dot{\varepsilon}^{\mathrm{Eng}}, G, \beta, \lambda_0, \lambda\right) = 3G \int_{\xi=0}^{(\lambda_0-\lambda)/\dot{\varepsilon}^{\mathrm{Eng}}} \exp\left(-\beta\left(\frac{\lambda_0-\lambda}{\dot{\varepsilon}^{\mathrm{Eng}}} - \xi\right)\right) \frac{-\dot{\varepsilon}^{\mathrm{Eng}}}{\lambda_0 - \xi\ \dot{\varepsilon}^{\mathrm{Eng}}} d\tau \quad \text{(B–34a)}$$

$$= 3G \exp\left(\frac{\beta\lambda}{\dot{\varepsilon}^{Eng}}\right)\left[\mathrm{Ei}\left(-\frac{\beta\lambda}{\dot{\varepsilon}^{Eng}}\right) - \mathrm{Ei}\left(-\frac{\beta\lambda_0}{\dot{\varepsilon}^{Eng}}\right)\right] \quad \text{(B–34b)}$$

,

the stress as a function of the stretch for the unloading phase of the first cycle is given by

$$\sigma_{I,\mathrm{unload}}^{\mathrm{True}}(\lambda) = \sum_{n=1}^{N} \mu_n\left(\lambda^{\alpha_n} - \lambda^{-\alpha_n/2}\right) \quad \text{(B–35a)}$$

$$+ \sum_{m=1}^{M} \exp\left(-\beta_m \frac{\lambda_I^{\mathrm{p}} - \lambda}{\dot{\varepsilon}^{\mathrm{Eng}}}\right) I_{\mathrm{load}}\left(\dot{\varepsilon}^{\mathrm{Eng}}, G_m, \beta_m, \lambda_I^{\mathrm{p}}\right) + \sum_{m=1}^{M} I_{\mathrm{unload}}\left(\dot{\varepsilon}^{\mathrm{Eng}}, G_m, \beta_m, \lambda_I^{\mathrm{p}}, \lambda\right) \quad \text{(B–35b)}$$

Substitution for I_{load} from Eq. (B–30b) and for I_{unload} from Eq. (B–34b) into Eq. (B–35b) gives

$$\begin{aligned}\sigma_{I,\mathrm{unload}}^{\mathrm{True}}(\lambda) = & \sum_{n=1}^{N} \mu_n\left(\lambda^{\alpha_n} - \lambda^{-\alpha_n/2}\right) \\ & + \sum_{m=1}^{M} 3G_m \exp\left(-\beta_m \frac{2\lambda_I^{\mathrm{p}} - \lambda}{\dot{\varepsilon}^{\mathrm{Eng}}}\right)\left[\mathrm{Ei}\left(\frac{\beta_m\lambda_I^{\mathrm{p}}}{\dot{\varepsilon}^{Eng}}\right) - \mathrm{Ei}\left(\frac{\beta_m}{\dot{\varepsilon}^{Eng}}\right)\right] \\ & + \sum_{m=1}^{M} 3G_m \exp\left(\frac{\beta_m\lambda}{\dot{\varepsilon}^{Eng}}\right)\left[\mathrm{Ei}\left(-\frac{\beta_m\lambda}{\dot{\varepsilon}^{Eng}}\right) - \mathrm{Ei}\left(-\frac{\beta_m\lambda_I^{\mathrm{p}}}{\dot{\varepsilon}^{Eng}}\right)\right]\end{aligned} \quad \text{(B–36)}$$

where there is no explicit dependence upon the time.

- Results for other cycles

One can obtain expression for the axial stress-axial stretch during subsequent cycles by using the integral splitting method in Eq. (B–32a,b) and functions I_{load} and I_{unload}. That is, the stress during a loading (or unloading) phase of a cycle is the sum of the viscoelastic stress derived for the first loading (or unloading) cycle, and of the viscoelastic stress existing at the beginning of the current phase with an exponential decay. The following expressions give the axial true stress as a function of the axial stretch without explicit dependence upon time (the stretch is a function of time). In order to show how they can be derived their expressions have not been fully simplified.

$$\begin{aligned}\sigma^{\text{True}}_{II,\text{load}}(\lambda) &= \sum_{n=1}^{N}\mu_n\left(\lambda^{\alpha_n}-\lambda^{-\alpha_n/2}\right)\\ &+\sum_{m=1}^{M}\exp\left(-\beta_m\left(\frac{\lambda_I^{\text{p}}-1}{\dot{\varepsilon}^{\text{Eng}}}+\Delta t+\frac{\lambda-1}{\dot{\varepsilon}^{\text{Eng}}}\right)\right)I_{\text{load}}\left(\dot{\varepsilon}^{\text{Eng}},G_m,\beta_m,\lambda_I^{\text{p}}\right)\\ &+\sum_{m=1}^{M}\exp\left(-\beta_m\left(\Delta t+\frac{\lambda-1}{\dot{\varepsilon}^{\text{Eng}}}\right)\right)I_{\text{unload}}\left(\dot{\varepsilon}^{\text{Eng}},G_m,\beta_m,\lambda_I^{\text{p}},1\right)\\ &+\sum_{m=1}^{M}I_{\text{load}}\left(\dot{\varepsilon}^{\text{Eng}},G_m,\beta_m,\lambda\right)\end{aligned} \tag{B–37}$$

$$\begin{aligned}\sigma^{\text{True}}_{II,\text{unload}}(\lambda) &= \sum_{n=1}^{N}\mu_n\left(\lambda^{\alpha_n}-\lambda^{-\alpha_n/2}\right)\\ &+\sum_{m=1}^{M}\exp\left(-\beta_m\left(\frac{\lambda_I^{\text{p}}-1}{\dot{\varepsilon}^{\text{Eng}}}+\Delta t+\frac{\lambda_{II}^{\text{p}}-1}{\dot{\varepsilon}^{\text{Eng}}}+\frac{\lambda_{II}^{\text{p}}-\lambda}{\dot{\varepsilon}^{\text{Eng}}}\right)\right)I_{\text{load}}\left(\dot{\varepsilon}^{\text{Eng}},G_m,\beta_m,\lambda_I^{\text{p}}\right)\\ &+\sum_{m=1}^{M}\exp\left(-\beta_m\left(\Delta t+\frac{\lambda_{II}^{\text{p}}-1}{\dot{\varepsilon}^{\text{Eng}}}+\frac{\lambda_{II}^{\text{p}}-\lambda}{\dot{\varepsilon}^{\text{Eng}}}\right)\right)I_{\text{unload}}\left(\dot{\varepsilon}^{\text{Eng}},G_m,\beta_m,\lambda_I^{\text{p}},1\right)\\ &+\sum_{m=1}^{M}\exp\left(-\beta_m\frac{\lambda_{II}^{\text{p}}-\lambda}{\dot{\varepsilon}^{\text{Eng}}}\right)I_{\text{load}}\left(\dot{\varepsilon}^{\text{Eng}},G_m,\beta_m,\lambda_{II}^{\text{p}}\right)\\ &+\sum_{m=1}^{M}I_{\text{unload}}\left(\dot{\varepsilon}^{\text{Eng}},G_m,\beta_m,\lambda_{II}^{\text{p}},\lambda\right)\end{aligned} \tag{B–38}$$

$$
\begin{aligned}
\sigma_{III,\mathrm{load}}^{\mathrm{True}}(\lambda) = & \sum_{n=1}^{N} \mu_n \left(\lambda^{\alpha_n} - \lambda^{-\alpha_n/2}\right) \\
& + \sum_{m=1}^{M} \exp\left(-\beta_m \left(\frac{\lambda_I^{\mathrm{p}} - 1}{\dot{\varepsilon}^{\mathrm{Eng}}} + \Delta t + 2\frac{\lambda_{II}^{\mathrm{p}} - 1}{\dot{\varepsilon}^{\mathrm{Eng}}} + \Delta t + \frac{\lambda - 1}{\dot{\varepsilon}^{\mathrm{Eng}}}\right)\right) I_{\mathrm{load}}\left(\dot{\varepsilon}^{\mathrm{Eng}}, G_m, \beta_m, \lambda_I^{\mathrm{p}}\right) \\
& + \sum_{m=1}^{M} \exp\left(-\beta_m \left(\Delta t + 2\frac{\lambda_{II}^{\mathrm{p}} - 1}{\dot{\varepsilon}^{\mathrm{Eng}}} + \Delta t + \frac{\lambda - 1}{\dot{\varepsilon}^{\mathrm{Eng}}}\right)\right) I_{\mathrm{unload}}\left(\dot{\varepsilon}^{\mathrm{Eng}}, G_m, \beta_m, \lambda_I^{\mathrm{p}}, 1\right) \\
& + \sum_{m=1}^{M} \exp\left(-\beta_m \left(\frac{\lambda_{II}^{\mathrm{p}} - 1}{\dot{\varepsilon}^{\mathrm{Eng}}} + \Delta t + \frac{\lambda - 1}{\dot{\varepsilon}^{\mathrm{Eng}}}\right)\right) I_{\mathrm{load}}\left(\dot{\varepsilon}^{\mathrm{Eng}}, G_m, \beta_m, \lambda_{II}^{\mathrm{p}}\right) \\
& + \sum_{m=1}^{M} \exp\left(-\beta_m \left(\Delta t + \frac{\lambda - 1}{\dot{\varepsilon}^{\mathrm{Eng}}}\right)\right) I_{\mathrm{unload}}\left(\dot{\varepsilon}^{\mathrm{Eng}}, G_m, \beta_m, \lambda_{II}^{\mathrm{p}}, \lambda_{II}^{\mathrm{p}}\right) \\
& + \sum_{m=1}^{M} I_{\mathrm{load}}\left(\dot{\varepsilon}^{\mathrm{Eng}}, G_m, \beta_m, \lambda\right)
\end{aligned}
\tag{B–39}
$$

$$
\begin{aligned}
\sigma_{III,\mathrm{unload}}^{\mathrm{True}}(\lambda) = & \sum_{n=1}^{N} \mu_n \left(\lambda^{\alpha_n} - \lambda^{-\alpha_n/2}\right) \\
& + \sum_{m=1}^{M} \left[\exp\left(-\beta_m \left(\frac{\lambda_I^{\mathrm{p}} - 1}{\dot{\varepsilon}^{\mathrm{Eng}}} + \Delta t + 2\frac{\lambda_{II}^{\mathrm{p}} - 1}{\dot{\varepsilon}^{\mathrm{Eng}}} + \Delta t + \frac{\lambda_{III}^{\mathrm{p}} - 1}{\dot{\varepsilon}^{\mathrm{Eng}}} + \frac{\lambda_{III}^{\mathrm{p}} - \lambda}{\dot{\varepsilon}^{\mathrm{Eng}}}\right)\right) \right. \\
& \qquad \left. I_{\mathrm{load}}\left(\dot{\varepsilon}^{\mathrm{Eng}}, G_m, \beta_m, \lambda_I^{\mathrm{p}}\right) \right] \\
& + \sum_{m=1}^{M} \left[\exp\left(-\beta_m \left(\Delta t + 2\frac{\lambda_{II}^{\mathrm{p}} - 1}{\dot{\varepsilon}^{\mathrm{Eng}}} + \Delta t + \frac{\lambda_{III}^{\mathrm{p}} - 1}{\dot{\varepsilon}^{\mathrm{Eng}}} + \frac{\lambda_{III}^{\mathrm{p}} - \lambda}{\dot{\varepsilon}^{\mathrm{Eng}}}\right)\right) \right. \\
& \qquad \left. I_{\mathrm{unload}}\left(\dot{\varepsilon}^{\mathrm{Eng}}, G_m, \beta_m, \lambda_I^{\mathrm{p}}, 1\right) \right] \\
& + \sum_{m=1}^{M} \exp\left(-\beta_m \left(\frac{\lambda_{II}^{\mathrm{p}} - 1}{\dot{\varepsilon}^{\mathrm{Eng}}} + \Delta t + \frac{\lambda_{III}^{\mathrm{p}} - 1}{\dot{\varepsilon}^{\mathrm{Eng}}} + \frac{\lambda_{III}^{\mathrm{p}} - \lambda}{\dot{\varepsilon}^{\mathrm{Eng}}}\right)\right) I_{\mathrm{load}}\left(\dot{\varepsilon}^{\mathrm{Eng}}, G_m, \beta_m, \lambda_{II}^{\mathrm{p}}\right) \\
& + \sum_{m=1}^{M} \exp\left(-\beta_m \left(\Delta t + \frac{\lambda_{III}^{\mathrm{p}} - 1}{\dot{\varepsilon}^{\mathrm{Eng}}} + \frac{\lambda_{III}^{\mathrm{p}} - \lambda}{\dot{\varepsilon}^{\mathrm{Eng}}}\right)\right) I_{\mathrm{unload}}\left(\dot{\varepsilon}^{\mathrm{Eng}}, G_m, \beta_m, \lambda_{II}^{\mathrm{p}}, \lambda_{II}^{\mathrm{p}}\right) \\
& + \sum_{m=1}^{M} \exp\left(-\beta_m \frac{\lambda_{III}^{\mathrm{p}} - \lambda}{\dot{\varepsilon}^{\mathrm{Eng}}}\right) I_{\mathrm{load}}\left(\dot{\varepsilon}^{\mathrm{Eng}}, G_m, \beta_m, \lambda_{II}^{\mathrm{p}}\right) \\
& + \sum_{m=1}^{M} I_{\mathrm{unload}}\left(\dot{\varepsilon}^{\mathrm{Eng}}, G_m, \beta_m, \lambda_{III}^{\mathrm{p}}, \lambda\right)
\end{aligned}
\tag{B–40}
$$

$$
\begin{aligned}
\sigma_{IV,\mathrm{load}}^{\mathrm{True}}(\lambda) = & \sum_{n=1}^{N} \mu_n \left(\lambda^{\alpha_n} - \lambda^{-\alpha_n/2} \right) \\
& + \sum_{m=1}^{M} \Bigg[\exp\left(-\beta_m \left(\frac{\lambda_I^{\mathrm{p}} - 1}{\dot{\varepsilon}^{\mathrm{Eng}}} + \Delta t + 2\frac{\lambda_{II}^{\mathrm{p}} - 1}{\dot{\varepsilon}^{\mathrm{Eng}}} + \Delta t + 2\frac{\lambda_{III}^{\mathrm{p}} - 1}{\dot{\varepsilon}^{\mathrm{Eng}}} + \Delta t + \frac{\lambda - 1}{\dot{\varepsilon}^{\mathrm{Eng}}} \right) \right) \\
& \qquad I_{\mathrm{load}}\left(\dot{\varepsilon}^{\mathrm{Eng}}, G_m, \beta_m, \lambda_I^{\mathrm{p}} \right) \Bigg] \\
& + \sum_{m=1}^{M} \Bigg[\exp\left(-\beta_m \left(\Delta t + 2\frac{\lambda_{II}^{\mathrm{p}} - 1}{\dot{\varepsilon}^{\mathrm{Eng}}} + \Delta t + 2\frac{\lambda_{III}^{\mathrm{p}} - 1}{\dot{\varepsilon}^{\mathrm{Eng}}} + \Delta t + \frac{\lambda - 1}{\dot{\varepsilon}^{\mathrm{Eng}}} \right) \right) \\
& \qquad I_{\mathrm{unload}}\left(\dot{\varepsilon}^{\mathrm{Eng}}, G_m, \beta_m, \lambda_I^{\mathrm{p}}, 1 \right) \Bigg] \\
& + \sum_{m=1}^{M} \Bigg[\exp\left(-\beta_m \left(\frac{\lambda_{II}^{\mathrm{p}} - 1}{\dot{\varepsilon}^{\mathrm{Eng}}} + \Delta t + 2\frac{\lambda_{III}^{\mathrm{p}} - 1}{\dot{\varepsilon}^{\mathrm{Eng}}} + \Delta t + \frac{\lambda - 1}{\dot{\varepsilon}^{\mathrm{Eng}}} \right) \right) \\
& \qquad I_{\mathrm{load}}\left(\dot{\varepsilon}^{\mathrm{Eng}}, G_m, \beta_m, \lambda_{II}^{\mathrm{p}} \right) \Bigg] \\
& + \sum_{m=1}^{M} \exp\left(-\beta_m \left(\Delta t + 2\frac{\lambda_{III}^{\mathrm{p}} - 1}{\dot{\varepsilon}^{\mathrm{Eng}}} + \Delta t + \frac{\lambda - 1}{\dot{\varepsilon}^{\mathrm{Eng}}} \right) \right) I_{\mathrm{unload}}\left(\dot{\varepsilon}^{\mathrm{Eng}}, G_m, \beta_m, \lambda_{II}^{\mathrm{p}}, \lambda_{II}^{\mathrm{p}} \right) \\
& + \sum_{m=1}^{M} \exp\left(-\beta_m \left(\frac{\lambda_{III}^{\mathrm{p}} - 1}{\dot{\varepsilon}^{\mathrm{Eng}}} + \Delta t + \frac{\lambda - 1}{\dot{\varepsilon}^{\mathrm{Eng}}} \right) \right) I_{\mathrm{load}}\left(\dot{\varepsilon}^{\mathrm{Eng}}, G_m, \beta_m, \lambda_{II}^{\mathrm{p}} \right) \\
& + \sum_{m=1}^{M} \exp\left(-\beta_m \left(\Delta t + \frac{\lambda - 1}{\dot{\varepsilon}^{\mathrm{Eng}}} \right) \right) I_{\mathrm{unload}}\left(\dot{\varepsilon}^{\mathrm{Eng}}, G_m, \beta_m, \lambda_{III}^{\mathrm{p}}, 1 \right) \\
& + \sum_{m=1}^{M} I_{\mathrm{load}}\left(\dot{\varepsilon}^{\mathrm{Eng}}, G_m, \beta_m, \lambda \right)
\end{aligned}
\tag{B–41}
$$

$$
\begin{aligned}
\sigma^{\text{True}}_{IV,\text{unload}}(\lambda) = & \sum_{n=1}^{N} \mu_n \left(\lambda^{\alpha_n} - \lambda^{-\alpha_n/2} \right) \\
& + \sum_{m=1}^{M} \left[\exp\left(-\beta_m \left(\frac{\lambda_I^{\text{p}} - 1}{\dot{\varepsilon}^{\text{Eng}}} + \Delta t + 2\frac{\lambda_{II}^{\text{p}} - 1}{\dot{\varepsilon}^{\text{Eng}}} + \Delta t + 2\frac{\lambda_{III}^{\text{p}} - 1}{\dot{\varepsilon}^{\text{Eng}}} + \Delta t \right.\right.\right. \\
& \qquad \left.\left.\left. + \frac{\lambda_{IV}^{\text{p}} - 1}{\dot{\varepsilon}^{\text{Eng}}} + \frac{\lambda_{IV}^{\text{p}} - \lambda}{\dot{\varepsilon}^{\text{Eng}}} \right) \right) I_{\text{load}}\left(\dot{\varepsilon}^{\text{Eng}}, G_m, \beta_m, \lambda_I^{\text{p}} \right) \right] \\
& + \sum_{m=1}^{M} \left[\exp\left(-\beta_m \left(\Delta t + 2\frac{\lambda_{II}^{\text{p}} - 1}{\dot{\varepsilon}^{\text{Eng}}} + \Delta t + 2\frac{\lambda_{III}^{\text{p}} - 1}{\dot{\varepsilon}^{\text{Eng}}} + \Delta t + \frac{\lambda_{IV}^{\text{p}} - 1}{\dot{\varepsilon}^{\text{Eng}}} + \frac{\lambda_{IV}^{\text{p}} - \lambda}{\dot{\varepsilon}^{\text{Eng}}} \right) \right) \right. \\
& \qquad \left. I_{\text{unload}}\left(\dot{\varepsilon}^{\text{Eng}}, G_m, \beta_m, \lambda_I^{\text{p}}, 1 \right) \right] \\
& + \sum_{m=1}^{M} \left[\exp\left(-\beta_m \left(\frac{\lambda_{II}^{\text{p}} - 1}{\dot{\varepsilon}^{\text{Eng}}} + \Delta t + 2\frac{\lambda_{III}^{\text{p}} - 1}{\dot{\varepsilon}^{\text{Eng}}} + \Delta t + \frac{\lambda_{IV}^{\text{p}} - 1}{\dot{\varepsilon}^{\text{Eng}}} + \frac{\lambda_{IV}^{\text{p}} - \lambda}{\dot{\varepsilon}^{\text{Eng}}} \right) \right) \right. \\
& \qquad \left. I_{\text{load}}\left(\dot{\varepsilon}^{\text{Eng}}, G_m, \beta_m, \lambda_{II}^{\text{p}} \right) \right] \qquad \text{(B–42)} \\
& + \sum_{m=1}^{M} \left[\exp\left(-\beta_m \left(\Delta t + 2\frac{\lambda_{III}^{\text{p}} - 1}{\dot{\varepsilon}^{\text{Eng}}} + \Delta t + \frac{\lambda_{IV}^{\text{p}} - 1}{\dot{\varepsilon}^{\text{Eng}}} + \frac{\lambda_{IV}^{\text{p}} - \lambda}{\dot{\varepsilon}^{\text{Eng}}} \right) \right) \right. \\
& \qquad \left. I_{\text{unload}}\left(\dot{\varepsilon}^{\text{Eng}}, G_m, \beta_m, \lambda_{II}^{\text{p}}, \lambda_{II}^{\text{p}} \right) \right] \\
& + \sum_{m=1}^{M} \exp\left(-\beta_m \left(\frac{\lambda_{III}^{\text{p}} - 1}{\dot{\varepsilon}^{\text{Eng}}} + \Delta t + \frac{\lambda_{IV}^{\text{p}} - 1}{\dot{\varepsilon}^{\text{Eng}}} + \frac{\lambda_{IV}^{\text{p}} - \lambda}{\dot{\varepsilon}^{\text{Eng}}} \right) \right) I_{\text{load}}\left(\dot{\varepsilon}^{\text{Eng}}, G_m, \beta_m, \lambda_{II}^{\text{p}} \right) \\
& + \sum_{m=1}^{M} \exp\left(-\beta_m \left(\Delta t + \frac{\lambda_{IV}^{\text{p}} - 1}{\dot{\varepsilon}^{\text{Eng}}} + \frac{\lambda_{IV}^{\text{p}} - \lambda}{\dot{\varepsilon}^{\text{Eng}}} \right) \right) I_{\text{unload}}\left(\dot{\varepsilon}^{\text{Eng}}, G_m, \beta_m, \lambda_{III}^{\text{p}}, 1 \right) \\
& + \sum_{m=1}^{M} \exp\left(-\beta_m \frac{\lambda_{IV}^{\text{p}} - \lambda}{\dot{\varepsilon}^{\text{Eng}}} \right) I_{\text{load}}\left(\dot{\varepsilon}^{\text{Eng}}, G_m, \beta_m, \lambda_{IV}^{\text{p}} \right) \\
& + \sum_{m=1}^{M} I_{\text{unload}}\left(\dot{\varepsilon}^{\text{Eng}}, G_m, \beta_m, \lambda_{IV}^{\text{p}}, \lambda \right)
\end{aligned}
$$

B.4 Stress-Strain Relations for Simple Shear

We consider the plane stress finite shear deformation at constant engineering shear strain rate of an incompressible material. The deformation field can be written

$$x = X + \gamma Y, y = Y, z = Z \tag{B–43}$$

where (x, y, z) and (X, Y, Z) are coordinates of the points occupied by the same material particle in the current and the reference configurations, respectively. Here γ is the engineering shear strain, and since $\dot{\gamma}$ is constant, $\gamma = \dot{\gamma} t$ (here t is the time and the deformation starts at $t = 0$). The deformation gradient $\mathbf{F}$ is given by

$$\mathbf{F} = \begin{pmatrix} 1 & \gamma & \\ & 1 & \\ & & 1 \end{pmatrix} \tag{B–44}$$

We find the polar decomposition $\mathbf{F} = \mathbf{V} \cdot \mathbf{R}$ with $\mathbf{V}$ symmetric positive definite and $\mathbf{R}$ proper orthogonal matrices. We denote by $\{\mathbf{v}_1, \mathbf{v}_2, \mathbf{v}_3\}$ and $\{\lambda_1, \lambda_2, \lambda_3\}$, respectively, the normalized eigenvectors and the eigenvalues of $\mathbf{V}$. They values are

$$\mathbf{v}_1 = \begin{pmatrix} 0 \\ 0 \\ 1 \end{pmatrix} \quad , \quad \mathbf{v}_2 = \frac{1}{\sqrt{2}\sqrt{4+\gamma^2-\gamma\sqrt{4+\gamma^2}}} \begin{pmatrix} \gamma - \sqrt{4+\gamma^2} \\ 2 \\ 0 \end{pmatrix} \quad , \quad \mathbf{v}_3 = \frac{1}{\sqrt{2}\sqrt{4+\gamma^2-\gamma\sqrt{4+\gamma^2}}} \begin{pmatrix} 2 \\ -\gamma + \sqrt{4+\gamma^2} \\ 0 \end{pmatrix} \tag{B–45a}$$

$$\lambda_1 = 1 \quad , \quad \lambda_2 = \frac{\sqrt{2+\gamma^2-\gamma\sqrt{4+\gamma^2}}}{\sqrt{2}} \quad , \quad \lambda_3 = \frac{\sqrt{2+\gamma^2+\gamma\sqrt{4+\gamma^2}}}{\sqrt{2}} \tag{B–45b}$$

and the rotation matrix $\mathbf{R}$ is given by

$$\mathbf{R} = \begin{pmatrix} \frac{2}{\sqrt{4+\gamma^2}} & \frac{\gamma}{\sqrt{4+\gamma^2}} & 0 \\ \frac{-\gamma}{\sqrt{4+\gamma^2}} & \frac{2}{\sqrt{4+\gamma^2}} & 0 \\ 0 & 0 & 1 \end{pmatrix} \tag{B–46}$$

The Cauchy stress corresponding to the nonlinear elastic contribution is

$$\boldsymbol{\sigma}^{\text{Ogden}} = \sum_{n=1}^{N} \left[\mu_n \sum_{i=1}^{3} \lambda_i^{\alpha_n} |\mathbf{v}_i\rangle\langle\mathbf{v}_i| \right] \tag{B–47}$$

To find the viscoelastic contribution we recall that the strain-rate tensor is the symmetric part of the velocity gradient $\mathbf{L} = \dot{\mathbf{F}} \cdot \mathbf{F}^{-1}$, and after defining the corotated quantities $\hat{\boldsymbol{\sigma}}_m^{\text{ve}} = \mathbf{R}^{\text{T}} \cdot \boldsymbol{\sigma}_m^{\text{ve}} \cdot \mathbf{R}$ and $\hat{\mathbf{D}} = \mathbf{R}^{\text{T}} \cdot \mathbf{D} \cdot \mathbf{R}$ (see Eq. (B–4)) the contribution of the *m*-th term of the Prony series to the viscoelastic response of the material is given by

$$\frac{d}{dt}\left(\hat{\boldsymbol{\sigma}}_m^{\text{ve}}\right) = 2G_m\hat{\mathbf{D}} - \beta_m\hat{\boldsymbol{\sigma}}_m^{\text{ve}} = G_m\mathbf{R}^{\text{T}} \cdot \begin{pmatrix} 0 & \dot{\gamma} & \\ \dot{\gamma} & 0 & \\ & & 0 \end{pmatrix} \cdot \mathbf{R} - \beta_m\hat{\boldsymbol{\sigma}}_m^{\text{ve}} \tag{B–48}$$

With the condition $\hat{\boldsymbol{\sigma}}_m^{\text{ve}}\big|_{t=0} = \mathbf{0}$ the differential equation (B–48) is numerically solved for the six independent components of the symmetric tensor $\hat{\boldsymbol{\sigma}}_m^{\text{ve}}$ using the "NDSolve" function of MATHEMATICA. Thus $\boldsymbol{\sigma}_m^{\text{ve}} = \mathbf{R} \cdot \hat{\boldsymbol{\sigma}}_m^{\text{ve}} \cdot \mathbf{R}^{\text{T}}$.

We find the hydrostatic pressure from the condition $\sigma_{zz} = -p + \sum_{n=1}^{N} \mu_n + \sum_{m=1}^{M} \left(\boldsymbol{\sigma}_m^{\text{ve}}\right)_{zz} = 0$. We note that due to the structure of the rotation matrix $\mathbf{R}$ the differential equation for $\left(\boldsymbol{\sigma}_m^{\text{ve}}\right)_{zz}$ is uncoupled from the differential equations for the remaining components, and we get $\left(\boldsymbol{\sigma}_m^{\text{ve}}\right)_{zz} = 0$ identically.

The (engineering) shear stress σ_{xy} can be computed from Eq. (B–47) and from the numerical solution of Eq.(B–48). The tangent shear modulus is then defined as $G_T = \partial\sigma_{xy} / \partial\gamma$ and is numerically evaluated.

References

[1] C. Hepburn, Polyurethane elastomers, Applied Science Publishers London, 1982.
[2] S.L. Cooper, A.V. Tobolsky, Properties of linear elastomeric polyurethanes, J Appl Polym Sci, 10 (1966) 1837-1844.
[3] M.S. Sanchez-Adsuar, J.M. Martin-Martinez, Structure, composition, and adhesion properties of thermoplastic polyurethane adhesives, J Adhes Sci Technol, 14 (2000) 1035-1055.
[4] J. Yi, M.C. Boyce, G.F. Lee, E. Balizer, Large deformation rate-dependent stress-strain behavior of polyurea and polyurethanes, Polymer, 47 (2006) 319-329.
[5] Z.S. Petrovic, J. Ferguson, Polyurethane Elastomers, Prog Polym Sci, 16 (1991) 695-836.
[6] K.G. Budinski, M.K. Budinski, Engineering materials, Nature, 25 (2009) 28.
[7] A. Tasdemirci, I.W. Hall, B.A. Gama, M. Guiden, Stress wave propagation effects in two- and three-layered composite materials, J Compos Mater, 38 (2004) 995-1009.
[8] K. Kihara, H. Isono, H. Yamabe, T. Sugibayashi, A study and evaluation of the shear strength of adhesive layers subjected to impact loads, Int J Adhes Adhes, 23 (2003) 253-259.
[9] S.S. Sarva, S. Deschanel, M.C. Boyce, W.N. Chen, Stress-strain behavior of a polyurea and a polyurethane from low to high strain rates, Polymer, 48 (2007) 2208-2213.
[10] R. Rivlin, D. Saunders, Large elastic deformations of isotropic materials, in: Collected Papers of RS Rivlin, Springer, 1997, pp. 157-194.
[11] J.L. Ericksen, Deformations possible in every isotropic, incompressible, perfectly elastic body, Zeitschrift für Angewandte Mathematik und Physik (ZAMP), 5 (1954) 466-489.
[12] R. Ogden, Large deformation isotropic elasticity-on the correlation of theory and experiment for incompressible rubberlike solids, Proceedings of the Royal Society of London. A. Mathematical and Physical Sciences, 326 (1972) 565-584.
[13] E.M. Arruda, M.C. Boyce, A 3-Dimensional Constitutive Model for the Large Stretch Behavior of Rubber Elastic-Materials, J Mech Phys Solids, 41 (1993) 389-412.
[14] B.D. Coleman, W. Noll, Foundations of linear viscoelasticity, Reviews of Modern Physics, 33 (1961) 239.
[15] R.M. Christensen, A Non-Linear Theory of Viscoelasticity for Application to Elastomers, J Appl Mech-T Asme, 47 (1980) 762-768.
[16] H.J. Qi, M.C. Boyce, Stress-strain behavior of thermoplastic polyurethanes, Mech Mater, 37 (2005) 817-839.
[17] M.C. Boyce, K. Kear, S. Socrate, K. Shaw, Deformation of thermoplastic vulcanizates, J Mech Phys Solids, 49 (2001) 1073-1098.
[18] M.C. Boyce, S. Socrate, K. Kear, O. Yeh, K. Shaw, Micromechanisms of deformation and recovery in thermoplastic vulcanizates, J Mech Phys Solids, 49 (2001) 1323-1342.
[19] G.O. Antoine, R.C. Batra, Low Speed Impact of Laminated Polymethylmethacrylate/Adhesive/Polycarbonate Plates, Compos Struct, 116 (2014) 193-210.
[20] R.W. Ogden, Non-linear elastic deformations, Courier Dover Publications, 1997.
[21] A.E. Green, P.M. Naghdi, A general theory of an elastic-plastic continuum, Archive for rational mechanics and analysis, 18 (1965) 251-281.
[22] R.C. Batra, Elements of continuum mechanics, American Institute of Aeronautics and Astronautics, Reston, VA, 2006.
[23] J.S. Stenzler, Impact mechanics of PMMA/PC multi-laminates with soft polymer interlayers, in, University Libraries, Virginia Polytechnic Institute and State University,, Blacksburg, VA., 2009.
[24] C.N. Bapat, R.C. Batra, Finite Plane-Strain Deformations of Nonlinear Viscoelastic Rubber-Covered Rolls, Int J Numer Meth Eng, 20 (1984) 1911-1927.
[25] J.C. Simo, R.L. Taylor, Penalty-Function Formulations for Incompressible Non-Linear Elastostatics, Comput Method Appl M, 35 (1982) 107-118.
[26] E. Kröner, Allgemeine kontinuumstheorie der versetzungen und eigenspannungen, Archive for Rational Mechanics and Analysis, 4 (1959) 273-334.

[27] E.H. Lee, Elastic-plastic deformation at finite strains, Stanford University, Divsion of Engineering Mechanics, 1968.

4 Sensitivity Analysis of Low-velocity Impact Response of Laminated Plates

G. O. Antoine and R. C. Batra*
Department of Biomedical Engineering and Mechanics, M/C 0219
Virginia Polytechnic Institute and State University
Blacksburg, VA 24061, USA
Email: antoineg@vt.edu; rbatra@vt.edu
*Corresponding author; Tel: 540-231-6051; Fax: 540-231-4574

This chapter has been prepared for submission to a refereed journal.

4.1 Abstract

We analyze the sensitivity to values of material parameters, the layer thickness and the impact speed of the plate deflection, the contact force between the impactor and the plate, the maximum length of a crack, and the energy dissipated during the low velocity impact at normal incidence of a clamped rectangular laminate by a rigid hemispherical-nosed cylinder. The laminate is comprised of a layer of polymethylmethacrylate (PMMA)/adhesive/polycarbonate (PC), and it's deformations are analyzed by the finite element method. The thermo-elasto-viscoplastic materials of the PMMA and the PC and the thermoviscoelastic material of the adhesive involve a large number of material parameters whose precise values are unknown. Here we consider values of eleven material parameters – five for the PMMA and the PC and one for the adhesive. It is found that values of Young's moduli and Poisson's ratios of the PMMA, the PC and the shear modulus of the adhesive strongly influence the plate deflection and the crack length. Values of material parameters of the PC that noticeably affect its plastic deformations also determine the energy dissipated and the second peak in the contact force between the impactor and the laminate. The PMMA layer thickness is found to influence the crack length and the PC layer thickness the energy dissipated.

Key Words: Sensitivity analysis, Analysis of variance, Correlation coefficients

4.2 Introduction

Mathematical models of engineering structures generally involve a system of either ordinary or partial differential equations whose coefficients depend upon values of numerous material parameters. For a fixed set of initial and boundary conditions, the structural response depends upon materials of structural components. A goal of sensitivity analysis is to explore the effect on structural response of variability or uncertainty in the knowledge of values of material and geometric parameters of the structure.

While studying the response of glass targets to hypervelocity impact by small impactors, Anderson and Holmquist [1, 2] analyzed the sensitivity of the computed results to small variations in the impact speed. For example, they considered impact velocities of 2238, 2238.0001, 2238.0002, 2066 and 2066.0001 m/s, and found that a small variation in the impact speed noticeably affected the propagation of the penetration and failure fronts. In particular, the final depth of the failure and the penetration fronts increased by about 20% and more than 10%, respectively, with a 0.0001 m/s or 5×10^{-5} % increase in the impact velocity, showing the high sensitivity of their computational model upon the impact speed. Poteet and Blosser [3]

used sensitivity analysis to find the design factor with the greatest effect in the hypervelocity impact resistance of a bumper metallic protection system comprised of three metallic layers with spacing between them. Taking the layer thickness and the spacing between two adjacent layers as design variables, and the damage to the substructure and the debris dispersion as measures of the structure performance, the parameters with the largest effect on structure's integrity were found to be the thickness of the first layer and the spacing between the layers.

Here we determine material and geometric parameters that significantly affect the laminate deflection, the energy dissipated, the contact force between the impactor and the laminate, and lengths of cracks, if any, formed in a layer. The laminated structures comprised of polymethylmethacrylate (PMMA)/adhesive/polycarbonate (PC) are impacted at normal incidence by a low-velocity smooth hemispherical-nosed rigid cylinder. The constitutive equations, used to model the thermoviscoelastic response of the PMMA and the PC, involve 32 material parameters whose values cannot be precisely determined. Here we first screen values of material parameters to find 5 material parameters each for the PMMA and the PC that significantly affect the system response. Subsequently, we use the sampling-based sensitivity method to ascertain the influence of these parameters on the system response by considering either 10% or 30% variation in the values of these parameters.

The rest of the paper is organized as follows. We describe the screening method and the selection of five important material parameters for the PMMA and the PC in Section 4.2. The details of the sensitivity analysis for the impact problem are given in Section 4.3, and conclusions of the work are summarized in Section 4.4.

4.3 Screening

4.3.1 Purpose of Screening

The constitutive equations for the PMMA and the PC have 16 material parameters each giving a total of 32 parameters. To reduce the number of variables for the sensitivity analysis it is expedient to identify a small subset of material parameters that are likely to have a large influence on the mechanical response of the materials, and hence on the impact response of the laminate. This can be accomplished by a screening analysis that gives qualitative indicators to rank the input parameters (e.g., values of the material parameters) in order of their importance for the variability of the output (here the stress-strain response of the material). The method used to identify the subset of important parameters is presented in the next paragraph. Then it is applied to find parameters for the PMMA and the PC that significantly affect their response to mechanical deformations.

4.3.2 Description of the Method

We use the global one-factor-at-a-time (OAT) screening method proposed by Morris [4], and illustrate it by considering a scalar-valued (response) function y of k input variables x_1 through x_k that have been normalized to take real values between 0 and 1. For the screening analysis we require the input factors to take values in the set $\{0,1/(p-1),\ldots,1\}$ where p is an integer. With the definition $\Delta = p/(2(p-1))$ the elementary effect of the i^{th} factor at the point $\mathbf{x} = (x_1,\ldots,x_k)$ is

$$d_i(\mathbf{x}) = \frac{1}{\Delta}\left[y(x_1,\ldots,x_{i-1},x_i+\Delta,x_{i+1},\ldots,x_k) - y(x_1,\ldots,x_k)\right] \tag{4–1}$$

The number $d_i(\mathbf{x})$ measures the sensitivity of the response function with respect to the i^{th} input factor at the point **x,** and can be interpreted as the finite-difference partial derivative of y with respect to x_i. Following Saltelli et al. [5], we choose an even integer p and then the following procedure to compute elementary effects of all input factors. In Morris's method the impact of each input factor is evaluated in turn.

First, a base vector $\mathbf{x}^*$ is chosen whose components are randomly taken from the set $\{0,1/(p-1),\ldots,1-\Delta\}$. A subset χ of the set $\{1,2,\ldots,k\}$ is then randomly chosen, and the vector $\mathbf{x}^{(1)} = (x_1^{(1)},\ldots,x_k^{(1)})$ is formed according to the following rule:

$$x_i^{(1)} = \begin{cases} x_i^* + \Delta & \text{if } i \in \chi, \\ x_i^* & \text{otherwise.} \end{cases} \tag{4–2}$$

The successive vectors $\mathbf{x}^{(1)},\ldots,\mathbf{x}^{(k+1)}$ are computed as follows. Assuming that the vector $\mathbf{x}^{(n)}$ ($n \le k$) is known, an index i such that the i^{th} component of the input has not been changed yet (i.e., $\forall m \le n$, $x_i^{(m)} = x_i^{(1)}$) is randomly selected and the vector $\mathbf{x}^{(n+1)}$ is defined as

$$x_i^{(n+1)} = \begin{cases} x_i^{(n)} - \Delta & \text{if } i \in \chi, \\ x_i^{(n)} + \Delta & \text{otherwise.} \end{cases} \tag{4–3}$$

The estimated elementary effect, $\tilde{d}_i$, of the factor i for the base vector $\mathbf{x}^*$ is then given by

$$\tilde{d}_i = \begin{cases} \frac{1}{\Delta}\left[y(\mathbf{x}^{(n)}) - y(\mathbf{x}^{(n+1)})\right] & \text{if } i \in \chi, \\ \frac{1}{\Delta}\left[y(\mathbf{x}^{(n+1)}) - y(\mathbf{x}^{(n)})\right] & \text{otherwise.} \end{cases} \tag{4–4}$$

A compact way to write and implement the procedure described above is the following. Define the orientation matrix $\mathbf{B}^*$ as the matrix whose rows are the $\mathbf{x}^{(n)}$'s, $1 \le n \le k+1$. That is,

$$\mathbf{B}^* = \left(\mathbf{J}_{k+1,1}\mathbf{x}^* + \frac{\Delta}{2}\left[(2\mathbf{T}_{k+1,k} - \mathbf{J}_{k+1,k})\mathbf{D}^* + \mathbf{J}_{k+1,k}\right]\right)\mathbf{P}^* \tag{4–5}$$

where $\mathbf{J}_{k+1,1}$ is the $(k+1)\times k$ matrix whose entries are all equal to 1, $\mathbf{x}^*$ is the $1\times k$ row base vector, $\mathbf{T}_{k+1,k}$ is the $(k+1)\times k$ strictly lower triangular matrix of 1's, $\mathbf{D}^*$ is a diagonal matrix with elements randomly chosen from the set $\{-1,+1\}$, and $\mathbf{P}^*$ is a random $k\times k$ permutation matrix. The response function y is evaluated by taking the rows of $\mathbf{B}^*$ as successive input points, and the elementary factors are calculated.

This provides one value of $\tilde{d}_i$ since each input factor is changed once. Repeating the procedure *r* times (*r* is an integer) with *r* random values for the base vector $\mathbf{x}^*$ and randomly selecting each time a new χ provides *r* independent measures of $\tilde{d}_i$. Since these values are independent one can compute their mean and standard deviation. The large mean values indicate factors that significantly affect the output. Thus mean values of $\tilde{d}_i$ rank the input factors according to their importance in the output variability. High values for the standard deviations indicate factors that have interactions with other inputs.

4.3.3 Results

The material parameters, x_i's, for the PMMA and the PC are $\dot{\gamma}^{\mathrm{p}}_{0,\alpha}$, ΔG_α, $\alpha^{\mathrm{p}}_\alpha$, h_α, t^{ss}_α, $\dot{\gamma}^{\mathrm{p}}_{0,\beta}$, ΔG_β, $\alpha^{\mathrm{p}}_\beta$, h_β, t^{ss}_β, C_{R}, N_l, c, ν, E (see Appendix I (or Mulliken and Boyce [6] and Varghese and Batra [7]) for their definitions). The components of the input vector **x** are values of the normalized material parameters $\hat{x}_i$ defined as

$$\hat{x}_i = \frac{\dfrac{x_i}{x_i^0} - \alpha_{\min}}{\alpha_{\max} - \alpha_{\min}} \tag{4–6}$$

For normalizing the x_i's we use their nominal values x_i^0 (given in Appendix I, [6] and [7]), and assume that $\alpha_{\min}$ = 0.7, $\alpha_{\max}$ = 1.3. The normalized parameters $\hat{x}_i$ are allowed to vary between 0 and 1, corresponding to ± 30% variation of the input factors about their respective nominal values. This implies that the assumed range of uncertainty in values of material parameters is 30%.

We use as response function *y* the stress-strain curve of the PMMA and the PC for uniaxial compression deformation at strain rate of 5000/s up to – 0.2 true axial strain. Since this is not a scalar-valued function, we replace $y\left(\mathbf{x}^{(n+1)}\right) - y\left(\mathbf{x}^{(n)}\right)$ in Eq. (4–4) by $\sqrt{\int_{\varepsilon=0}^{0.2} \left(\sigma\left(\mathbf{x}^{(n+1)}, -\varepsilon\right) - \sigma\left(\mathbf{x}^{(n)}, -\varepsilon\right)\right)^2 d\varepsilon}$ where $\sigma(\mathbf{x}, \varepsilon)$ is the true axial stress for true strain ε and values of material parameters corresponding to point **x**.

For the present study we set $r = 8$ and compare results obtained with $p = 4$ and $p = 12$. Therefore 128 stress-strain curves are necessary for each value of *p* and each material for a total of 512 simulations. The mean and the standard deviations of the elementary effects, $\tilde{d}_i$, are depicted in Fig.4–1.

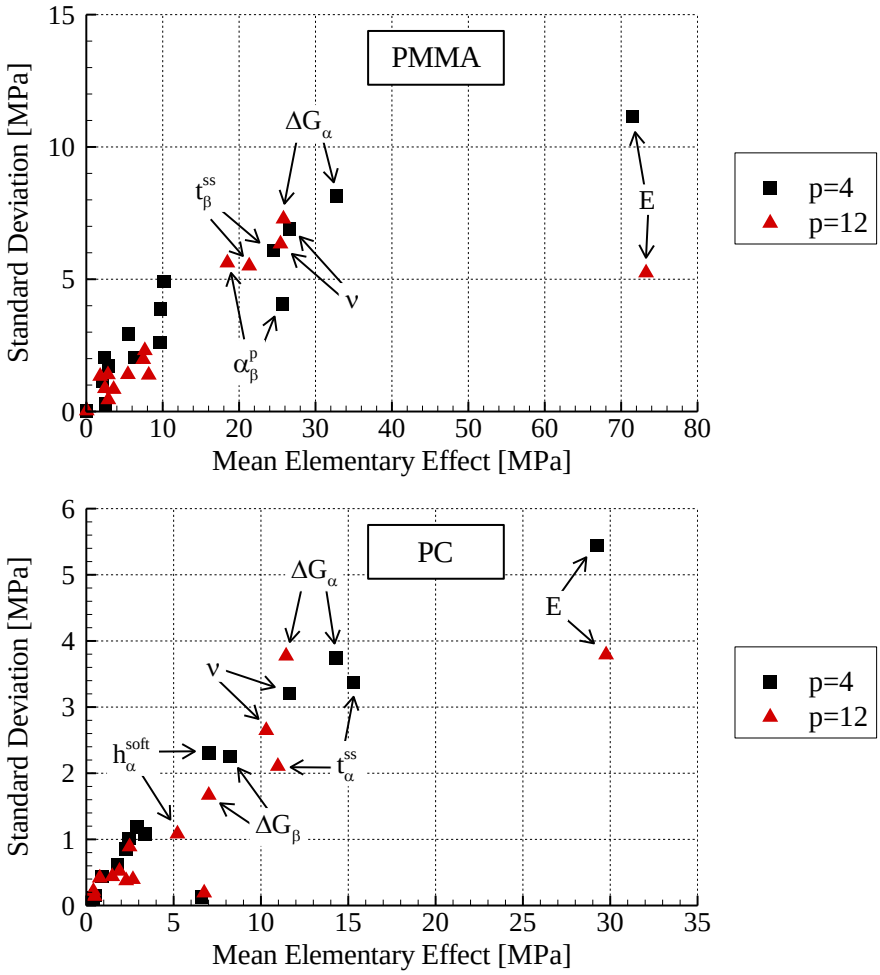

Fig.4–1: The standard deviation vs. the mean elementary effect for the uniaxial compression of PMMA and PC at 5000/s true strain rate.

We have indicated in Fig.4–1 the variables whose elementary effects are clearly separated from the group of points with low mean and low standard deviations. We notice that results obtained with p = 4 and 12 are qualitatively similar, and in particular the five material parameters with the highest mean effects are E, ν, ΔG_α, α_β^p, t_β^{ss} for the PMMA and E, ν, ΔG_α, t_α^{ss}, ΔG_β for the PC. We conduct the sensitivity analysis of the impact problem with respect to these material parameters.

4.4 Sensitivity Analysis of the Impact Problem

4.4.1 Problem Description

We perform sensitivity analysis of the impact problem schematically sketched in Fig. 2 and described in Antoine and Batra [8]. The hemispherical nosed rigid impactor of mass 28.5g and 6.9J initial kinetic energy impacts at normal incidence a clamped flat $L_1 \times L_2 \times h$ (= $h_1 + h_2 + h_3$) rectangular plate. We refer the reader to [8] for details of the analysis of deformations of the laminate by the finite element method (FEM) using the commercial FE software, LS-DYNA, in which the material models for the PC, the

PMMA and the adhesive have been implemented as user defined subroutines. In the present analysis a fixed FE mesh comprised of 8-node brick elements has been employed, and deformations of only a quarter of the laminate have been analyzed due to the symmetry of the problem geometry, and initial and boundary conditions. The FE mesh used and other details of the computational work are described in [8]. Results have been computed for $L_1 = L_2 = 127$ mm, $h_1 = h_3 = 1.5875$ mm and $h_2 = 0.635$ mm.

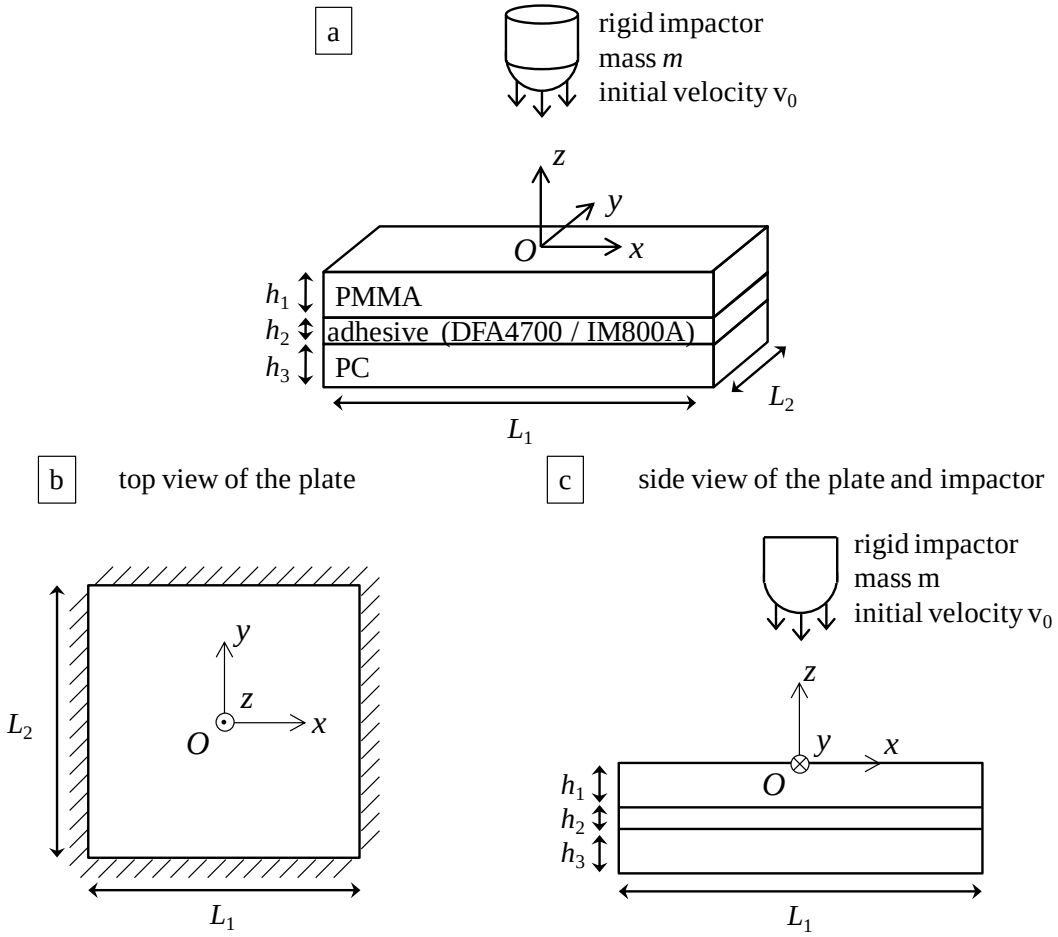

Fig.4–2: Schematic sketch of the impact problem studied.

4.4.2 Method

4.4.2.1 Input Factors for Material Parameters

The adhesive DFA4700 interlayer is modeled as a nearly incompressible viscoelastic material with the elastic response given by the Ogden strain energy function, and the viscous response by the Prony series (e.g., see Antoine and Batra [8]). Because of the presence of more than one shear modulus in the constitutive relation for the adhesive, for the sensitivity analysis we assume that all shear moduli, μ_n and G_m, are multiplied by the same scaling factor while exponents, α_n, of the stretches in the expression for the Ogden strain energy density and the decay constants (inverse of relaxation times) of the Prony series

are left unchanged. Consequently the instantaneous shear modulus G_0 of the modified material is different from that of the original material. The initial Poisson's ratio of the adhesive is set to 0.498 and is unchanged during the sensitivity study. With 5 material parameters for the PMMA, 5 for the PC and 1 for the DFA4700 listed in Table 4–1, there are 11 material parameters (or input factors) for the sensitivity study.

Material	Parameters selected for the sensitivity study
PMMA	E, ν, ΔG_α, $\alpha_\beta^{\mathrm{p}}$, t_β^{ss}
PC	E, ν, ΔG_α, t_α^{ss}, ΔG_β
adhesive	$G_0 \left(= \sum_{n=1}^{N} \frac{1}{2} \mu_n \alpha_n + \sum_{m=1}^{M} G_m \right)$

Table 4–1: Material parameters included for the sensitivity study of the impact problem.

The material parameters are normalized with respect to their nominal values (see Eq. (4–6)) either with $\alpha_{\min}$ = 0.7, $\alpha_{\max}$ = 1.3 or with $\alpha_{\min}$ = 0.9, $\alpha_{\max}$ = 1.1. The normalized variables vary between 0 and 1 leading to either 30% or 10% variation about their nominal values.

4.4.2.2 Input Factors for the Geometric Parameters and Impact Velocity

The input factors are the thicknesses h_1, h_2 and h_3, of the three layers and the impact velocity v_0. The manufacturer gives ± 0.0762 mm uncertainty in the thicknesses. Therefore the three thicknesses are allowed ± 0.0762 mm variation with uniform probability. In the list of impact velocities reported by Stenzler [9] the experimental v_0 ranges between 21 m/s and 23 m/s, therefore 1 m/s uncertainty with uniform probability in the impact velocity about the nominal value 22 m/s is assumed.

4.4.2.3 Description of the Method

To investigate the effect of uncertainty in the inputs (e.g., the material parameters) on the output (the plate response) we use a sampling-based method, which has been shown to be robust with relatively small samples (~200) [10, 11]. It estimates the uncertainty in the output generated by uncertainty in the inputs, and assesses the importance of the individual input factors on the uncertainty in the results. More specifically, results considered are the post-impact length of cracks formed in the PMMA layer, the total energy dissipated in the laminate, the history of the contact force between the impactor and the laminate, and the maximum deflection of the laminate.

We use the Latin-hypercube sampling method to generate different inputs. The normalized input $\hat{x}_k$, given by Eq. (4–6), varies between 0 and 1 with an assumed uniform distribution. The corresponding cumulative probability is $f(\hat{x}) = \hat{x}$ if $0 \le \hat{x} \le 1$ and $f(\hat{x}) = 0$ otherwise. Assuming that the input factors are not correlated, the Latin-hypercube sampling method can be performed in a simple way. First, the number of samples is chosen. We use here 300 samples, which is large enough to limit the correlation of the 11 input variables and small enough to be computationally reasonable since only 300 impact simulations are required. Then, the interval [0, 1] is partitioned into 300 segments $[a_{j-1}, a_j]$,

$a_j = (j-1)/300,\ \ j = 1 \ldots 300$ of equal size. The values $b_j = f^{-1}(a_j)$ are then determined and a random value $\hat{x}_k^{(j)}$ is selected in each of the $[b_{j-1}, b_j]$ intervals for the k^{th} normalized input factor $\hat{x}_k$. The procedure is repeated independently for each of the 11 input variables, giving a list of 300 values for each input. The values are then randomly paired to form 300 samples, i.e., a set of 300 vectors of length 11. The impact problem is then analyzed for each of the 300 sets of values for the material parameters with 10% ($\alpha_{\min} = 0.9, \alpha_{\max} = 1.1$) and 30% ($\alpha_{\min} = 0.7, \alpha_{\max} = 1.3$) uncertainty in the values of material parameters. Since it is easier to determine values of the elastic parameters for the PMMA and the PC than those of the remaining material parameters both studies described above are also carried out with Young's moduli and Poisson's ratios of the PMMA and the PC materials set to their nominal values. In the later cases the 9 remaining inputs are varied. Thus four studies (comprising 300 simulations each) are performed for a total of 1200 simulations. The study of the sensitivity upon the layer thicknesses and impact velocity is carried out with 100 additional simulations.

4.4.3 Results

4.4.3.1 Distribution of the Results for Variations in Values of Material Parameters

The distribution of results is shown in the box plots of Fig.4–3 wherein the convention used for the box plots is also given.

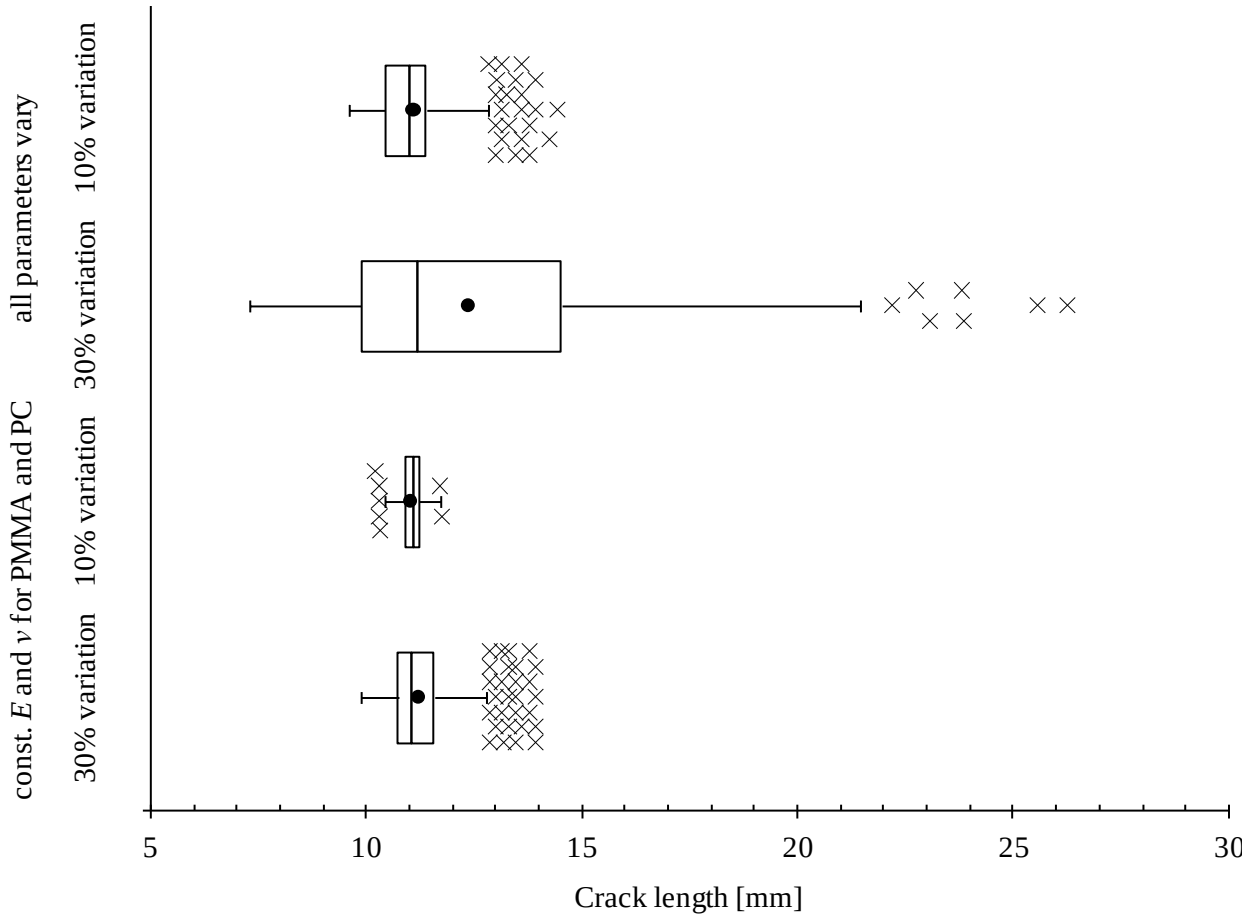
const. E and ν for PMMA and PC
all parameters vary
30% variation
10% variation
30% variation
10% variation
5
10
15
20
25
30
Crack length [mm]

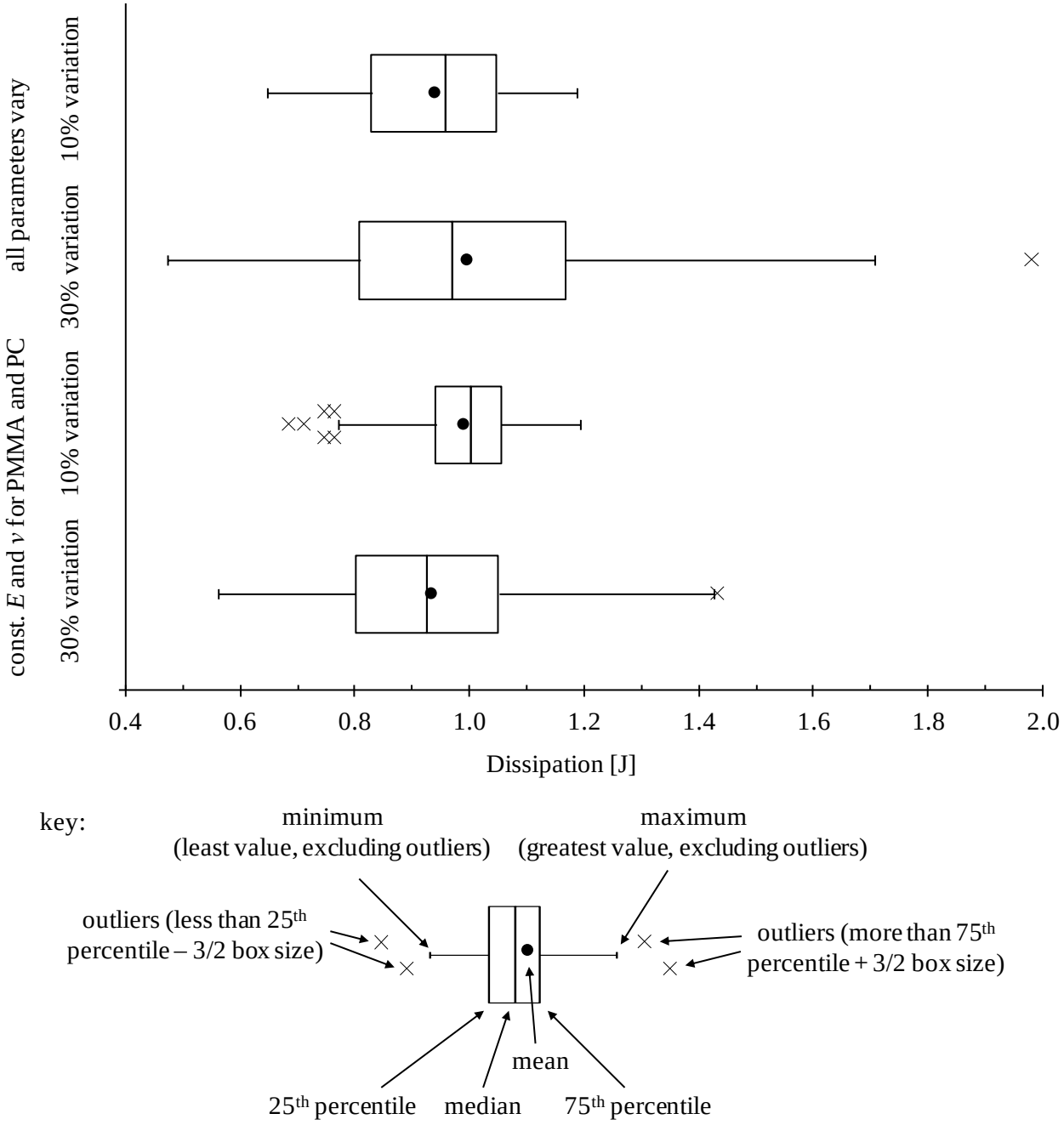

Fig.4–3: Box plots of the energy dissipation and the post-impact crack length for 10 and 30% variations in values of input parameters with and without varying Young's moduli and Poisson's ratios of the PMMA and the PC.

The distribution shown in the box plots is consistent with the expectation that the scattering of the data is more important when the variation range of the material parameters is larger. In particular we note that when the elastic properties of the PMMA and the PC are fixed and 10% variation in values of the remaining four material parameters is allowed the scattering of the crack length is small (10.2 vs. 11.8 mm) while it is extremely large when values of all parameters are allowed to vary by 30% (7.3 vs. 26.4

mm) since there is a factor of 3.6 between the largest and the smallest observations in the latter case. For the energy dissipation the scatter is considerable even with 10% variation in values of all parameters except for E and ν of the PMMA and the PC (0.69 vs. 1.19 J, ratio = 1.7). It is not surprising that with fixed values of E and ν for the PMMA and the PC the variability in the crack length is much smaller than that in the energy dissipation. The brittle failure of the PMMA is mostly affected by its Young's modulus while the main source of energy dissipation is plastic deformations of the PC which are affected by values of three parameters, ΔG_α, t_α^{ss} and ΔG_β.

In Fig.4–4 we have displayed the min, 10th, 50th (median), 90th percentiles, the max and the mean values of the contact force as a function of time. These values are determined as follows: for each value of time the reaction forces obtained from different samples are collected and their percentiles and mean are determined. Thus the curve corresponding to, for example, the minimum value of the contact force does not necessarily correspond to the contact force of the same sample throughout the entire impact duration.

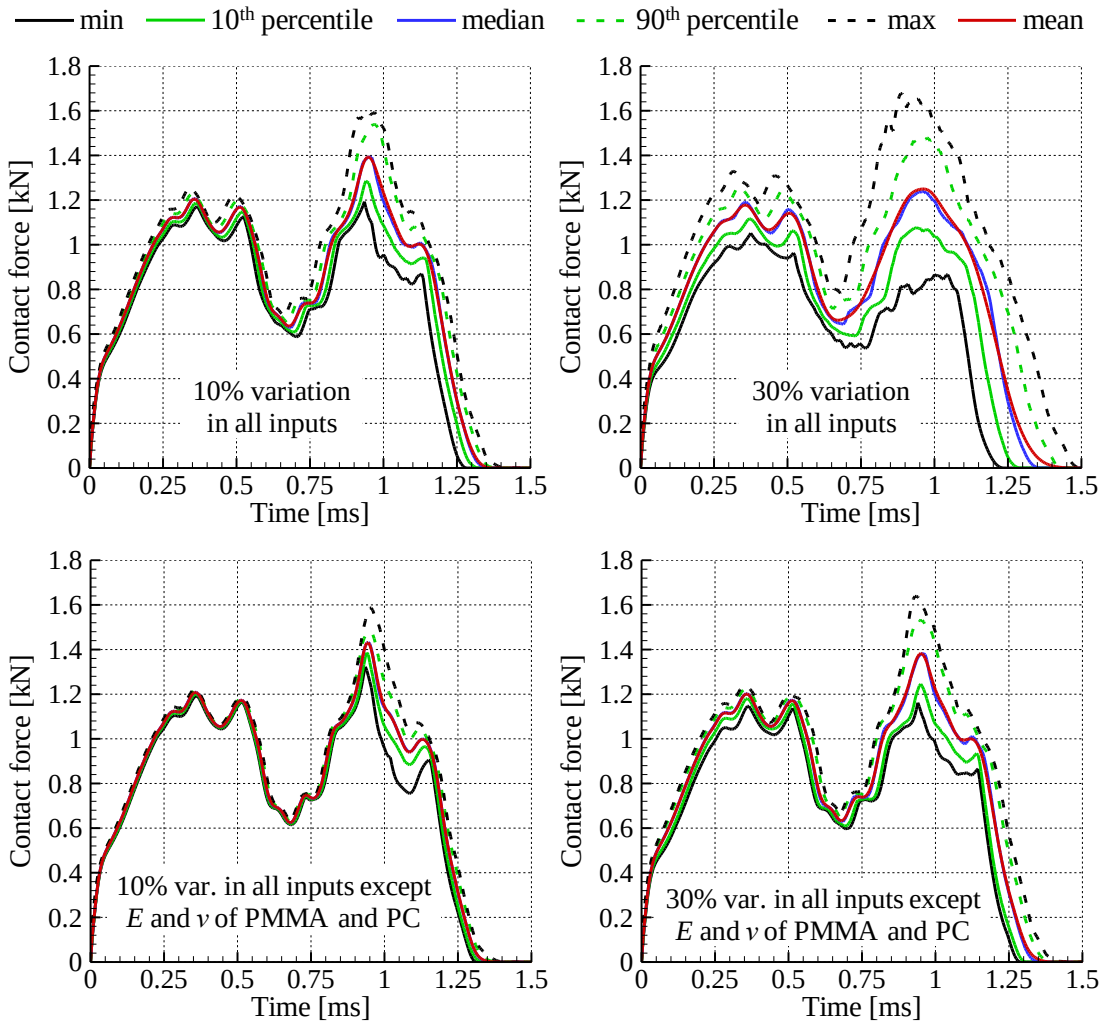

Fig.4–4: Time histories of the minimum, 10th, 50th and 90th percentiles and the mean of the contact force.

In order to quantify the scatter in the contact force, the L²-norm of the contact force is computed for each set of input values. The computed difference between the mean and the max values of the L²-norm, and that between the mean and the min values of the L²-norm are listed in Table 4–2. Similar results for the deflection of the centroid of the bottom surface of the laminate are presented in Fig.4–5 and Table 4–2.

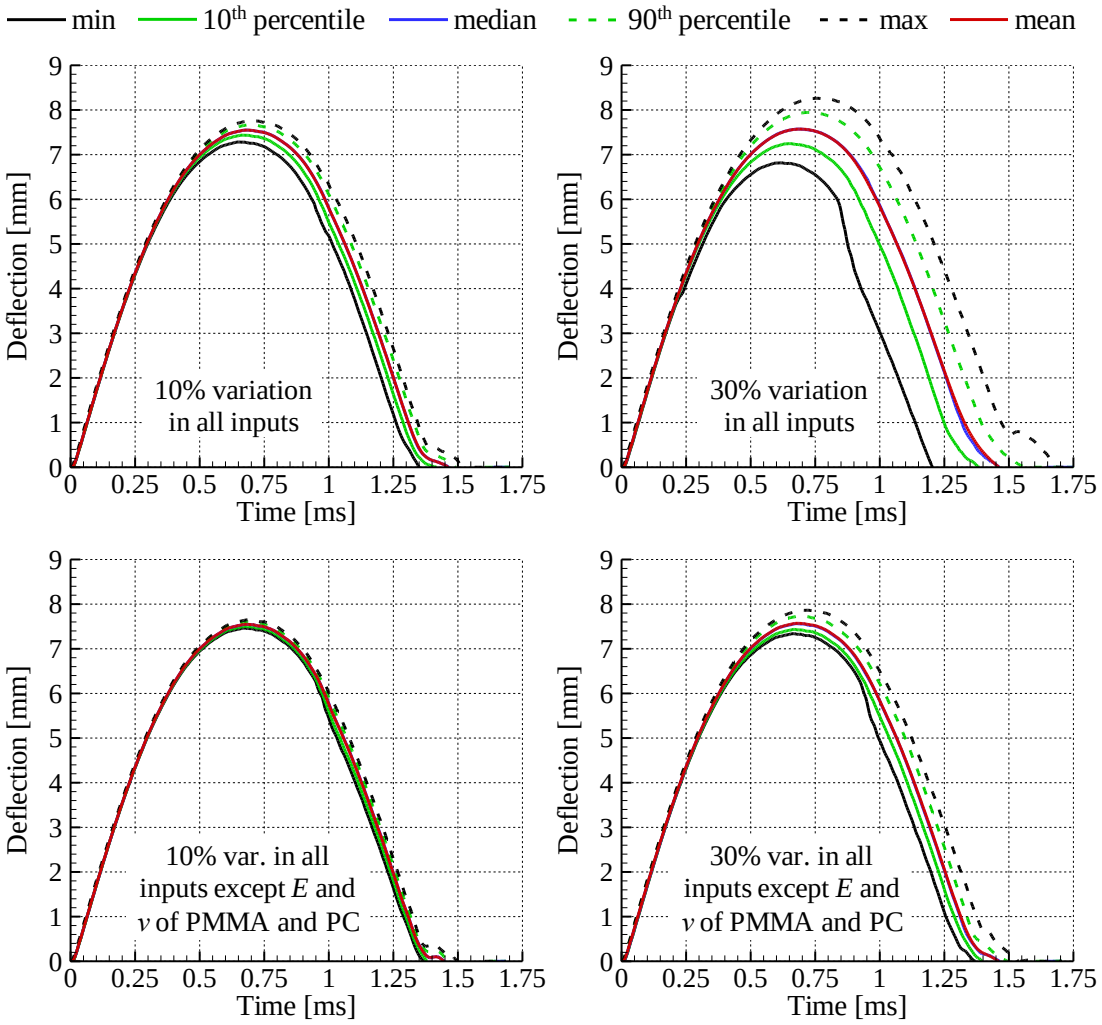

Fig.4–5: Time histories of the minimum, 10th, 50th and 90th percentiles, and the mean of the deflection of the centroid of the bottom surface of the laminate.

For the 10% (30%) uncertainty in the input variables, the mean differs from the min and the max values of the deflection by about 10% (33%). For the reaction force the corresponding values are 15% (33%). However, when E and ν for the PMMA and the PC are not varied, then the maximum difference between the mean and the min/max values of the deflection and the reaction force are less than 15%. Thus the uncertainty in the values of the reaction force and the maximum deflection is about the same as that in the values of the input variables considered. It may be interpreted as follows: the output of these two variables continuously depends upon the input values of the material parameters.

	Reaction force		Deflection	
	Difference between min and mean	Difference between max and mean	Difference between min and mean	Difference between max and mean
±10% variation in all inputs	15.1%	13.9%	10.4%	7.33%
±30% variation in all inputs	30.2%	32.8%	33.1%	24.1%
±10% variation, constant E and v for PMMA and PC	9.06%	8.64%	5.89%	4.58%
±30% variation, constant E and v for PMMA and PC	14.4%	14.6%	11.9%	10.4%

Table 4–2: Differences between the min and the max values of the L^2-norms of the reaction force and the maximum laminate deflection for 10% and 30% uncertainties in values of the input variables (taking the mean force/deflection as the reference).

It can be concluded from results presented in Table 4–2 that the experimentally measurable outputs such as the crack length, the reaction force, and the laminate deflection show less scatter than the energy dissipation which cannot be measured in physical tests. Therefore it is possible that the computed energy dissipation is far from the actual one even when the mathematical model has been validated by ensuring that the experimentally measurable outputs agree well with the computed ones. We also note that for the reaction force time history there is more scatter in values of the second peak than that in values of the first peak and of the "valley" defined as the value of the local minimum occurring at about 0.7 ms.

4.4.3.2 Distribution of the Results for Variations in Values of Geometric Parameters and Impact Velocity

The distribution of results of the impact simulations for variations in values of geometric parameters and impact velocity are shown in the box plots of Fig.4–6.

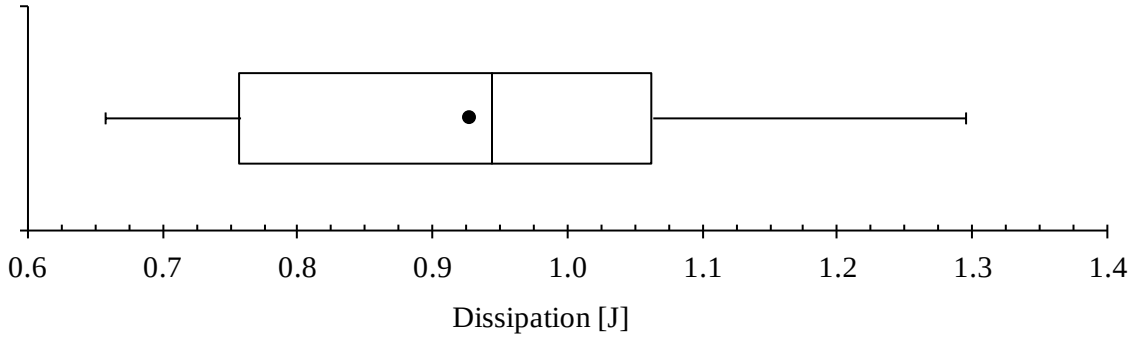

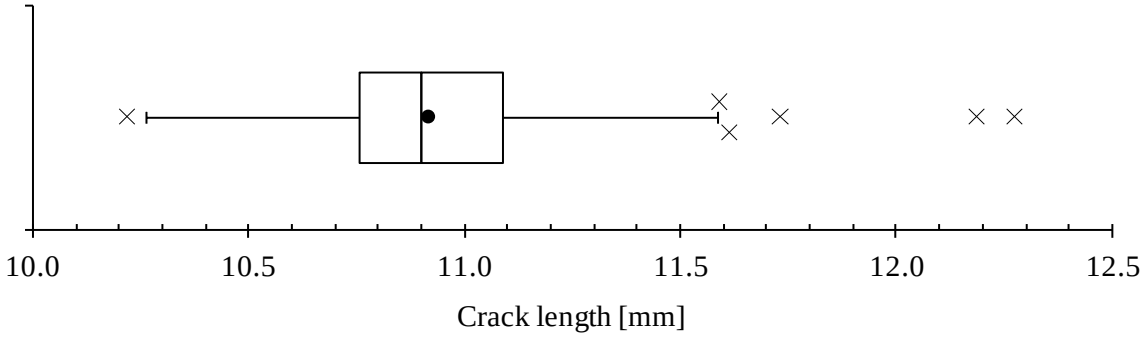

Fig.4–6: Box plots of the energy dissipation and the post-impact crack length for variations in the geometric parameters.

Fig.4–4 displays the min, the 10th, the 50th (median), the 90th percentiles, the max and the mean of the values of the contact force and the deflection as a function of time.

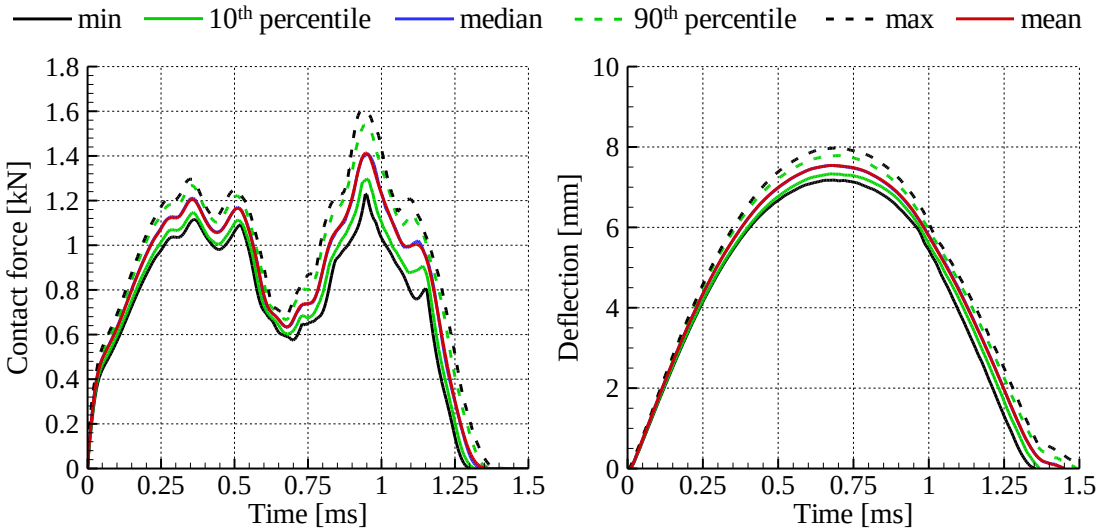

Fig.4–7: Histories of the minimum, 10th percentile, 50th and 90th percentiles and mean of the contact force and deflection.

In order to quantify the scatter in the contact forces the average deviations (L^2-norm) between the mean and the max values, and those between the mean and the min values are given in Table 4–3.

Reaction force		Deflection	
Deviation between min and mean	Deviation between max and mean	Deviation between min and mean	Deviation between max and mean
13.8%	13.7%	7.28%	7.06%

Table 4–3: Average L²-norm deviations between the mean contact force and the minimum and the maximum forces (taking the mean force as reference) for variations in the values of plate thicknesses.

4.4.3.3 Sensitivity Analysis and Correlation

Correlation is an important measure of characterizing the effect of input factors (i.e., material parameters) on the outputs (i.e., simulation results). The correlation *r* between two variables ξ_1 and ξ_2 is defined as

$$r = \frac{\sum_{i=1}^{n}\left(\xi_1^{(i)} - \bar{\xi}_1\right)\left(\xi_2^{(i)} - \bar{\xi}_2\right)}{\sqrt{\sum_{i=1}^{n}\left(\xi_1^{(i)} - \bar{\xi}_1\right)^2}\sqrt{\sum_{i=1}^{n}\left(\xi_2^{(i)} - \bar{\xi}_2\right)^2}} \tag{4–7}$$

where *n* is the total number of observations, $\xi_1^{(i)}$ and $\xi_2^{(i)}$ are values of the variables corresponding to the i^{th} observation, and $\bar{\xi}_1$ and $\bar{\xi}_2$ are mean values of variables ξ_1 and ξ_2 over the *n* observations, respectively. Because of the inner product inequality, the value of r is in the interval [-1, 1] and describes simultaneous variations of the variables. For instance r is positive when ξ_1 and ξ_2 vary "in the same manner" [12]. Eq. (4–7) can be used to compute the correlation between the inputs and the outputs, and correlations among the input factors. In the present work, since the inputs are assumed to be independent of each other, it is important that their correlations be small, since otherwise output results will have no significance. In the present study the maximum magnitude of the correlation among the inputs is 0.089 for variations of the material parameters and 0.05 for the other study; e.g., see Tables given in the Appendix.

The sensitivity coefficients quantify the effect of varying an input factor on the output. In order to find these we assume that the output *y* follows the relation

$$y_{\text{model}} = b_0 + \sum_{j=1}^{m} b_j \hat{x}_j \tag{4–8}$$

Since the output may not exactly follow the relation (8), therefore, we write the observations $y^{(i)}$, $i = 1 \ldots n$ as

$$y^{(i)} = b_0 + \sum_{j=1}^{m} b_j \hat{x}_j^{(i)} + \varepsilon^{(i)} \tag{4–9}$$

where $\varepsilon^{(1)} \ldots \varepsilon^{(n)}$ are the errors. Values of coefficients $\mathbf{b}$ minimizing $\|\boldsymbol{\varepsilon}\|_2$ are called the sensitivity coefficients. The quantity, R^2, defined by

$$R^2 = \frac{\sum_{i=1}^{n} \left(y^{(i)} - \bar{y} \right)^2}{\sum_{i=1}^{n} \left(y_{\text{model}}^{(i)} - \bar{y} \right)^2} \tag{4–10}$$

indicates the proportion of the output variability accounted for by the model. The value of R^2 close to 1.0 indicates that most of the variability of the output is accounted for by the model while smaller values indicate that the model does not successfully capture variations of the response.

To assess the importance of the input factor $\hat{x}_{j_0}$ we define the new model

$$\tilde{y}_{\text{model},j_0} = b_0 + \sum_{j=1, j \neq j_0}^{m} b_j \hat{x}_j \tag{4–11}$$

and find the set of optimal parameters $\left\{ \tilde{b}_j \right\}_{j=1,..j_0-1,j_0+1,...,m}$ by minimizing the error. The sum of squares (SS) associated with $\hat{x}_{j_0}$ and defined by

$$\text{SS}_{j_0} = \sum_{i=1}^{n} \left(y_{\text{model}}^{(i)} - \bar{y} \right)^2 - \sum_{i=1}^{n} \left(\tilde{y}_{\text{model},j_0}^{(i)} - \bar{y} \right)^2 \tag{4–12}$$

measures the importance of the j_0^{th} input factor.

In order to determine whether coefficients $\mathbf{b}$ appear to be zero or not we use Student's t-test with 5% threshold to reject the zero hypothesis. That is, it is assumed that a term of $\mathbf{b}$ is significant/non-zero if the hypothesis that its actual value be zero has less than 5% probability. Even though the distributional assumptions that lead to the *p*-values of Student's t-test are not satisfied in sampling-based sensitivity studies these *p*-values still provide a useful criterion for assessing the importance of a variable (Saltelli et al. [5]).

Results of the sensitivity analysis for the crack length are given in Table 4–4 for 30% variation in values of all input factors. We have listed in the Table only the significant input factors (less than 5% chance of being zero). Detailed analyses of the variance are provided in the Appendix. Similar results were obtained for 10% variation in the values of the input variables (the five inputs with the most effect are the same, with comparable relative weight and normalized sensitivity coefficients). The sensitivity coefficients were normalized with the largest magnitude of the coefficients that preserves their signs. Thus a positive value of the coefficient indicates that an increase in the input factors induces an increase in the output while it is the opposite for a negative value of the coefficient. We can conclude from results listed in Table 3 that the cumulated SS corresponding to the five elastic moduli of the plate materials accounts for more than 99% of the variability of the output. The factor with the largest coefficient is Young's modulus *E* for the PMMA. The coefficient is positive meaning that an increase of *E* induces an increase of the crack length.

This is because the threshold stress for the brittle failure was kept constant in the study, meaning that with an increase of E the strain at failure decreases. We also note that the sensitivity coefficient of G_0 is negative, meaning that a softer interlayer will result in larger cracks in the PMMA. This agrees with the experimental results of Stenzler [9] for the softer IM800A interlayer and with the results computed by Antoine and Batra [8] for this interlayer material.

Material	Parameter	% total SS	Normalized sensitivity coefficient
PMMA	E	70.9	1.0
PC	E	12.2	-0.41
Adhesive	G_0	9.45	-0.37
PC	ν	3.57	-0.23
PMMA	ν	2.91	0.20
PC	ΔG_β	0.66	-0.096
Total		99.7	

Table 4–4: Summary of the six parameters with the most influence on the variability of the crack length in the PMMA for the impact of the laminate with 30% variation in values of all input factors. $R^2 = 0.83$.

A similar investigation has been carried out for the total energy dissipation and results for 10% and 30% variation of the input factors are summarized in Table 4–5 and Table 4–6 where only significant factors are listed.

The main source of energy dissipation is plastic deformations of the PC material. Thus it is not surprising to find three material parameters of the PC among the five most important parameters for 10% and 30% variation in values of input parameters. In particular two of these parameters are related to its plastic deformations. The three parameters of the PC are Young's modulus, the activation energy of phase α, ΔG_α (plastic yielding), and the softening parameter t_α^{ss} (plastic softening). The two remaining parameters among the five most important ones are Young's modulus of the PMMA and the shear modulus of the interlayer. The signs of the sensitivity coefficients of these five parameters are the same for the two amplitudes of variation, however, Young's modulus of the PMMA is at the second place for the 10% variation study and at the fourth place for the 30% variation study while the remaining parameters have the same relative rankings. In both cases the cumulated SS of these five parameters represents more than 94% of the total SS. Finally we note that the R^2 of the fits of the energy dissipation is smaller than those of the crack length. This might be due to the fact that for the crack length one parameter (E of the PMMA) is clearly dominant while for the energy dissipation many parameters have similar SS, which could indicate that more interactions (not accounted for by the linear model of Eq.(4–8)) are present.

Material	Parameter	% total SS	Normalized sensitivity coefficient
PC	E	31.4	-1.0
PMMA	E	25.6	0.91
PC	ΔG_α	20.7	-0.81
PC	t_α^{ss}	10.7	-0.59
Adhesive	G_0	5.90	0.44
PC	ΔG_β	3.79	0.35
PMMA	ν	1.64	0.23
Total		99.7	

Table 4–5: Parameters with the most influence on the output variability of the energy dissipation for the impact problem with 10% variation in all input factors. $R^2 = 0.63$.

Material	Parameter	% total SS	Normalized sensitivity coefficient
PC	E	39.5	-1.0
PC	ΔG_α	21.3	-0.73
PC	t_α^{ss}	13.7	-0.59
PMMA	E	12.6	0.57
Adhesive	G_0	9.24	0.49
PMMA	ν	2.18	0.24
PMMA	ΔG_α	1.05	-0.16
Total		99.6	

Table 4–6: Parameters with the most influence on the output variability of the energy dissipation for the study with 30% variation in all input factors. $R^2 = 0.78$.

The correlation between the dissipation and the crack length cannot be established when the elastic moduli of the PMMA and the PC are fixed since regression analyses yield their correlation to be insignificant. However, when all parameters vary a significant correlation exists. Thus the crack length and the dissipation seem to be correlated via the elastic moduli of the PMMA and the PC.

In order to investigate the reaction force time history we introduce scalar quantities which characterize it. Three noticeable features of the reaction force time history are the first peak, the subsequent minimum

value of the force (called "valley" in the following), and the second peak of the force (see Fig.4–4). We define the first peak of the reaction force as its local maximum between 0.0 and 0.65 ms, the second peak as its local maximum between 0.75 and 1.6 ms, and the valley value as its local minimum between times 0.5 and 0.9 ms.

Linear models of the form of Eq. (4–8) including all the input factors could be fitted to accurately capture the 1st peak and the valley of the reaction forces ($R^2 > 0.95$, see values in the left column of Table 4–7). Thus the magnitudes of the 1st peak and the valley in the reaction force can be expressed as linear functions of the material parameters. Moreover, when the elastic moduli of the PC and the PMMA are varied, E and v of the PMMA and the PC and G_0 of the adhesive account for more than 85% of the variability of the model (their cumulated partial SS is larger than 85% of the total SS) for the 1st peak and the valley.

A satisfactory linear model giving the amplitude of the 2nd peak as an affine function of the input factors cannot be found since R^2-values of 0.62 and 0.59 were obtained for 10% and 30% variations of the inputs, respectively (see Table 4–7, left column). Upon studying the correlation Tables given in the Appendix we notice that the 2nd peak of the reaction force time history is strongly correlated with the energy dissipated. In order to investigate this correlation, a simple model expressing the 1st peak, the valley and the 2nd peak as linear functions of the dissipation only are fitted to the numerical results. The corresponding R^2-values are listed in Table 4–7.

Case	Variables as function of all material parameters			Variables as function of the dissipation only		
	1st peak	valley	2nd peak	1st peak	valley	2nd peak
All inputs ±10%	0.986	0.990	0.624	0.019	0.088	0.756
All inputs ±30%	0.957	0.983	0.593	0.107	0.081	0.686
Fixed E and v for PMMA and PC, other inputs ±10%	0.955	0.934	0.529	0.042	0.014	0.511
Fixed E and v for PMMA and PC, other inputs ±30%	0.873	0.943	0.640	0.345	0.239	0.627

Table 4–7: Values of R^2 for the reaction force as a function of either the material parameters or the dissipation alone.

The correlation between the 2nd peak in the reaction force time history and the energy dissipation is clear since expressing the value of the 2nd peak as an affine function of the energy dissipated gives $R^2 = \sim 0.7$ in the first two cases as compared to R^2 between 0.5 and 0.6 with fixed values of E for the PMMA and the PC. To visualize this correlation the 2nd peak of the contact force is plotted as a function of the energy dissipated in Fig.4–8.

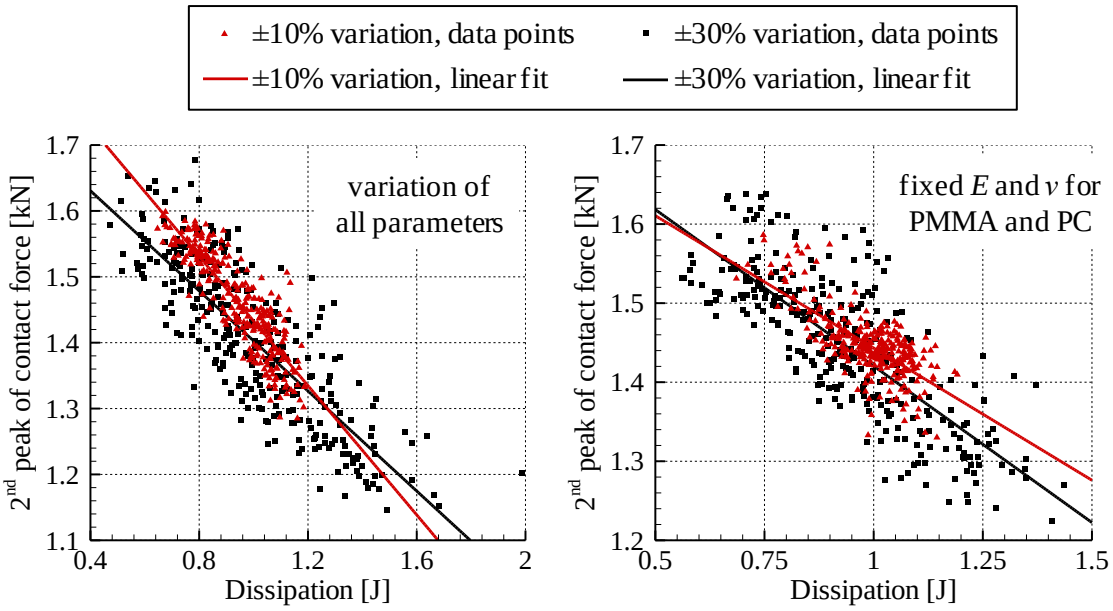

Fig.4–8: Value of the 2nd peak of the reaction force as a function of the energy dissipation and affine fit for all cases studied.

The linear fits in Fig.4–8 have negative slopes meaning that the energy dissipated and the 2nd peak of the contact force have opposite variations. This implies that when the plate dissipates more energy it has less elastic energy to bounce back. Thus the contact force corresponding to the rebound of the impactor (2nd peak of the reaction force, see [8]) has smaller magnitude.

One could argue that since the dissipation and the elastic properties of the PMMA and the PC are correlated, a correlation between the 2nd peak in the reaction force time history and the energy dissipated may simply mean that the 2nd peak is correlated with the elastic properties of these materials. This can be refuted by observing that the correlation between the dissipation and the 2nd peak of the reaction force still holds when the elastic properties of the PMMA and the PC materials are fixed to their nominal values (see the two last lines of Table 4–7).

	Regression coefficient (kN/J)
All inputs ±10%	-0.490
All inputs ±30%	-0.380
Fixed *E* and *v* for PMMA and PC, other inputs ±10%	-0.335
Fixed *E* and *v* for PMMA and PC, other inputs ±30%	-0.396

Table 4–8: Regression coefficients of energy dissipated for the 2nd peak of the reaction force as an affine function of the energy dissipated.

The slopes of the linear fits of Fig.4–8 are given in Table 4–8. We note that the coefficients are similar for all cases suggesting that the underlying mechanisms that correlate the 2nd peak of the reaction force and the energy dissipated are identical whether or not the elastic properties of the PMMA and the PC are varied.

For variations in values of the geometric parameters and the impact speed, results of the sensitivity study of the dissipation and of the crack length are summarized in Table 4–4 and Table 4–10, respectively. For the dissipation all parameters except the thickness of the PC are significant (with 95% confidence). For the crack length the thickness of the PC plate and the impact speed are significant but the thickness of the PMMA plate and of the adhesive have negligible effect.

Parameter	% total SS	Sensitivity coefficient
Thickness of PMMA	34.4	-2.17 J/mm
Thickness of adhesive	13.3	-1.35 J/mm
Thickness of PC	0.54	-0.271 J/mm
Impact velocity	51.8	0.203 J/(m/s)
Total	100	

Table 4–9: Summary of the dissipation variability. $R^2 = 0.88$.

Parameter	% total SS	Sensitivity coefficient
Thickness of PMMA	0.00	- 0.039 mm/mm
Thickness of adhesive	1.37	0.785 mm/mm
Thickness of PC	36.2	- 4.03 mm/mm
Impact velocity	62.43	0.403 mm/(m/s)
Total	100.0	

Table 4–10: Summary of the crack length variability. $R^2 = 0.71$.

4.5 Conclusions

For the PMMA and the PC we have identified material parameters that significantly affect their stress-train response in uniaxial compression. Those and other parameters have then been used to perform sensitivity analyses of the low velocity impact by a rigid impactor of a laminated PMMA/DFA4700/PC plate. The variations in the shear modulus of the DFA4700 interlayer have also been considered in the sensitivity study.

The effect of uncertainties in values of material parameters on variations in the response of the laminated plate has been investigated. It has been found that the elastic properties of the constituents of the plate dominantly affect the plate response, which is good since they can be easily measured experimentally. However, the energy dissipated is mostly affected by parameters that affect the plastic yielding and the plastic softening of the PC, which is consistent with the previously reported result that the energy dissipated is mostly due to plastic deformations of the PC. Thus even when the experimentally measurable quantities such as the plate deflection, the crack length and the reaction force agree with their corresponding experimental values and have very little variability due to the uncertainly in the values of material parameters, the scatter in the energy dissipation may be considerable. This indicates that even if a mathematical model has been validated by establishing a close agreement between its predictions of plate deflections etc. with the experimental results the computed energy dissipated may be far from that actually dissipated in the plate. Interactions among different material parameters could explain this larger scatter in the energy dissipated.

We found that the 1^{st} peak and the valley but not the 2^{nd} peak in the reaction force time history can be accurately expressed as functions of material parameters of the constituents of the plate. The 2^{nd} peak in the reaction force time history is correlated with the energy dissipated in the plate. It suggests that capturing the amplitude of the 2^{nd} peak of the reaction force history requires that the mathematical model of the problem accurately predict the energy dissipated during the impact event.

4.6 Acknowledgments

This research was sponsored by the US Army Research Laboratory and was accomplished under Cooperative Agreement Number W911NF-06-2-0014. The views and conclusions contained in this document are those of the authors and should not be interpreted as representing the official policies, either expressed or implied, of the Army Research Laboratory or the U.S. Government. The U.S. Government is authorized to reproduce and distribute reprints for Government purposes notwithstanding any copyright notation hereon.

Appendix C: Variations in the Material Parameters

C.1 Correlation of the Inputs and the Outputs

(a)

	x1	x2	x3	x4	x5	x6	x7	x8	x9	x10	x11	y1	y2	y3	y4	y5
x1	1.000															
x2	-0.021	1.000														
x3	-0.034	-0.035	1.000													
x4	0.084	0.023	-0.026	1.000												
x5	0.056	-0.054	-0.055	-0.080	1.000											
x6	0.011	-0.021	0.008	-0.022	0.003	1.000										
x7	-0.018	0.033	-0.070	-0.054	0.000	-0.063	1.000									
x8	-0.021	0.008	-0.019	-0.002	0.030	-0.029	-0.004	1.000								
x9	-0.014	-0.022	-0.061	0.059	-0.007	0.029	-0.043	0.001	1.000							
x10	-0.001	0.010	-0.032	-0.026	-0.060	-0.001	0.022	0.013	-0.043	1.000						
x11	0.036	0.049	0.035	0.071	-0.044	-0.027	-0.033	0.007	0.089	-0.017	1.000					
y1	0.410	0.116	0.030	0.067	-0.029	-0.441	0.040	-0.348	-0.269	0.157	0.198	1.000				
y2	0.751	0.059	-0.005	0.098	0.044	-0.273	-0.102	-0.083	-0.093	-0.048	-0.251	0.551	1.000			
y3	0.516	0.045	-0.042	0.000	0.031	0.693	0.292	0.154	0.110	0.281	0.039	-0.138	0.086	1.000		
y4	0.710	0.564	-0.047	0.072	0.008	0.185	0.194	-0.065	-0.036	-0.139	0.262	0.297	0.431	0.556	1.000	
y5	-0.528	-0.136	0.008	-0.051	0.013	0.460	0.014	0.257	0.205	0.063	-0.018	-0.869	-0.682	0.152	-0.361	1.000

(b)

	x1	x2	x3	x4	x5	x6	x7	x8	x9	x10	x11	y1	y2	y3	y4	y5
x1	1.000															
x2	-0.021	1.000														
x3	-0.034	-0.035	1.000													
x4	0.084	0.023	-0.026	1.000												
x5	0.056	-0.054	-0.055	-0.080	1.000											
x6	0.011	-0.021	0.008	-0.022	0.003	1.000										
x7	-0.018	0.033	-0.070	-0.054	0.000	-0.063	1.000									
x8	-0.021	0.008	-0.019	-0.002	0.030	-0.029	-0.004	1.000								
x9	-0.014	-0.022	-0.061	0.059	-0.007	0.029	-0.043	0.001	1.000							
x10	-0.001	0.010	-0.032	-0.026	-0.060	-0.001	0.022	0.013	-0.043	1.000						
x11	0.036	0.049	0.035	0.071	-0.044	-0.027	-0.033	0.007	0.089	-0.017	1.000					
y1	0.327	0.156	-0.068	0.018	-0.034	-0.558	0.024	-0.394	-0.322	-0.022	0.268	1.000				
y2	0.772	0.131	-0.044	0.071	0.040	-0.301	-0.154	-0.029	-0.083	-0.070	-0.240	0.494	1.000			
y3	0.559	0.084	-0.018	0.016	0.044	0.673	0.292	0.140	0.118	0.160	0.015	-0.328	0.128	1.000		
y4	0.682	0.556	-0.032	0.070	-0.008	0.222	0.239	-0.070	-0.043	-0.045	0.309	0.285	0.431	0.655	1.000	
y5	-0.355	-0.023	0.043	-0.010	0.017	0.566	-0.004	0.263	0.245	0.099	-0.030	-0.829	-0.573	0.317	-0.153	1.000

(c)

	x3	x4	x5	x8	x9	x10	x11	y1	y2	y3	y4	y5
x3	1.000											
x4	-0.026	1.000										
x5	-0.055	-0.080	1.000									
x8	-0.019	-0.002	0.030	1.000								
x9	-0.061	0.059	-0.007	0.001	1.000							
x10	-0.032	-0.026	-0.060	0.013	-0.043	1.000						
x11	0.035	0.071	-0.044	0.007	0.089	-0.017	1.000					
y1	0.311	0.008	-0.043	-0.510	-0.320	0.146	0.218	1.000				
y2	0.304	-0.012	-0.015	-0.132	-0.072	0.005	-0.507	0.373	1.000			
y3	-0.030	0.008	-0.044	0.488	0.301	0.773	0.148	-0.204	-0.156	1.000		
y4	-0.066	0.064	0.004	-0.200	-0.051	-0.547	0.758	0.119	-0.476	-0.455	1.000	
y5	-0.391	0.012	0.027	0.430	0.340	0.314	0.022	-0.715	-0.479	0.561	-0.136	1.000

(d)

	x3	x4	x5	x8	x9	x10	x11	y1	y2	y3	y4	y5
x3	1.000											
x4	-0.026	1.000										
x5	-0.055	-0.080	1.000									
x8	-0.019	-0.002	0.030	1.000								
x9	-0.061	0.059	-0.007	0.001	1.000							
x10	-0.032	-0.026	-0.060	0.013	-0.043	1.000						
x11	0.035	0.071	-0.044	0.007	0.089	-0.017	1.000					
y1	0.277	-0.015	-0.053	-0.651	-0.437	-0.054	0.295	1.000				
y2	0.093	-0.089	0.024	-0.101	-0.157	-0.171	-0.817	-0.043	1.000			
y3	0.001	0.042	-0.019	0.604	0.410	0.549	0.185	-0.587	-0.409	1.000		
y4	-0.005	0.052	-0.031	-0.252	-0.065	-0.215	0.901	0.489	-0.753	-0.160	1.000	
y5	-0.482	-0.007	0.014	0.498	0.368	0.232	-0.012	-0.792	-0.244	0.565	-0.191	1.000

Table C–1: Correlations between the inputs and the outputs.
(a) ±10% variation for all variables, (b) ±30% variation for all variables, (c) ±10% variation for all variables except for *E* and *ν* of PMMA and PC, (d) ±30% variation for all variables except for *E* and *ν* of PMMA and PC.

key to the inputs and outputs

x1:	PMMA, E	x5:	PMMA, t_β^{ss}	x9:	PC, t_α^{ss}	y2:	crack length
x2:	PMMA, ν	x6:	PC, E	x10:	PC, ΔG_β	y3:	rcforc, 1st peak
x3:	PMMA, ΔG_α	x7:	PC, ν	x11:	Adhesive, G_0	y4:	rcforc, valley
x4:	PMMA, α_β^p	x8:	PC, ΔG_α	y1:	dissipation	y5:	rcforc, 2nd peak

C.2 Analysis of Variance (ANOVA) and Sensitivity Factors

Input factor		Dissipation		Crack length	
		Normalized sensitivity coefficient	*p*-value	Normalized sensitivity coefficient	*p*-value
PMMA	E	0.91	**<0.0001**	1.00	**<0.0001**
	ν	0.23	**0.0057**	0.114	**0.003**
	ΔG_α	0.061	0.46	0.031	0.42
	$\alpha_\beta^{\mathrm{p}}$	0.060	0.47	0.055	0.15
	t_β^{ss}	-0.033	0.69	-0.003	0.94
PC	E	-1.00	**<0.0001**	-0.388	**<0.0001**
	ν	0.024	0.77	-0.153	**<0.0001**
	ΔG_α	-0.81	**<0.0001**	-0.098	**0.011**
	t_α^{ss}	-0.59	**<0.0001**	-0.071	0.066
	ΔG_β	0.35	**<0.0001**	-0.067	0.082
Adhesive	G_0	0.44	**<0.0001**	-0.387	**<0.0001**
R^2		0.63		0.76	

Table C–2: Normalized sensitivity coefficients, *p*- and R^2 values for ±10% variation of all input factors.

Material	Parameter	Sum of Squares (SS)	% total SS	DOF	Mean SS	F
PC	E	0.972	31.36	1	0.972	148.2
PMMA	E	0.795	25.64	1	0.795	121.2
PC	ΔG_α	0.641	20.68	1	0.641	97.75
PC	t_α^{ss}	0.332	10.7	1	0.332	50.59
Adhesive	G_0	0.183	5.9	1	0.183	27.90
PC	ΔG_β	0.117	3.79	1	0.117	17.91
PMMA	ν	0.051	1.64	1	0.051	7.75
PMMA	ΔG_α	0.004	0.11	1	0.004	
PMMA	$\alpha_\beta^{\mathrm{p}}$	0.003	0.11	1	0.003	
PMMA	t_β^{ss}	0.001	0.03	1	0.001	
PC	ν	0.001	0.02	1	0.001	
Total		3.099	100			

Table C–3: ANOVA for the dissipation for ±10% variation of all input factors.

Material	Parameter	Sum of Squares (SS)	% total SS	DOF	Mean SS	F
PMMA	E	137.4	73.51	1	137.4	683.9
PC	E	20.87	11.16	1	20.87	103.9
Adhesive	G_0	20.46	10.94	1	20.46	101.8
PC	ν	3.233	1.73	1	3.233	16.08
PMMA	ν	1.799	0.96	1	1.799	8.95
PC	ΔG_α	1.324	0.71	1	1.324	6.59
PC	t_α^{ss}	0.685	0.37	1	0.685	
PC	ΔG_β	0.613	0.33	1	0.613	
PMMA	$\alpha_\beta^{\mathrm{p}}$	0.417	0.22	1	0.417	
PMMA	ΔG_α	0.131	0.07	1	0.131	
PMMA	t_β^{ss}	0.001	0	1	0.001	
Total		187.0	100			

Table C–4: ANOVA for the crack length for ±10% variation of all input factors.

Input factor		Dissipation		Crack length	
		Normalized sensitivity coefficient	*p*-value	Normalized sensitivity coefficient	*p*-value
PMMA	E	0.565	**<0.0001**	1.00	**<0.0001**
	ν	0.235	**<0.0001**	0.202	**<0.0001**
	ΔG_α	-0.164	**0.001**	-0.022	0.487
	$\alpha_\beta^{\mathrm{p}}$	-0.057	0.264	0.006	0.837
	t_β^{ss}	-0.055	0.274	-0.014	0.651
PC	E	-1.00	**<0.0001**	-0.413	**<0.0001**
	ν	-0.041	0.412	-0.225	**<0.0001**
	ΔG_α	-0.733	**<0.0001**	-0.028	0.374
	t_α^{ss}	-0.592	**<0.0001**	-0.058	0.062
	ΔG_β	-0.058	0.245	-0.096	**0.0022**
Adhesive	G_0	0.486	**<0.0001**	-0.366	**<0.0001**
R^2		0.778		0.831	

Table C–5: Normalized sensitivity coefficients, *p*- and R^2 values for ±30% variation of all input factors.

Material	Parameter	Sum of Squares (SS)	% total SS	DOF	Mean SS	F
PC	E	6.005	39.52	1	6.005	397.1
PC	ΔG_α	3.239	21.32	1	3.239	214.2
PC	t_α^{ss}	2.082	13.7	1	2.082	137.7
PMMA	E	1.907	12.55	1	1.907	126.1
Adhesive	G_0	1.403	9.24	1	1.403	92.8
PMMA	ν	0.332	2.18	1	0.332	21.93
PMMA	ΔG_α	0.159	1.05	1	0.159	10.51
PC	ΔG_β	0.021	0.13	1	0.021	
PMMA	$\alpha_\beta^{\mathrm{p}}$	0.019	0.12	1	0.019	
PMMA	t_β^{ss}	0.018	0.12	1	0.018	
PC	ν	0.01	0.07	1	0.01	
Total		15.19	100			

Table C–6: ANOVA for the dissipation for ±30% variation of all input factors.

Material	Parameter	Sum of Squares (SS)	% total SS	DOF	Mean SS	F
PMMA	E	2251.	70.89	1	2251.	1034.
PC	E	386.7	12.17	1	386.7	177.5
Adhesive	G_0	300.3	9.45	1	300.3	137.9
PC	ν	113.5	3.57	1	113.5	52.12
PMMA	ν	92.38	2.91	1	92.38	42.41
PC	ΔG_β	20.83	0.66	1	20.83	9.56
PC	t_α^{ss}	7.650	0.24	1	7.650	
PC	ΔG_α	1.726	0.05	1	1.726	
PMMA	ΔG_α	1.054	0.03	1	1.054	
PMMA	t_β^{ss}	0.446	0.01	1	0.446	
PMMA	$\alpha_\beta^{\mathrm{p}}$	0.093	0	1	0.093	
Total		3176.3	100			

Table C–7: ANOVA for the crack length for ±30% variation of all input factors.

Input factor		Dissipation		Crack length	
		Normalized sensitivity coefficient	*p*-value	Normalized sensitivity coefficient	*p*-value
PMMA	E	N/A		N/A	
	ν				
	ΔG_α	0.549	**<0.0001**	0.616	**<0.0001**
	$\alpha_\beta^{\mathrm{p}}$	0.040	0.615	0.063	0.482
	t_β^{ss}	0.013	0.867	-0.026	0.769
PC	E	N/A		N/A	
	ν				
	ΔG_α	-1.0	**<0.0001**	-0.235	**0.009**
	t_α^{ss}	-0.628	**<0.0001**	-0.016	0.861
	ΔG_β	0.300	**0.0002**	0.014	0.880
Adhesive	G_0	0.475	**<0.0001**	-1.00	**<0.0001**
R^2		0.52		0.38	

Table C–8: Normalized sensitivity coefficients, *p*- and R^2 values for ±10% variation of all input factors except for Young's moduli and Poisson's ratios of PMMA and PC.

Material	Parameter	Sum of Squares (SS)	% total SS	DOF	Mean SS	F
PC	ΔG_α	0.572	49.98	1	0.572	157.36
PC	t_α^{ss}	0.222	19.43	1	0.222	61.17
PMMA	ΔG_α	0.171	14.91	1	0.171	46.94
Adhesive	G_0	0.127	11.12	1	0.127	35.00
PC	ΔG_β	0.051	4.48	1	0.051	14.11
PMMA	$\alpha_\beta^{\mathrm{p}}$	0.001	0.08	1	0.001	
PMMA	t_β^{ss}	0.0001	0.01	1	0.0001	
Total		1.145	100			

Table C–9: ANOVA for the dissipation for ±10% variation of all input factors except the elastic moduli of PMMA and PC.

Material	Parameter	Sum of Squares (SS)	% total SS	DOF	Mean SS	F
Adhesive	G_0	5.569	69.35	1	5.569	124.77
PMMA	ΔG_α	2.122	26.42	1	2.122	47.53
PC	ΔG_α	0.311	3.88	1	0.311	6.97
PMMA	$\alpha_\beta^{\mathrm{p}}$	0.022	0.28	1	0.022	
PMMA	t_β^{ss}	0.004	0.05	1	0.004	
PC	t_α^{ss}	0.001	0.02	1	0.001	
PC	ΔG_β	0.001	0.01	1	0.001	
Total		8.03	100			

Table C–10: ANOVA for the crack length for ±10% variation of all input factors except for the elastic moduli of PMMA and PC.

Input factor		Dissipation		Crack length	
		Normalized sensitivity coefficient	*p*-value	Normalized sensitivity coefficient	*p*-value
PMMA	E	N/A		N/A	
	ν				
	ΔG_α	0.343	**<0.0001**	0.132	**0.001**
	$\alpha_\beta^{\mathrm{p}}$	-0.015	0.725	-0.037	0.328
	t_β^{ss}	-0.022	0.606	-0.022	0.558
PC	E	N/A		N/A	
	ν				
	ΔG_α	-1.0	**<0.0001**	-0.112	**0.003**
	t_α^{ss}	-0.702	**<0.0001**	-0.104	0.006
	ΔG_β	-0.083	0.051	-0.228	**<0.0001**
Adhesive	G_0	0.511	**<0.0001**	-1.0	**<0.0001**
R^2		0.784		0.732	

Table C–11: Normalized sensitivity coefficients, *p*- and R^2 values for ±30% variation of all input factors except for Young's moduli and Poisson's ratios of PMMA and PC.

Material	Parameter	Sum of Squares (SS)	% total SS	DOF	Mean SS	F
PC	ΔG_{α}	4.203	53.53	1	4.203	565.79
PC	t_{α}^{ss}	2.041	26	1	2.041	274.73
Adhesive	G_0	1.084	13.81	1	1.084	145.97
PMMA	ΔG_{α}	0.491	6.26	1	0.491	66.15
PC	ΔG_{β}	0.028	0.36	1	0.028	
PMMA	t_{β}^{ss}	0.002	0.03	1	0.002	
PMMA	$\alpha_{\beta}^{\mathrm{p}}$	0.001	0.01	1	0.001	
Total		7.85	100			

Table C–12: ANOVA for the dissipation for ±30% variation of all input factors except for the elastic moduli of PMMA and PC.

Material	Parameter	Sum of Squares (SS)	% total SS	DOF	Mean SS	F
Adhesive	G_0	159.1	91.31	1	159.1	713.27
PC	ΔG_{β}	8.345	4.79	1	8.345	37.42
PMMA	ΔG_{α}	2.762	1.59	1	2.762	12.38
PC	ΔG_{α}	2.007	1.15	1	2.007	9
PC	t_{α}^{ss}	1.728	0.99	1	1.728	7.75
PMMA	$\alpha_{\beta}^{\mathrm{p}}$	0.214	0.12	1	0.214	
PMMA	t_{β}^{ss}	0.077	0.04	1	0.077	
Total		174.2	100			

Table C–13: ANOVA for the crack length for ±30% variation of all input factors except for the elastic moduli of PMMA and PC.

Appendix D: Variations in the Layer Thicknesses and in the Impact Velocity

D.1 Correlation of the Inputs and the Outputs

x1	1.000								
x2	0.053	1.000							
x3	-0.004	0.048	1.000						
x4	-0.053	0.041	-0.012	1.000					
y1	-0.589	-0.338	-0.088	0.674	1.000				
y2	-0.033	0.101	-0.507	0.673	0.561	1.000			
y3	0.179	0.137	0.168	0.953	0.476	0.559	1.000		
y4	-0.108	-0.343	-0.288	0.882	0.761	0.681	0.747	1.000	
y5	0.855	0.093	0.165	-0.013	-0.637	-0.161	0.218	-0.126	1.000
	x1	x2	x3	x4	y1	y2	y3	y4	y5

Table D–1: Histories of minimum, 10th percentile, 50th and 90th percentiles and mean of the contact force and deflection.

key to the inputs and outputs

x1:	thickness of PMMA	x4:	impact velocity v_0	y3:	rcforc, 1st peak
x2:	thickness of adhesive	y1:	dissipation	y4:	rcforc, valley
x3:	thickness of PC	y2:	crack length	y5:	rcforc, 2nd peak

D.2 ANOVA

Parameter	Sum of Squares (SS)	% total SS	DOF	Mean SS	F
impact velocity	1.367	51.78	1	1.367	338.66
thickness of PMMA	0.908	34.4	1	0.908	224.99
thickness of adhesive	0.351	13.29	1	0.351	86.9
thickness of PC	0.014	0.54	1	0.014	
Total	2.64	100			

Table D–2: ANOVA for the dissipation for variations in the layer thicknesses and in the impact velocity.

Parameter	Sum of Squares (SS)	% total SS	DOF	Mean SS	F
impact velocity	5.404	62.43	1	5.404	143.87
thickness of PC	3.133	36.2	1	3.133	83.42
thickness of adhesive	0.118	1.37	1	0.118	
thickness of PMMA	0.00	0.00	1	0.00	
Total	8.655	100			

Table D–3: ANOVA for the crack length for variations in the layer thicknesses and in the impact velocity.

Appendix E: Material model for the Transparent Material

The material models for the PMMA and the PC differ only in the values of material parameters. We thus briefly describe material model for the PC, and refer the reader to Mulliken and Boyce [6] and Varghese and Batra [7] for details. We assume that the total Cauchy stress tensor $\boldsymbol{\sigma}$ at a material point equals the sum of contributions from three phases, namely B, α and β, i.e., $\boldsymbol{\sigma} = \boldsymbol{\sigma}_{\mathrm{B}} + \boldsymbol{\sigma}_{\alpha} + \boldsymbol{\sigma}_{\beta}$. The three phases coexist at a material point and have the same value of the deformation gradient **F**. The phase B behaves like a non-linear elastic Langevin spring for which

$$\boldsymbol{\sigma}_{\mathrm{B}} = \frac{C_{\mathrm{R}}}{3}\frac{\sqrt{N_l}}{\lambda^{\mathrm{p}}} L^{-1}\left(\frac{\lambda^{\mathrm{p}}}{\sqrt{N_l}}\right)\overline{\mathbf{B}}'_{\mathrm{B}} \tag{E–1}$$

Here $\boldsymbol{\sigma}_{\mathrm{B}}$ is the Cauchy stress tensor, $\overline{\mathbf{B}}'_{\mathrm{B}}$ the deviatoric part of $\overline{\mathbf{B}}_{\mathrm{B}} = (J)^{-2/3}\mathbf{F}\mathbf{F}^{\mathrm{T}}$, $\lambda^{\mathrm{p}} = \sqrt{\mathrm{tr}(\overline{\mathbf{B}}_{\mathrm{B}})/3}$ a measure of stretch, $\mathrm{tr}()$ the trace operator, $\mathbf{F}$ the deformation gradient, J the determinant of $\mathbf{F}$, L^{-1} the inverse of the Langevin function defined by $L(\beta) \equiv \coth\beta - 1/\beta$, N_l the limiting stretch, $C_{\mathrm{R}} \equiv n_{\mathrm{R}} k\theta$ the rubbery modulus, θ the temperature in Kelvin, k Boltzmann's constant, and n_{R} a material parameter.

The other two phases, α and β, are modeled with the same constitutive equation but with different values of material parameters. For each phase the deformation gradient **F** is decomposed into elastic and plastic parts, $\mathbf{F} = \mathbf{F}^{\mathrm{e}}_{\alpha}\mathbf{F}^{\mathrm{p}}_{\alpha} = \mathbf{F}^{\mathrm{e}}_{\beta}\mathbf{F}^{\mathrm{p}}_{\beta}$. The rate of the plastic deformation gradient, $\dot{\mathbf{F}}^{\mathrm{p}}_{\alpha}$, in phases α and β is given by

$$\dot{\mathbf{F}}^{\mathrm{p}}_{\alpha} = \mathbf{F}^{\mathrm{e}\,-1}_{\alpha}\tilde{\mathbf{D}}^{\mathrm{p}}_{\alpha}\mathbf{F} \quad , \quad \dot{\mathbf{F}}^{\mathrm{p}}_{\beta} = \mathbf{F}^{\mathrm{e}\,-1}_{\beta}\tilde{\mathbf{D}}^{\mathrm{p}}_{\beta}\mathbf{F} \tag{E–2}$$

where $\tilde{\mathbf{D}}^{\mathrm{p}}_{i}$ is the plastic strain rate tensor in phase i ($i = \alpha, \beta$), and it has been assumed that the plastic spin tensors in phases α and β identically vanish.

The Hencky elastic strain tensors of phases α and β are defined as

$$\boldsymbol{\varepsilon}^{\mathrm{e}}_{\alpha} = \ln\left(\sqrt{\mathbf{F}^{\mathrm{e}}_{\alpha}\mathbf{F}^{\mathrm{e}\,\mathrm{T}}_{\alpha}}\right) \quad , \quad \boldsymbol{\varepsilon}^{\mathrm{e}}_{\beta} = \ln\left(\sqrt{\mathbf{F}^{\mathrm{e}}_{\beta}\mathbf{F}^{\mathrm{e}\,\mathrm{T}}_{\beta}}\right) \tag{E–3}$$

and the corresponding Cauchy stress tensors are given by

$$\boldsymbol{\sigma}_{\alpha} = \frac{1}{J}\left[2\mu_{\alpha}\boldsymbol{\varepsilon}^{\mathrm{e}}_{\alpha} + \lambda_{\alpha}\mathrm{tr}(\boldsymbol{\varepsilon}^{\mathrm{e}}_{\alpha})\boldsymbol{\delta}\right] \quad , \quad \boldsymbol{\sigma}_{\beta} = \frac{1}{J}\left[2\mu_{\beta}\boldsymbol{\varepsilon}^{\mathrm{e}}_{\beta} + \lambda_{\beta}\mathrm{tr}(\boldsymbol{\varepsilon}^{\mathrm{e}}_{\beta})\boldsymbol{\delta}\right] \tag{E–4}$$

where Young's moduli of phases α and β of the PC and consequently Lame's constants, λ and μ, are temperature and strain-rate dependent. We note that Eq. (E–4) is valid for finite deformations and accounts for all geometric nonlinearities.

The plastic strain rates, $\tilde{\mathbf{D}}^{\mathrm{p}}_{\alpha}$, are assumed to be coaxial with the deviatoric Cauchy stress tensors in their respective phases, that is,

$$\tilde{\mathbf{D}}_{\alpha}^{\mathrm{p}} = \dot{\gamma}_{\alpha}^{\mathrm{p}} \frac{\boldsymbol{\sigma}_{\alpha}^{'}}{\left|\boldsymbol{\sigma}_{\alpha}^{'}\right|} \quad , \quad \tilde{\mathbf{D}}_{\beta}^{\mathrm{p}} = \dot{\gamma}_{\beta}^{\mathrm{p}} \frac{\boldsymbol{\sigma}_{\beta}^{'}}{\left|\boldsymbol{\sigma}_{\beta}^{'}\right|} \tag{E–5}$$

where $\boldsymbol{\sigma}_i^{'}$ ($i = \alpha, \beta$) is the deviatoric part of the Cauchy stress in phase i, $\left|\boldsymbol{\sigma}_i^{'}\right| = \sqrt{\mathrm{tr}\left(\boldsymbol{\sigma}_i' \boldsymbol{\sigma}_i'\right)}$ is the magnitude of $\boldsymbol{\sigma}_i^{'}$, and $\dot{\gamma}_i^{\mathrm{p}}$ is the effective plastic strain rate in phase i. This equation implies that $\mathrm{tr}(\tilde{\mathbf{D}}_i^{\mathrm{p}}) = 0$.

The effective plastic strain rates in α and β phases are given by

$$\dot{\gamma}_i^{\mathrm{p}} = \dot{\gamma}_{0i}^{\mathrm{p}} \exp\left[-\frac{\Delta G_i}{k\theta} \left(1 - \frac{\tau_i}{t_i \hat{s}_i + \alpha_i^{\mathrm{p}} p} \right) \right] \quad , \quad i = \alpha, \beta \tag{E–6}$$

where $\dot{\gamma}_{0i}^{\mathrm{p}}$ ($i = \alpha, \beta$) is the pre-exponential factor, ΔG_i the activation energy, $p = -\mathrm{tr}(\boldsymbol{\sigma})/3$ the pressure, $\tau_i = \sqrt{0.5\mathrm{tr}\left(\boldsymbol{\sigma}_i^{'} \boldsymbol{\sigma}_i^{'}\right)}$ the effective stress, α_i^{p} the pressure coefficient, $\hat{s}_i = 0.077\mu_i/(1-\nu_i)$ the athermal shear strength, ν_i Poisson's ratio, k Boltzmann's constant, and t_i an internal variable that evolves with plastic deformations. The evolution of internal variable t_i in phases α and β is given by

$$\dot{t}_i = \frac{h_i}{\hat{s}_i^0} \left(1 - \frac{t_i}{t_i^{\mathrm{ss}}} \right) \dot{\gamma}_i^{\mathrm{p}} \quad , \quad i = \alpha, \beta \tag{E–7}$$

where t_i^{ss} and h_i are softening parameters, and $\hat{s}_i^0$ is the reference value of $\hat{s}_i$ given by the reference values of μ_i and ν_i.

We postulate that the energy dissipated during plastic deformations in the α and β phases is converted into heat, that is

$$\dot{Q} = J\left(\boldsymbol{\sigma}_{\alpha} : \tilde{\mathbf{D}}_{\alpha}^{\mathrm{p}} + \boldsymbol{\sigma}_{\beta} : \tilde{\mathbf{D}}_{\beta}^{\mathrm{p}} \right) \tag{E–8}$$

where $\dot{Q}$ is the heat generated per unit volume in the reference configuration.

We refer the reader to Mulliken's thesis [13], Mulliken and Boyce [6] and Varghese and Batra [7] for the determination of values of the 16 material parameters from the test data for the PC that are given in Table E–1, and for the comparison of the computed and experimental axial stress vs. axial strain curves.

	Phase α	Phase β	Phase B	Common
v_i	0.38	0.38		
$\dot{\gamma}_{0i}^{\mathrm{p}}$ [/s]	2.94×10^{16}	3.39×10^{5}		
ΔG_i [J]	3.744×10^{-19}	3.769×10^{-20}		
α_i^{p}	0.168	0.245		
h_i [MPa]	125	400		
t_i^{ss}	0.33	2.00		
C_{R} at 300K [MPa]			35.0	
N_l			12.25	
ρ [g/cm^3]				1.20
E [GPa] at 300K, 5000/s	1.678	0.344		

Table E–1: Nominal values of material parameters for the PC.

References

[1] C.E. Anderson, T.J. Holmquist, Application of a computational glass model to compute propagation of failure from ballistic impact of borosilicate glass targets, Int J Impact Eng, 56 (2013) 2-11.
[2] C.E. Anderson Jr, T.J. Holmquist, Computational modeling of failure for hypervelocity impacts into glass targets, Procedia Engineering, 58 (2013) 194-203.
[3] C.C. Poteet, M.L. Blosser, Improving metallic thermal protection system hypervelocity impact resistance through numerical simulations, J Spacecraft Rockets, 41 (2004) 221-231.
[4] M.D. Morris, Factorial Sampling Plans for Preliminary Computational Experiments, Technometrics, 33 (1991) 161-174.
[5] A. Saltelli, K. Chan, E.M. Scott, Sensitivity analysis, Wiley New York, 2000.
[6] A.D. Mulliken, M.C. Boyce, Mechanics of the rate-dependent elastic-plastic deformation of glassy polymers from low to high strain rates, Int J Solids Struct, 43 (2006) 1331-1356.
[7] A.G. Varghese, R.C. Batra, Constitutive equations for thermomechanical deformations of glassy polymers, Int J Solids Struct, 46 (2009) 4079-4094.
[8] G.O. Antoine, R.C. Batra, Low Speed Impact of Laminated Polymethylmethacrylate/Adhesive/Polycarbonate Plates, Compos Struct, 116 (2014) 193-210.
[9] J.S. Stenzler, Impact mechanics of PMMA/PC multi-laminates with soft polymer interlayers, in, University Libraries, Virginia Polytechnic Institute and State University,, Blacksburg, VA., 2009.
[10] R.L. Iman, J.C. Helton, J.E. Campbell, An Approach to Sensitivity Analysis of Computer-Models .1. Introduction, Input Variable Selection and Preliminary Variable Assessment, J Qual Technol, 13 (1981) 174-183.
[11] R.L. Iman, J.C. Helton, J.E. Campbell, An Approach to Sensitivity Analysis of Computer-Models .2. Ranking of Input Variables, Response-Surface Validation, Distribution Effect and Technique Synopsis, J Qual Technol, 13 (1981) 232-240.
[12] F. Comets, Introduction aux probabilités et à la simulation aléatoire-Polycopié du Département de Mathématiques Appliquées, Ecole Polytechnique-Edition, (2004).
[13] A.D. Mulliken, Mechanics of amorphous polymers and polymer nanocomposites during high rate deformation, in, Massachusetts Institute of Technology, 2006, pp. 290 p.

5 Optimization of Transparent Laminates for Specific Energy Dissipation under Low Velocity Impact using Genetic Algorithm

G. O. Antoine and R. C. Batra*
Department of Biomedical Engineering and Mechanics, M/C 0219
Virginia Polytechnic Institute and State University
Blacksburg, VA 24061, USA
Email: antoineg@vt.edu; rbatra@vt.edu
*Corresponding author; Tel: 540-231-6051; Fax: 540-231-4574

5.1 Abstract

We employ a genetic algorithm to maximize the energy dissipated per unit areal density in laminates composed of layers of poly-methyl-metha-acrylate (PMMA), adhesive and polycarbonate (PC) impacted at low velocity by a rigid hemi-spherical nosed cylinder. Sources of energy dissipation considered are plastic deformations of the PC and the PMMA, cracking of the PMMA, viscous deformations of the adhesive, and the energy used to deform failed elements that are deleted from the analysis domain. Some of the challenging issues are appropriate constitutive relations for the three materials, failure criteria, and numerical techniques to accurately analyze finite deformations of different constituents. We model the PC and the PMMA as thermo-elasto-visco-plastic materials with constitutive relations proposed by Mulliken and Boyce and modified by Varghese and Batra, the adhesive as a thermo-visco-elastic material, and use the commercial finite element software LS-DYNA in which these material models have been implemented as user defined subroutines. This software is coupled with a genetic algorithm to optimize the layup of the PC, the PMMA and the adhesive layers of the same thickness under the constraints that the top and the bottom layers are not adhesive, the PC and the PMMA layers must have an adhesive layer between them, and the total number of layers is fixed.

Key Words: Low-velocity impact, genetic algorithm, optimal design, energy dissipation

5.2 Introduction

Optimizing the impact performance of laminated structures can save mass and hence cost. Furthermore, using a computational algorithm to optimize the design can minimize the number of prototypes to be built and tested. Florence [1] gave an analytical expression for estimating the ballistic limit of a two-component ceramic-faced armor as a function of the impactor mass and radius, and of the ply thicknesses, mass densities, failure strains and the ultimate tensile strength of the armor materials. Ben-Dor et al. [2] modified the expression by scaling the predicted ballistic limit with a parameter that is determined from the available experimental data and formulated a condition of optimality for the armor design for constant areal density but the thicknesses of the two plates as variables. Ben-Dor et al. [3] used the modified expression to optimally design armor, provided closed-form simple solutions to the optimization problem and showed that the range of possible designs giving almost identical ballistic performance is broad. Hetherington [4] used Florence's [1] expression to optimally design a ceramic/aluminum armor by keeping the areal density constant and analytically finding the range of thickness ratios for the highest ballistic limit of the armor. Hetherington found that the impact performance is better when the ceramic tile is thicker than the backing plate, and verified the optimal design through physical tests.

Here we use a genetic algorithm (GA) to maximize the energy dissipated during the low-velocity impact (below the perforation limit) of a rectangular laminate clamped on all edges of a given areal density. The laminate is composed of different layers of poly-methyl-metha-acrylate (PMMA), adhesive and polycarbonate (PC). Since the mass density of the three materials is nearly the same, the design variables are the arrangement of layers under the constraint that the adhesive layer cannot be one of the major surfaces and the PMMA and the PC layers must have an adhesive layer between them. The problem has been simplified by assuming that each layer is of the same thickness, and the adjacent layers are perfectly bonded to each other. Thus only the arrangement (or the layup) of layers is to be determined. This optimization problem is similar to that of a fiber-reinforced laminate with the fiber orientation angle in each layer as the design variable; e.g. see Batra and Jin [5]. Qian and Batra [6], Goupee and Vel [7] and Batra [8] studied the spatial variation of elastic moduli to optimize either the fundamental frequency or the stress distribution in a structure. The optimization problem of minimizing a laminate weight while fulfilling requirements of the strength, fundamental frequency, buckling load and/or strain limit have been studied, amongst others, by Nagendra et al. [9, 10], Gantovnik et al. [11], Nagendra et al. [12], Kogiso et al. [13], Gantovnik et al. [14], and Malott et al. [15]. Another class of problems is to maximize a structural property, typically the buckling load, while keeping the number of plies or the weight constant; e.g., see Soremekun et al. [16].

Punch et al. [17] and Punch et al. [18] used a GA to optimally design a laminated beam for the maximum energy absorption when a point load is suddenly applied at the center of the top surface. Poirier et al. [19] used the GA to analyze a multi-objective problem for a laser welded steel beam.

The major contribution of the present work is in applying the GA technique to a transient coupled thermo-elasto-viscoplastic problem involving finite deformations, material failure, cracking and significant plastic deformations.

5.3 Problem definition and method

5.3.1 Initial-boundary-value problem

A schematic sketch of the impact problem studied is depicted in Fig.5–1. A $L_1 \times L_2$ rectangular clamped laminated plate made of n layers of thickness h_1 through h_n and total thickness $h = \Sigma h_i$ is impacted at normal incidence by a hemispherical nosed rigid impactor of mass m moving at velocity v_0. The layers are made of PMMA, PC, DFA4700 or IM800A. The PMMA and the PC are glassy transparent polymers, while the DFA4700 and the IM800A are transparent viscous adhesives. The thermo-elasto-visco-plastic material model developed by Mulliken and Boyce [20] and modified by Varghese and Batra [21] is used for the PMMA and the PC. The DFA4700 and the IM800A are modeled as nearly incompressible viscous rubbery materials with the elastic response represented by the Ogden energy potential and the viscoelastic response by a hereditary type integral. Effects of both geometric and material nonlinearities are considered. The different layers are assumed to be perfectly bonded and the continuity of displacements and surface tractions is imposed between adjacent layers. Thus successive layers made of the same material are equivalent to one thick layer. The mass densities of the PMMA, the PC, the DFA4700 and the IM800A are taken to equal 1.2, 1.2, 1.1 and 1.0 g/cm^3. The constitutive relations and values of material parameters for these materials are given in [20-22]. Similarly, partial differential equations governing deformations of the system, and the initial and the boundary conditions are summarized in

[22]. In the present work we take L_1=L_2=120 mm, h=4.0 mm, n = 12 and h_1 through h_n = 0.33 mm. The spherical rigid impactor of radius R = 5 mm and mass m = 35 g impacts the plate center at v_0 = 20 m/s.

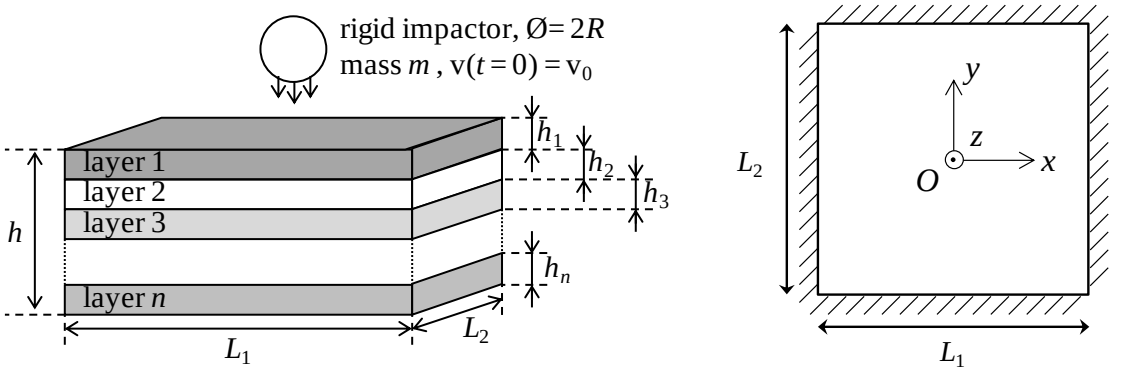

Fig.5–1: Sketch of the impact problem studied.

5.3.2 Optimization problem

Our goal is to find the material of the 12 layers that will maximize the energy dissipated during the impact. Whereas one usually considers the constraint of constant areal density (e.g. see [2-4]), here the layers are assumed to have fixed thickness. Since mass densities of the materials vary between 1.04 and 1.20 g/cm^3, variations in the areal density among the layers are small. We impose the constraint that layers 1 and 12 are made of either PMMA or PC and that the PMMA and the PC layers within the laminated plate cannot have common interfaces but must be bonded with an adhesive layer.

Material	PMMA	DFA4700	IM800A	PC
Code (value of the variable x_i)	1	2	3	4

Table 5–1: Coding of the materials.

We assign each material an integer between 1 and 4 as listed in Table 5–1 and denote the energy dissipation by the function f. Thus f is a function of x_1 through x_{12}, where the x_i is the material of the i^{th} layer, and the optimization problem is:

$$\text{maximize} \qquad f(x_1, x_2, \ldots, x_{12}) \tag{5–1a}$$

$$\text{subject to} \qquad x_1 = 1 \text{ or } x_1 = 4 \tag{5–1b}$$

$$x_{12} = 1 \text{ or } x_{12} = 4 \tag{5–1c}$$

$$|x_{i+1} - x_i| \le 2 \quad \text{for } 1 \le i \le 11 \tag{5–1d}$$

With constraints defined by Eq. (5–1b-d) there is a total of 885,922 admissible designs. The computational cost of evaluating the fitness of each design is unrealistically high which motivates the use of an optimization algorithm to explore the design space.

5.3.3 Genetic Algorithm

The optimization problem described by Eq. (5–1a-d) is solved by using a GA. A GA is a direct search method that uses ideas based on natural selection to explore the search space for finding a global optimum. Population initialization, parent selection, crossover, mutation and selection of the fittest are common elements in most GAs, e.g. see [16] and [23]. A GA generally involves the following steps: (i) generate an initial population of individuals, (ii) develop a scheme to select members for mating in the existing population with preference given to the fittest individuals (individuals with the highest objective function value), (iii) create children through mating, and (iv) replace the existing population. We follow guidelines presented in Refs. [16] and [23] for selecting individuals for mating, generating children, and enforcing the constraints. A random number generator is used to simulate approximate uniform distribution where evolution is directed by random numbers. The function of the GA is depicted in Fig.5–2.

5.3.3.1 Selection strategy for new parents

In a typical GA after a new population is formed the previous population is killed and is replaced by the new one. However, there is no guarantee that an individual in the new generation has higher fitness than that of the best individual in the previous one. In other words, there is no guarantee that the new generation is an improvement over the previous one in terms of fitness. Elitist selection strategies remedy this problem by keeping information about the best individual(s) from the previous generation and preserving the largest value of the objective function. In the present work we rely on two multiple elitist selection strategies, ME_1 and ME_2, introduced by Soremekun et al. [16]. These strategies and their comparison to the simple elitist selection strategy are briefly described below for the sake of completeness.

In the simple elitist selection strategy the weakest child of the new generation is replaced by the strongest parent of the previous one. After children are created from the parent population as described in the next section their fitnesses are evaluated. In a typical GA they become the new parent population and the process is repeated. The elitist selection strategy modifies the simple elitist strategy and replaces the child with the lowest fitness by the best parent which is thus carried over to the next generation. All children (except the weakest one) and the best parent become the new parents from which the new children are born. Thus information about the best individual is preserved and the algorithm is prevented from regressing.

The multiple elitist strategies ME_1 and ME_2 are variants of the elitist selection strategy. With P equaling the size of the population, and given P parents and P children whose fitnesses are known, the number N_k between 1 and P of the best individuals from the union of the children and parents (size $2P$) are carried over to the next parent population. In both strategies the parents and children are ranked according to their fitnesses and the N_k best individuals become new parents. ME_1 and ME_2 differ in the way the $(P–N_k)$ remaining spots in the new parent population are filled. In ME_1 they are filled with the $(P–N_k)$ best children that are still available for selection, while in ME_2 they are filled with $(P–N_k)$ children selected randomly from the remaining ones. The choice of N_k is crucial since it affects the reliability of the algorithm and the richness of the population. Soremekun et al. [16] have proved that the choice $N_k \ll P$ ensures reliability of the multiple elitist selection schemes while maintaining enough richness. They used

P = 20 and N_k = 4 in one of their studies and here we take P = 16 and N_k = 3 which gives the ratio N_k /P about the same as that in Soremekun et al. [16].

5.3.3.2 Formation of the children

Starting with a parent population the goal is to create a children population by combining genes of the parents giving preference to the best parents. The different steps are selection for mating, combination, and mutation.

The roulette-wheel selection is used to select two parents for mating. The probability is biased such that the best parents have more chance of being selected than parents with lower fitness. After ranking the parent population according to their fitness the i^{th} best parent is given the fraction

$$p_i = \frac{2(P+1-i)}{P(P+1)} \tag{5–2}$$

of the roulette-wheel. Formally, the interval $[\varphi_{i-1}, \varphi_i[$ is attributed to the i^{th} best parent where $\varphi_0 = 0$ and $\varphi_i = \varphi_{i-1} + p_i$. Then, a random number in [0,1[is generated and the parent whose interval contains this number is selected. To form a pair of parents for mating the roulette-wheel selection is repeated until two distinct parents are selected for mating.

The mating parents are then combined to form two children. We use here one-point crossover: a position is randomly chosen along with the chromosome of one mating parent and the tails of the parent chromosomes (i.e., the genes located after the chosen position) are exchanged. Two children are created in this process, thus the size of the population remains constant. The purpose of the crossover is to exchange good building blocks between individuals to explore new designs.

A small variability is added by mutations in order to create new designs throughout the generations. Each gene of each child has a fixed small probability of undergoing mutation. If a gene is selected for mutation its value is randomly changed to a different one.

Specific operators tailored for stacking sequence optimization of laminates have been introduced, such as ply addition, deletion, swap and permutation (e.g., see Adams et al. [23]). They are, however, not included in the present study.

There is a chance that the new designs created after crossover and mutation do not satisfy the condition (5–1d). The children that violate this constraint go through the process described below before being included in the new parent population.

5.3.3.3 Constraints

The simple bound constraints listed in Eq.(5–1b, c) are not violated by crossover or mutation. However, the constraint given by Eq.(5–1d) that PMMA and PC layers don't have common interfaces is more complex. Rather than using a penalty-method we adopt a repair technique to satisfy this constraint. After the children are born their genes are modified to respect the constraint. Michalewicz [24] and Michalewicz and Schoenauer [25] used a reparation method to satisfy constraints. Coello [26] and Watanabe [27] have reported that the reparation algorithm is a good choice when an infeasible solution

can be easily transformed into a feasible solution. A limitation of this method, however, is that the repair algorithm is problem-specific. Here we use a reparation algorithm to remove constraint violations while preserving (as far as possible) the total number of PC and PMMA layers and their relative positions since they contribute to the energy dissipated during the impact. When needed, the following procedure is followed to repair the chromosomes. When two consecutive layers are made of either the PC or the PMMA, one of these layers is deleted and the "empty space" created in the chromosome is used to shift the genes and insert an adhesive (randomly IM800A or DFA4700) layer. If the constraint is still violated after this step then we look for and delete consecutive layers made of either the PMMA or the PC. If all constraints are still not satisfied then the algorithm replaces the material of one layer at each remaining PMMA/PC interface with an adhesive. Thus the constraints are always respected. The rationale for these modifications is that viscous deformations of the adhesive materials dissipate negligible amount of energy and their purpose is only to bond the PMMA and the PC layers. It was observed that in most cases the first two steps suffice to satisfy all constraints. Thus the reparation method described here has the advantage of rarely modifying the number of the PMMA and the PC layers or their respective positions within the plate.

5.3.3.4 Fitness evaluation

For the problem studied here, the fitness of an individual is the amount of energy dissipated during the impact event. This energy is numerically evaluated using the finite element (FE) software LS-DYNA. The computational cost is reduced by studying deformations of a quarter of the plate-impactor system with symmetry boundary conditions applied on appropriate surfaces and using a coarse FE mesh of 35,854 elements. The thickness of each layer is discretized using two 8-node brick elements with one integration point in each element. A minimum of two such FEs through the thickness are needed to consider the bending stiffness of a layer. Elements have nearly 1:1:1 aspect ratio in the vicinity of the center of impact. Results for the optimized configuration are checked by using a finer FE mesh as described in section 5.4. Computing the fitness values of the 16 members of a generation requires about 1.5 hours clock time with the MPP version of LS-DYNA on 48 Intel Xeon 2.5 GHz processors with a FDR-10 (40Gbps) Infiniband.

One of the outputs of LS-DYNA is the eroded energy of deleted elements that form cracks. For the intact elements the energy dissipated per unit volume due to plastic and viscous deformations is found, and the total dissipated energy is determined.

The GA software has been developed in FORTRAN. The population fitness (i.e., the energy dissipated) is found as described in the preceding paragraph. The GA forms the new population which is used in the FE simulations, and the cycle repeated till the optimum solution has been found as described in the following flow chart.

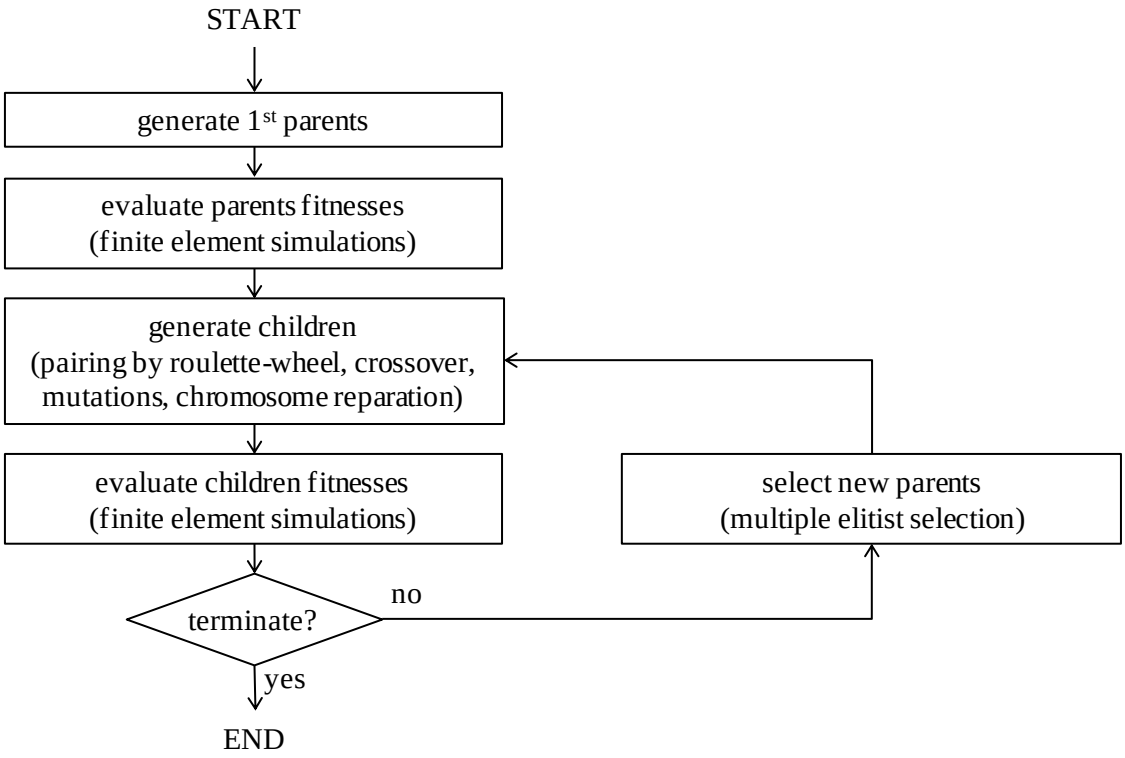

Fig.5–2: Schematic representation of the genetic algorithm.

5.4 Results and discussion

5.4.1 Performance of the algorithm

Four optimizations for each selection scheme, ME_1 and ME_2 , have been carried out. The maximum number of generations is set to 100 and the mutation probability to 0.0833 (one mutation per individual on average). In Fig.5–3 we show the average of the best individuals of each optimization run and the overall best individual as a function of the generation for the two selection schemes.

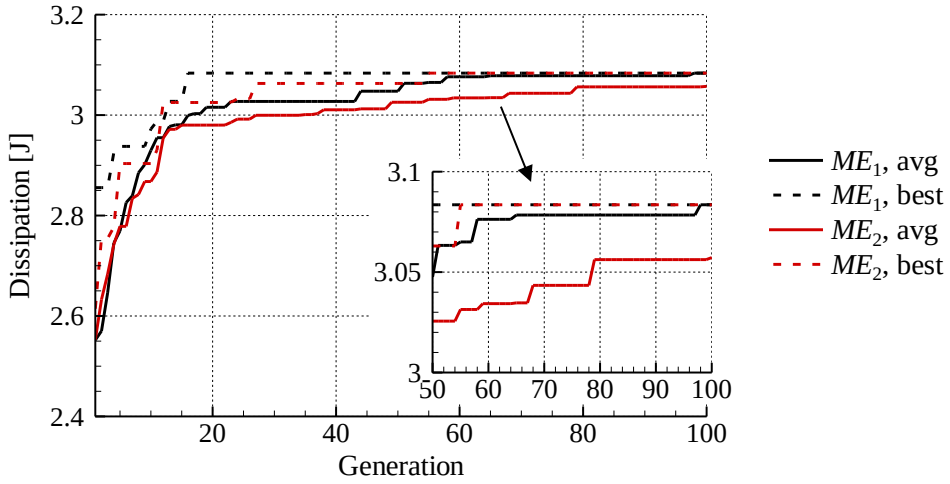

Fig.5–3: Maximum and average fitness of the best individuals of the populations as a function of the generation number.

Design improvements obtained with the optimization algorithm are summarized in Table 5–2. The best initial fitness and the best final fitness as well as the corresponding relative improvement are given for each run.

	ME_1 selection scheme				ME_2 selection scheme			
	run 1	run 2	run 3	run 4	run 1	run 2	run 3	run 4
Best initial fitness [J]	2.54	2.40	2.42	2.86	2.60	2.56	2.43	2.61
Best final fitness [J]	3.08	3.08	3.08	3.08	3.03	3.08	3.03	3.08
Improvement	22%	29%	28%	8%	17%	20%	25%	18%

Table 5–2: Summary of design improvements.

About 20% improvement in the laminate performance could be obtained in all cases in less than 100 generations. The four runs using the ME_1 selection scheme yielded the same best design (see Table 5–3) and energy dissipation = 3.08 J. This design was found in two runs using ME_2 while the two remaining runs did not find it and yielded sub-optimal designs (see Table 5–3).

Fitness	Stacking sequence											
3.084 J	PC	IM	PC	IM	PMMA	IM	IM	PMMA	PMMA	PMMA	DFA	PC
3.032 J	PC	IM	PC	IM	PMMA	PMMA	IM	PMMA	PMMA	PMMA	DFA	PC
3.030 J	PC	IM	DFA	PC	IM	PC	IM	PMMA	PMMA	PMMA	PMMA	PMMA

Table 5–3: Final designs found by the GA. The best design was found in all runs using ME_1 and two runs using ME_2. The remaining runs with ME_2 gave designs of rows 2 and 3 of the Table.

In order to analyze the energy dissipated in different layers of the best design, and to verify the accuracy of the energy dissipation, an impact simulation using the best design and a finer mesh was performed. The number of FEs in each spatial direction is multiplied by 1.5 to give a mesh with 116,644 elements versus

35,854 for the initial mesh. Note that in the initial mesh there are two elements through the thickness of each layer while the finer mesh has three elements. The total energy dissipated using the finer mesh was found to be 2.98 J which is 3.3% less than that found with the coarse mesh. This shows that the simulations using the coarse mesh provided reasonable values of the dissipated energy and hence the population fitness.

5.4.2 Analysis of the best design

For the best design configuration we have summarized in Table 5–4 the energy dissipated due to various mechanisms in each layer. It is clear that in the PMMA material, the energy is dissipated mainly through

Layer #	Material	Eroded Energy (cracking) [J]	Plastic deformations [J]	**Total [J]**
1	PC	0.000	0.563	**0.563**
2	IM	0.000	0.000	**0.000**
3	PC	0.000	0.639	**0.639**
4	IM	0.000	0.000	**0.000**
5	PMMA	0.086	0.002	**0.087**
6	IM	0.000	0.000	**0.000**
7	IM	0.000	0.000	**0.000**
8	PMMA	0.105	0.001	**0.106**
9	PMMA	0.104	0.001	**0.105**
10	PMMA	0.113	0.002	**0.115**
11	DFA	0.000	0.000	**0.000**
12	PC	0.000	1.367	**1.367**
Total [J]		**0.407**	**2.575**	**2.982**

Table 5–4: Energy dissipated in each layer for the best design.

cracking (modeled with element deletion) while the energy dissipated due to its plastic deformations is small. The PC material can undergo large plastic deformations without failing and didn't fail in the simulations. The eroded energy in the PC layers is null but that due to its plastic dissipation is large. The energy dissipated in the IM800A and DFA4700 adhesives is negligible. Therefore the main sources of energy dissipation are the cracking of the PMMA and plastic deformations of the PC, which agrees with the results presented in [22] for the impact of PMMA/IM800A/PC and PMMA/DFA4700/PC laminates (layer thicknesses 1.5875, 0.635 and 1.5875 mm, 28.5 g spherical impactor with 5 mm radius and 12 or 22 m/s impact velocity).

We now provide a few observations on the optimal design of the laminate. The optimal design has very few thin PC layers and thus will have large plastic deformations for maximizing the energy dissipated. This will degrade laminate response to subsequent impacts. However, that was not a design criterion for the problem studied. A possibility is to modify the design criterion in future for considering more than one impact.

The time history of the contact force between the plate and the impactor is shown in Fig.5–4. There are two peaks separated by a local minimum ("valley") at time t = 0.9 ms. We note that the reaction force

exhibits oscillations of increasing amplitude before reaching the first peak at 0.75 ms with magnitude 1.1 kN. The second peak of about 1.3 kN is reached at time t = 1.15 ms. Similar time histories of the contact force low velocity impacts of laminates have been reported in [28, 29].

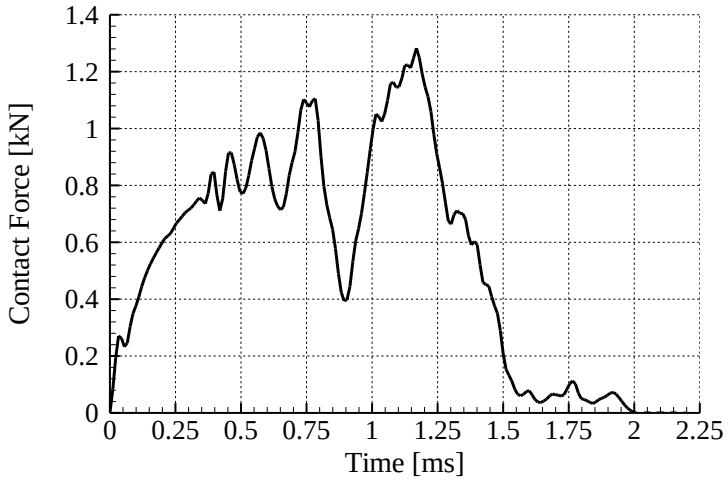

Fig.5–4: Time history of the reaction force for the 20 m/s impact of the best design.

Contours of the equivalent plastic strain in the PC layers near the center of impact are exhibited in Fig.5–5 and crack patterns in the PMMA material of the 5th, 8th, 9th and 10th layers are shown in Fig.5–6.

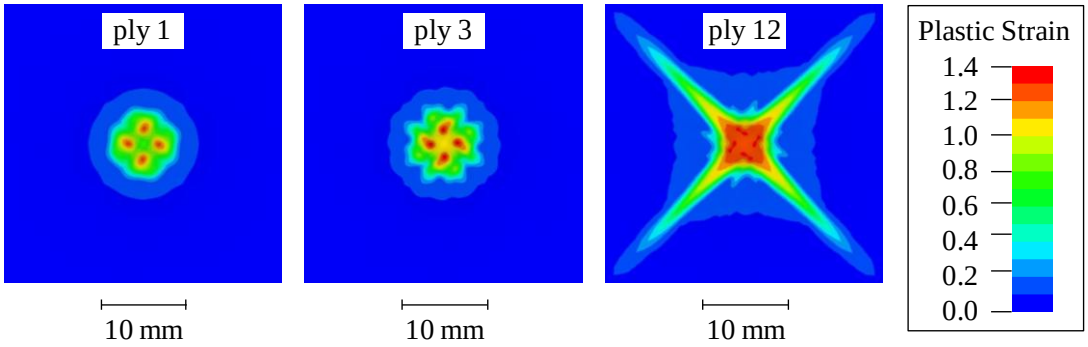

Fig.5–5: Details of the effective plastic strains in the PC layers of the best design.

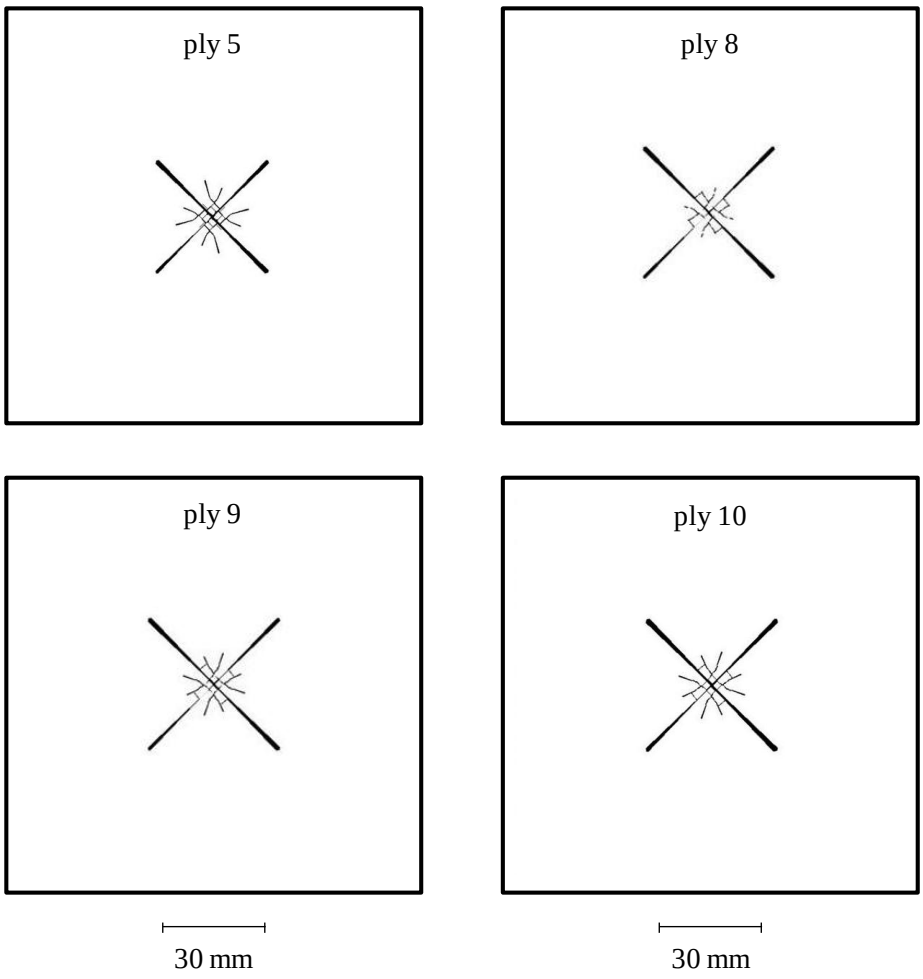

Fig.5–6: Crack pattern in the PMMA material of the 5th, 8th, 9th and 10th layers.

The largest plastic strains in the 1st, 3rd and 12th layers are 1.31, 1.40 and 1.38, respectively. The plastic deformations are highly localized in layers 1 and 3 and become negligible 5 mm away from the center of impact. In the rear layer, however, significant plastic deformations occur within 25 mm from the plate center. The crack patterns of plies 5 and 10 are comparable in terms of general appearance (long radial cracks and short secondary cracks that bifurcate) as well as length of the cracks. Penalizing the crack length in the objective function could give designs with smaller crack lengths which is an advantage since they degrade the transparency of the laminate.

5.5 Conclusions

The mathematical and computational models of the low-velocity impact of poly-methyl-metha-acrylate (PMMA)/adhesive/polycarbonate (PC) laminate developed previously have been supplemented with a genetic algorithm (GA) to find the layup of layers of the materials involved that will maximize the energy dissipated during the deformations. It has been assumed that all layers have the same thickness, the total number of layers is fixed, the adjacent PMMA and the PC layers must have an adhesive layer between them, and the top and the bottom layers are not adhesive. It is found that 20% increase in the value of the objective function (energy dissipated) could be achieved in 100 generations. Values of the energy

dissipated in each layer for the best design have shown that the PC layer has the most energy dissipated, and the viscous adhesive layers the least. Contrary to the laminate configuration often used in experiments, the layup with the PC rather than the PMMA layer at the top impacted surface enhances the energy dissipated. It is primarily due to the observation that the brittle failure of the PMMA layer consumes very little energy as compared to that need to plastically deform the PC layer. The significance of the work is in optimizing the design of a laminate whose constituents undergo large transient thermo-elasto-visco-plastic deformations.

5.6 Acknowledgments

This research was sponsored by the Army Research Laboratory and was accomplished under Cooperative Agreement Number W911NF-06-2-0014. The views and conclusions contained in this document are those of the authors and should not be interpreted as representing the official policies, either expressed or implied, of the Army Research Laboratory or the U.S. Government. The U.S. Government is authorized to reproduce and distribute reprints for Government purposes notwithstanding any copyright notation hereon.

References

[1] A. Florence, Interaction of projectiles and composite armour, part II. Standard Research Institute Menlo Park, California, in, AMMRC-CR-69-15, 1969.
[2] G. Ben-Dor, A. Dubinsky, T. Elperin, N. Frage, Optimization of two component ceramic armor for a given impact velocity, Theor Appl Fract Mec, 33 (2000) 185-190.
[3] G. Ben-Dor, A. Dubinsky, T. Elperin, Optimization of two-component composite armor against ballistic impact, Compos Struct, 69 (2005) 89-94.
[4] J.G. Hetherington, The Optimization of Two Component Composite Armors, Int J Impact Eng, 12 (1992) 409-414.
[5] R.C. Batra, J. Jin, Natural frequencies of a functionally graded anisotropic rectangular plate, J Sound Vib, 282 (2005) 509-516.
[6] L.F. Qian, R.C. Batra, Design of bidirectional functionally graded plate for optimal natural frequencies, J Sound Vib, 280 (2005) 415-424.
[7] A.J. Goupee, S.S. Vel, Two-dimensional optimization of material composition of functionally graded materials using meshless analyses and a genetic algorithm, Comput Method Appl M, 195 (2006) 5926-5948.
[8] R. Batra, Optimal design of functionally graded incompressible linear elastic cylinders and spheres, Aiaa J, 46 (2008) 2050-2057.
[9] S. Nagendra, R.T. Haftka, Z. Gurdal, Genetic Algorithms for the Design of Composite Panels, Eng Appl Fr, 14 (1995) 129-143.
[10] S. Nagendra, R.T. Haftka, Z. Gurdal, Stacking-Sequence Optimization of Simply Supported Laminates with Stability and Strain Constraints, Aiaa J, 30 (1992) 2132-2137.
[11] V.B. Gantovnik, C.M. Anderson-Cook, Z. Gurdal, L.T. Watson, A genetic algorithm with memory for mixed discrete-continuous design optimization, Comput Struct, 81 (2003) 2003-2009.
[12] S. Nagendra, D. Jestin, Z. Gurdal, R.T. Haftka, L.T. Watson, Improved genetic algorithm for the design of stiffened composite panels, Comput Struct, 58 (1996) 543-555.
[13] N. Kogiso, L.T. Watson, Z. Gürdal, R.T. Haftka, S. Nagendra, Design of composite laminates by a genetic algorithm with memory, Mechanics of Composite Materials and Structures, 1 (1994) 95-117.
[14] V.B. Gantovnik, Z. Gurdal, L.T. Watson, A genetic algorithm with memory for optimal design of laminated sandwich composite panels, Compos Struct, 58 (2002) 513-520.
[15] B. Malott, R. Averill, E. Goodman, Y. Ding, W. Punch, Use of genetic algorithms for optimal design of laminated composite sandwich panels with bending-twisting coupling, in: Proceedings of 37th AIAA/ASME/AHS/ASC Structures, Structural Dynamics, and Materials Conference, Salt Lake City, UT, 1996, pp. 1874-1881.
[16] G.A. Soremekun, Z. Gürdal, R.T. Haftka, L.T. Watson, Improving Genetic Algorithm Efficiency and Reliability in the Design and Optimization of Composite Structure, Department of Computer Science, Virginia Polytechnic Institute and State University, 1996.
[17] W.F. Punch, R.C. Averill, E.D. Goodman, S.C. Lin, Y. Ding, Y.C. Yip, Optimal-Design of Laminated Composite Structures Using Coarse-Grain Parallel Genetic Algorithms, Comput Syst Eng, 5 (1994) 415-423.
[18] W.F. Punch, R.C. Averill, E.D. Goodman, S.C. Lin, Y. Ding, Using Genetic Algorithms to Design Laminated Composite Structures, Ieee Expert, 10 (1995) 42-49.
[19] J.D. Poirier, S.S. Vel, V. Caccese, Multi-objective optimization of laser-welded steel sandwich panels for static loads using a genetic algorithm, Eng Struct, 49 (2013) 508-524.
[20] A.D. Mulliken, M.C. Boyce, Mechanics of the rate-dependent elastic-plastic deformation of glassy polymers from low to high strain rates, Int J Solids Struct, 43 (2006) 1331-1356.
[21] A.G. Varghese, R.C. Batra, Constitutive equations for thermomechanical deformations of glassy polymers, Int J Solids Struct, 46 (2009) 4079-4094.
[22] G.O. Antoine, R.C. Batra, Low Speed Impact of Laminated Polymethylmethacrylate/Adhesive/Polycarbonate Plates, Compos Struct, 116 (2014) 193-210.

[23] D.B. Adams, L.T. Watson, Z. Gurdal, Optimization and blending of composite laminates using genetic algorithms with migration, Mech Adv Mater Struc, 10 (2003) 183-203.
[24] Z. Michalewicz, A survey of constraint handling techniques in evolutionary computation methods, Com Adap Sy, (1995) 135-155.
[25] Z. Michalewicz, M. Schoenauer, Evolutionary Algorithms for Constrained Parameter Optimization Problems, Evol Comput, 4 (1996) 1-32.
[26] C.A.C. Coello, Theoretical and numerical constraint-handling techniques used with evolutionary algorithms: a survey of the state of the art, Comput Method Appl M, 191 (2002) 1245-1287.
[27] K. Watanabe, M.M.A. Hashem, Evolutionary computations : new algorithms and their applications to evolutionary robots, Springer, Berlin ; New York, 2004.
[28] J.S. Stenzler, N. Goulbourne, Impact mechanics of transparent multi-layered polymer composites, in: Society for Experimental Mechanics-SEM Annual Conference and Exposition on Experimental and Applied Mechanics, 2009, pp. V3.
[29] H.Y.T. Wu, F.K. Chang, Transient Dynamic Analysis of Laminated Composite Plates Subjected to Transverse Impact, Comput Struct, 31 (1989) 453-466.

6 Conclusions

The dissertation is composed of five chapters. The contents of chapter one have appeared in Composite Structures, and those of chapters two through four have been submitted to refereed journals for possible publication. The contents of chapter five will be submitted for publication in the near future.

In this work we present a mathematical model for analyzing the transient response of transparent laminates impacted at normal incidence by a low-speed rigid hemispherical-nosed cylinder. The model includes equations describing contact between the impactor and the plate and contact between different layers. Constitutive equations and failure criteria for two glassy transparent polymers (PMMA and PC) are selected from the literature and those for two rubbery viscous adhesives (DFA4700 and IM880A) are proposed. Delamination between adjacent layers is considered via traction-separation laws which account for progressive interface damage and softening. The constitutive relations have been implemented in the commercial finite element software LS-DYNA as user-defined material models. Failed elements are deleted from the analysis domain.

In the first chapter we analyze the impact response of monolithic PMMA and PC plates as well as laminated PMMA/DFA4700/PC and PMMA/IM800A/PC plates. The mathematical model has been validated by showing that the computed results agree well with the corresponding experimental results available in the literature. Subsequently, the low-velocity impact response of the laminated plates is extensively studied and interactions between their constituents are analyzed. The main sources of energy dissipation are identified as cracking of the brittle PMMA and plastic deformations of the PC while viscous deformations of the adhesive interlayer and delamination between adjacent layers dissipate negligible amounts of energy. This work provides a complete model (delamination, constitutive relations including strain-rate effects, temperature effects, plasticity, viscosity and failure criteria) for the analysis of the impact response of laminated transparent laminates.

In the second chapter the mathematical and the computational models are applied to the special case of the low- and high-velocity impact of doubly curved monolithic PC plates. The agreement between the predicted perforation velocity of flat panels and experimental results from the literature is found to be excellent. Compared with flat panels, curved plates are found to have increased impact resistance, as demonstrated by a decrease in the magnitude of the stresses inside the PC material in the vicinity of the impact zone. This could be due to stronger interaction between stretching and bending deformations than that in flat panels. It is found that with negative curvature the deformations of the PC plate are more localized which leads to larger plastic strains and degraded impact performance. Conversely, positive curvature increases the impact resistance of the panels. The effect of curvature on the impact resistance becomes less evident when the plate thickness is increased.

In the third chapter we explore the effect of various adhesives on the impact response of laminated structures. We propose constitutive equations to model mechanical deformations of nearly incompressible rubbery viscous adhesives and a methodology to find values of the material parameters. This technique is used to find values of three sets of material parameters for the DFA4700 and the IM800A adhesives. The constitutive equations for the adhesives are implemented in LS-DYNA, and the impact response of the laminated plates of the first chapter is studied. We compare the results obtained with the three sets of

parameters for each adhesive and show that the viscous energy dissipated by the adhesive interlayer depends on the values of these material parameters while the contact force, the crack length and the total energy dissipated have minor dependence upon values of these parameters. We draw the counter-intuitive conclusion that viscous dissipation of the adhesives does not necessarily increase when their response exhibits higher strain-rate sensitivity.

A large number of material parameters appear in the constitutive equations of the PMMA, the PC and the adhesive materials. The errors or uncertainties in the determination of their numerical values could either lead to instabilities in the numerical algorithms or give erroneous results. The preliminary sensitivity study presented in chapter four quantifies the effect of uncertainty in these values on the low-velocity impact response of a laminated plate. We identify five dominant parameters that are expected to significantly affect responses of the PMMA and the PC subjected to uniaxial deformations. These ten parameters and the elastic shear modulus of the DFA4700 adhesive are selected for a sensitivity study of the low-velocity impact of the laminated plate analyzed in the first chapter. A range of uncertainty is assumed for the values of material parameters and correlations between the individual parameters and the response of the plate are examined. We find that the dominant parameters are the elastic moduli of the PMMA, parameters strongly affecting plastic deformations of the PC, and the shear modulus of the adhesive. This work also reveals a strong correlation between the energy dissipated and the second peak in the time history of the contact force between the impactor and the laminate. This seems to be the first extensive study to relate variability of the impact response of a laminated plate to uncertainties in the values of material parameters of its constituents. Effects of uncertainties in geometric parameters and the impact speed on the response of a laminated plate to impact have also been studied.

In chapter five we integrate the mathematical model with a genetic algorithm to build an optimization tool. This tool is used to find plate designs that maximize the energy dissipated during the low-velocity impact of a laminated plate made of twelve layers. This has the advantage of replacing physical tests with numerical simulations for finding the optimal design of a plate tailored for a given impact scenario. It also seems to be the first study in which a computational algorithm is used with full-scale impact simulations to optimally design armor.

This work shows the advantages of using validated, science-based mathematical and computational models to simulate the response of plates to impact. Besides replacing expensive physical tests by reliable numerical simulations, it enhances our understanding of the thermo-mechanical response of laminates to impact loading. Moreover the proposed techniques can be used to efficiently find the optimal designs of armor that can be tested and verified with a reduced number of physical tests.

Appendix F: Sample input file

We give below an input file for use with LS-DYNA to simulate the impact of a laminated plate made of three materials (top layer, interlayer, bottom layer) with CZM elements placed at the two interlayer interfaces.

The PMMA and the PC were modeled as thermo-elasto-viscoplastic with a user-defined material model implemented in the "umat41" subroutine of the "dyn21.f" file of LS-DYNA. Their material cards are replaced here by cards for a linear elastic material with elastic constants corresponding to 2000/s strain rate and 300K temperature.

The DFA4700 and the IM800A materials were modeled as nearly incompressible viscoelastic rubbers with a user-defined material model implemented in the "umat44" subroutine of the "dyn21.f" file. They are replaced here with their "equivalent materials" from LS-DYNA material library, i.e, "MAT_OGDEN_RUBBER".

This input file is written for the 7.0.0 release of LS-DYNA with the double precision and SMP version. The name of the LS-DYNA package is "ls-dyna_smp_d_r7_0_0_x64_redhat57_ifort101.tgz".

```
*KEYWORD
$
$ this is a typical input deck for the 7.0.0 SMP double precision version of LS-DYNA
$ name of original LS-DYNA library: "ls-dyna_smp_d_r7_0_0_x64_redhat57_ifort101.tgz"
$
$    PRMR1      VAL1     PRMR2      VAL2     PRMR3      VAL3     PRMR4      VAL4
*PARAMETER
$ termination time  |   safety factor
R   endtim    4000.0R       sf      0.80
$# of hsv in d3plot | # of hsv in ASCII |   dt for ASCII    |   dt for ascii    |
I   hsvd3p        21I   hsvasc        58R    dtd3p     200.0R  dtAscii       5.0
$
$
*PARAMETER_EXPRESSION
$
$
$ impactor mass [mg]
R       mi 28.5e+3
$ impactor mass density [mg/mm^3]
R     rhoi &mi/((4.0/3.0)*3.14159265*5.0**3)
$
$
$ impact velocity [mm/us]   (initial gap 0.1mm is assumed betw. plate and impactor)
R       v0 22.0e-3
$
$
$  materials of the plate layers     1:PMMA  2:PC  3:DFA4700  4:IM800A
$  properties of the CZM at the adhesive interfaces are automatically deduced from "&mat02"
I    mat01      1
I    mat02      3
I    mat03      2
$
$
*TITLE
Impact PMMA/DFA4700/PC plate -- CZM 0.05mm
*COMMENT
Units used: mass=mg , length=mm , time=us
```

```
$
$                      ****************************************
$                      !        UNITS TO USE IN THE INPUT FILE  !
$                      !  mass:   mg      _\       force:  kN   !
$                      !  length: mm      _ )      stress: GPa  !
$                      !  time:   us       /       energy: J    !
$                      ****************************************
$
$                                 *  *  *  *  *  *  *
$
$                    ------------------------------------------------
$                    !             Material Definition              !
$                    ------------------------------------------------
$
$
*MAT_ELASTIC_TITLE
impactor
$ (switched to rigid later in the input deck)
$      MID       RHO         E        PR
        99&rhoi           15.0      0.30
$
*MAT_ELASTIC_TITLE
PMMA
$      MID       RHO         E        PR
         1   1.19e+0      4.32      0.35
*MAT_ELASTIC_TITLE
PC
$      MID       RHO         E        PR
         2   1.20e+0      1.96      0.38
*MAT_OGDEN_RUBBER_TITLE
DFA4700
$      MID        RO        PR         N        NV         G      SIGF
         3   1.08e+0     0.498         0         0
$      mu1       mu2       mu3       mu4       mu5       mu6       mu7       mu8
  6.958e-6 -3.318e-4
$   alpha1    alpha2    alpha3    alpha4    alpha5    alpha6    alpha7    alpha8
     7.954    -6.047
$       g1     beta1
  1.189e-3  3.750e-9
$       g2     beta2
 0.8255e-3 0.5305e-6
$       g3     beta3
  2.661e-3  6.136e-6
*MAT_ADD_EROSION_TITLE
sigp1=225MPa
$      MID      EXCL    MXPRES     MNEPS    EFFEPS    VOLEPS    NUMFIP       NCS
         3
$   MNPRES     SIGP1     SIGVM     MXEPS     EPSSH     SIGTH   IMPULSE    FAILTM
             0.225
*MAT_OGDEN_RUBBER_TITLE
IM800A
$      MID        RO        PR         N        NV         G      SIGF
         4   1.04e+0     0.498         0         0
$      mu1       mu2       mu3       mu4       mu5       mu6       mu7       mu8
  1.363e-3 -9.025e-5
$   alpha1    alpha2    alpha3    alpha4    alpha5    alpha6    alpha7    alpha8
     1.664    -6.642
$       g1     beta1
 0.2480e-3  2.602e-8
$       g2     beta2
 0.3587e-3  2.974e-6
```

```
*MAT_ADD_EROSION_TITLE
sigp1=170MPa
$      MID      EXCL    MXPRES     MNEPS    EFFEPS    VOLEPS    NUMFIP       NCS
         4
$   MNPRES     SIGP1     SIGVM     MXEPS     EPSSH     SIGTH   IMPULSE    FAILTM
              0.170
$
*MAT_COHESIVE_MIXED_MODE_TITLE
interface DFA-glass ; GIIc=2*GIc -- deltaF=0.05mm in mode I
$      MID       RHO     ROFLG   INTFAIL        EN        ET       GIC      GIIC
         5    1.0E-4         0         1     41.92     41.92    0.0262    0.0524
$      XMU         T         S       UND       UTD
     2.000                           0.05  0.070711
$
*MAT_COHESIVE_MIXED_MODE_TITLE
interface IM-glass ; GIIc=2*GIc -- deltaF=0.05mm in mode I
$      MID       RHO     ROFLG   INTFAIL        EN        ET       GIC      GIIC
         6    1.0E-4         0         1      27.2      27.2    0.0170    0.0340
$      XMU         T         S       UND       UTD
     2.000                           0.05  0.070711
$
$                                    *  *  *  *  *  *  *
$
$                     ----------------------------------------------
$                     !                   Controls                 !
$                     ----------------------------------------------
$
$                                 ********************
$                            ***  TIME CONTROL KEYWORDS  ***
$                                 ********************
$
*CONTROL_TERMINATION
$   ENDTIM    ENDCYC     DTMIN    ENDNEG    ENDMAS     NOSOL
&endtim
*TERMINATION_NODE
$      NID      STOP      MAXC      MINC
$ node 12 is the node at the bottom of the impactor (x=y=0,z=0.1 at t=0)
$ termination happens when node 12 reaches z=5 after bouncing back from the plate
        12         3       5.0  -1.0e+20
$
*CONTROL_TIMESTEP
$   DTINIT    TSSFAC      ISDO    TSLIMT     DT2MS      LCTM     ERODE     MS1ST
       0.0&sf                                            99
*PARAMETER_EXPRESSION
$ “&begtim” is the time at which contact actually begins (0.1mm gap is assumed)
$ the purpose of the other variables is to momentarily decrease the time step when the
$ contact starts to avoid possible issues (large initial interpenetrations for instance)
R   begtim 0.1/&v0
R       t1 &begtim-0.50
R       t2 &begtim-0.49
R       t3 &begtim-0.06
R       t4 &begtim-0.05
R       t5 &begtim+1.00
R       t6 &begtim+1.50
R       t7 &begtim+2.00
R   fintim &begtim+&endtim
*DEFINE_CURVE_TITLE
time step control
$     LCID      SIDR       SFA       SFO      OFFA      OFFO    DATTYP
        99         0       1.0    1.0E+0       0.0       0.0         0
$      Abcissa(time)     Ordinate(tstep)
```

```
             0.0000              2.5e-2
&t1                              2.5e-2
&t2                              1.0e-2
&t3                              1.0e-2
&t4                              1.0e-3
&t5                              1.0e-3
&t6                              1.0e-2
&t7                              7.5e-2
&fintim                          7.5e-2
$
$                              ******************************
$                         ***  SOLUTION/MESH CONTROL KEYWORDS  ***
$                              ******************************
$
*CONTROL_SOLUTION
$     SOLN       NLQ     ISNaN     LCINT
                             1
$
*CONTROL_SOLID
$    ESORT    FMATRX   NIPTETS    SWLOCL    PSFAIL
                                           99
*SET_PART_LIST_TITLE
 psfail
$      SID       DA1       DA2       DA3       DA4
        99
$     PID1      PID2      PID3      PID4      PID5      PID6      PID7      PID8
         2         3         4
$
$                                  ********************
$                                ***  ARTIFICIAL VISCOSITY  ***
$                                  ********************
$
*CONTROL_BULK_VISCOSITY
$       Q1        Q2      TYPE
       1.5      0.06         1
$
$                                   *  *  *  *  *  *  *
$
$                     ------------------------------------------------
$                     !             Boundary Conditions              !
$                     ------------------------------------------------
$
$                                  ********************
$                                ***  BOUNDARY CONDITIONS  ***
$                                  ********************
$
*BOUNDARY_SPC_SET_ID
$     NSID       CID      DOFX      DOFY      DOFZ     DOFRX     DOFRY     DOFRZ
         1     clamped plate sides
         5         0         1         1         1         0         0         0
$
$                                   ****************
$                                ***  INITIAL VELOCITY  ***
$                                   ****************
$
*PARAMETER_EXPRESSION
R       vi   -&v0
*INITIAL_VELOCITY
$       ID    NSIDEX     BOXID    IRIGID
         1         0         0         0
$       VX        VY        VZ       VXR       VYR       VZR
```

```
      0.0       0.0&vi              0.0       0.0       0.0
$
$                                   *  *  *  *  *  *
$
$                    ------------------------------------------------
$                    !              Contact Definition              !
$                    ------------------------------------------------
$
$ SSTYP=MSTYP=0 <=> SEGMENT SET ID for SSID and MSID
$ SSTYP=MSTYP=2 <=> PART SET ID for SSID and MSID
$ SSTYP=MSTYP=3 <=> PART ID for SSID and MSID
$ SSTYP=MSTYP=4 <=> NODE SET ID for SSID and MSID
$
$                                    ***************
$                                ***  CONTACT CONTROL  ***
$                                    ***************
$
*CONTROL_CONTACT
$   SLSFAC    RWPNAL    ISLCHK    SHLTHK    PENOPT    THKCHG     ORIEN     ENMASS
                                                0                               0
$   USRSTR    USRFAC     NSBCS    INTERM     XPENE     SSTHK      ECDT   TIEDPRJ
                                                                     0
$
$                                    ****************
$                                ***  CONTACT KEYWORDS  ***
$                                    ****************
$
*CONTACT_ERODING_SINGLE_SURFACE_ID
$      CID          HEADING
         1          eroding frictionless contact
$     SSID      MSID     SSTYP     MSTYP    SBOXID    MBOXID       SPR       MPR
         0                 5                                       1         1
$       FS        FD        DC        VC       VDC    PENCHK        BT        DT
       0.0       0.0       0.0       0.0      20.0         0       0.0   1.0e+20
$      SFS       SFM       SST       MST      SFST      SFMT       FSF       VSF
       1.0       1.0       0.0       0.0       1.0       1.0       1.0       1.0
$     ISYM    EROSOP      IADJ
         0         1         1
$     SOFT    SOFSCL    LCIDAB    MAXPAR     SBOPT     DEPTH     BSORT    FRCFRQ
         2     0.500                                               1
$
*CONTACT_FORCE_TRANSDUCER_PENALTY_ID
$      CID          HEADING
        91          reaction force on impactor
$     SSID      MSID     SSTYP     MSTYP    SBOXID    MBOXID       SPR       MPR
         1                 3                                       1         1
$       FS        FD        DC        VC       VDC    PENCHK        BT        DT

$      SFS       SFM       SST       MST      SFST      SFMT       FSF       VSF

$
$                                   *  *  *  *  *  *  *
$
$                    ------------------------------------------------
$                    !            Data Output Settings              !
$                    ------------------------------------------------
$
$                                    **************
$                                ***  OUTPUT CONTROL  ***
$                                    **************
$
```

```
*CONTROL_OUTPUT
$    NPOPT    NEECHO    NREFUP    IACCOP     OPIFS    IPNINT    IKEDIT    IFLUSH
         1
$    IPRTF    IERODE     TET10    MSGMAX    IPCURV      GMDT
                   0
*CONTROL_ENERGY
$     HGEN      RWEN    SLNTEN     RYLEN
         2         2         2         2
*DATABASE_FORMAT
$    IFORM   IBINARY
                   1
$
*PARAMETER_EXPRESSION
R   t1safe 0.5*&begtim
R   tfsafe 10.0*&endtim
$
$ due to the initial gap betw. impactor and plate the output times are defined with a curve
$ the first output time (after t=0) is set when contact begins
$ the next ones are regularly spaced (“dtd3p” for d3plot, “dtAscii” for ASCII files)
$
*DEFINE_CURVE_TITLE
d3plot output
$     LCID      SIDR       SFA       SFO      OFFA      OFFO    DATTYP
        97         0       1.0       1.0       0.0       0.0         0
$      Abcissa(time)  Ordinate(interval)
                 0.0&begtim
&t1safe             &dtd3p
&endtim             &dtd3p
&tfsafe             &dtd3p
*DEFINE_CURVE_TITLE
Ascii output
$     LCID      SIDR       SFA       SFO      OFFA      OFFO    DATTYP
        98         0       1.0       1.0       0.0       0.0         0
$      Abcissa(time)  Ordinate(interval)
                 0.0&begtim
&t1safe             &dtAscii
&endtim             &dtAscii
&tfsafe             &dtAscii
$
$                                 *****************
$                              ***  STATE PLOT OUTPUT  ***
$                                 *****************
$
*DATABASE_BINARY_D3PLOT
$  DT/CYCL   LCDT/NR      BEAM     NPLTC    PSETID
                  97         0         0         0
$    IOOPT
         1
*DATABASE_EXTENT_BINARY
$              shell     shell              shell     shell     shell     shell
$    NEIPH     NEIPS    MAXINT    STRFLG    SIGFLG    EPSFLG    RLTFLG    ENGFLG
&hsvd3p            0         0         1         0         0         0         0
$   CMPFLG    IEVERP
         0         0
*DATABASE_RCFORC
$       DT    BINARY      LCUR     IOOPT
                           98         1
*DATABASE_BNDOUT
$       DT    BINARY      LCUR     IOOPT
                           98         1
$
```

```
$
*DATABASE_ELOUT
$       DT    BINARY      LCUR     IOOPT     NEIPH
                            98         1&hsvasc
*DATABASE_HISTORY_SOLID_SET
$      ID1       ID2       ID3       ID4       ID5       ID6       ID7       ID8
       999
$
*DATABASE_NODOUT
$       DT    BINARY      LCUR     IOOPT
                            98         1
*DATABASE_HISTORY_NODE_SET
$      ID1       ID2       ID3       ID4       ID5       ID6       ID7       ID8
       999
$
$                                  ******************
$                              ***  ENERGY DATA OUTPUT  ***
$                                  ******************
$
*DATABASE_MATSUM
$       DT    BINARY      LCUR     IOOPT
                            98         1
*DATABASE_GLSTAT
$       DT    BINARY      LCUR     IOOPT
                            98         1
*DATABASE_SLEOUT
$       DT    BINARY      LCUR     IOOPT
                            98         1
$
$                                    *  *  *  *  *  *  *
$
$                     ------------------------------------------------
$                     !         Geometry and Mesh Definition         !
$                     ------------------------------------------------
$
*SECTION_SOLID_TITLE
$  SECID    ELFORM       AET
 red. int.
       1         1         0
 S/R int.
       2         2         0
 full. int.
       3         3         0
 CZM
       4        19         0
$
*HOURGLASS_TITLE
$     HGID       IHQ        QM       IBQ        Q1        Q2    QB/VDC        QW
hg6(0.20)
         1         6      0.20
hg6(0.20)
         2         6      0.20
hg5(0.05)
         3         5      0.05
hg5(0.06)
         4         5      0.06
$
*PART
$      PID     SECID       MID     EOSID      HGID      GRAV    ADPOPT      TMID
impactor
         1         1        99         0         1         0         0         0
```

```
*DEFORMABLE_TO_RIGID
$      PID       MRB
         1         0
$
*PARAMETER_EXPRESSION
I   matCZM   &mat02+2
*PART
$      PID     SECID       MID     EOSID      HGID      GRAV    ADPOPT      TMID
layer 1
         2         1&mat01             0&mat01             0         0         0
adhesive
         3         1&mat02             0&mat02             0         0         0
layer 2
         4         1&mat03             0&mat03             0         0         0
CZM 1
         5         4&matCZM            0                   0         0         0
CZM 2
         6         4&matCZM            0                   0         0         0
$
$                                   *  *  *  *  *  *  *
$
$              ---------------------------------------------------------------
$              !          Nodes, Connectivity, Node- & Segment-Sets          !
$              ---------------------------------------------------------------
$
*INCLUDE
Meshfile.txt
$
$ description of “Meshfile.txt”:
$ contains list of nodes, element connectivity and node sets;
$ part 1: impactor
$ part 2: top layer
$ part 3: interlayer
$ part 4: bottom layer
$ part 5: flat elements at top layer-interlayer interface
$ part 6: flat elements at interlayer-bottom layer interface
$
$ node set 5 contains the nodes of the plate sides
$ node set 999 contains nodes whose information is printed in “nodout”
$ solid set 999 contains elements whose information is printed in “elout”
$
*END
```